

**Springer Theses**

Recognizing Outstanding Ph.D. Research

Amy Laura Parker

# InSAR Observations of Ground Deformation

Application to the Cascades Volcanic Arc



Springer

# **Springer Theses**

Recognizing Outstanding Ph.D. Research

## **Aims and Scope**

The series “Springer Theses” brings together a selection of the very best Ph.D. theses from around the world and across the physical sciences. Nominated and endorsed by two recognized specialists, each published volume has been selected for its scientific excellence and the high impact of its contents for the pertinent field of research. For greater accessibility to non-specialists, the published versions include an extended introduction, as well as a foreword by the student’s supervisor explaining the special relevance of the work for the field. As a whole, the series will provide a valuable resource both for newcomers to the research fields described, and for other scientists seeking detailed background information on special questions. Finally, it provides an accredited documentation of the valuable contributions made by today’s younger generation of scientists.

### **Theses are accepted into the series by invited nomination only and must fulfill all of the following criteria**

- They must be written in good English.
- The topic should fall within the confines of Chemistry, Physics, Earth Sciences, Engineering and related interdisciplinary fields such as Materials, Nanoscience, Chemical Engineering, Complex Systems and Biophysics.
- The work reported in the thesis must represent a significant scientific advance.
- If the thesis includes previously published material, permission to reproduce this must be gained from the respective copyright holder.
- They must have been examined and passed during the 12 months prior to nomination.
- Each thesis should include a foreword by the supervisor outlining the significance of its content.
- The theses should have a clearly defined structure including an introduction accessible to scientists not expert in that particular field.

More information about this series at <http://www.springer.com/series/8790>

Amy Laura Parker

# InSAR Observations of Ground Deformation

Application to the Cascades Volcanic Arc

Doctoral Thesis accepted by  
University of Bristol, UK

 Springer

*Author*

Dr. Amy Laura Parker  
Department of Spatial Sciences  
Curtin University  
Perth  
Australia

*Supervisors*

Dr. Juliet Biggs  
School of Earth Science  
University of Bristol  
Bristol  
UK

Prof. Kathy Cashman  
School of Earth Science  
University of Bristol  
Bristol  
UK

Prof. Tim J. Wright  
School of Earth and Environment  
University of Leeds  
Leeds  
UK

Prof. Zhong Lu  
Roy M. Huffington Department of Earth  
Sciences  
Southern Methodist University  
Dallas, TX  
US

ISSN 2190-5053

Springer Theses

ISBN 978-3-319-39033-8

DOI 10.1007/978-3-319-39034-5

ISSN 2190-5061 (electronic)

ISBN 978-3-319-39034-5 (eBook)

Library of Congress Control Number: 2016950747

© Springer International Publishing AG 2017

This work is subject to copyright. All rights are reserved by the Publisher, whether the whole or part of the material is concerned, specifically the rights of translation, reprinting, reuse of illustrations, recitation, broadcasting, reproduction on microfilms or in any other physical way, and transmission or information storage and retrieval, electronic adaptation, computer software, or by similar or dissimilar methodology now known or hereafter developed.

The use of general descriptive names, registered names, trademarks, service marks, etc. in this publication does not imply, even in the absence of a specific statement, that such names are exempt from the relevant protective laws and regulations and therefore free for general use.

The publisher, the authors and the editors are safe to assume that the advice and information in this book are believed to be true and accurate at the date of publication. Neither the publisher nor the authors or the editors give a warranty, express or implied, with respect to the material contained herein or for any errors or omissions that may have been made.

Printed on acid-free paper

This Springer imprint is published by Springer Nature

The registered company is Springer International Publishing AG

The registered company address is: Gewerbestrasse 11, 6330 Cham, Switzerland

*I dedicate this thesis to my Nana who, in our last conversation, told me to write down what I knew in a book one day. Well Nana, consider it done.*

# Supervisor's Foreword

Over two hundred volcanoes are known to be deforming, yet the processes responsible are unclear in many cases. Measurements of ground deformation from satellite radar have the potential to play a key role in understanding volcanic and magmatic processes throughout the eruption cycle.

In her thesis, Amy Parker approaches this problem in the context of the Cascades Volcanic Arc. The thesis starts with a technical review of the influence of atmospheric uncertainties on satellite maps of volcano deformation, and the use of regional-scale weather models to assess this a priori. Next, it presents detailed geodetic studies of two case studies: Medicine Lake Volcano and Lassen Volcanic Centre. Both systems are subsiding, but with contrasting characteristics. The observations are used to constrain a thermal model of cooling intrusions, a new approach to combining geophysical and petrologic observations. The novelty and range of topics covered in this thesis mean that it is a key work in volcanic and magmatic studies, which lays the foundations for future studies both in the Cascades and elsewhere.

The thesis acts as an introduction to volcano geodesy in general, and to the understanding of magmatic processes leading to deformation on decadal timescales. It combines novel methods of measuring and modelling deformation with new case studies of specific examples. The four chapters together present timely research into magmatic processes occurring on decadal timescales.

Bristol, UK  
Septemeber 2016

Dr. Juliet Biggs

**Parts of this thesis have been published in the following journal articles:**

**Parker, A. L.**, J. Biggs, and Z. Lu (2014), Investigating long-term subsidence at Medicine Lake Volcano, CA, using multitemporal InSAR, *Geophysical Journal International*, 199(2), 844–859, doi: [10.1093/gji/ggu304](https://doi.org/10.1093/gji/ggu304).

**Parker, A. L.**, J. Biggs, R. J. Walters, S. K. Ebmeier, T. J. Wright, N. A. Teanby, and Z. Lu (2015), Systematic assessment of atmospheric uncertainties for InSAR data at volcanic arcs using large-scale atmospheric models: application to the Cascade volcanoes, *Remote Sensing of Environment*, 170, 102–114, doi:[10.1016/j.rse.2015.09.003](https://doi.org/10.1016/j.rse.2015.09.003).



# Acknowledgments

I am touched by the number of people who deserve to be thanked for their role in my Ph.D. and my life over the last 4 years.

Juliet Biggs has been an inspirational supervisor and I thank her for always pushing me, for her patience, her guidance, her honesty, and her intellectual generosity. Zhong Lu hosted me at the Cascades Volcano Observatory for two memorable summers, and always offered his knowledge, guidance and support with a smile. Kathy's knowledge of the Cascade volcanoes has been a fantastic resource, and I have valued her encouragement and enthusiasm. Tim has also hosted me on numerous visits to Leeds, and has helped me to develop ideas throughout this thesis. I am lucky to have begun my research career under the supervision of such a talented and approachable group of people.

Susi Ebmeier has been an endless source of advice, and I thank her for patiently proof reading and providing feedback on many occasions in the last 2 years. I have also enjoyed collaborating with Rich and Catherine, both of whom were extremely generous with their time and encouragement. During trips to the US, the staff at the Cascades Volcano Observatory welcomed me and shared their knowledge, experience and passion for the Cascade volcanoes. Back in the UK, the Bristol Geophysics group has also been a great source of help and entertainment. Through drinking coffee and beer together, they have helped and encouraged me to broaden my own research interests, and I hope to continue working with them in the future.

My time in Bristol has been incredible. This city is an absolute pleasure to live in and has given so much to me. The friends I have made in the Wills Memorial Building have made coming to work each day a joy, and I hope to keep in touch with them as we go our separate ways. In particular, Hickey and Dave have joined me in every success and every frustration sat in G10. Maricel has given me so much warmth and laughter, and has been an absolute rock in supporting me throughout my early 20s. Brioch, Tom, Matt, KT, Jon and Jessie have also been fantastic friends in the office, in the pub, and whilst travelling. With the friendship and support of these people, I have grown as much as a person as I have a scientist, and it is with some sadness that I am finishing my time with them.

My Ph.D. has allowed me to begin to travel the world, and for that I am extremely thankful. I began this journey with a love of the United States, and two summers spent in Washington/Oregon only enriched this. Kristin, Vance, Quinn and Zia invited me into their home, and evenings spent looking out over the vines to Mount St. Helens will always be a fond memory. Scott, Dani, Bill and Cathy also allowed me to see more sides of this fantastic country. In my third year I participated in fieldwork in Ethiopia, which I found to be a vibrant, beautiful and humbling place. The experience I have gained in Bristol has given me the confidence and opportunity to continue travelling, and I now move on to Australia, where I will continue my research.

My family has been, and always will be, the foundation behind anything I do. I thank them for being proud of me and for sharing my sense of achievement in completing this thesis. I also thank Hugo, whose dreams are as big as mine, and whose patience and optimism helped to keep me smiling to the very end. You put the wind in my hair and the seasalt on my skin, and without you I imagine this would all be ending very differently.

# Contents

<b>1</b>	<b>Introduction</b>	1
1.1	Motivation	1
1.2	InSAR	2
1.3	InSAR Observations of Ground Deformation at Volcanoes	8
1.4	The Cascades Volcanic Arc	9
1.4.1	Tectonic Setting	10
1.4.2	Magma Production and Storage	10
1.4.3	Monitoring	11
1.5	Thesis Structure	14
	References	17
<b>2</b>	<b>Investigating Long-Term Subsidence at Medicine Lake Volcano, CA, Using Multi Temporal InSAR</b>	25
2.1	Introduction	26
2.1.1	Tectonic and Geological Setting	28
2.1.2	Previous Studies of Ground Deformation at Medicine Lake Volcano	28
2.2	InSAR Data and Interferogram Formation	29
2.2.1	Coherence	30
2.2.2	Sources of Noise	30
2.3	InSAR Methods	35
2.3.1	Stacking	35
2.3.2	Poly-Interferogram Rate and Time-Series Estimator ( $\pi$ -RATE)	37
2.3.3	Persistent Scatterer InSAR (PSInSAR)	38
2.4	Results of Multi Temporal InSAR Analysis Techniques	38
2.4.1	Stacking	39
2.4.2	$\pi$ -RATE	39
2.4.3	PSInSAR	40
2.4.4	Comparison to Past Geodetic Studies	42
2.4.5	Horizontal and Vertical Displacements	43

2.5	Modelling: Estimates of Source Geometry and Volume Change . . . . .	45
2.5.1	Selection of InSAR Data for Use in Modelling. . . . .	47
2.5.2	Point Source . . . . .	47
2.5.3	Sills. . . . .	47
2.6	Discussion . . . . .	50
2.6.1	Causes of Subsidence . . . . .	51
2.7	Conclusions . . . . .	52
	Appendix . . . . .	53
	References. . . . .	54
<b>3</b>	<b>Systematic Assessment of Atmospheric Uncertainties for InSAR Data at Volcanic Arcs Using Large-Scale Atmospheric Models: Application to the Cascade Volcanoes. . . . .</b>	<b>59</b>
3.1	Introduction . . . . .	59
3.1.1	The Cascades Volcanic Arc . . . . .	60
3.2	Atmospheric Noise in InSAR Studies at Volcanoes . . . . .	61
3.2.1	Causes and Effects . . . . .	61
3.2.2	Atmospheric Corrections for Volcano InSAR Studies. . . . .	63
3.3	Methods . . . . .	65
3.3.1	InSAR. . . . .	65
3.3.2	Atmospheric Models . . . . .	66
3.4	Case Study Volcanoes . . . . .	68
3.4.1	Comparison Between ERA-I and NARR . . . . .	68
3.4.2	Correcting Stratified and Turbulent Atmospheric Delays Using NARR. . . . .	69
3.5	Arc-Wide Assessment of Atmospheric Uncertainties . . . . .	72
3.5.1	Method . . . . .	72
3.5.2	Elevation-Delay Gradients. . . . .	74
3.5.3	Temporal Atmospheric Variability . . . . .	74
3.6	Discussion . . . . .	75
3.6.1	Detection Thresholds for InSAR Studies at the Cascade Volcanoes . . . . .	78
3.6.2	Applicability to Regional Volcano InSAR Studies . . . . .	81
3.7	Conclusions . . . . .	82
	Appendix . . . . .	83
	References. . . . .	86
<b>4</b>	<b>Time Constraints on Magma Intrusion from Thermal Models of Long-Term Subsidence: Medicine Lake Volcano, CA . . . . .</b>	<b>91</b>
4.1	Introduction . . . . .	91
4.2	Model Setup. . . . .	94
4.3	Results . . . . .	97
4.3.1	Evolving Crystal Assemblage . . . . .	98
4.3.2	Parameter Space Exploration. . . . .	100

- 4.4 Application to Medicine Lake Volcano . . . . . 105
  - 4.4.1 Model Constraints . . . . . 107
  - 4.4.2 Comparison to the Geodetic Record . . . . . 108
  - 4.4.3 Constraints upon Magma Intrusion at Medicine Lake Volcano . . . . . 108
- 4.5 Additional Factors . . . . . 111
  - 4.5.1 Incremental Magma Intrusion . . . . . 111
  - 4.5.2 Convection . . . . . 113
  - 4.5.3 Gas Loss . . . . . 113
- 4.6 Discussion . . . . . 115
  - 4.6.1 Further Applications . . . . . 116
- 4.7 Conclusions . . . . . 117
- References. . . . . 118
- 5 Constraining Mechanisms of Volcanic Subsidence at Lassen Volcanic Center, CA, Using InSAR. . . . . 125**
  - 5.1 Introduction . . . . . 125
    - 5.1.1 Tectonic and Geological Setting . . . . . 126
    - 5.1.2 Hydrothermal and Seismic Activity. . . . . 127
  - 5.2 Methods . . . . . 129
    - 5.2.1 InSAR Data and Processing . . . . . 129
    - 5.2.2 Stacking . . . . . 130
    - 5.2.3 Source Modelling . . . . . 131
    - 5.2.4 Time-Series . . . . . 132
  - 5.3 Results . . . . . 134
    - 5.3.1 Stacking . . . . . 134
    - 5.3.2 Source Modelling . . . . . 135
    - 5.3.3 Time-Series of Source Volume Change . . . . . 137
    - 5.3.4 Comparison with Past Geodetic Measurements . . . . . 140
  - 5.4 Discussion . . . . . 140
    - 5.4.1 Comparison with Medicine Lake Volcano . . . . . 140
    - 5.4.2 Causes of Subsidence at LaVC . . . . . 141
  - 5.5 Conclusions . . . . . 144
- Appendix . . . . . 144
- References. . . . . 145
- 6 Summary and Outlook . . . . . 151**
  - 6.1 Application of InSAR Data in the Cascades Volcanic Arc . . . . . 151
  - 6.2 Volcano Deformation in the Southern Cascades . . . . . 154
  - 6.3 Long-Term Volcanic Subsidence . . . . . 155
  - 6.4 Future Role of InSAR in Volcanology . . . . . 156
  - References. . . . . 157
- Curriculum Vitae . . . . . 161**

# Author Contributions

Juliet Biggs provided supervision throughout all chapters of this thesis. All InSAR data were obtained from the WInSAR data archive and Alaska SAR Facility. Additional guidance and datasets were received during visits to the U.S. Geological Survey from Z. Lu, M. Poland, D. Dzurisin, M. Lisowski, and D. Ramsey. Support using InSAR analysis software was received from H. Wang ( $\pi$ -RATE), D. Bekaert, K. Spaans and A. Hooper (StaMPS). N.A. Teanby provided assistance in formatting atmospheric reanalysis data used in Chap. 3, and R. J. Walters then provided the codes used to produce atmospheric phase screens, which were modified for application to NARR. C. Annen provided the thermal model used in Chap. 4.

# Chapter 1

## Introduction

Measurements of ground deformation have been used by geodesists to investigate natural and man-made phenomena since the 19th century. Since the early 1990s, Interferometric Synthetic Aperture Radar (InSAR) has changed the way that geodesists view the Earth, facilitating deformation monitoring in remote and inaccessible locations, and providing insight into spatially and temporally complex processes. Unsurprisingly, InSAR observations have pushed forth a new era in volcano deformation studies from both a monitoring and research perspective.

InSAR observations of volcanic ground deformation enable the detection of subsurface magma, and therefore play a key role in eruptive hazard assessments. However, these observations have also shed new light on all aspects of volcanic behaviour, contributing to our understanding of the eruption cycle, hydrothermal systems and the formation of continental crust. One of the most significant achievements of volcano InSAR has been the identification and characterisation of magma inputs into the crust that would have otherwise gone unnoticed (e.g. Lu and Dzurisin 2014). Such observations of magma movement and other slow, long-term processes are crucial in determining how magmatic plumbing develops and evolves beneath a volcano (Dzurisin 2003; Cashman and Biggs 2014), but the mechanism responsible is often ambiguous.

### 1.1 Motivation

The application of InSAR in volcanic environments is often challenging, and in order for these observations to be a useful tool in volcanology we require (1) better ways of detecting low magnitude deformation signals and (2) physically reasonable ways of interpreting commonly observed deformation signals. A significant number of volcanoes have exhibited periods of subsidence over decadal time-scales (Fig. 1.1), but the mechanisms driving such deformation remain poorly understood. Whilst long-term volcanic subsidence is not immediately linked to eruption, it can be used to provide insight into magma storage conditions and longer-term processes related to tectonic

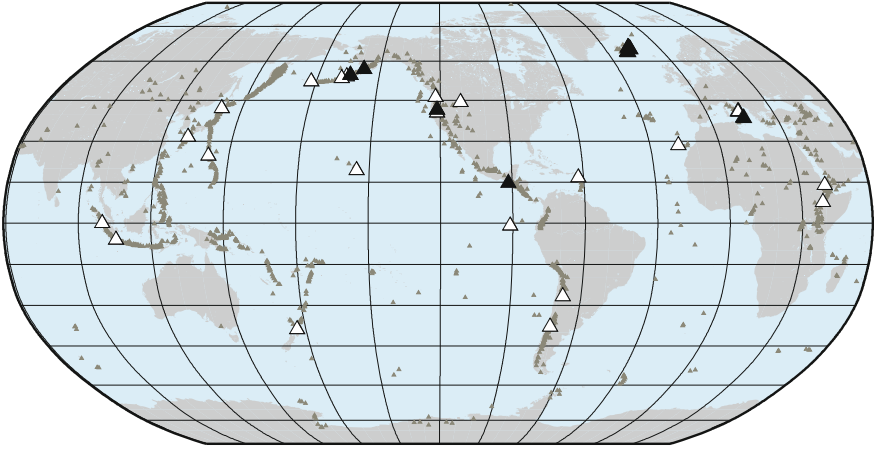


**Fig. 1.1** Global map of subsiding volcanoes. *Small triangles* mark the Holocene volcanoes from the global volcanism database of the Smithsonian Institution. *White triangles* mark volcanoes that have subsided as observed using InSAR. *Black triangles* mark volcanoes where subsidence is attributed to cooling and crystallisation of magmatic material, which is the focus of Chap. 4

setting, hydrothermal systems, and the building of crustal plutons. The Cascades Volcanic Arc contains three volcanoes that have exhibited subsidence for >10 years, and therefore presents an ideal place to add to observations of, and constrain the driving mechanisms behind, long-term volcanic subsidence.

In this thesis I therefore focus on the application of InSAR to the Cascades Volcanic Arc and the processes that cause long-term volcanic subsidence. In this introduction, I first provide a brief description of InSAR (Sect. 1.1) and its role in volcanology (Sect. 1.2), before introducing the Cascades Volcanic Arc (Sect. 1.3). In Chaps. 2 and 3, I address the challenges involved in making InSAR measurements in this setting. In Chaps. 4 and 5, I then use two examples from the southern Cascades to add to the known examples of volcanic subsidence, and develop a new modelling approach to characterise the long-term geodetic response to cooling magma intrusions.

## 1.2 InSAR

InSAR is an active satellite-based remote sensing tool capable of measuring mm-scale ground displacements at a spatial resolution of <5–10 s meters over large (100 km-scale) regions. InSAR has captured ground deformation resulting from the earthquake cycle (Wright 2002); aquifer depletion (Galloway and Burbey 2011); landslides (Ye et al. 2004); mining collapse (Plattner et al. 2010); underground storage of CO<sub>2</sub> (Vasco et al. 2010); cryospheric processes (Goldstein et al. 1993); and the eruptive



**Table 1.1** SAR satellite systems used in this study and that are currently operational

Satellite	Operator	Repeat interval (days)	Band	Resolution <sup>a</sup> (m)	Dates
ERS 1/2	ESA	35	C	30	1992–2000
ENVISAT	ESA	35	C	30	2002–2012
ALOS	JAXA	46	L	10	2007–2011
Sentinel-1A	ESA	12	C	5 × 5	2014–present
ALOS 2	JAXA	14	L	3–10	2014–present
TerraSAR-X	DLR	11	X	3	2008–present
COSMO-SkyMed	ASI	16 (1, 3, 4, 8)	X	3 × 3	2008–present
RADARSAT 2	CSA	24	C	1 × 3	2008–present

*Top* Satellite systems used in this study. *Bottom* satellite systems currently operational

Satellite wavelengths: X band -  $\sim 3.1$  cm; C band -  $\sim 5.6$  cm; L band -  $\sim 23.5$  cm

<sup>a</sup>Single look in stripmap mode

cycle (Pinel et al. 2014). Unlike ground-based geodetic techniques such as leveling or GPS campaigns, InSAR imagery is capable of capturing the full extent and spatial complexity of the deformation field. The technique is cost effective, replacing long field campaigns with repeat satellite imagery available in increasingly small time intervals (Table 1.1). The remote nature of InSAR also enables measurements to be made in locations that are inaccessible, remote, or hazardous (e.g. Wauthier et al. 2013). The success of InSAR in measuring many processes, notably earthquakes and sudden eruptions, has also lain in the ability to design experiments in retrospect due to the semi-regular acquisition schedule of satellites.

Here we focus on the use of Synthetic Aperture Radar (SAR) imagery to measure displacements of Earth’s surface due to subsurface volcanic processes, but advances have also been made in using SAR derived products to measure topographic change (Wadge et al. 2010), the emplacement of lava flows (Dietterich et al. 2012), and shallow-seated flank instabilities (Ebmeier et al. 2014). This thesis utilises a large archive of InSAR data acquired for the Cascade volcanoes between 1992–2011 by European Space Agency (ESA) satellites ERS-1/2 and ENVISAT, and the Japanese Aerospace Exploration Authority (JAXA) satellite ALOS. These systems are no longer operational, but lay the basis for future studies using the 5 SAR satellite systems currently in orbit (Table 1.1).

Several reviews describe SAR and SAR interferometry in detail (e.g. Massonnet and Feigl 1998; Rosen et al. 2000; Hanssen 2001; Bürgmann et al. 2000; Simons and Rosen 2007), and standard processing packages are now available on both an open access (e.g. ROI\_PAC: Rosen et al. 2004) and commercial (e.g. GAMMA: Werner et al. 2000) basis. Here I provide a brief overview of SAR, including the steps used to produce high resolution radar images. I describe how SAR images are then combined to produce interferograms, and introduce the limitations of using this method in volcanic settings.

## Synthetic Aperture Radar

SAR satellites travel in a quasi-polar orbit that is either ascending (south - north) or descending (north - south). Imagery is acquired in a side-looking geometry to eliminate ambiguities between points on the left and right of the satellite (Fig. 1.2). The satellite looks down to the Earth's surface at an oblique angle ( $\sim 10\text{--}50^\circ$ ), recording information in the satellite line of sight (LOS). Like conventional radar, SAR operates by illuminating the target (in this case Earth's surface) with microwave pulses (frequency 0.3–300 GHz). The microwave pulses are reflected from scatterers on Earth's surface and received back at the antenna as a set of complex numbers recording both an amplitude and a phase. The amplitude is dependent upon the reflectivity of the Earth's surface, including terrain slope and surface roughness, whereas the phase records many different effects, and essentially varies randomly between  $0\text{--}360^\circ$  (Massonnet and Feigl 1998).

A focussed SAR image is produced by applying range (across track) and azimuth (along track) compression to focus the raw radar echoes (Elachi 1988; Curlander and McDonough 1991). Range resolution of the radar image,  $\Delta R_g$ , is limited by the radar pulse duration,  $\tau$ , according to:

$$\Delta R_g = \frac{c\tau}{2\sin\theta}, \quad (1.1)$$

where  $c$  is the speed of light and  $\theta$  is the incidence angle. To achieve a resolution of  $<5\text{--}10$  m requires very short pulse durations (50 ns), but the power supply of such a short pulse is not large enough to give the returned pulse a sufficient signal-to-noise ratio. Instead, a chirped (frequency modulated) pulse is used, and the required range resolution is achieved using a technique called range compression, described by Hanssen (2001). The range compressed signal with bandwidth  $B_r$  has a shorter effective pulse length,  $\tau_e$ , equal to  $1/B_r$ . The resolution then becomes:

$$\Delta R_r = \frac{c}{2B_r\sin\theta}. \quad (1.2)$$

Focussing in the azimuth direction utilises the synthetic aperture of the radar, achieved by having a moving antenna. Azimuth resolution,  $\Delta A_g$ , is limited by the antenna length,  $L_a$ , and the slant range of the satellite orbit,  $R_m$ :

$$\Delta A_g = R_m \frac{\lambda}{L_a}, \quad (1.3)$$

where  $\lambda$  is the satellite wavelength (for values see Table 1.1). To achieve a resolution comparable to that in the across track direction would require an antenna on the order of 5 km for a satellite orbiting at  $\sim 800$  km (Bürgmann et al. 2000). Instead, a synthetic aperture is used by combining a series of consecutive radar pulses that illuminate the same point on the ground. The echoes from a given point are isolated using the two-way travel time of the radar pulse, which defines a circle of equal distances on the ground directly beneath the satellite (Fig. 1.2). Doppler frequency shifts, which

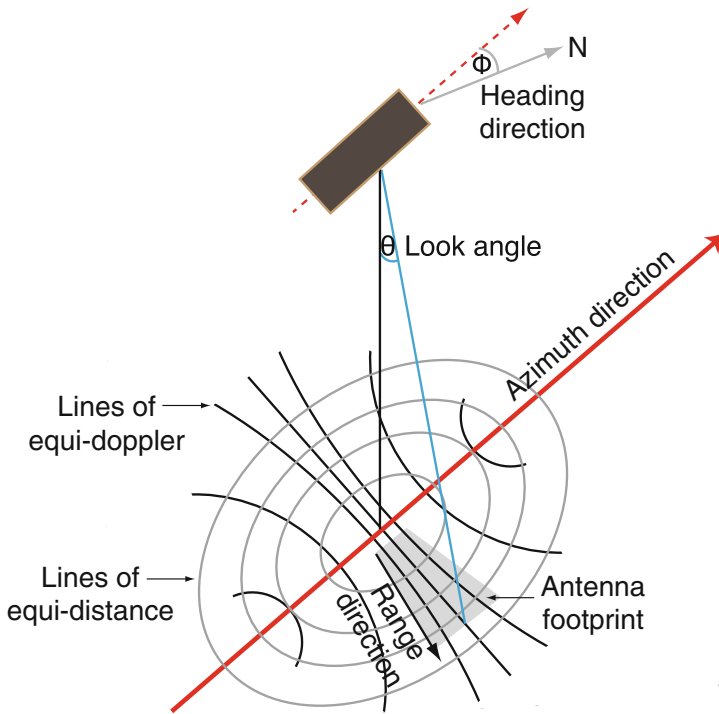


**Fig. 1.2** SAR satellite geometry for a right-looking, ascending (south–north) orbit adapted from Massonnet and Feigl (1998). Position of the returned radar echoes are determined using the two way travel time, as shown by *lines* of equi-distance. Doppler frequency shifts are then used to sort samples in the azimuth direction

occur as the antenna moves along track, are then used to define a hyperbola of equal Doppler on the ground (Fig. 1.2). The location of the target is identified by finding the overlap between the two. By using an antenna of synthetic aperture, the resolution in azimuth is improved by 3 orders of magnitude from 5–10 km to <5–10 m.

As described, targets on the ground are identified by the range between the target and the satellite. In regions of significant topography, geometrical distortions occur. Layover, where returns from scatterers at high elevations occur before returns from scatterers in low-lying areas, displaces the top of mountains, and shadow occurs as the radar beam is blocked by topography. These effects are particularly problematic at steep-sided stratovolcanoes, but may be reduced by using a larger look angle (Pinel et al. 2011).

### Interferogram Formation and Sources of Error

Interferograms are produced using two focussed SAR images, a master and slave, that cover the same area and are aligned to within a fraction of a pixel. The master image is multiplied by the complex conjugate of the slave image, and the interferogram

amplitude is therefore the amplitude of the master multiplied by the amplitude of the slave, whereas the interferogram phase is the phase difference between the two.

As previously described, the phase of a pixel within a SAR image is based upon the contribution from many scatterers distributed within the corresponding ground resolution element (Fig. 1.3) and is random. If the scattering characteristics of the ground remain the same in the time period between the two acquisitions, differencing the two SAR images would remove the random contribution. However, in reality changes in the phase response of scatterers causes the scatterer contributions to sum differently (Zebker and Villasenor 1992). This is quantified by interferometric correlation,  $\gamma$ , which measures the coherence of a group of pixels in, for example, a  $3 \times 3$  window. Stable targets act as coherent backscatterers with  $\gamma = 1$ , whereas pixels with a phase response independent between two acquisitions are incoherent,  $\gamma = 0$  (Seymour and Cumming 1994). The most dominant sources of incoherence are environmental changes over time (temporal decorrelation), caused by vegetation, unstable volcanic deposits, or snow cover. Larger scatterers, such as outcrops or buildings, tend to be more stable than smaller scatterers, such as leaves. As more energy is returned from scatterers that are comparable to the radar wavelength, L-Band satellites (Table 1.1) exhibit the least temporal decorrelation (Massonnet et al. 1996; Rosen et al. 1996). Geometrical decorrelation occurs due to differences in the satellite viewing geometry between orbits. Total decorrelation occurs when the difference in path length across a pixel is greater than the radar wavelength,  $\lambda$  due to a large topographic slope ( $\zeta$ ), such as at a steep-sided stratovolcano, or when there is a large spatial separation (baseline) between satellite orbits. The critical baseline,  $B_{crit}$ , is the perpendicular baseline above which complete decorrelation occurs:

$$B_{crit} = \frac{\lambda R_m \tan(\theta - \zeta)}{2 \Delta R_m}. \quad (1.4)$$

Thus interferogram decorrelation increases with the temporal- or spatial-separation between acquisitions. Small baseline (SB) approaches therefore use interferograms with short spatial and temporal baselines to minimise changes in the phase contributions from scatterers and overcome decorrelation (Berardino et al. 2002; Schmidt and Bürgmann 2003). This is the approach used to produce interferograms in this thesis. Decorrelation is further reduced by applying a power spectrum filter (Goldstein and Werner 1988). The result may then be multi-looked by averaging in range and azimuth to increase the signal to noise ratio and produce square pixels.

Some ground elements may contain a persistently dominant scatter with a phase response that varies little over time, despite changes in surrounding scatterers. This is referred to as a persistent scatterer (PS) (Hooper et al. 2004, 2007), (Fig. 1.3). PSInSAR describes a different way of selecting pixels by assessing phase variance in either time (e.g. Ferretti et al. 2001) or space (e.g. Hooper et al. 2004). The former requires an a priori model of the deformation in time. The latter utilises iterative spatial bandpass filtering to estimate the spatially correlated component of phase. The spatially correlated component is subtracted, and residual DEM errors for the whole dataset are modelled and then also removed. This isolates the contribution due

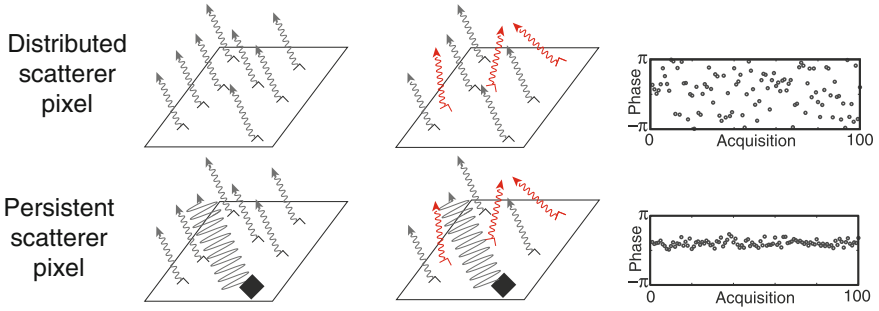


**Fig. 1.3** Schematic comparing the phase response of distributed and persistent scatterers. Adapted from Hooper et al. (2007)

to noise, which is not correlated in either space or time (Hooper et al. 2004). PS pixels are those where the noise term is small enough that it does not completely obscure the signal (Hooper et al. 2007). This approach of selecting PS pixels provides better coverage of PS in rural environments (Sousa et al. 2011), and is more suitable for measuring deformation that is non-linear in time (Hooper et al. 2012).

PS pixels are not necessarily coherent in SB interferograms, and distributed scatterer pixels coherent in SB interferograms are not necessarily identified as PS. Methods have therefore been developed to combine both approaches to optimise interferogram coherence (Hooper 2008; Ferretti et al. 2011). PSInSAR has been successfully applied in a number of volcanic settings (e.g. Pinel et al. 2011; Ofeigsson et al. 2011) including Three Sisters in the Oregon Cascades (Riddick and Schmidt 2011), and this method is implemented in Chap. 2.

The interferogram phase,  $\phi_{LOS}$ , is dependent upon path length, which can be used to measure ground deformation. In addition to the component caused by deformation of Earth's surface ( $\Delta\phi_{def}$ ),  $\phi_{LOS}$  contains several nuisance terms:

$$\phi_{LOS} = \Delta\phi_{def} + \Delta\phi_{geom} + \Delta\phi_{topo} + \Delta\phi_{atm} + \phi_{error}. \quad (1.5)$$

The term  $\Delta\phi_{geom}$  arises due to differences in the satellite viewing geometry. Precise orbits are used to estimate the perpendicular baseline between satellite orbits, and the effects of baseline separation are initially removed during processing by approximating the surface of the earth to be a smooth ellipsoid. However, errors in the predicted satellite orbit occur due to e.g. solar radiation pressure (Ziebart et al. 2005), resulting in a residual, long wavelength phase ramp (Zebker et al. 1994). Empirical corrections used to remove this error contribution are discussed in Chap. 2. A digital elevation model (DEM) is also used during processing to remove the phase arising from topography. However, any discrepancies between the DEM and the true topography generates phase errors that also contribute to  $\Delta\phi_{geom}$ .

The largest sources of error are phase changes due to variations in the refractivity of the atmospheric between acquisitions ( $\Delta\phi_{atm}$ ). Methods of identifying and quantifying atmospheric errors are introduced in Chap. 2, with a more thorough

discussion of cause, effects, and mitigation in Chap. 3.  $\phi_{error}$  is an additional noise term describing phase noise due to variations in scattering and instrument thermal noise.

The interferogram phase is initially wrapped (modulo  $2\pi$ ), where a phase change of  $2\pi$  is equal to ground motion with magnitude of  $\lambda/2$ . For the SB interferograms produced in this thesis, phase unwrapping is implemented by masking pixels with  $\gamma < 0.1$  and integrating the phase gradient using a branch-cut algorithm (Goldstein and Werner 1988). The integrated field should be conservative i.e. the integral around a closed loop should be zero. Non-zero path integrals are identified, and regions with adjacent positive and negative residues are cut and cannot be integrated across, with phase integration continuing along another path (Goldstein and Werner 1988). Where coherence is discontinuous, the phase difference between neighbouring coherent patches can be estimated and bridged. To convert to displacement, the phase is multiplied by  $-\lambda/4\pi$ , where  $\lambda$  is the satellite wavelength, and the negative sign follows the convention that movement towards the satellite (uplift) is positive.

### 1.3 InSAR Observations of Ground Deformation at Volcanoes

InSAR has been used to make observations of ground deformation at over 500 volcanoes worldwide (Biggs et al. 2014). These observations have been used in making timely hazard assessments, and to better understand the behaviour of volcanoes throughout the eruptive cycle. A recent review by Pinel et al. (2014) summarises the volcanological insights and advances resulting from the last 2 decades of volcano InSAR studies. This includes the detection of magma storage regions and characterisation of storage geometries, which may involve multiple components (e.g. Kilauea: Baker and Amelung 2013). Pathways of magma transport have also been mapped (e.g. Yellowstone: Wicks et al. 1998), with measurements showing the role of faults in segregating magmatic fluids (e.g. Chaiten: Wicks et al. 2011). Prior to eruption, magmatic intrusions may link to open conduits, where viscous flow induces near field displacements (e.g. Mount St Helens: Anderson et al. 2010). Surface deformation may also originate from shallow hydrothermal systems, where cyclical displacements reveal the formation and breaching of a self sealing zone (e.g. Campi Flegrei: Chiodini et al. 2015).

In all cases, the interpretation of volcano deformation signals requires the use of modelling. Simple analytical source models embedded in an isotropic, elastic half space are an established, quick to use, and widely applicable way of providing first order constraints upon the source of deformation (Mogi 1958; Okada 1985; Fialko et al. 2001a). Whilst these models do not account for crustal heterogeneities or rheological variations, they provide a remarkably good fit to deformation signals at volcanoes in a range of tectonic settings (Dzurisin 2007; Segall 2010). The results of analytical source modelling have also been used as input to other models, which

is the approach taken in Chap. 4. Examples include linking intrusion geometry with coulomb stress models to investigate the stresses induced by magma bodies (e.g. Jónsson 2009). This provides a mode of combining deformation measurements with other datasets such as seismicity or petrology.

When more information about crustal structure is available, finite element modelling (FEM) may be used to allow for irregular source geometries, crustal layering, and non-elastic crustal rheology. This approach has been successful in detailed studies of individual cases such as Uturuncu, Bolivia (Hickey et al. 2013) and the Socorro magma body, New Mexico (Pearse and Fialko 2010). However, these models require a large number of parameters such that testing the parameter space, obtaining useful error estimates, and accounting for non-unique solutions, remains challenging (Pyle et al. 2013). Other important factors to consider when modelling magmatic sources include the compressibility of the magma (Mastin et al. 2009), and the role of pre-existing structures that act to focus crustal stresses.

Of the catalogue of volcano deformation measurements, an increasing number are derived from systematic surveys on the scale of volcanic arcs e.g. Central America: (Ebmeier et al. 2013b); Central Andes: (Pritchard and Simons 2004a); and Sunda: (Chaussard and Amelung 2012). Measurements made on these scales are not only advantageous for regional hazard monitoring, but also facilitate investigations into volcano-tectonic interactions (e.g. Biggs et al. 2009b), global patterns of magma storage depth (Biggs et al. 2014), and the fundamental controls upon magma storage (Chaussard and Amelung 2014). Regional studies have also identified unrest at volcanos previously thought to be quiescent (e.g. Biggs et al. 2009a) and off edifice deformation that may not have been identified by ground based surveys centered on the edifice (e.g. Three Sisters, Oregon: Riddick and Schmidt 2011). Recent increases in the number of deformation observations means we are beginning to address questions in volcanology on either a case-by-case or generalised basis, identifying possible commonalities in behaviour (Chaussard and Amelung 2014) whilst also highlighting the unique and changing behaviour of individual systems (Cashman and Biggs 2014).

## 1.4 The Cascades Volcanic Arc

The Cascades Volcanic Arc dominates the topography of the western U.S., spanning over 1000 km from northern California to southern British Columbia. Throughout Washington, Oregon and California, the arc consists of 21 Holocene volcanos (as recognised by the global volcanism database of the Smithsonian Institution), but over 3400 Quaternary vents have been identified (Hildreth 2007). As is observed for other volcanic arcs (e.g. Central America: Stoiber and Carr 1973; Burkart and Self 1985), the Cascade volcanoes are separated into segments: (1) the Garibaldi Volcanic Belt, (2) Mount Rainier to Mount Hood, (3) the rest of the Oregon Cascades, (4) the Mount Shasta region, and (5) the Lassen region (Guffanti and Weaver 1988) (Fig. 1.4).

### ***1.4.1 Tectonic Setting***

The Cascades Volcanic Arc marks the western rim of the Pacific Ring of Fire at the boundary between the North American and Pacific plates. The relative motion between these plates is largely accommodated by spreading at the Juan de Fuca Ridge and subduction beneath Cascadia (Fig. 1.4), but 20–25% of the motion is distributed within the overriding continental plate as block rotations and translations, the most significant of which is the clockwise rotation of Oregon (Wilson 1993; Wells et al. 1998), (Fig. 1.5).

In California, plate motion is dominated by the movement of the Pacific plate northwest relative to North America at a rate of  $\sim 50$  mm/yr (Atwater 1970). This motion is taken up on the San Andreas fault and the Walker Lane fault zone, a broad and discontinuous region of faulting that impinges upon the southernmost Cascade volcanoes (Hammond and Thatcher 2005; Wesnousky 2005). Between the Lassen and Shasta arc segments, dextral shear transitions to clockwise block rotation of Oregon (Simpson and Cox 1977), reflecting the transition from a strike-slip to convergent plate boundary (McCaffrey et al. 2007).

Convergence between the Juan de Fuca and North America plates increases from 30 mm/yr off the coast of Oregon, where subduction is margin-oblique, to 45 mm/yr off the coast of Washington, where subduction is arc-normal (Wilson 1993; McCaffrey et al. 2007). North of  $\sim 48^\circ$ , the subduction zone exhibits trenchward-concave curvature, and the Juan de Fuca plate bends into an arc plunging eastwards, as imaged by seismicity and seismic tomography (Crosson and Owens 1987; Weaver and Baker 1988; Bostock and VanDecar 1995).

In the north of the arc, northward movement of the 400 km long Oregon block causes shortening (Wells et al. 1998) (Fig. 1.5). In the southern Cascades, the block rotation of Oregon creates extension along the trailing edge. This is further facilitated by westward migration of the east-west extensional Basin and Range province, located east of the Cascades axis (e.g. Wells et al. 1998; McCaffrey et al. 2007). Consequently, extension plays a significant role in Cascade volcanism (Guffanti and Weaver 1988), vent distributions and hydrothermal heat discharge (Ingebritsen and Mariner 2010), and is thought to be a controlling factor in segmentation of the arc (Hildreth 2007). For example in the southern Cascades, faulting in the gaps between arc segments indicates northwest-southeast dextral motion, whereas the volcanic centres are seen to be dominated by north-south orientated normal faults that facilitate extension (Blakely et al. 1997; Janik and McLaren 2010).

### ***1.4.2 Magma Production and Storage***

Magma production and extrusion throughout the history of the Cascades Volcanic Arc is thought to be a function of convergence rate and upper plate stress regime (Priest 1990): lower eruption volumes are linked to slower, more oblique subduc-



tion (Verplanck and Duncan 1987), and high erupted volumes are related to extension (Priest 1990). The relatively large across-axis width of the arc (up to 100 km) is thought to imply the widespread availability and penetration of basaltic magma (Hildreth 2007). Where the arc is widest, e.g. the Lassen segment (Fig. 1.4), extreme subduction-component-enriched magmas occur in the fore-arc, and more intraplate magmas occur in the back-arc (Bacon et al. 1997).

There are at least 3 end-member primitive magma sources throughout the Cascades Volcanic Arc (Bacon et al. 1997). Primitive high-Al olivine tholeiite (comparable to mid-oceanic ridge basalt) is erupted from northern California as far north as southern Washington, with vents marked by low shield summits, pit craters and small spatter cones (Bacon et al. 1997). These magmas are related to high-temperature, extensional environments (e.g. Donnelly-Nolan 1988), and are thought to result from nearly anhydrous melting of depleted mantle that had previously been enriched with a subduction component (Donnelly-Nolan et al. 1991; Baker et al. 1994). More silicic calc-alkaline (arc) basalts and basaltic andesites are abundant at the arc-axis (Bacon et al. 1997). These higher viscosity, lower temperature lavas, have higher H<sub>2</sub>O contents due to the transport of H<sub>2</sub>O to the mantle wedge during subduction (Brandon and Draper 1996). Variations in the concentration of SiO<sub>2</sub> and incompatible elements varies with latitude throughout the arc, and is thought to be associated with the enrichment of a third, subduction component (Bacon et al. 1997). More evolved erupted products including dacites (e.g. Mount St Helens: Pallister et al. 2008) and rhyolites (e.g. Medicine Lake Volcano: Grove et al. 1997), are thought to originate from mafic crustal inputs (Hildreth 1981) and have been produced by magma mixing, fractional crystallisation and crustal melting (the FARM model: Baker et al. 1991).

Petrological and geophysical studies throughout the Cascades provide evidence of magma storage at depths of ~7–10 km e.g. Mount St Helens: (Rutherford et al. 1985; Pallister et al. 1992; Scandone and Malone 1985; Moran 1994); cinder cones near North Sister: (Ruscitto et al. 2010); Mount Rainier: (Venezky and Rutherford 1997); Three Sisters: (Riddick and Schmidt 2011). Magma storage is thought to occur on a relatively small scale. For example at Mount St Helens, melt-rich magma is thought to be stored in a widened conduit at 5–10 km depth with a volume of ~4 km<sup>3</sup> (Gardner et al. 1995; Pallister et al. 2008). Small-scale magma storage is also supported by compositional variability between neighboring vents separated by only 1–12 km (Hildreth 2007).

### 1.4.3 Monitoring

Cascade volcanoes threaten major populations and development (Ewert et al. 2005). Consequently, monitoring of the arc is undertaken by the U.S. Geological Survey's Volcano Hazards Program at the Cascades and California Volcano Observatories. The main monitoring infrastructure in the Cascades consists of seismic and continuous GPS networks, with variable coverage throughout the arc.

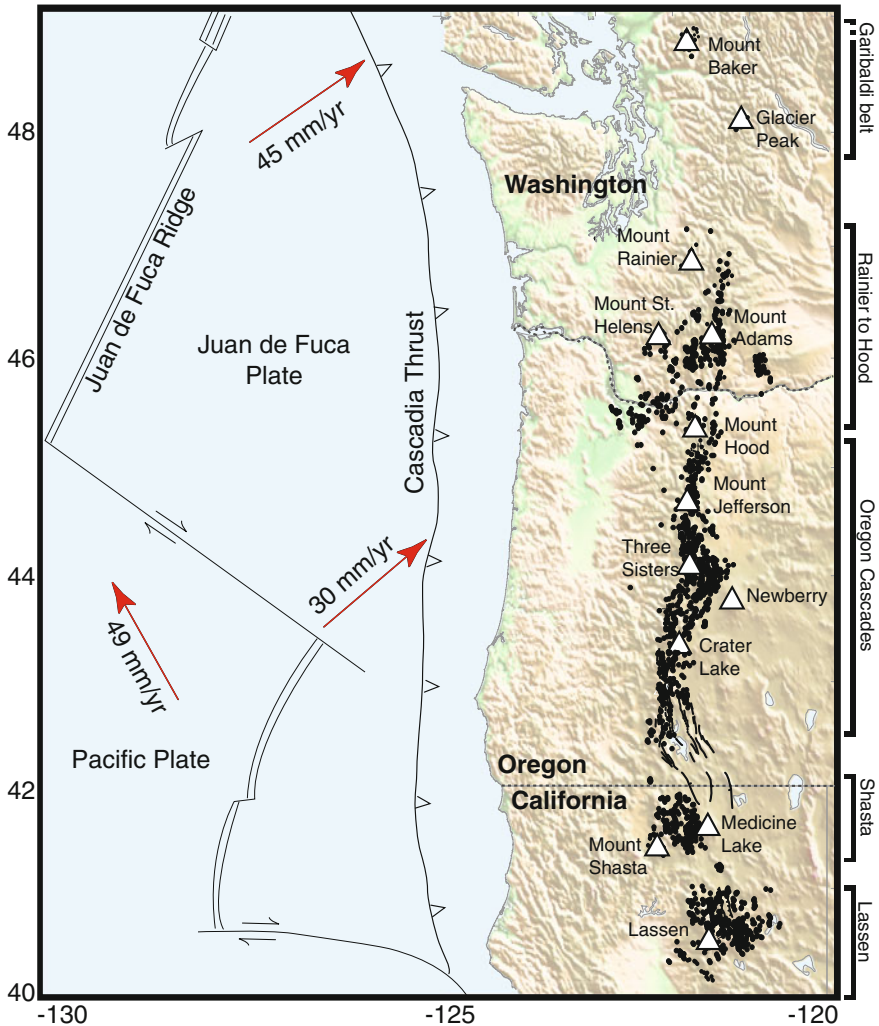


**Fig. 1.4** Tectonic map of the Cascades Volcanic Arc with Quaternary vent locations (*black dots*) and major faults (*black lines*) from Hildreth (2007) and plate velocities from McCaffrey et al. (2007). The 13 main volcanic edifices are labelled and shown by *white triangles*. On the right are the arc segments after Guffanti and Weaver (1988)

In the northern Cascades, routine seismic monitoring has been undertaken by the Pacific Northwest Seismic Network from the University of Washington since the 1970s. In the southern Cascades, the Northern California Seismic Network is operated by the U.S. Geological Survey and the University of California, Berkeley. Levels of seismicity are variable throughout the arc, as are detection thresholds of the seismic network (Moran 2004). In addition to volcano-tectonic events, seismicity is

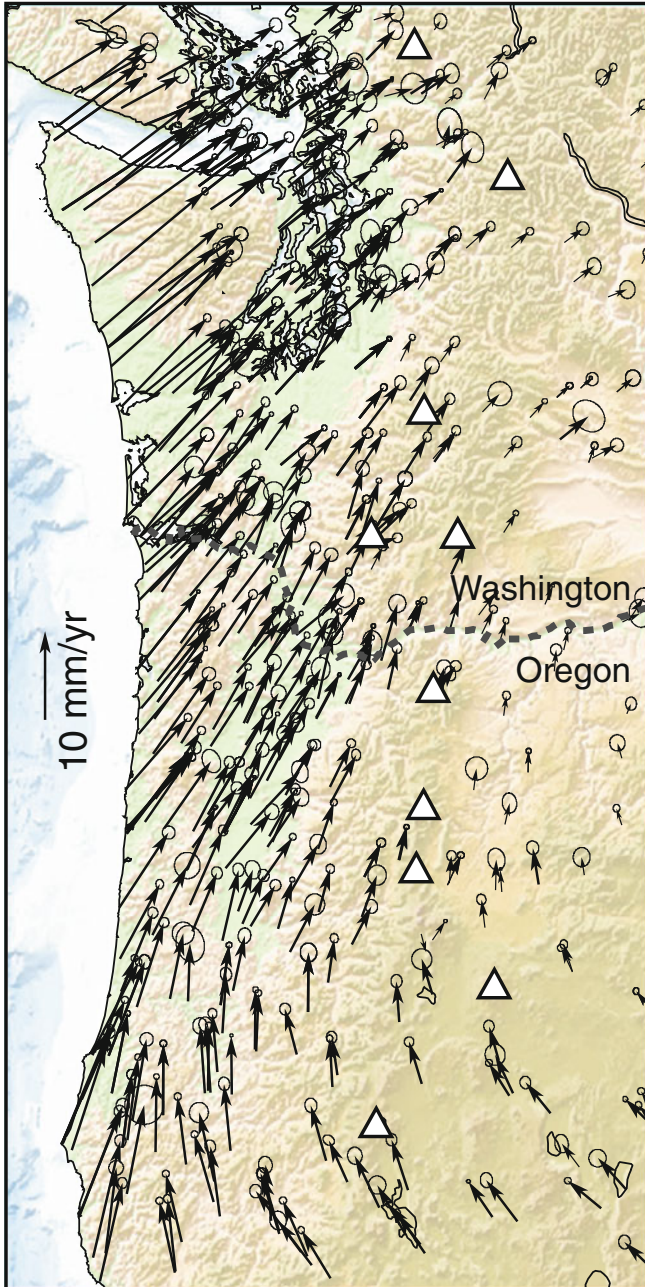


**Fig. 1.5** GPS velocities (1993–2011) in Washington and Oregon showing block-wise rotation of Oregon. GPS velocities are relative to North America and *error ellipses* mark 70% confidence. Adapted from McCaffrey et al. (2013). The 13 main volcanic edifices are shown by *white triangles* as in Fig. 1.4

attributed to glaciers e.g. Mount Baker: Nichols et al. 2011), hydrothermal systems (e.g. Lassen Volcanic Center: Janik and McLaren 2010), and seasonal groundwater recharge (e.g. Mount Hood: Saar and Manga 2003). Deep, long-period earthquakes are also observed, and between 1980 and 2009, 31 events were detected at Mount Baker, 9 at Glacier Peak, 9 at Mount Rainier, 9 at Mount St Helens, 1 at Three Sisters, and 1 at Crater Lake (Nichols et al. 2011). Long-period events are also detected beneath Lassen Volcanic Center, with 11 events on average recorded each year between 2003–2011 (A. M. Pitt, unpublished data in Clynne et al. 2012). These events are thought to represent fluid/magma transport along pre-existing tectonic structures (Nichols et al. 2011).

Importantly, shallow seismicity is not necessarily a strong indicator of magmatic activity at Cascade volcanoes (e.g. Mount Baker: Crider et al. 2011; Three Sisters: Riddick and Schmidt 2011). Geodetic observations are therefore a key component of monitoring the arc. Of the 12 high - very high threat Cascade volcanoes (as ranked in the National Volcano Early Warning System: Ewert et al. 2005), 9 are monitored by at least 1 continuous GPS station (Table 1.2). Continuous GPS (cGPS) data for the Cascade volcanoes is primarily collected by UNAVCO and is available online in near-real time via the U.S. Geological Survey Earthquakes Hazard Program. In addition to cGPS, 10 of the 12 high - very high threat volcanoes have undergone additional geodetic surveys, with baseline measurements established as far back as the 1930s (e.g. Newberry: Yamashita and Doukas 1987), and campaign GPS measurements made as recently as 2014 (e.g. Mount St Helens) (Table 1.2).

The archive of InSAR data for the Cascades is large. ENVISAT data for Mount St Helens alone includes three ascending satellite tracks and one descending track, totalling over 140 separate data acquisitions between 2003–2010. Accordingly, the existence of baseline InSAR imagery is considered to be the most basic level of deformation monitoring of Cascade volcanoes (Ewert et al. 2005). However, as this thesis describes, the application of InSAR data in the Cascades has been limited by incoherence caused by dense vegetation and snow cover, and extensive atmospheric artefacts (e.g. Mount St. Helens: Poland and Lu 2008).

## 1.5 Thesis Structure

This thesis contains two ongoing themes (1.) the application of InSAR data in the Cascades, an environment associated with incoherence and high levels of noise; and (2.) causes of long-term volcanic subsidence, with a focus on two volcanoes in the southern Cascades. Chapter 2 is published in *Geophysical Journal International* (Parker et al. 2014), and a modified version of Chap. 3 is published in *Remote Sensing of Environment* (Parker et al. 2015). Chaps. 4 and 5 are currently in preparation for submission to journals and are therefore subject to peer-review.

Chapter 2 describes the application of multi temporal analysis techniques to improve the application of InSAR at Medicine Lake Volcano. Past geodetic studies show that the volcano has subsided at a steady rate since the 1950s, and the

**Table 1.2** Geodetic monitoring of high - very high threat Cascade volcanoes

Volcano name	Last eruption	Geodetic monitoring	cGPS stations	Deformation observed	References
Mount Baker <sup>a</sup>	1880	EDM, GPS (campaign) 80–84, 04–09	0	2mm/yr subsidence between 1985–2009 in response to thermal unrest	Chadwick et al. (1985), Hodge and Crider (2010)
Glacier Peak <sup>a</sup>	1700	–	0	–	–
Mount Rainier <sup>a</sup>	1894	EDM, tiltmeter, GPS (campaign, continuous) 80–84, 06–present	5	–	Dzurisin et al. (1983), Chadwick et al. (1985)
Mount St Helens <sup>a</sup>	1980	EDM, tiltmeter 80–present		Preeruptive inflation up to 2.5m/day	Lipman and Mullineaux (1981)
				Post-eruptive subsidence	
	2004	GPS (campaign, continuous), tiltmeter, InSAR 97–present	25	Coeruptive subsidence (3 cm) short wavelength tilt cycles	Sherrod et al. (2008)
				Post-eruptive inflation (up to 1 cm)	Anderson et al. (2010)
Mount Adams <sup>b</sup>	–0950	–	0	–	
Mount Hood <sup>a</sup>	1865	EDM, GPS (continuous) 80–84, 05–present	2	–	Chadwick et al. (1985)
Three Sisters <sup>a</sup>	0440	EDM, leveling, InSAR GPS(campaign, continuous) 85–86, 92–present	3	Uplift of 3–5 cm/yr decreasing in rate to 1.4 cm/yr	Yamashita and Doukas (1987), Wicks et al. (2002), Dzurisin et al. (2006, 2009), Riddick and Schmidt (2011)
Newberry <sup>a</sup>	0690	Leveling, GPS (campaign, continuous) 31, 85, 86, 94, 02–09, 11–present	8	–	Yamashita and Doukas (1987), Dzurisin (1999)

(continued)

**Table 1.2** (continued)

Volcano name	Last eruption	Geodetic monitoring	cGPS stations	Deformation observed	References
Crater Lake <sup>a</sup>	–2850	EDM, GPS (continuous) 80–84, 09–present	4	–	Chadwick et al. (1985)
Medicine Lake <sup>b</sup>	1080	Leveling, InSAR, GPS(campaign, continuous) 54, 88–90, 96–present	3	Subsidence of ~1 cm/yr	Dzurisin et al. (1991, 2002), Poland et al. (2006), Parker et al. (2014)
Mount Shasta <sup>a</sup>	1786	EDM, GPS (continuous) 80–84, 05–present	9	–	Chadwick et al. (1985)
Lassen <sup>a</sup>	1914	EDM, leveling, tiltmeter, InSAR, GPS (campaign, continuous) 32–34, 80–84, 90, 96–00, 07–present	8	Subsidence of ~1 cm/yr onset since 1980s	Chadwick et al. (1985), Dzurisin (1999), Poland et al. (2004)

<sup>a</sup>Very high threat and <sup>b</sup>high threat, as categorised by Ewert et al. (2005)

results of InSAR analysis are used to extend the geodetic record to 2011 and show that deformation continues at historical rates. The high spatial resolution of deformation measurements from InSAR are then used to provide improved constraints upon the source geometry, and therefore the driving mechanism of subsidence.

Chapter 3 continues to focus on the application of InSAR data in the Cascades, and uses large-scale atmospheric models to investigate atmospheric uncertainties on an arc-wide scale. Rather than focusing on correcting atmospheric uncertainties retrospectively, this chapter describes a strategy to produce a priori estimates of atmospheric uncertainties, that can be used in near-real time. This is achieved by investigating the influence of volcano topography and geography upon atmospheric uncertainties, which are used to estimate detection thresholds for long-term monitoring of small magnitude signals, and short-term monitoring of pre-eruptive ground deformation in the Cascades.

Chapter 4 investigates the long-term geodetic response to cooling and crystallisation of magmatic intrusions. Geometrical and petrological constraints from Medicine Lake Volcano are input to a thermal model, which is used to assess the influence of intrusion geometry and composition upon the magnitude and time-scales of resulting surface deformation. Comparing the results to the geodetic history at Medicine Lake Volcano yields a suite of best-fitting models that are used to constrain the timing of intrusion. Consideration is given to the effects of convection, incremental intrusions, and volume loss due to degassing, and the impacts of these factors upon interpretations of the timing of intrusion.

Chapter 5 uses the methods described in Chaps. 2 and 3 to apply InSAR data at Lassen Volcanic Center. Multiple datasets are used to constrain the spatial and temporal characteristics of the deformation field, and by incorporating past geodetic datasets, the onset of deformation is inferred. The style of deformation and best-fitting source geometry are compared to those for Medicine Lake Volcano, and causes of subsidence are evaluated in light of seismic and hydrothermal activity at the volcano.

## References

- Anderson, K., Lisowski, M., & Segall, P. (2010). Cyclic ground tilt associated with the 2004–2008 eruption of Mount St. Helens. *Journal of Geophysical Research*, *115*(B11).
- Atwater, T. (1970). Implications of plate tectonics for the Cenozoic tectonic evolution of western North America. *Geological Society of America Bulletin*, *81*(12), 3513–3536.
- Bacon, C. R., Bruggman, P. E., Christiansen, R. L., Clynne, M. A., Donnelly-Nolan, J. M., & Hildreth, W. (1997). Primitive magmas at five Cascades volcanic fields: Melts from hot, heterogeneous sub-arc mantle. *Canadian Mineralogist*, *35*, 397–424.
- Baker, S., & Amelung, F. (2013). Top-down inflation and deflation at the summit of Kilauea Volcano, Hawaii observed with InSAR. *Journal of Geophysical Research*, *117*(B12406).
- Baker, M. B., Grove, T. L., Kinzler, R. J., Donnelly-Nolan, J. M., & Wandless, G. A. (1991). Origin of compositional zonation (high-alumina basalt to basaltic andesite) in the Giant Crater Lava Field, Medicine Lake Volcano, northern California. *Journal of Geophysical Research*, *96*(B13), 21819–21842.
- Baker, M. B., Grove, T. L., & Price, R. (1994). Primitive basalts and andesites from the Mt. Shasta region, N. California: Products of varying melt fraction and water content. *Contributions to Mineralogy and Petrology*, *118*(2), 111–129.
- Berardino, P., Fornaro, G., Lanari, R., & Sansosti, E. (2002). A new algorithm for surface deformation monitoring based on small baseline differential SAR interferograms. *IEEE Transactions on Geoscience and Remote Sensing*, *40*, 2375–2383.
- Biggs, J., Ebmeier, S. K., Aspinall, W. P., Lu, Z., Pritchard, M. E., Sparks, R. S. J., & Mather, T. A. (2014). Global link between deformation and volcanic eruption quantified by satellite imagery. *Nature Communications*, *5*, 3471.
- Biggs, J., Anthony, E. Y., & Ebinger, C. J. (2009a). Multiple inflation and deflation events at Kenyan volcanoes East African rift. *Geology*, *37*(11), 979–982.
- Biggs, J., Robinson, D. P., & Dixon, T. H. (2009b). The 2007 Pisco, Peru, earthquake (M8.0): Seismology and geodesy. *Geophysical Journal International*, *176*, 657–669.
- Blakely, R. J., Christiansen, R. L., Guffanti, M., Wells, R. E., Donnelly-Nolan, J. M., Muffler, L. J. P., et al. (1997). Gravity anomalies, Quaternary vents and Quaternary faults in the southern Cascade Range, Oregon and California; implications for arc and backarc evolution. *Journal of Geophysical Research*, *102*, 22513–22527.
- Bostock, M. G., & VanDecar, J. C. (1995). Upper mantle structure of the northern Cascadia subduction zone. *Canadian Journal of Earth Sciences*, *32*(1), 1–12.
- Brandon, A. D., & Draper, D. S. (1996). Constraints on the origin of the oxidation state of mantle overlying subduction zones: an example from Simcoe, Washington. *USA. Geochimica et Cosmochimica Acta*, *60*(10), 1739–1749.
- Bürgmann, R., Rosen, P. A., & Fielding, E. J. (2000). Synthetic aperture radar interferometry to measure Earth's surface topography and its deformation. *Annual Review of Earth and Planetary Sciences*, *28*(1), 169–209.
- Burkart, B., & Self, S. (1985). Extension and rotation of crustal blocks in northern Central America and effect on the volcanic arc. *Geology*, *13*(1), 22–26.

- Cashman, K., & Biggs, J. (2014). Common processes at unique volcanoes—a volcanological conundrum. *Frontiers in Earth Science*, 2, 28.
- Chadwick, W. W., Iwatsubo, E. Y., Swanson, D. A., & Ewert, J. W. (1985). Measurements of Slope Distances and Vertical Angles at Mount Baker and Mount Rainier, Washington, Mount Hood and Crater Lake, Oregon and Mount Shasta and Lassen Peak, California, 1980–1984. U.S. Geological Survey Open File Report (85-205).
- Chaussard, E., & Amelung, F. (2012). Precursory inflation of shallow magma reservoirs at west Sunda volcanoes detected by InSAR. *Geophysical Research Letters*, 39(21).
- Chaussard, E., & Amelung, F. (2014). Regional controls on magma ascent and storage in volcanic arcs. *Geochemistry, Geophysics, Geosystems*, 15(4), 1407–1418.
- Chiodini, G., Vandemeulebrouck, J., Caliro, S., D’Auria, L., De Martino, P., Mangiacapra, A., et al. (2015). Evidence of thermal-driven processes triggering the 2005–2014 unrest at Campi Flegrei caldera. *Earth and Planetary Science Letters*, 414, 58–67.
- Clyne, M. A., Robinson, J. E., Nathenson, M., & Muffler, L. J. P. (2012). Volcano Hazards Assessment for the Lassen Region, Northern California. U.S. Geological Survey Scientific Investigations Report 2012-5176-A, 56 p.
- Crider, J. G., Frank, D., Malone, S. D., Poland, M. P., Werner, C., & Caplan-Auerbach, J. (2011). Magma at depth: A retrospective analysis of the 1975 unrest at Mount Baker, Washington USA. *Bulletin of Volcanology*, 73(2), 175–189.
- Crosson, R. S., & Owens, T. J. (1987). Slab geometry of the Cascadia subduction zone beneath Washington from earthquake hypocenters and teleseismic converted waves. *Geophysical Research Letters*, 14(8), 824–827.
- Curlander, J. C., & McDonough, R. N. (1991). *Synthetic aperture radar: Systems and signal processing*. New York: Wiley-Intersci.
- Dietterich, H. R., Poland, M. P., Schmidt, D. A., Cashman, K. V., Sherrod, D. R., & Espinosa, A. T. (2012). Tracking lava flow emplacement on the east rift zone of Kilauea, Hawaii, with synthetic aperture radar coherence. *Geochemistry, Geophysics, Geosystems*, 13(5).
- Donnelly-Nolan, J. M., Champion, D. E., Grove, T. L., & an Baker, M. B., Taggart Jr, J. E., Bruggman, P. E., (1991). The Giant Crater lava field: geology and geochemistry of a compositionally zoned, high-alumina basalt to basaltic andesite eruption at Medicine Lake volcano. *California Journal of Geophysical Research*, 96(B13), 21843–21863.
- Donnelly-Nolan, J. M. (1988). A magmatic model of medicine lake volcano, California. *Journal of Volcanology and Geothermal Research*, 93, 4412–4420.
- Dzurisin, D. (2003). A comprehensive approach to monitoring volcano deformation as a window on the eruption cycle. *Reviews of Geophysics*, 41(1).
- Dzurisin, D., Johnson, D. J., & Symonds, R. B. (1983). Dry Tilt Network at Mount Rainier, Washington. U.S. Geological Survey Fact Sheet (83-277), 18 p.
- Dzurisin, D., Poland, M. P., & Bürgmann, R. (2002). Steady subsidence of Medicine Lake Volcano, Northern California, revealed by repeated levelling surveys. *Journal of Geophysical Research*, 107(B12).
- Dzurisin, D. (1999). Results of repeated leveling surveys at Newberry Volcano, Oregon and near Lassen Peak Volcano California. *Bulletin of Volcanology*, 61(1–2), 83–91.
- Dzurisin, D. (2007). *Volcano deformation: Geodetic monitoring techniques*. Chichester, UK: Springer-Praxis.
- Dzurisin, D., Donnelly-Nolan, J. M., Evans, J. R., & Walter, S. R. (1991). Crustal subsidence, seismicity and structure near Medicine Lake volcano California. *Journal of Geophysical Research*, 96(B10), 16319–16333.
- Dzurisin, D., Lisowski, M., & Wicks, C. W. (2009). Continuing inflation at Three Sisters volcanic center, central Oregon Cascade Range, USA, from GPS, leveling and InSAR observations. *Bulletin of Volcanology*, 71(10), 1091–1110.
- Dzurisin, D., Lisowski, M., Wicks, C. W., Poland, M. P., & Endo, E. T. (2006). Geodetic observations and modeling of magmatic inflation at the Three Sisters volcanic center, central Oregon Cascade Range, USA. *Journal of Volcanology and Geothermal Research*, 150(1), 35–54.



- Ebmeier, S. K., Biggs, J., Mather, T. A., & Amelung, F. (2013b). On the lack of InSAR observations of magmatic deformation at Central American volcanoes. *Journal of Geophysical Research*, *118*(5), 2571–2585.
- Ebmeier, S. K., Biggs, J., Muller, C., & Avard, G. (2014). Thin-skinned mass-wasting responsible for widespread deformation at Arenal volcano. *Frontiers in Earth Science*, *2*, 35.
- Elachi, C. (1988). *Spaceborne radar remote sensing: Applications and techniques*. New York, US: IEEE Press.
- Ewert, J. W., Guffanti, M., & Murray, T. L. (2005). An assessment of volcanic threat and monitoring capabilities in the United States: framework for a National Volcano Early Warning System NVEWS. U.S. Geological Survey Open File Report (2005-1164).
- Ferretti, A., Fumagalli, A., Novali, F., Prati, C., Rocca, F., & Rucci, A. (2011). A new algorithm for processing interferometric data-stacks: SqueeSAR. *IEEE Transactions on Geoscience and Remote Sensing*, *49*(9), 3460–3470.
- Ferretti, A., Prati, C., & Rocca, F. (2001). Permanent scatterers in SAR interferometry. *IEEE Transactions on Geoscience and Remote Sensing*, *39*(1), 8–20.
- Fialko, Y., Khazan, Y., & Simons, M. (2001a). Deformation due to a pressurised horizontal circular crack in an elastic half-space, with applications to volcano geodesy. *Geophysical Journal International*, *146*(1), 181–190.
- Galloway, D. L., & Burbey, T. J. (2011). Review: regional land subsidence accompanying groundwater extraction. *Hydrogeology Journal*, *19*(8), 1459–1486.
- Gardner, J. E., Rutherford, M., Carey, S., & Sigurdsson, H. (1995). Experimental constraints on pre-eruptive water contents and changing magma storage prior to explosive eruptions of Mount St Helens volcano. *Bulletin of Volcanology*, *57*(1), 1–17.
- Goldstein, R. M., Engelhardt, H., Kamb, B., & Frolich, R. M. (1993). Satellite radar interferometry for monitoring ice sheet motion: Application to an Antarctic ice stream. *Science*, *262*(5139), 1525–1530.
- Goldstein, R., Zebker, H., & Werner, C. (1988). Satellite radar interferometry: Two dimensional phase unwrapping. *Radio Science*, *23*(4), 713–720.
- Grove, L. T., Donnelly-Nolan, J. M., & Housh, T. (1997). Magmatic processes that generated the rhyolite of Glass Mountain, Medicine Lake Volcano N. California. *Contributions to Mineralogy Petrology*, *127*, 205–223.
- Guffanti, M., & Weaver, C. S. (1988). Distribution of late Cenozoic volcanic vents in the Cascade Range: Volcanic arc segmentation and regional tectonic considerations. *Journal of Geophysical Research*, *93*(B6), 6513–6529.
- Hammond, W. C., & Thatcher, W. (2005). Northwest Basin and Range tectonic deformation observed with the Global Positioning System, 1999–2003. *Journal of Geophysical Research*, *110*(B10).
- Hanssen, R. F. (2001). *Radar interferometry: Data interpretation and analysis*. Norwell, MA, US: Kluwer Acad.
- Hickey, J., Gottsmann, J., & Potro, R. (2013). The large-scale surface uplift in the Altiplano-Puna region of Bolivia: A parametric study of source characteristics and crustal rheology using finite element analysis. *Geochemistry, Geophysics, Geosystems*, *14*(3), 540–555.
- Hildreth, W., 2007. Quaternary magmatism in the Cascades - geological perspectives. U.S. Geological Survey Professional Paper (1744).
- Hildreth, W. (1981). Gradients in silicic magma chambers: Implications for lithospheric magmatism. *Journal of Geophysical Research*, *86*(B11), 10153–10192.
- Hodge, B. E., & Crider, J. G. (2010). Investigating mechanisms of edifice deflation 1981–2007, at Mount Baker volcano, Washington, United States. *Journal of Geophysical Research*, *105*, 25671–25684.
- Hooper, A. (2008). A multi-temporal InSAR method incorporating both persistent scatterer and small baseline approaches. *Geophysical Research Letters*, *35*(16).

- Hooper, A., Segall, P., & Zebker, H. (2007). Persistent scatterer interferometric synthetic aperture radar for crustal deformation analysis, with application to Volcán Alcedo, Galápagos. *Journal of Geophysical Research*, 112(B7),
- Hooper, A., Zebker, H., Segall, P., & Kampes, B. (2004). A new method for measuring deformation on volcanoes and other natural terrains using InSAR persistent scatterers. *Geophysical Research Letters*, 31(23),
- Hooper, A., Bekaert, D., Spaans, K., & Arikan, M. (2012). Recent advances in SAR interferometry time series analysis for measuring crustal deformation. *Tectonophysics*, 514, 1–13.
- Ingebritsen, S. E., & Mariner, R. H. (2010). Hydrothermal heat discharge in the Cascade Range, northwestern United States. *Journal of Volcanology and Geothermal Research*, 196(3), 208–218.
- Janik, C. J., & McLaren, M. K. (2010). Seismicity and fluid geochemistry at Lassen Volcanic National Park, California: Evidence for two circulation cells in the hydrothermal system. *Journal of Volcanology and Geothermal Research*, 189(3), 257–277.
- Jónsson, S. (2009). Stress interaction between magma accumulation and trapdoor faulting on Sierra Negra volcano Galápagos. *Tectonophysics*, 471(1), 36–44.
- Lipman, P. W., & Mullineaux, D. R. E. (1981). The 1980 Eruptions of Mount St. Helens, Washington. *U.S. Geological Survey Professional Paper*, 1250, 844p.
- Lu, Z., & Dzurisin, D. (2014). *InSAR imaging of Aleutian volcanoes: Monitoring a volcanic arc from space*. Chichester, UK: Springer-Praxis.
- Massonnet, D., Feigl, K. L., Vadon, H., Rossi, M., 1996. Coseismic deformation field of the M = 6.7 Northridge, California earthquake of January 17. (1994). recorded by two radar satellites using interferometry. *Geophysical Research Letters*, 23(9), 969–972.
- Massonnet, D., & Feigl, K. L. (1998). Radar interferometry and its application to changes in the Earth's surface. *Reviews of Geophysics*, 36(4), 44–500.
- Mastin, L., Lisowski, M., Roeloffs, E., & Beeler, N. (2009). Improved constraints on the estimated size and volatile content of the Mount St. Helens magma system from the 2004–2008 history of dome growth and deformation. *Geophysical Research Letters*, 36(L20304).
- McCaffrey, R., King, R. W., Payne, S. J., & Lancaster, M. (2013). Active tectonics of northwestern US inferred from GPS-derived surface velocities. *Journal of Geophysical Research*, 118(2), 709–723.
- McCaffrey, R., Qamar, A. I., King, R. W., Wells, R., Khazaradze, G., Williams, C. A., et al. (2007). Fault locking, block rotation and crustal deformation in the Pacific Northwest. *Geophysical Journal International*, 169(3), 1315–1340.
- Mogi, K. (1958). Relations between eruptions of various volcanoes and the deformations of the ground surfaces around them. *Bulletin of the Earthquake Research Institute of the University of Tokyo*, 36, 99–134.
- Moran, S. C., (2004). Seismic Monitoring at Cascade Volcanic Centers, 2004 - Status and Recommendations. U.S. Geological Survey Scientific Investigations Report (2004-5211).
- Moran, S. C. (1994). Seismicity at Mount St. Helens, 1987–1992: Evidence for repressurization of an active magmatic system. *Journal of Geophysical Research*, 99(B3), 4341–4354.
- Nichols, M. L., Malone, S. D., Moran, S. C., Thelen, W. A., & Vidale, J. E. (2011). Deep long-period earthquakes beneath Washington and Oregon volcanoes. *Journal of Volcanology and Geothermal Research*, 200, 116–128.
- Ofeigsson, B. G., Hooper, A., Sigmundsson, F., Sturkell, E., & Grapenthin, R. (2011). Deep magma storage at Hekla volcano, Iceland, revealed by InSAR time series analysis. *Journal of Geophysical Research*, 116(B5), B05401.
- Okada, Y. (1985). Surface deformation due to shear and tensile faults in a half-space. *Bulletin of the Seismological Society of America*, 75(4), 1135–1154.
- Pallister, J. S., Hoblitt, R. P., Crandell, D. R., & Mullineaux, D. R. (1992). Mount St. Helens a decade after the, (1980). eruptions: Magmatic models, chemical cycles and a revised hazards assessment. *Bulletin of Volcanology*, 54(2), 126–146.

- Pallister, J. S., Thornber, C. R., Cashman, K. V., Clynne, M. A., Lowers, H. A., & Mandeville, C. W., et al. (2008). Petrology of the 2004–2006 Mount St. Helens lava dome-implications for magmatic plumbing and eruption triggering. U.S. Geological Survey Professional Paper 1750.
- Parker, A. L., Biggs, J., & Lu, Z. (2014). Investigating long-term subsidence at Medicine Lake Volcano, CA, using multi temporal InSAR. *Geophysical Journal International*, 199(2), 844–859.
- Parker, A. L., Biggs, J., Walters, R. J., Ebmeier, S. K., Wright, T. J., Teanby, N. A., et al. (2015). Systematic assessment of atmospheric uncertainties for InSAR data at volcanic arcs using large-scale atmospheric models: Application to the Cascade volcanoes, United States. *Remote Sensing of Environment*, 170, 102–114.
- Pearse, J., & Fialko, Y. (2010). Mechanics of active magmatic intraplate in the Rio Grande Rift near Socorro, New Mexico. *Journal of Geophysical Research*, 115(B7).
- Pinel, V., Hooper, A., De la Cruz-Reyna, S., Reyes-Davila, G., Doin, M.-P., & Bascou, P. (2011). The challenging retrieval of the displacement field from InSAR data for andesitic stratovolcanoes: Case study of Popocatepetl and Colima Volcano, Mexico. *Journal of Volcanology and Geothermal Research*, 200(1), 49–61.
- Pinel, V., Poland, M. P., & Hooper, A. (2014). Volcanology: Lessons learned from synthetic aperture radar imagery. *Journal of Volcanology and Geothermal Research*, 289, 81–113.
- Plattner, C., Wdowinski, S., Dixon, T. H., & Biggs, J. (2010). Surface subsidence induced by the Crandall Canyon Mine (Utah) collapse: InSAR observations and elasto-plastic modelling. *Geophysical Journal International*, 183(3), 1089–1096.
- Poland, M., Bawden, G., Lisowski, M., Dzurisin, D. (2004). Newly discovered subsidence at Lassen Peak, southern Cascade Range, California, from InSAR and GPS. [abs.]: Eos (American Geophysical Union Transactions) v. 85, Fall Meeting Supplement, abs. G51A-0068.
- Poland, M. P., Bürgmann, R., Dzurisin, D., Lisowski, M., Masterlark, T., Owen, S., et al. (2006). Constraints on the mechanism of long-term, steady subsidence at Medicine Lake volcano, northern California, from GPS, levelling and InSAR. *Journal of Volcanology and Geothermal Research*, 150(1), 55–78.
- Poland, M. P., & Lu, Z. (2008). Radar Interferometry Observations of Surface Displacements During Pre- and Coeruptive Periods at Mount St. Helens, Washington, 1992–2005. *U. S. Geological Survey Professional Paper*, 1750, 361–382.
- Priest, G. R. (1990). Volcanic and tectonic evolution of the Cascade Volcanic Arc, central Oregon. *Journal of Geophysical Research*, 95(B12), 19583–19599.
- Pritchard, M. E., & Simons, M. (2004a). An InSAR-based survey of volcanic deformation in the central Andes. *Geochemistry, Geophysics, Geosystems*, 5(2).
- Pyle, D. M., Mather, T. A., & Biggs, J. (2013). Remote sensing of volcanoes and volcanic processes: Integrating observation and modelling-introduction. *Geological Society, London, Special Publications*, 380(1), 1–13.
- Riddick, S. N., & Schmidt, D. A. (2011). Time-dependent changes in volcanic inflation rate near Three Sisters, Oregon, revealed by InSAR. *Geochemistry, Geophysics, Geosystems*, 12(12).
- Rosen, P., Hensley, S., Peltzer, G., & Simons, M. (2004). Updated repeat orbit interferometry package released. EOS, Trans. AGU 85 (5).
- Rosen, P. A., Hensley, S., Joughin, I. R., Li, F. K., Madsen, S. N., Rodriguez, E., et al. (2000). Synthetic aperture radar interferometry. *Proceedings of the IEEE*, 88(3), 333–382.
- Rosen, P. A., Hensley, S., Zebker, H. A., & Webb, F. H. (1996). Surface deformation and coherence measurements of Kilauea Volcano, Hawaii, from SIR-C radar interferometry. *Journal of Geophysical Research*, 101(E10), 23109–23125.
- Ruscitto, D. M., Wallace, P. J., Johnson, E. R., Kent, A. J. R., & Bindeman, I. N. (2010). Volatile contents of mafic magmas from cinder cones in the central oregon high cascades: Implications for magma formation and mantle conditions in a hot arc. *Earth and Planetary Science Letters*, 298(1), 153–161.

- Rutherford, M. J., Sigurdsson, H., Carey, S., & Davis, A. (1985). The May 18, 1980, eruption of Mount St. Helens: 1. Melt composition and experimental phase equilibria. *Journal of Geophysical Research*, 90(B4), 2929–2947.
- Saar, M. O., & Manga, M. (2003). Seismicity induced by seasonal groundwater recharge at Mt. Hood, Oregon. *Earth and Planetary Science Letters*, 214(3), 605–618.
- Scandone, R., & Malone, S. D. (1985). Magma supply, magma discharge and readjustment of the feeding system of Mount St. Helens during 1980. *Journal of Volcanology and Geothermal Research*, 23(3), 239–262.
- Schmidt, D. A., & Bürgmann, R. (2003). Time-dependent land uplift and subsidence in the Santa Clara valley, California, from a large interferometric synthetic aperture radar data set. *Journal of Geophysical Research*, 108(B9),
- Segall, P. (2010). *Earthquake and volcano deformation*. Princeton, New Jersey, US: Princeton University Press.
- Seymour, M., & Cumming, I. (1994). Maximum likelihood estimation for SAR interferometry. Institute of Electrical and Electronics Engineers, Piscataway, NJ (pp. 2272–2275).
- Sherrod, D. R., Scott, W. E., Stauffer, P. H. E. (2008). A Volcano Rekindled: The Renewed Eruption of Mount St. Helens, 2004–2006. U.S. Geological Survey Professional Paper (1750), 856 p.
- Simons, M., & Rosen, P. A. (2007). *Interferometric synthetic aperture radar geodesy* (vol. 3, pp. 391–446).
- Simpson, R. W., & Cox, A. (1977). Paleomagnetic evidence for tectonic rotation of the Oregon Coast Range. *Geology*, 5(10), 585–589.
- Sousa, J. J., Hooper, A. J., Hanssen, R. F., Bastos, L. C., & Ruiz, A. M. (2011). Persistent scatterer InSAR: A comparison of methodologies based on a model of temporal deformation vs. spatial correlation selection criteria. *Remote Sensing of Environment*, 115(10), 2652–2663.
- Stoiber, R. E., & Carr, M. J. (1973). Quaternary volcanic and tectonic segmentation of Central America. *Bulletin of Volcanology*, 37(3), 304–325.
- Vasco, D. W., Rucci, A., Ferretti, A., Novali, F., Bissell, R. C., & Ringrose, P. S., et al. (2010). Satellite-based measurements of surface deformation reveal fluid flow associated with the geological storage of carbon dioxide. *Geophysical Research Letters*, 37(3).
- Venezky, D. Y., & Rutherford, M. J. (1997). Preeruption conditions and timing of dacite-andesite magma mixing in the 2.2 ka eruption at mount rainier. *Journal of Geophysical Research*, 102(B9), 20069–20086.
- Verplanck, E. P., & Duncan, R. A. (1987). Temporal variations in plate convergence and eruption rates in the Western Cascades Oregon. *Tectonics*, 6(2), 197–209.
- Wadge, G., Zhu, M., Holley, R. J., James, I. N., Clark, P. A., Wang, C., et al. (2010). Correction of atmospheric delay effects in radar interferometry using a nested mesoscale atmospheric model. *Journal of Applied Geophysics*, 72(2), 141–149.
- Wauthier, C., Cayol, V., Poland, M., Kervyn, F., dOreye, N., Hooper, A., Samsonov, S., Tiampo, K., & Smets, B. (2013). Nyamulagiras magma plumbing system inferred from 15 years of InSAR. *Geological Society, London, Special Publications*, 380(1), 39–65.
- Weaver, C. S., & Baker, G. E. (1988). Geometry of the Juan de Fuca plate beneath Washington and northern Oregon from seismicity. *Bulletin of the Seismological Society of America*, 78(1), 264–275.
- Wells, R. E., Weaver, C. S., & Blakely, R. J. (1998). Fore-arc migration in Cascadia and its neotectonic significance. *Geology*, 26(8), 759–762.
- Werner, C., Wegmuller, U., Strozzi, T., & Weismann, A. (2000). Gamma SAR and interferometric processing software. In *ERS—ENVISAT Symposium*.
- Wesnousky, S. G. (2005). The San Andreas and Walker Lane fault systems, western North America: Transpression, transtension, cumulative slip and the structural evolution of a major transform plate boundary. *Journal of Structural Geology*, 27(8), 1505–1512.
- Wicks, C. W., Dzurisin, D., Ingebritsen, S., Thatcher, W., Lu, Z., & Iverson, J. (2002). Magmatic activity beneath the quiescent Three Sisters volcanic center, central Oregon Cascade Range. *USA. Geophysical Research Letters*, 29(7), 26–1.

- Wicks, C., de La Llera, J. C., Lara, L. E., & Lowenstern, J. (2011). The role of dyking and fault control in the rapid onset of eruption at Chaitén volcano Chile. *Nature*, 478(7369), 374–377.
- Wicks, C., Thatcher, W., & Dzurisin, D. (1998). Migration of fluids beneath Yellowstone caldera inferred from satellite radar interferometry. *Science*, 282(5388), 458–462.
- Wilson, D. S. (1993). Confidence intervals for motion and deformation of the Juan de Fuca plate. *Journal of Geophysical Research*, 98(B9), 16053–16071.
- Wright, T. J. (2002). Remote monitoring of the earthquake cycle using satellite radar interferometry. *Philosophical Transactions of the Royal Society of London A: Mathematical, Physical and Engineering Sciences*, 360(1801), 2873–2888.
- Yamashita, K. M., & Doukas, M. P. (1987). Precise level lines at Crater Lake, Newberry Crater and South Sister. U.S. Geological Survey Open File Report (87-293), 32 pp.
- Ye, X., Kaufmann, H., & Guo, X. F. (2004). Landslide monitoring in the three gorges area using D-InSAR and corner reflectors. *Photogrammetric Engineering and Remote Sensing*, 70(10), 1167–1172.
- Zebker, H., Rosen, P., & Goldstein, R. M. (1994). On the derivation of co-seismic displacement fields using differential radar interferometry: The landers earthquake. *Journal of Geophysical Research*, 99(B10), 19617–19634.
- Zebker, H. A., & Villasenor, J. (1992). Decorrelation in interferometric radar echoes. *IEEE Transactions on Geoscience and Remote Sensing*, 30(5), 950–959.
- Ziebart, M., Adhya, S., Sibthorpe, A., Edwards, S., & Cross, P. (2005). Combined radiation pressure and thermal modelling of complex satellites: Algorithms and on-orbit tests. *Advances in Space Research*, 36(3), 424–430.

## Chapter 2

# Investigating Long-Term Subsidence at Medicine Lake Volcano, CA, Using Multi Temporal InSAR

**Abstract** Long-term volcanic subsidence provides insight into inter-eruptive processes, which comprise the longest portion of the eruptive cycle. Ground based geodetic surveys of Medicine Lake Volcano (MLV), northern CA, document subsidence at rates of  $\sim -10$  mm/yr between 1954 and 2004. The long observation period plus the duration and stable magnitude of this signal presents an ideal opportunity to study long-term volcanic deformation, but this first requires accurate knowledge of the geometry and magnitude of the source. Best-fitting analytical source models to past leveling and GPS datasets show conflicting source parameters - primarily the model depth. To overcome this, we combine multiple tracks of InSAR data, each with a different look angle, to improve upon the spatial resolution of ground based measurements. We compare the results from InSAR to those of past geodetic studies, extending the geodetic record to 2011 and demonstrating that subsidence at MLV continues at  $\sim -10$  mm/yr. Using geophysical inversions, we obtain the best-fitting analytical source model - a sill located at 9–10 km depth beneath the caldera. This model geometry is similar to those of past studies, providing a good fit to the high spatial density of InSAR measurements, whilst accounting for the high ratio of vertical to horizontal deformation derived from InSAR and recorded by existing leveling and GPS datasets. We discuss possible causes of subsidence and show that this model supports the hypothesis that deformation at MLV is driven by tectonic extension, gravitational loading, plus a component of volume loss at depth, most likely due to cooling and crystallisation within the intrusive complex that underlies the edifice. Past InSAR surveys at MLV, and throughout the Cascades, are of variable success due to dense vegetation, snow cover and atmospheric artefacts. In this study, we demonstrate how InSAR may be successfully used in this setting by applying a suite of multi temporal analysis methods that account for atmospheric and orbital noise sources. These methods include: a stacking strategy based upon the noise characteristics of each dataset; pixel-wise rate-map formation ( $\pi$ -RATE); and persistent scatterer InSAR (StaMPS).

## 2.1 Introduction

Medicine Lake Volcano (MLV), northern California, is one of several Cascade volcanoes known to have exhibited ground deformation in recent years. The first leveling measurements at MLV were made in 1954 (Dzurisin et al. 1991, 2002) and, with the addition of campaign GPS surveys (Poland et al. 2006), comprise a geodetic record that spans 50 years. Few volcanoes have such long geodetic histories, but what is most unique about MLV is that deformation has been recorded at a constant rate of  $\sim -10$  mm/yr since measurements began.

Past geodetic surveys provide an extensive history of ground deformation, with leveling measurements providing good constraints upon the vertical component of deformation, and GPS measurements best constraining horizontal displacements (Poland et al. 2006). However, the temporal and spatial resolution of measurements is limited (Fig. 2.1) and there are discrepancies between the best fitting analytical models to these past datasets. In this study we use measurements from Interferometric Synthetic Aperture Radar (InSAR), which are made at a much higher spatial density than ground based surveys. The side-looking nature of InSAR satellites means that measurements contain a component of both horizontal and vertical motion in the line of sight (LOS) of the satellite. By combining data acquired from multiple viewing geometries, InSAR measurements have the potential to better constrain both horizontal and vertical deformation fields at MLV (Wright et al. 2004b), in addition to providing measurements at a higher temporal and spatial resolution than past ground-based studies.

InSAR is a frequently used volcano monitoring tool, providing measurements of ground deformation in regions both with and without other geodetic equipment (e.g. Sparks et al. 2012; Pyle et al. 2013; Lu and Dzurisin 2014). For regions that contain numerous volcanoes, such as the Andes or Central America, InSAR may be used to carry out large-scale deformation surveys without the expense or risks associated with deploying equipment on the ground (Biggs et al. 2014). However, as is the case in many volcanic settings, the application of InSAR at MLV and throughout the Cascades has been limited by incoherence and noise.

In recent years, various multi temporal analysis methods have been developed to improve the use of InSAR in challenging conditions, and are now becoming widely used due to their accessibility online. This includes those that assume the signal remains constant over time such as: stacking (e.g. de Zeeuw-van Dalssen et al. 2012), rate-map formation (e.g. Poly-Interferogram Rate and Time-series Estimator:  $\pi$ -RATE; Biggs et al. 2007; Elliott et al. 2008; Wang et al. 2009, 2012), and persistent scatterer InSAR (Ferretti et al. 2001; Hooper et al. 2004, 2007); and those designed to investigate the temporal evolution of deformation, such as the small baseline subset algorithm (Berardino et al. 2002), and persistent scatterer InSAR time-series (Hooper et al. 2004, 2007). We test the application of multi temporal analysis methods in the Cascades using multiple sets of InSAR data acquired at MLV, where the apparent steady state of ground deformation and abundance of geodetic data presents

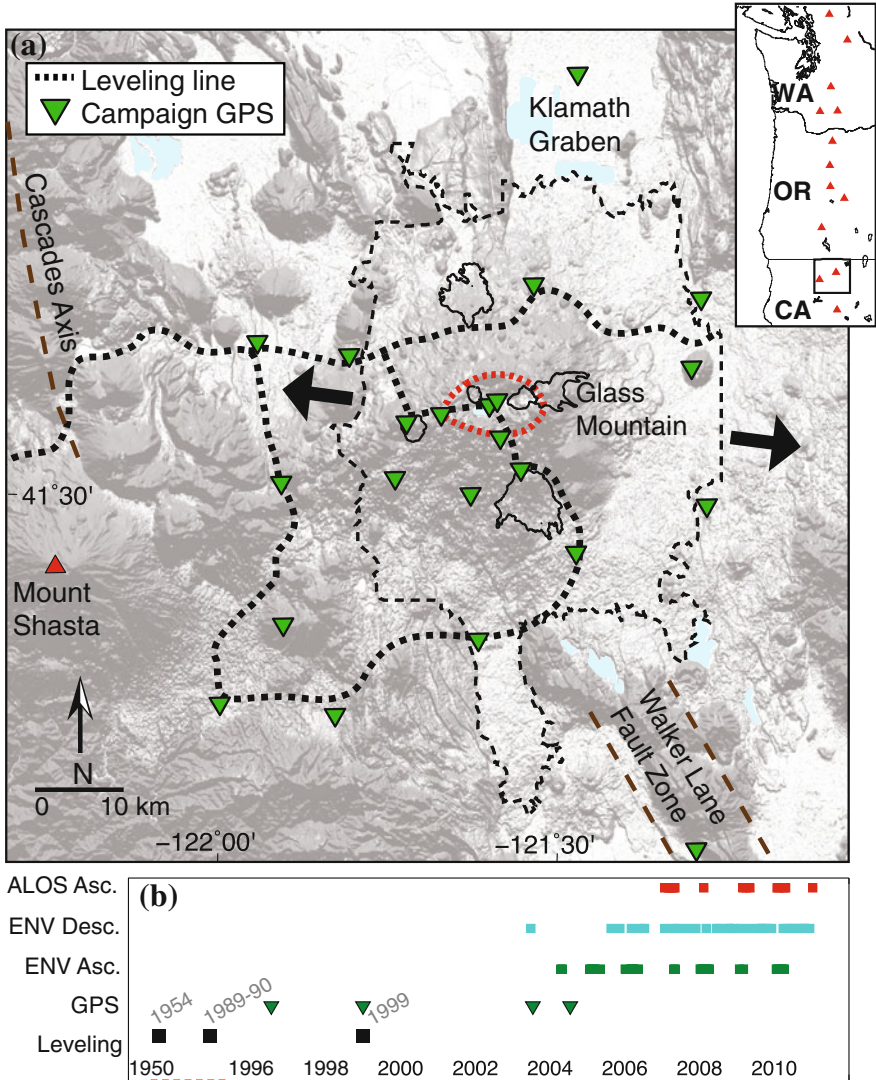


**Fig. 2.1** **a** Map of Medicine Lake Volcano including main structural features and direction of tectonic extension after Donnelly-Nolan et al. (2008), plus U.S. Geological Survey geodetic networks. The extent of MLV lavas and major Holocene lava flows are shown by dashed and solid black lines respectively (Donnelly-Nolan 2010). The summit caldera is shown by the dotted red line. The site of the last eruption, 1 ka at Glass Mountain, is labelled. These features are overlain on a 30 m SRTM digital elevation model. *Inset* map shows the location of the main map in relation to the other Cascade volcanoes. **b** Timeline showing the temporal resolution of geodetic datasets at MLV. Note the discontinuous time axis. Leveling measurements are labelled with dates and are from Dzurisin et al. (2002). GPS measurements are from Poland et al. (2006) (color figure online)



an ideal opportunity to assess the application of techniques that assume a linear rate of deformation.

The results of multi temporal InSAR analysis provide improved constraints upon the deformation field at MLV. Comparing the results from InSAR to those of past geodetic studies, we extend the geodetic record to 2011 and determine whether subsidence at MLV continues at historical rates. The improved spatial resolution of InSAR measurements is then used to constrain analytical models of the source of deformation.

### ***2.1.1 Tectonic and Geological Setting***

Located east of the main Cascades axis on the Modoc Plateau, MLV is considered to be a rear-arc volcano at the southern end of the Cascades Volcanic Arc (Donnelly-Nolan et al. 2008) (Fig. 2.1a). This region marks the interaction between subduction along the Cascadia subduction zone and extension of the Basin and Range province (e.g. Hildreth 2007), both of which control the structure and behaviour of MLV. The edifice marks a kink in regional fault orientations (Blakely et al. 1997) and zones of crustal weakness including a lineament of vents that extend SW to Mount Shasta; the NW extension of the Walker Lane fault zone; and the southern extension of the Klamath Graben (Donnelly-Nolan et al. 2008) (Fig. 2.1a).

The total area covered by MLV lavas is  $>2000\text{ km}^2$  - about 10 times the area of Mount St Helens (Donnelly-Nolan 1988) - and the total erupted volume is estimated to be  $\sim 600\text{ km}^3$  (Heiken 1978) making MLV the largest volcano by volume in the Cascades (e.g. Donnelly-Nolan 1988; Hildreth 2007). Despite its large volume, MLV is a broad, inconspicuous, volcano with an E-W orientated,  $7 \times 12\text{ km}$  summit caldera (Fig. 2.1a).

Volcanism at MLV began about half a million years ago (Donnelly-Nolan and Lanphere 2005) and the volcano has one of the highest Holocene eruption rates in the Cascades, with nine eruptions having occurred in the last 5.2 ka (Donnelly-Nolan et al. 2008). Magmatic products show signatures of both subduction and extension, with hydrous calcalkaline basalts and dry high-alumina olivine tholeiite erupted close together in space and time (Donnelly-Nolan 1988). The most recent eruption at MLV was  $\sim 1\text{ ka}$  at Glass Mountain on the eastern edge of the caldera (Fig. 2.1a).

### ***2.1.2 Previous Studies of Ground Deformation at Medicine Lake Volcano***

The U.S. Geological Survey has made repeated measurements of two geodetic networks covering MLV and nearby Mount Shasta: a leveling line and a campaign GPS network (Fig. 2.1b). The first leveling survey of the MLV/Mount Shasta region took

place in 1954. Smaller scale surveys were carried out in 1988 in response to a small earthquake swarm, and in 1989–1990, the U.S. Geological Survey Volcano Hazards Program remeasured the MLV circuit (Dzurisin et al. 1991, 2002). These surveys revealed volcano wide subsidence and an additional survey of the summit region in 1999 confirmed subsidence at a rate of  $-8.6 \pm 0.9$  mm/yr (Dzurisin et al. 2002).

Campaign GPS surveys of the volcano took place in 1996, 1999, 2003 and 2004 (Fig. 2.1b). The horizontal measurements provided by these GPS campaigns have been essential in discriminating between possible source geometries, as they reveal that deformation at MLV is almost all vertical, with very small horizontal displacements (Poland et al. 2006).

Poland et al. (2006) present InSAR results in conjunction with their GPS study, summing three temporally consecutive ERS-1/2 interferograms to produce a stack spanning 1993–2000. However, Poland et al. (2006) found that ERS-1/2 data exhibit poor coherence in the caldera region, and offer limited additional information to GPS measurements.

## 2.2 InSAR Data and Interferogram Formation

To address the application of InSAR at MLV, we use the significant archive of InSAR data covering the volcano acquired between 1993 and 2011 by the European Space Agency C-band satellites ERS-1/2 and ENVISAT, plus L-band data from the JAXA satellite ALOS. In total we use: 26 acquisitions from ERS-1/2 descending track 342; 32 acquisitions from ENVISAT ascending track 163; 32 acquisitions from ENVISAT descending track 342; and 15 acquisitions from ALOS ascending track 220 (Fig. 2.1b). Both C-band satellites have a repeat interval of 35 days but offer variable coverage throughout their operation time. ALOS data span 2007–2011 with a repeat time of 46 days, providing useful constraint on deformation in more recent years.

Interferograms were processed using the JPL/Caltech ROI\_PAC software (Rosen et al. 2004), filtered using a power spectrum filter (Goldstein and Werner 1998) and unwrapped using a branch cut algorithm (Goldstein and Werner 1988). Topography was removed using a 30 m SRTM DEM (Farr and Kobrick 2000). We guide interferogram formation using time versus perpendicular baseline plots to identify image pairs with short temporal and/or spatial baselines (Fig. 2.9 in the Appendix). To improve the coherence of C-band interferograms we made alterations to the processing sequence including additional filtering steps, unwrapping manually using bridges to connect isolated coherent patches and increasing the number of looks (coarsening resolution to approx. 300 m) (e.g. Goldstein and Werner 1988; Jónsson et al. 2002). The final set of C-band interferograms is produced by unwrapping the phase at 16 looks, allowing us to maximise coherence without over smoothing the signal.

### 2.2.1 Coherence

The use of InSAR across the Cascades has been limited by incoherence. Coherence is quantified in terms of interferometric correlation,  $\gamma$ , measured across a  $3 \times 3$  pixel window. For stable pixels,  $\gamma = 1$ , and for pixels that have independent backscattering phases,  $\gamma = 0$  (Seymour and Cumming 1994; Hanssen 2001). We use a threshold of  $\gamma = 0.1$ , as this produces a smooth phase field in unwrapping whilst maximising the number of coherent pixels.

At MLV, incoherence is mostly caused by snow, and dense vegetation, which cause the properties of scatterers to vary over time (temporal decorrelation). Geometrical decorrelation may also result from steep topography, such as the caldera walls. Throughout all datasets we observe good coherence in the arid region surrounding MLV. Pine trees across the flanks and caldera of the volcano significantly reduce the coherence of C-Band data (e.g. Fig. 2.10 in the Appendix), but are less detrimental to L-Band data, as the longer radar wavelength is better able to penetrate vegetation (Rosen et al. 1996; Massonnet et al. 1996; Ebmeier et al. 2013b; Lu and Dzurisin 2014). These regions of high elevations are also affected by snow cover between November and May, which impacts all datasets.

We quantitatively assess the coherence of each dataset by calculating the percentage of coherent pixels in a  $0.2^\circ \times 0.1^\circ$  box surrounding the summit caldera. We then rank the interferograms by coherence and plot a trade-off curve of interferogram number versus coherence (Fig. 2.2b). L-Band ALOS data exhibits the most complete coherence (more than 90 % interferograms are  $>30\%$  coherent at the summit), whereas ENVISAT data shows much poorer coherence, with fewer than 45 % of ascending track interferograms and 35 % of descending track interferograms exceeding 30 % coherence at the summit. As was the case for the study of Poland et al. (2006), we find that the coherence of ERS-1/2 data at MLV is extremely poor, with fewer than 30 % of interferograms exceeding 25 % coherence at the summit. In addition to the causes of geometrical and temporal decorrelation highlighted above, such poor coherence can also be attributed to instrument limitations (e.g. Zebker and Villasenor 1992; Hanssen 2001). As the operation time of ERS-1/2 is also covered by leveling and GPS surveys we chose to discard this dataset.

### 2.2.2 Sources of Noise

Interferometric phase is not just a product of ground deformation but also contains several noise terms that compromise accuracy. The LOS displacement ( $d_{LOS}$ ) may be split into (a) the phase contribution from the difference in ground deformation between acquisitions  $t_1$  and  $t_2$  ( $\Delta\phi_{def}$ ), (b) the difference in the orbital contribution between acquisitions  $t_1$  and  $t_2$  ( $\Delta\phi_{orb}$ ) (see Sect. 2.2.2), (c) the difference in the atmospheric delay between acquisitions  $t_1$  and  $t_2$  ( $\Delta\phi_{atm}$ ) (see Sect. 2.2.2), and (d) the phase contribution due to other noise ( $\phi_{error}$ ):

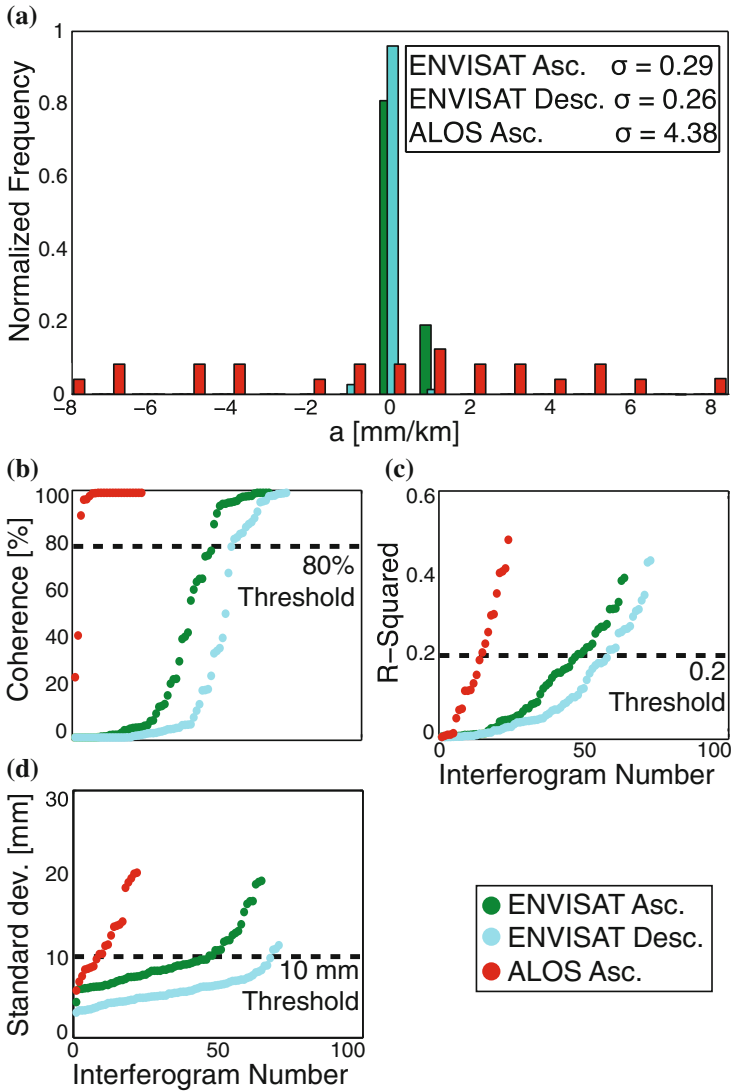


**Fig. 2.2** Summary of the coherence and noise of datasets used. **a** Histogram showing the distribution of the orbital parameter  $a$  from Eq. 2.2 for each dataset. ALOS data has a wider distribution of orbital parameters than ENVISAT as seen by the larger standard deviation. **b–d** show trade-off curves summarising the coherence and atmospheric noise of each dataset. Marked thresholds are those used in noise based stacking described in Sect. 2.3.1. **b** Interferograms are ranked by the percentage of coherent pixels in a  $0.2^\circ \times 0.1^\circ$  box surrounding the summit caldera. **c** Interferograms are ranked by the  $r^2$  value found by plotting elevation versus phase of each interferogram pixel. **d** Interferograms are ranked by the value of standard deviation found using Eq. 2.3

**Table 2.1** Datasets used in this study and associated noise properties described in Sect. 2.2. *Top* individual interferograms. *Bottom* results of  $\pi$ -RATE

Dataset	No. of scenes	Repeat time	Coherence <sup>a</sup> (%)	Orbital parameters <sup>b</sup>			Covariance <sup>c</sup>		$r^2$ <sup>d</sup>
				a	b	c	$\tilde{\sigma}$	$\tilde{\alpha}$	
ENVISAT ascending	32	35 days	41	0.29	0.21	$2.8 \times 10^4$	7.3	16	0.19
ENVISAT descending	32	35 days	30	0.26	0.24	$2.3 \times 10^4$	5.8	8.3	0.055
ALOS ascending	15	46 days	90	4.38	1.88	$2.5 \times 10^5$	10.8	11.2	0.058
ENVISAT ascending			100	0.0025	-0.0007	-0.97	2.96	2.25	$2.5 \times 10^{-4}$
ENVISAT descending			62	0.0032	-0.0013	-0.81	3.0	6.46	$160 \times 10^{-4}$
ALOS ascending			93	0.0003	0.0011	-1.23	6.8	1.65	$4.7 \times 10^{-4}$

<sup>a</sup>Percentage of coherent pixels within a  $0.2^\circ \times 0.1^\circ$  box surrounding the summit caldera

<sup>b</sup>Standard deviations of parameters a, b and c (Eq. 2.2) describing orbital contribution to phase

<sup>c</sup>Median values of  $\sigma$  and  $\alpha$  (Eq. 2.3) describing spatial correlation of the data

<sup>d</sup>Mean  $r^2$  value describing the correlation between pixel phase and elevation

$$d_{LOS} = -\frac{4\pi}{\lambda}(\Delta\phi_{def} + \Delta\phi_{orb} + \Delta\phi_{atm} + \phi_{error}). \quad (2.1)$$

In the following, we analyse the orbital and atmospheric contributions to each dataset, with parameters summarised in Table 2.1.

### Orbital Errors

Each satellite acquisition is made from a different location above the ground due to forces that act upon the satellite trajectory. Precise orbits are used to determine the exact separation of the satellite orbits, but not all forces can be fully modelled. Our knowledge of the orbital parameters is therefore imperfect, resulting in a long wavelength orbital error that remains in the interferogram (Fig. 2.10 in the Appendix) (Zebker et al. 1994). As the unmodeled accelerations are small, the error changes slowly in the along track direction (Hanssen 2001) and most authors approximate the orbital contribution using a first or second order 2-D polynomial (Biggs et al. 2007; Gourmelen et al. 2010). Accordingly, we investigate the orbital phase contribution to each dataset by finding the perturbation to the orbital parameters which best matches the observed phase using a linear empirical approximation of the form:

$$z = ax + by + c, \quad (2.2)$$

where  $[x, y]$  are the pixel coordinates,  $a$  and  $b$  are gradient parameters, and  $c$  is the intercept. We mask the edifice and solve for  $a$ ,  $b$  and  $c$  for each interferogram using a linear least squares inversion. For all datasets we find that both  $x$ - and  $y$ -gradients have a roughly normal distribution centred on zero (Fig. 2.2a). Using the standard deviation of the orbital parameters we find that the orbital contributions are greater for ALOS data than for ENVISAT data (Fig. 2.2a). This is in agreement with the large perpendicular baselines observed between consecutive ALOS acquisitions when constructing time versus baseline plots (see Fig. 2.9 in the Appendix).

### Atmospheric Errors

The atmospheric contribution to the phase results from changes in pressure, temperature and water vapour between acquisitions, as each of these factors controls the effective path length between the satellite and the ground. The most variable of these factors is tropospheric water vapour - vertically stratified water vapour causes a phase contribution that tends to correlate with topography, whereas turbulent water vapour causes 3D heterogeneities in refractivity that manifest as spatially correlated patterns in interferograms (Hanssen 2001). From visual inspection of interferograms at MLV, we find that the main source of atmospheric noise in this setting is turbulent water vapour across the Modoc Plateau, resulting in phase heterogeneities that do not correlate with topography (Fig. 2.10 in the Appendix).

We investigate the effects of water vapour stratification by looking at the relation between elevation and phase in each dataset. We begin by removing an orbital phase ramp (as described in Sect. 2.2.2), masking the edifice and identifying pixels that are coherent in all interferograms. We then use an SRTM 30 m DEM to plot the

elevation versus phase of each pixel in the interferogram. We then perform a linear regression to obtain the  $r^2$  value, using this as a measure of the correlation between elevation and phase - interferograms with  $r^2 > 0.2$  are deemed to be dominated by non-turbulent atmospheric noise. Using the values of  $r^2$ , we rank the interferograms in each dataset and plot a trade-off curve of interferogram number versus  $r^2$ . As MLV is of relatively low relief compared to the surrounding basin ( $\sim 1300$  m), we find that most interferograms do not show a strong relation between elevation and phase, and have  $r^2 < 0.2$  (Fig. 2.2c).

In reality, interferograms are highly spatially correlated (Hanssen 2001; Jónsson et al. 2002; Lohman and Simons 2005), and to account for spatial correlation of the signal, we use an exponentially-decaying form of covariance function to approximate the overall atmospheric phase contribution to each interferogram (Hanssen 2001). We assume that the statistical properties of the atmosphere are radially symmetric (Hanssen 2001) and use a 1D covariance function of the form:

$$c_{jk} = \sigma^2 e^{-d_{jk}\alpha}, \quad (2.3)$$

where  $c_{jk}$  is the covariance between pixels  $j$  and  $k$ ,  $\sigma^2$  is the variance,  $d_{jk}$  is the distance between the pixels and  $\alpha$  is the inverse of the e-folding wavelength - a measure of the spatial correlation of the signal.

We observe median values of  $\sigma = 7.3$  mm and  $\alpha = 16.0$  km for ENVISAT ascending data,  $\sigma = 5.8$  mm and  $\alpha = 8.3$  km for ENVISAT descending data (Fig. 2.3), and  $\sigma = 10.8$  mm and  $\alpha = 11.2$  km for ALOS ascending data, all of which are comparable to the studies of Biggs et al. (2007) in Alaska ( $\tilde{\sigma} = 7.5$  mm and  $\tilde{\alpha} = 12.3$  km) and Lyons and Sandwell (2003) in California ( $\tilde{\sigma} = 8.13$  mm).

We use the values of  $\sigma^2$  to rank the interferograms in each dataset by phase standard deviation ( $\sigma$ ), plotting a trade-off curve of interferogram number versus standard deviation. We find that all datasets have a similar distribution of standard deviation: the majority of interferograms have values  $< 10$  mm, with standard deviation increasing linearly until the kink in the trade-off curve, at which point we reach interferograms with much higher levels of noise (Fig. 2.2d).

Both water vapour stratification and turbulence are more significant in regions of significant topography (e.g. Chaussard et al. 2013). This is shown by Ebmeier et al. (2013b), who derive a relation between the relief of the edifice and RMS variation in range change across the summit, using examples from volcanoes in Central America. According to this relation, the relief of MLV compared to the surrounding plateau ( $\sim 1300$  m) would result in  $\sim 35$  mm RMS range change variation. This is  $\sim 3.5$  times larger than the amount of deformation we expect to observe each year at the rates obtained from leveling and GPS, emphasising the importance of using multi temporal methods in this setting.

Numerous studies have developed techniques for reducing the effects of atmospheric noise including: calibration of the signal with an external data source such as GPS (e.g. Li et al. 2006b); the use of weather models (e.g. Foster et al. 2006; Doin et al. 2009; Wadge et al. 2010; Chap. 3); and those based upon the statistical information contained within the interferograms themselves, such as the correlation

of phase with topography (e.g. Elliott et al. 2008). We take this statistical approach and use three multi temporal techniques each of which employs statistical information within the interferograms to reduce the effects of atmospheric noise.

## 2.3 InSAR Methods

Various analysis techniques have been developed to improve the coherence and signal-to-noise ratio of InSAR data in problematic settings. Past geodetic studies at MLV suggest that deformation is occurring at a constant rate (Dzurisin et al. 2002), and as such we test three techniques that each assume the deformation rate is linear: stacking, rate-map formation ( $\pi$ -RATE-Poly-Interferogram Rate and Time-Series Estimator: Biggs et al. 2007), and the Stanford Method for Persistent Scatterers (StaMPS: Hooper et al. 2007). Our choice of these techniques is also motivated by the accessibility of the software, as both  $\pi$ -RATE and StaMPS are available online with an element of user support. Each technique has a different approach to combining interferograms and minimising the effects of noise; by identifying common features between the results we are able to better determine the extent and magnitude of the deformation field.

### 2.3.1 Stacking

A common approach to increasing the signal-to-noise ratio of an InSAR dataset is combining multiple interferograms by stacking. This technique has been used elsewhere in the Cascades at Mount St. Helens, WA (Poland and Lu 2008), Three Sisters, OR (Riddick and Schmidt 2011) and previously at MLV (Poland et al. 2006). This simple method assumes that the signal within the interferograms accumulates at a constant rate whilst the noise is random. By adding together  $N$  interferograms of equal duration, the signal has a magnitude  $N$  times bigger than that of an individual interferogram, whereas the noise is only  $\sqrt{N}$  times larger (Biggs et al. 2007).

Stacking methods can often be further improved by stacking chains of interferograms (e.g. Johanson and Bürgmann 2005; Biggs et al. 2007), where the slave image of one interferogram is the master image of the next. In this approach, the noise contribution from the slave image of the first interferogram will be cancelled when it is used as the master image of the second interferogram, until the remaining noise contribution is due only to the first and last acquisitions within the chain. This is beneficial in cases when short duration interferograms are significantly more coherent than longer duration interferograms. This is not the case for the datasets used here, and we find that chain stacking introduces many small unwrapping errors that are of the same magnitude as the subsidence signal across the caldera or, in the case of ALOS, errors due to large perpendicular baselines between consecutive satellite acquisitions.



## Noise Based Data Selection for Stacking

Due to the extent of incoherence and phase heterogeneities caused by atmospheric errors, we adopt a stacking strategy designed to optimise the trade-off between the number of interferograms in each stack and the levels of atmospheric noise. This approach is based upon the analysis of coherence and noise sources presented in Sect. 2.2.

The main limitation of stacking is that it is only applicable to pixels that are coherent in all interferograms. To combat this we remove any interferograms with  $<80\%$  coherent pixels in a  $0.2^\circ \times 0.1^\circ$  box surrounding the summit caldera. This coherence threshold is selected through a process of trial and error. We begin with a lower value, resulting in poorer coherence when we sum all remaining interferograms, and increase this value until we achieve a minimum of  $\sim 30\%$  coherence when summing together all remaining interferograms. The result of this step is a smaller but more coherent dataset (Fig. 2.2b).

As the primary cause of atmospheric errors at MLV is atmospheric turbulence, the next step is to use phase variance analysis to remove interferograms that are dominated by large magnitude phase heterogeneities. When ranking the interferograms by phase standard deviation in Sect. 2.2.2, we identified a trade-off between the number of interferograms and the maximum standard deviation: including many interferograms increases the maximum standard deviation, whereas including few interferograms reduces the maximum standard deviation but also reduces the temporal coverage of the stack (Fig. 2.2d). We select a threshold standard deviation to optimise the stack using linear regression to identify the kink in the trade-off curve of each dataset. We perform separate linear regressions to the first and last 20% of data points in each dataset and use the intersection of these linear regressions to mark a standard deviation threshold. Applying this method to each dataset we find that a value of 10 mm provides a good fit to both ALOS and ENVISAT data (Fig. 2.2d).

The final stage of data selection is designed to minimise the dependence of phase upon topography caused by atmospheric stratification. As discussed previously, most interferograms do not exhibit a strong correlation between elevation and phase ( $r^2 > 0.2$ ) (Fig. 2.2c). We therefore set a threshold of  $r^2 = 0.2$ , only removing a small set of interferograms with larger  $r^2$  values.

The final stack for each dataset is produced by referencing interferograms to a far field region to account for different starting points used in phase unwrapping. We sum the phase at each pixel, divide by the total duration to calculate the rate at each pixel, and finally remove a linear phase ramp to account for the orbital phase contribution. For robustness we use a bootstrap approach to ensure that no single interferogram dominates the final stack. To do this we sequentially remove interferograms from the stack, checking that the maximum LOS displacement remains within  $1.5\sigma$  of that for the final stack.

In addition to stacking pixels that are coherent in all interferograms, we also test stacks of pixels that are coherent in a certain percentage of interferograms. However, testing different thresholds, we find that this approach is not robust and

results in noisier pixel values that are sensitive to the inclusion or exclusion of single interferograms.

### 2.3.2 *Poly-Interferogram Rate and Time-Series Estimator ( $\pi$ -RATE)*

Whereas the stacking methods described above only retain information from pixels that are coherent in all interferograms, Poly-Interferogram Rate And Time-series Estimator ( $\pi$ -RATE) employs a pixel-wise approach to calculate deformation rates at pixels that are coherent in different numbers of interferograms. This ensures that useful information about the magnitude and spatial extent of the deformation field is not lost. This advanced stacking approach originates from the multi interferogram method proposed by Biggs et al. (2007), with further development by Elliott et al. (2008) and Wang et al. (2009). The technique has been very successful in measuring fault related processes in regions such as Tibet (e.g. Wang et al. 2009; Wang and Wright 2012; Garthwaite et al. 2013), but has not previously been applied to volcanic datasets.

Unlike the stacking strategy outlined above,  $\pi$ -RATE corrects for sources of noise using networked corrections rather than removing noisy interferograms. In this approach, constraints from many interferograms are used to calculate the noise contribution at each acquisition rather than at each interferogram (Biggs et al. 2007; Wang et al. 2009). Networked corrections are used to correct orbital errors and topographically-correlated atmospheric errors, which are assumed to vary linearly with height as a first-order approximation (Elliott et al. 2008).

$\pi$ -RATE formally accounts for the error at each pixel using an appropriate variance-covariance matrix,  $\Sigma$ . This contains estimates of spatially correlated noise from the covariance function described in Eq. 2.3, whilst considering the temporal covariance between interferograms arising from common master or slave dates. The final stack is produced by solving for the best fitting LOS displacement rate at each pixel,  $r_{LOS}$  using a pixel-wise linear least squares inversion of the form:

$$\Sigma^{-1}T = \Sigma^{-1}r_{LOS}P, \quad (2.4)$$

where  $T$  is the duration of each interferogram coherent at that pixel and  $P$  is the phase of each interferogram. To improve computation time we downsample the interferograms, testing downsampling factors between 1 and 10. We choose a downsampling factor of 5, optimising the trade off between the spatial resolution and computation time. We then solve for all pixels that are coherent in at least 2 interferograms to maximise the coherence of the signal.

### 2.3.3 *Persistent Scatterer InSAR (PSInSAR)*

The final technique we use is persistent scatterer InSAR (PSInSAR). PSInSAR methods overcome incoherence by identifying persistent scatterer pixels using amplitude and phase stability characteristics (Ferretti et al. 2001). Within an interferogram, the phase of each pixel is dependent upon the phase returns from all scatterers in the corresponding element on the ground (Chap. 1). Some pixels contain stable scatterers whose phase return remains constant over time despite changes in surrounding scatterers. These persistent scatterers dominate the phase return of the pixel and act to reduce the amplitude and phase variance (Hooper et al. 2007).

We use the Stanford Method for Persistent Scatterers (StaMPS) developed by Hooper et al. (2007). This method has proven beneficial in other volcanic settings, such as Three Sisters, OR (Riddick et al. 2012), plus several volcanoes in Iceland (e.g. Hooper et al. 2009; Ofeigsson et al. 2011) and Mexico (Pinel et al. 2011), all of which suffer incoherence due to steep topography, snow cover and vegetation. Like  $\pi$ -RATE, this method includes a correction for atmospheric and orbital noise based upon spatial correlation characteristics of the signal (see Hooper et al. (2007) for details). We apply StaMPS to all available acquisitions from the ENVISAT ascending, ENVISAT descending and ALOS datasets. Using information from the California Department of Water Resources, we also investigate the effects of snow on PSInSAR by applying StaMPS to a subset of SAR scenes that were acquired during snow-free months. Although this greatly increases the number of PS pixels, the reduced number of SAR scenes compromises estimations of noise terms and we do not take this approach further.

## 2.4 Results of Multi Temporal InSAR Analysis Techniques

The results from all datasets and analysis methods suggest that ground deformation at MLV continues in the 21st century. All datasets show subsidence of a similar region centred on the summit caldera (Fig. 2.3), with maximum LOS displacements of  $\sim -13$  mm/yr for ascending datasets and  $\sim -7$  mm/yr for descending datasets. The methods are of variable degrees of success, with  $\pi$ -RATE offering significant improvements to coherence compared to the InSAR results from Poland et al. (2006). In this section we assess the results from each method in terms of the improvement in coherence and the reduction of noise sources. To investigate the magnitude and spatial extent of subsidence recorded by each dataset, we take displacement profiles that are coincident with the short and long axes of the caldera (N-S and E-W respectively) (Fig. 2.4). As was the case for rate-maps, these profiles demonstrate broad agreement in the spatial extent of subsidence. The profiles highlight some variability in the magnitude of deformation when using different InSAR analysis techniques, which we attribute to different interferograms being used by each method, but overall the magnitude of deformation is consistent between the three datasets.

### 2.4.1 *Stacking*

Within the stacking results for ENVISAT ascending data, the region SW of the volcano is largely incoherent (Fig. 2.3). Where there is coherence, displacement profiles show maximum LOS subsidence rates of  $\sim -13$  mm/yr. For ALOS ascending data, which exhibit good coherence at MLV, stacking is more successful, and profiles show maximum deformation rates of  $\sim -9$  mm/yr (Fig. 2.4). However, subsidence of  $\sim -5$  mm/yr is also observed across the highland between MLV and Mount Shasta (Fig. 2.3), suggesting that there is a remaining contribution from atmospheric stratification. For profiles of both ENVISAT and ALOS data, we observe other phase signals outside of the caldera, but these are not consistent between datasets and are considered to be due to noise.

Stacks of ENVISAT descending data show significant variability. Using the bootstrap test described in Sect. 2.3.1, we find that individual interferograms change the LOS deformation rate by  $>2\sigma$ , as many interferograms exhibit extensive phase heterogeneities, although the overall variance of the dataset is similar to that for ascending data (Fig. 2.2d). The edifice is also surrounded by larger regions of incoherence, causing many unwrapping errors in almost all scenes. We therefore find that stacking is not a robust method for dealing with this dataset.

### 2.4.2 *$\pi$ -RATE*

The results of  $\pi$ -RATE for ENVISAT ascending data show almost continuous coherence about the caldera, a significant improvement upon the results of stacking. The magnitude of the deformation signal is reduced by a factor of  $\sim 1.5$  compared to stacking, which we attribute to a reduction in the effects of atmospheric stratification. However, we do observe anomalous phase signals to the NW of the caldera which do not correlate with the results of other datasets (Fig. 2.3). For ALOS ascending data, displacement profiles taken across the results of  $\pi$ -RATE are of comparable magnitude to those for stacking and show similar distributions of displacements (Fig. 2.4).  $\pi$ -RATE is a much more successful method for ENVISAT descending data than stacking, reducing the effects of atmospheric turbulence and removing unwrapping errors by summing round loops of interferograms and masking any residuals (Biggs et al. 2007). Although the results for ENVISAT descending data remain more incoherent and noisy than those for both ascending datasets, displacement profiles show a clear subsidence signal with maximum LOS displacements of  $\sim -7$  mm/yr, which is in agreement with the results of ascending data (Fig. 2.4).

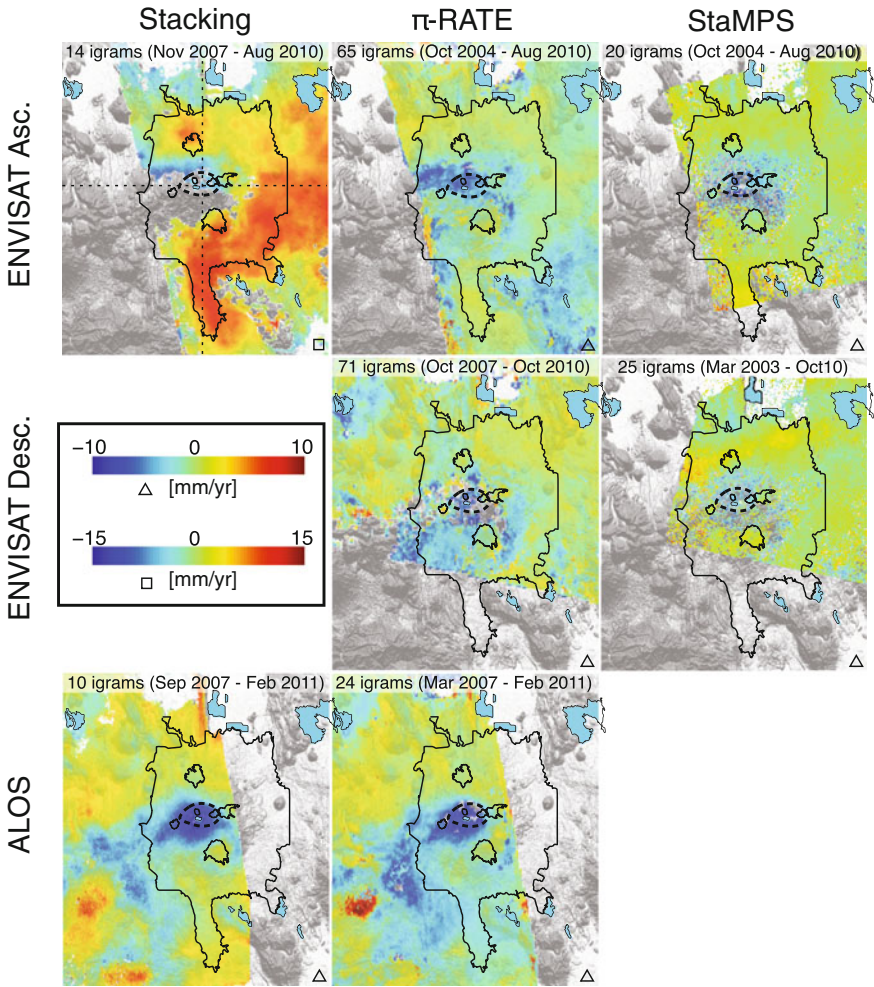


**Fig. 2.3** Results of multi temporal InSAR analysis using ENVISAT ascending, ENVISAT descending and ALOS ascending datasets and three methods (noise-based stacking,  $\pi$ -RATE and StaMPS). Each result is labelled with number of interferograms used and dates spanned. Outlined in black are MLV lava flows (*solid lines*) and caldera (*dashed line*) as in Fig. 2.1. *Squares* and *triangles* indicate the colour scale used. *Dashed lines* on the results of ENVISAT ascending stacking shows the location of the profiles drawn in Fig. 2.4

### 2.4.3 PSInSAR

Applying StaMPS to ENVISAT data significantly improves coherence compared to the raw interferograms, although coherence is not as continuous as for the results of  $\pi$ -RATE. Most PS pixels in the vicinity of the caldera are coincident with large surficial lava flows (Fig. 2.3), which helps to constrain the extent of the deformation

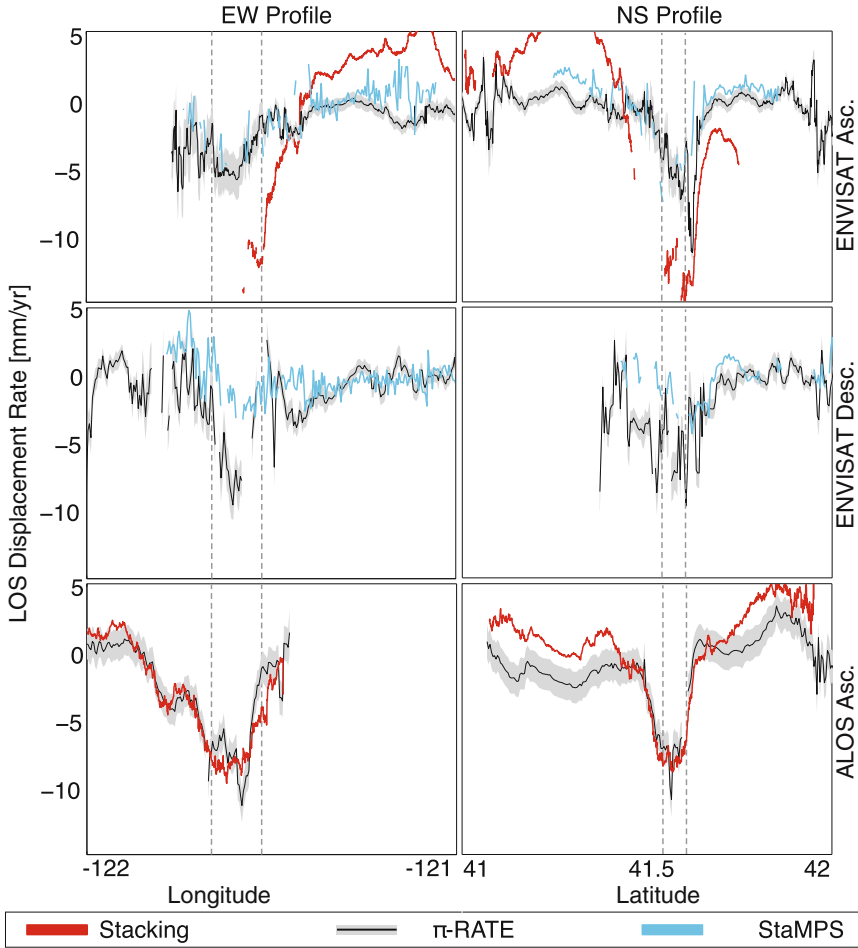


**Fig. 2.4** Displacement profiles for multi temporal InSAR analysis taken across the long and short axes of the caldera (EW and NS directions respectively - see Fig. 2.3). The extent of the caldera is marked on all profiles with *dashed grey lines*. Error bounds on the results of  $\pi$ -RATE are calculated using the variance-covariance matrix in Eq. 2.4. There is good agreement in the spatial extent of the signal between different InSAR analysis techniques but for ENVISAT data we observe some variation in the magnitude of the signal due to different interferograms being used for each method

field. Lava flows with fewer PS pixels are sparsely vegetated. From reconnaissance field analysis we find that another possible control upon PS density at lava flows is modal block size - at Burnt Lava Flow directly south of the caldera we found that regions with fewer PS corresponded to a smaller modal block size (20–50 cm) compared to the average block size of the flow (50–100 cm). Other PS pixels are coincident with road intersections, smaller outcrops and clearings within the forest.

These findings are similar to those of Riddick et al. (2012) in their study of PS in central Oregon, although a possible relation between PS density and block size has not previously been noted.

The deformation field obtained with StaMPS for ENVISAT ascending data has a similar extent to that observed with stacking and  $\pi$ -RATE: deformation is focussed on the caldera between lava flows to the north, east, south and west, with maximum displacements of  $\sim -8$  mm/yr at Medicine Lake Glass Flow in the NW of the caldera (Fig. 2.3). However, the anomalous phase signals observed NW of the caldera in the results of  $\pi$ -RATE have been reduced. Similar results are observed for ENVISAT descending data. Deformation is again constrained within a region bound by lava flows to the north, east, south and west of the caldera, however displacements are of smaller magnitude (up to  $\sim -5$  mm/yr) and there is still some evidence of atmospheric turbulence north of the volcano (Fig. 2.3). Unlike ENVISAT data, ALOS ascending data is highly coherent at MLV and, due to the success of both stacking and  $\pi$ -RATE, we do not include the results of StaMPS analysis for this dataset.

#### 2.4.4 Comparison to Past Geodetic Studies

Past geodetic studies at MLV show that the rate of subsidence remained constant (to within detection limits) between 1954 and 2004 (Dzurisin et al. 2002; Poland et al. 2006). To assess whether this observation can be extended to 2011, we compare the most coherent set of InSAR results (those produced using  $\pi$ -RATE) to the results of leveling from Dzurisin et al. (2002).

The section of the leveling line that covers MLV caldera extends northwards from Burnt Lava Flow south of the caldera, to the centre of the caldera, before continuing west across the long-axis of the caldera (see map in Fig. 2.5). We select pixels within 1500 m of each leveling station (ensuring that we use the values from  $>10$  pixels) and calculate the average deformation rate before referencing to pixels coincident with the reference leveling station. We assume the deformation is vertical and, as InSAR measurements are made oblique to vertical, project the leveling measurements into the LOS using the satellite look vector as defined in Wright et al. (2004b). Error bars on InSAR measurements are then  $1 \sigma$  calculated by propagating the error values at each pixel, which are obtained using the formal error estimation of  $\pi$ -RATE (Eq. 2.4).

Both ENVISAT datasets are in agreement with the results of past leveling surveys, with maximum displacements coincident with the caldera (Fig. 2.5). ALOS ascending data are also in close agreement with ENVISAT on the S-N portion of the line. On the E-W portion of the line there is an increase in the magnitude of the signal recorded by ALOS, which we attribute to under correction of residual atmospheric artefacts across the highland between MLV and Mount Shasta (Fig. 2.5). Overall, we find no evidence of a decrease in the rate of subsidence since 1954, as the results of InSAR analysis fall within error of leveling measurements. This suggests that the constant rate of subsidence detected by Dzurisin et al. (2002) continued until at least the last ALOS acquisition in 2011. Deformation at MLV has therefore been sustained at a steady rate for over 60 years.

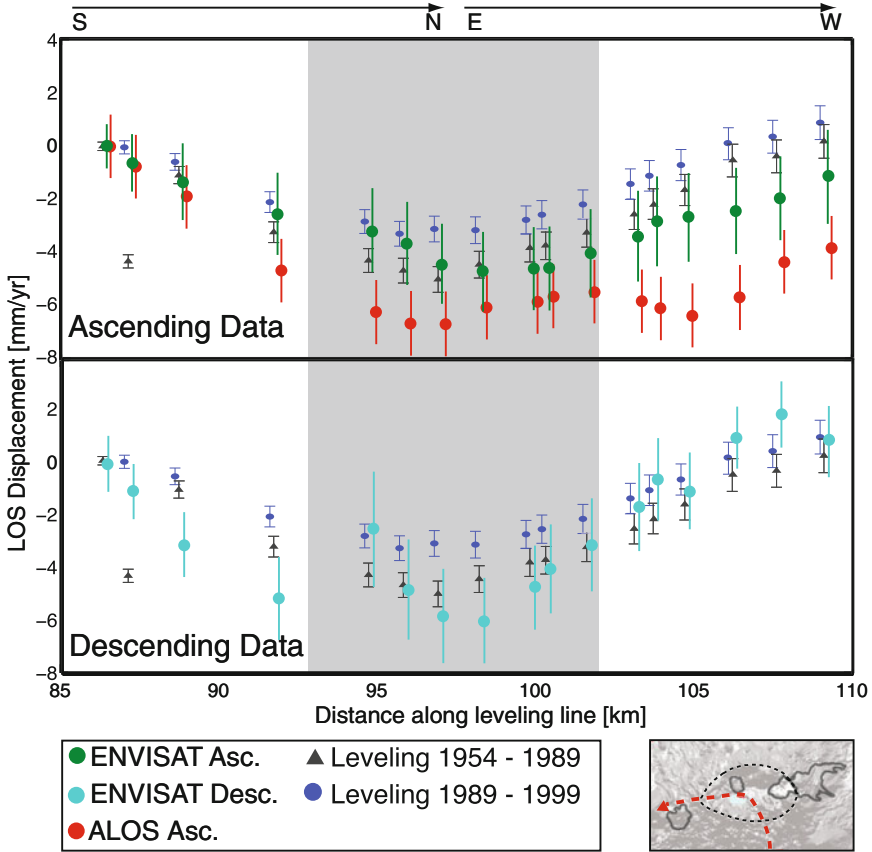


**Fig. 2.5** Comparison between the results of leveling from Dzurisin et al. (2002) and InSAR. Profiles are offset to aid viewing. The section of the leveling line used is shown by the red line in the small map, where black lines show MLV caldera and lavas as in Fig. 2.1. The shaded grey region of the profiles corresponds to the extent of the caldera. We average pixels within 1500 m of each leveling station and reference to pixels at the reference leveling station. Errorbars on InSAR measurement are  $1\sigma$  and are calculated by propagating the error on individual pixels from the variance-covariance matrix in Eq. 2.4 (color figure online)

### 2.4.5 Horizontal and Vertical Displacements

The side-looking nature of InSAR satellites means that measurements contain a component of both horizontal and vertical motion in the LOS of the satellite (for details see e.g. Rosen et al. 2000). We can therefore use multiple tracks of data, each of which has a different satellite look direction, to decompose the LOS motion into horizontal and vertical components (e.g. Wright et al. 2004b; Biggs et al. 2009b). This allows us to better constrain the 3D deformation field at MLV, in addition to



providing measurements at a higher temporal and spatial resolution than past geodetic campaigns.

Using the results for ENVISAT ascending and ENVISAT descending data, we solve for the EW and vertical components of motion only,  $\mathbf{u} = (u_E, u_Z)^T$ , as InSAR measurements are less sensitive to NS motion. We use the equation  $\mathbf{R} = \mathbf{S}\mathbf{u}$ , where  $\mathbf{R}$  is a vector of the LOS displacements for each dataset and  $\mathbf{S}$  is a  $2 \times 2$  matrix containing the unit satellite look vectors for each dataset (Wright et al. 2004b). We solve for  $\mathbf{u}$  at each pixel, weighting the inversion using a covariance matrix for errors in the observed range change  $\Sigma_R$  (Wright et al. 2004b).  $\Sigma_R$  contains values based upon covariance analysis from Eq. 2.3, and is used to find the covariance matrix for the estimated vector components,  $\Sigma_u$ .

The relative magnitudes of the resulting horizontal and vertical displacement fields are in agreement with measurements from leveling and GPS (Fig. 2.6). GPS

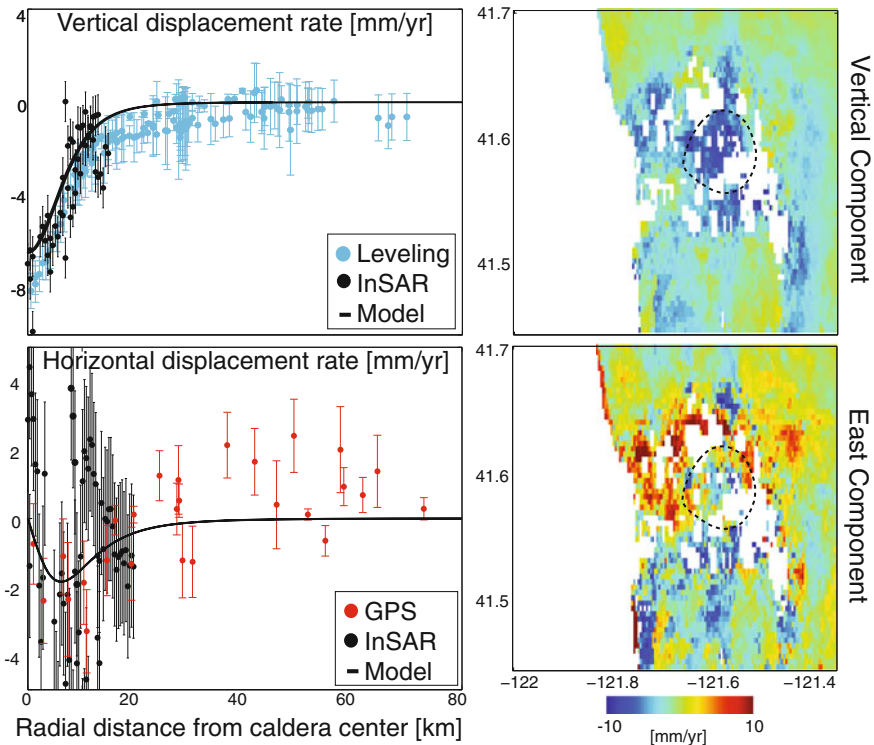


**Fig. 2.6** Left comparison between vertical and horizontal components of motion derived from InSAR and from past geodetic studies. Leveling measurements are from Dzurisin et al. (2002) and GPS measurements are from Poland et al. (2006). Errorbars on InSAR data are found using the covariance matrix  $\Sigma_u$  described in Sect. 2.4.5. The solid black line shows model displacements for the best fitting analytical model to InSAR data described in Sect. 2.5.3 and Table 2.2. Right vertical and horizontal displacements found by inverting multiple tracks of InSAR data as described in Sect. 2.4.5. The caldera is marked by a dashed black line

surveys of MLV revealed the high ratio of vertical to horizontal displacements (Poland et al. 2006) and we find that this is confirmed by InSAR data, with InSAR derived horizontal displacements of  $\sim 3$  mm/yr, compared to vertical displacements of up to  $\sim -8$  mm/yr (Fig. 2.6). Both horizontal and vertical deformation fields are broadly symmetrical and centered on the caldera centre, with vertical deformation extending for  $\sim 20$  km (Fig. 2.6).

## 2.5 Modelling: Estimates of Source Geometry and Volume Change

The past studies of Dzurisin et al. (2002) and Poland et al. (2006) consider possible sources of subsidence at MLV. Both authors acknowledge the tectonic contribution due to extension of the Basin and Range province, plus a component of surface loading due to the large volume of emplaced material. However, they also recognise that, to fully explain the deformation field, a component of volume loss at depth is required. The authors model this by first using idealised, elastic models - a well established and widely used approach to obtain information about source geometries from geodetic data (e.g. Dzurisin 2007; Segall 2010). As mentioned previously, there are discrepancies between the best fitting source models to each dataset, as leveling and GPS measurements are sensitive to different components of the deformation field. Both datasets favour a sill rather than a point source, but leveling data prefer a smaller ( $10.3$  km  $\times$   $4.4$  km), deeper ( $11$  km) source that strikes NE-SW ( $221^\circ$ ) (Dzurisin et al. 2002), whereas GPS data prefer a larger ( $18.2$  km  $\times$   $9.2$  km), shallower ( $5$  km) source that strikes E-W ( $267^\circ$ ) (Poland et al. 2006) (Table 2.2).

We address analytical models of the deformation source using the improved spatial resolution of all available InSAR measurements. As the problem is highly non-linear, we use a Monte Carlo type simulated annealing algorithm as an optimisation tool to minimise the misfit function (Amelung and Bell 2003). This combines the efficiency of a derivative based search algorithm whilst testing a wide range of source parameters to avoid local minima. We simultaneously solve for all datasets, reducing the number of data points by downsampling (e.g. Biggs et al. 2010; Hamling et al. 2014, and others). We downsample to a regular grid rather than by quadtree partitioning, as regions of high phase gradients are associated with atmospheric noise in addition to ground deformation. As source models of this nature are inherently non-unique, we investigate the trade-offs between model parameters and the bounds upon each model parameter using a Monte Carlo algorithm (e.g. Wright et al. 2004a; Biggs et al. 2009a). This is done by using the parameterised values of the covariance function (Eq. 2.3) to create 100 sets of synthetic atmospheric noise for each dataset, which are then added to the results selected in Sect. 2.5.1 before rerunning the same inversion procedure. The best fitting parameters and  $1\sigma$  error bounds from Monte Carlo analysis are summarised in Table 2.2, and histograms showing the distribution of the model parameters are shown in Fig. 2.11 in the Appendix. Cayol and Cornet

**Table 2.2** Summary of analytical source models from this study and past geodetic studies. Top: Best fitting point source model. Bottom: Best fitting rectangular sill model. Upper and lower bounds on source parameters to InSAR data are  $1\sigma$  from Monte Carlo Error Analysis described in Sect. 2.5

Data	Long. [°W]	Lat. [°N]	Depth [km]	Length [km]	Width [km]	Strike [°]	Opening [m/yr]	$\Delta$ volume [km <sup>3</sup> /yr]	Misfit <sup>a</sup>
Leveling <sup>1</sup>	121.580	41.590	10	-	-	-	-	-0.0031	18.31
	121.590	41.580	6	-	-	-	-	-0.0010	1.24
InSAR	121.562	41.573	5.8	-	-	-	-	-0.00095	5.33 mm
	121.569	41.576	6.2	-	-	-	-	-0.0013	
Leveling <sup>1</sup>	121.410	41.566	11	10.3	4.4	221	-0.0446	-0.0020	18.33
	121.559	41.637							
GPS <sup>2</sup>	121.499	41.623	5	18.2	9.2	267	-0.0151	-0.0025	0.96
	121.718	41.616							
InSAR	121.566	41.576	9.1	1.0 <sup>b</sup>	1.0 <sup>b</sup>	245	-1.10	-0.0011	5.31 mm
	121.572	41.580	9.8			255	-1.33	-0.0013	

<sup>a</sup>Misfit values are not comparable between studies but lower values indicates a better model fit

<sup>b</sup>Misfit for this study is the total RMS error between the model and each dataset

<sup>c</sup>Parameter value is fixed in the inversion of InSAR data

Parameters and bounds are from the following references: <sup>1</sup>Dzurisin et al. (2002), <sup>2</sup>Poland et al. (2006)

(1998) discuss the bias introduced in analytical modelling by steep topography, but we choose not to account for the effects of topography as MLV has low relief compared to the surrounding plateau and topographic slopes do not exceed  $2\text{--}3^\circ$ .

### ***2.5.1 Selection of InSAR Data for Use in Modelling***

We use all datasets to model the deformation at MLV, selecting the most successful multi temporal InSAR approach in each case. For ENVISAT ascending data we use the results of StaMPS, as this offers the best deformation signal, avoiding anomalous phase signals to the NW of the volcano that are not observed in other datasets (Fig. 2.3). For ENVISAT data, we select the results of  $\pi$ -RATE, as the improvement to coherence is greater than that with StaMPS, as is the reduction of atmospheric turbulence (Fig. 2.3). Both stacking and  $\pi$ -RATE offer comparable results for ALOS data, but the application of  $\pi$ -RATE has reduced the magnitude of topographically correlated atmospheric delays observed near Mount Shasta (Fig. 2.3), and we use this as the final input for modelling.

### ***2.5.2 Point Source***

We begin by solving for the simplest point source geometry parameterised in terms of: [x, y] location, depth and volume change (Mogi 1958; Dzurisin et al. 2002; Poland et al. 2006). We allow the location to vary over the extent of the caldera and depth to vary between 2 and 20 km. The best fitting source parameters are similar to those found by Dzurisin et al. (2002) for leveling data and Poland et al. (2006) for GPS data (Table 2.2), with a source depth of 6 km and rate of volume change of  $-0.0012\text{ km}^3/\text{yr}$ . Using Monte Carlo error analysis we find that the location of the source is well constrained SE of the caldera centre (Fig. 2.7a). We also identify a strong trade-off between depth and source strength as smaller volume changes at shallow depths produce a similar magnitude of deformation as larger volume changes at greater depths (Fig. 2.7b). Although we do not expect a point source to be the most representative source geometry (Dzurisin et al. 2002; Poland et al. 2006), the results of this modelling provide good constraints upon the location of the deformation source at MLV.

### ***2.5.3 Sills***

We test more complicated source geometries that are representative of sill-like intrusions, using an approximation of a horizontal, rectangular dislocation (Okada 1985) (the preferred model for both leveling (Dzurisin et al. 2002) and GPS data (Poland

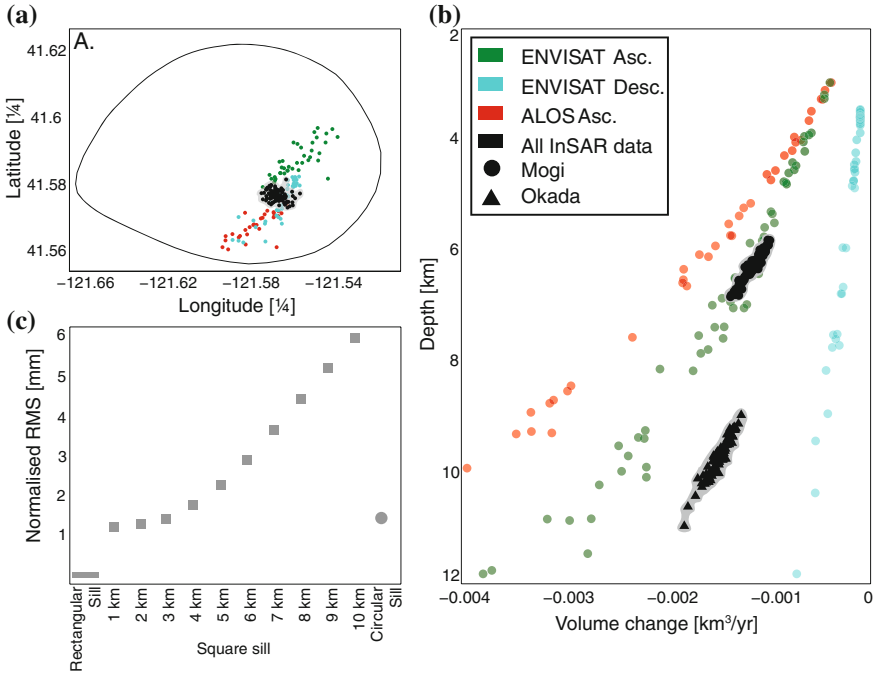


**Fig. 2.7** **a** results of Monte Carlo error analysis for inversions of a point source to constrain the source location. *Coloured circles* represent inversions of individual datasets and *black circles* are for joint inversions of all InSAR data. *Black line* shows the extent of the summit caldera. **b** trade-off curves obtained from Monte Carlo analysis showing the trade-off between source strength and depth for different source geometries. **c** summary of the RMS misfit for different model geometries found by inverting all InSAR datasets. Square sills with width and length <4 km fit the data to within 1 % of the RMS misfit for the best fitting rectangular and circular sills (color figure online)

et al. 2006)). The source is parameterised in terms of:  $[x, y]$  location, depth, length, width, strike, dip and opening. We assume a dip of  $0^\circ$  given the apparent symmetry of the deformation signal and the similarity between ascending and descending interferograms. The remaining model parameters are constrained between a set of bounds to reduce the size of the parameter space. We set bounds upon the location using the results of point source modelling described above. For the remaining free parameters (length, width and strike) we run a selected range of forward models, varying a single parameter in each case. We then calculate the RMS and plot a curve of RMS versus model parameter. Bounds are then set based upon regions of low RMS. In addition to geometrical parameters, we specify a Poisson’s Ratio of 0.25. As was observed for a point source, solutions are non unique, and we identify a trade-off between the magnitude of the source and the depth (Fig. 2.7b).

From Monte Carlo analysis we find that rectangular sills tend towards lengths in excess of 20 km due to residual atmospheric stratification across the highland to the south west of the volcano, which elongates the subsidence signal (Figs. 2.1a and 2.4).

These lengths are unrealistic: a sill of this size does not fit with models of leveling or GPS data. To overcome this, we rerun the inversion procedure solving for a square sill (length-to-width ratio = 1). We find that square sills with length and width <4 km fit the data to within 1 % of the RMS for the best fitting rectangular sill (Fig. 2.7c).

The best fitting source geometry found by inverting all datasets is a square sill with length and width 1 km, located at 9.5 Km depth with maximum opening of -1.2 m/yr (Table 2.2 and Fig. 2.8). This model gives RMS values of 1.67, 1.16 and 2.48 mm for ENVISAT ascending, ENVISAT descending and ALOS datasets respectively. (Figure 2.8) We estimate the expected error ( $\sigma$ ) of each InSAR result using covariance analysis (Eq. 2.3). As each InSAR result is produced using multiple interferograms, the expected error is reduced to  $\sigma/\sqrt{N}$ , where  $N$  is the number of observations and  $\sigma$  is assumed to be uncorrelated between observations (e.g. Parks et al. 2011). We obtain expected error values of 1.4, 1.1 and 2.5 mm for ENVISAT ascending, ENVISAT descending and ALOS datasets, which are of the same order as the RMS between the best fitting model and each dataset.

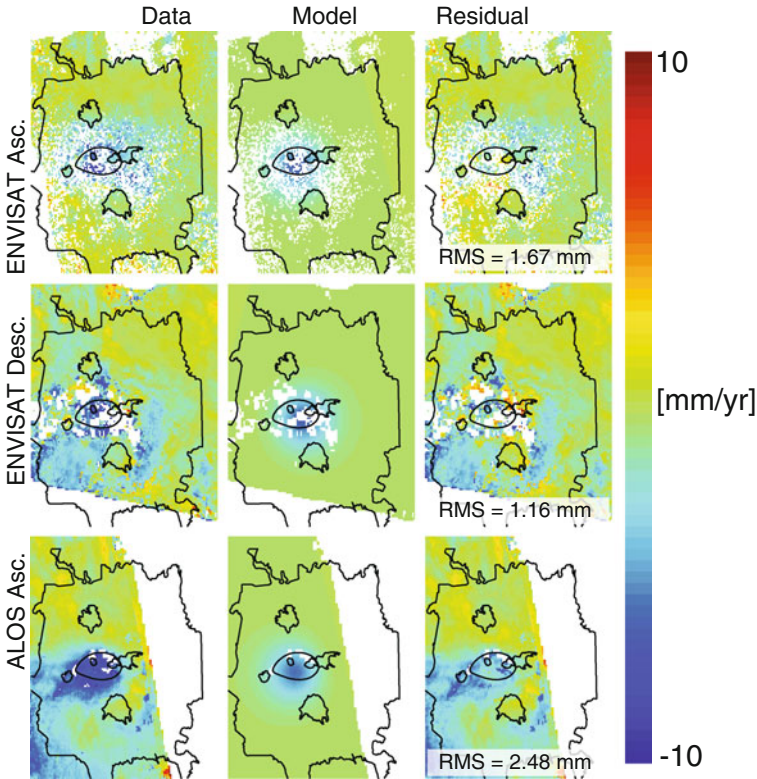


**Fig. 2.8** Results of inverse modelling. Data are the InSAR analysis results defined in Sect. 2.5.1 and the best fitting model is a square sill with parameters specified in Table 2.2. Plots of residual are labelled with RMS values

The final step of the modelling procedure is to ensure that the model accounts for the high ratio of vertical to horizontal displacements recorded by InSAR. We compare profiles of horizontal and vertical model displacements to the components of motion derived from InSAR data, and also consider the magnitude of horizontal and vertical measurements from GPS and leveling (Fig. 2.6). The vertical displacements predicted by the model provide a good fit to the vertical measurements from InSAR (RMS 1.88 mm), with maximum displacements of  $\sim -7$  mm/yr, and subsidence extending for  $\sim 20$  km. Model displacements are also mostly within error of the vertical measurements from leveling, although maximum displacements are 1–2 mm/yr smaller than those recorded by leveling. The horizontal displacements from InSAR are more variable than the vertical measurements, and are of the same magnitude as the errors (Fig. 2.6). However, profiles do show that the horizontal model displacements are within the error bounds of the InSAR measurements. In accordance with GPS observations, the horizontal displacements predicted by the model are a factor of  $\sim 3$  smaller than vertical displacements, and at radial distances  $< 20$  km, the model displacements are within error of the GPS measurements.

Through modelling all available InSAR data, we confirm that the best fitting source geometry at MLV is sill-like. However, uniform opening of a rectangle is not a physically realistic model, and we test this solution against a uniform pressure solution - an axi-symmetric, horizontal, penny shaped crack parameterised in terms of:  $[x, y]$  location, depth, radius and pressure change (Fialko et al. 2001a; Biggs et al. 2009a). This model has been used in other settings where large ratios of vertical to horizontal displacements have been observed (e.g. Campi Flegrei, Italy; Battaglia et al. 2006). We follow the same procedure described above to solve for the best fitting circular sill and investigate the bounds upon the source parameters. As for the rectangular sill, we find from Monte Carlo error analysis that the sill radius tends towards unrealistically large values, and we therefore opt to constrain the radius of the sill to 1 km, emulating the geometry of the best-fitting square sill. The best fitting circular sill is located within 1 km of the best fitting square sill, has the same source depth of 9.5 km and predicts displacements that vary by only up to 1 mm from those predicted by the square shaped sill. This suggests that the depth, location and overall nature of the source are well constrained, but we are unable to distinguish the exact shape of the source.

## 2.6 Discussion

Subsidence of MLV is unique in both duration and stable magnitude, with surveys of U.S. Geological Survey geodetic networks since 1954 providing a long and detailed geodetic history of the volcano. The focus of this work has been to use the significant archive of InSAR data acquired at MLV to build upon the long-term record of subsidence, extending the geodetic history to 2011 and investigating the spatial and temporal pattern of deformation at higher resolution. Although the application of these data in this region is problematic, by using a range of datasets from differ-

ent satellites and a suite of new analysis methods, we have been able to use InSAR data to demonstrate that deformation remains at historical rates of  $\sim -10$  mm/yr. Of the methods used, we find that  $\pi$ -RATE provides the greatest improvement to coherence, with the coverage of ENVISAT datasets increased by 30% compared to the raw interferograms (Table 2.1). Comparing the mean values of the orbital and covariance parameters (Eqs. 2.2 and 2.3) before and after application of  $\pi$ -RATE, we also find that this technique reduces the level of noise of each dataset (Table 2.1).

### 2.6.1 Causes of Subsidence

Past studies attribute subsidence at MLV to a combination of factors including tectonic extension and surface loading, due to the volume of the edifice and its location at the western edge of the Basin and Range extensional province (Dzurisin et al. 2002; Poland et al. 2006). However, GPS measurements show that there is no resolvable extensional strain across the region (Poland et al. 2006), and surface loading is at odds with drill hole data, which suggests that subsidence rates are anomalously high in the present day, as downwarping of the crust beneath the edifice would have occurred within only  $\sim 10\%$  of the lifespan of the volcano (Dzurisin et al. 2002). Poland et al. (2006) suggest that these larger scale processes would enhance subsidence, rather than be the primary cause, and infer an additional component to account for volume loss at depth. Poland et al. (2006) and Dzurisin et al. (2002) discuss the likelihood of various possible mechanisms: volume loss due to eruption; drainage to a deeper reservoir; hydrothermal fluid withdrawal; and cooling and crystallisation at depth. Of these possibilities, Poland et al. (2006) deem drainage or cooling and crystallisation to be most likely: the last eruption at MLV occurred 1 ka, and the steady nature of the deformation since the 1950s does not agree with a hydrothermal source, as hydrothermal systems generally exhibit cycles of deformation that occur over shorter timescales (e.g. Dzurisin et al. 1999). The hypothesis of cooling and crystallising magmatic material is also supported by elevated temperatures discovered by geothermal drilling, thought to be due to either the reservoir beneath Glass Mountain or basalt intruded at depth in late Holocene times (Donnelly-Nolan et al. 1990).

The depth of the modelled source is significant when considering cooling and crystallisation as a deformation mechanism at MLV. Rather than the presence of a central magma chamber, the results of geophysical and geological surveys suggest that MLV is underlain by an extensive intrusive complex of sills and dikes with varying compositions (e.g. Finn and Williams 1982; Zucca et al. 1986; Fuis et al. 1987; Evans and Zucca 1998; Lowenstern et al. 2003). Seismic tomography studies of the volcano reveal a small magma body located beneath Glass Mountain (the site of most recent eruption  $\sim 1$  ka) at 3–7 km depth (Evans and Zucca 1998), but they also indicate that a subsolidus pluton could be present within the larger intrusive complex (Ritter and Evans 1997). A shallower source depth may therefore suggest deformation related to material imaged at Glass Mountain, whereas a greater source depth may be indicative of cooling within the underlying intrusive complex.



The best fitting analytical source model identified in this study fits with the source mechanisms presented by previous authors and accounts for the high ratio of vertical to horizontal displacements derived from InSAR data. The depth of the model (9.5 km) suggests that, if cooling and crystallisation is the cause of volume loss, the source is likely to be located within the intrusive complex beneath the volcano, rather than the body of melt imaged at 3–7 km depth. In their study, Dzurisin et al. (2002) state that an unrealistically large volume would be required to result in 50 years of subsidence due to cooling and crystallisation. However, simple thermoelastic calculations (e.g. Turcotte and Schubert 1982) do not account for the geotherm, which in this region is thought to be relatively high, or the underlying intrusive complex, which geodetic models suggest is the location of the deformation source. This intrusive complex is described by Poland et al. (2006) as a “relatively hot, roughly cylindrical volume”, and is likely to play a role in driving the active geothermal system. Elevated temperatures surrounding an intrusion would decrease the rate of cooling, as would the production of latent heat during the transition from a liquid to a solid phase. Thus, it is important not to disregard cooling and crystallisation as a possible cause of deformation.

## 2.7 Conclusions

This study demonstrates how InSAR data may be successfully applied in mountainous, vegetated regions by using multiple datasets, careful data selection and a suite of multi temporal analysis methods that account for atmospheric and orbital noise sources. Both StaMPS and  $\pi$ -RATE are freely accessible online and offer user support, which plays a fundamental role in helping the community use these methods to better apply InSAR data in challenging regions. The application of these advanced InSAR techniques will be key to the success of data analysis from the new generation of SAR satellites, with the limiting factor likely to be the acquisition rate of the satellite.

Using the results of multi temporal analysis at MLV, we show that the rate of subsidence constrained by InSAR data is comparable to that obtained from leveling studies throughout the 20th century, suggesting that current rates of deformation at the volcano have been continuous for over 60 years. We confirm that, as was observed with GPS measurements, the deformation field is characterised by high ratios of vertical to horizontal displacements, which is a key constraint upon source models of deformation. We use geophysical inversion methods and Monte Carlo error analysis to obtain the best fitting source geometry to InSAR data, which we find to be a horizontal sill located at 9.5 km depth beneath the caldera. This geometry accounts for the relative magnitudes of horizontal and vertical components of deformation as recorded by both InSAR and past ground based surveys. The model is similar to those constrained by past datasets, and fits the hypothesis that deformation at MLV is caused by a combination of tectonic mechanisms, plus a component of volume loss at depth. The most likely cause of volume loss is either drainage or cooling and crystallisation of magmatic material. If cooling and crystallisation is the cause of

present day deformation, the depth of the model suggests that it is related to material within the intrusive complex imaged beneath the volcano.

The next step of studies at MLV will be to use the high resolution of InSAR data and these first order estimates of source geometry to constrain models of magmatic and tectonic causes of deformation. This will provide further insight into magmatic conditions in northern California, but it is also an opportunity to test hypotheses related to long-term intrusive processes that occur during inter-eruptive periods (e.g. Caricchi et al. 2014).

## Appendix

See Figs. 2.9, 2.10 and 2.11.

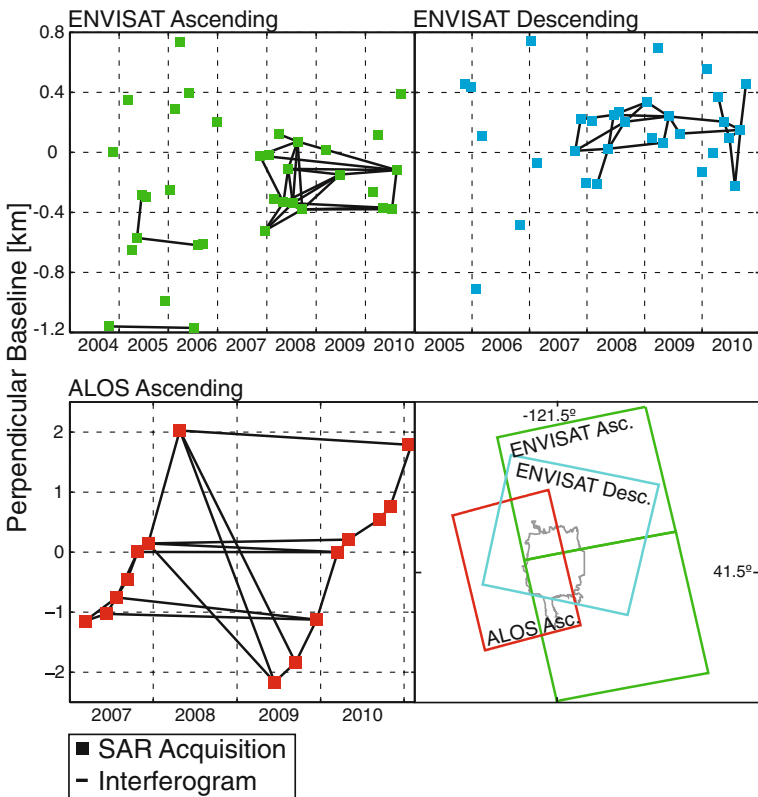


**Fig. 2.9** Time versus perpendicular baseline plots for InSAR datasets at Medicine Lake Volcano. Interferograms are those with >30% coherence at the summit of the volcano. Map shows the coverage of each InSAR track with respect to the extent of Medicine Lake Volcano lavas

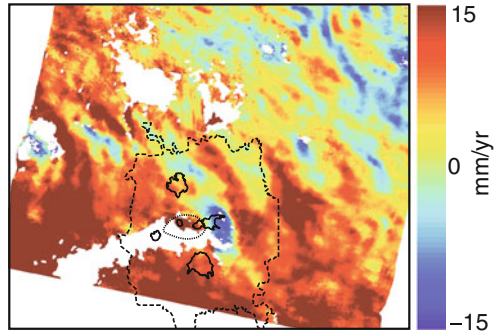
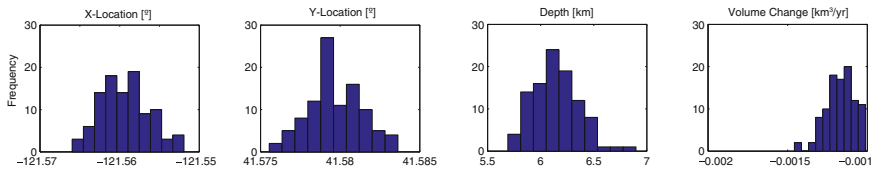


**Fig. 2.10** Example of incoherence, orbital phase ramp and turbulent atmospheric noise commonly observed at Medicine Lake Volcano in ENVISAT descending data. The outline of the extent of Medicine Lake Volcano lavas is shown by *long-dashed line*. The caldera is shown by the *short-dashed line* and major surgical lava flows are shown by *solid black lines*

MOGI SOURCE



OKADA SOURCE

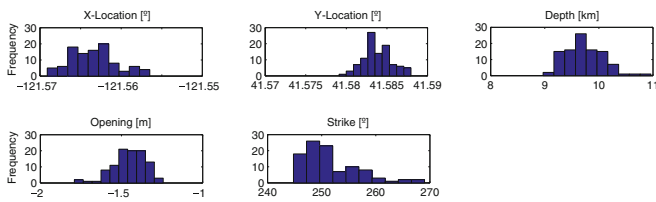


**Fig. 2.11** Histograms for each model parameter from Monte Carlo error analysis. Histograms are used to calculate the  $1\sigma$  error bounds on the source parameters

## References

Amelung, F., & Bell, J. (2003). Interferometric synthetic aperture radar observations of the 1994 Double Spring Flat, Nevada, earthquake (M5.9): Main shock accompanied by triggered slip on a conjugate fault. *Journal of Geophysical Research*, *108*(B9), 2433.

Battaglia, M., Troise, C., Obrizzo, F., Pingue, F., & De Natale, G. (2006). Evidence for fluid migration as the source of deformation at Campi Flegrei caldera, (Italy). *Geophysical Research Letters*, *33*, L01307.

Berardino, P., Fornaro, G., Lanari, R., & Sansosti, E. (2002). A new algorithm for surface deformation monitoring based on small baseline differential SAR interferograms. *IEEE Transactions on Geoscience and Remote Sensing*, *40*, 2375–2383.

- Biggs, J., Wright, T., Lu, Z., & Parsons, P. (2007). Multi-interferogram method for measuring inter seismic deformation: Denali Fault, Alaska. *Geophysical Journal International*, 170, 1165–1179.
- Biggs, J., Anthony, E. Y., & Ebinger, C. J. (2009a). Multiple inflation and deflation events at Kenyan volcanoes. *East African Rift. Geology*, 37(11), 979–982.
- Biggs, J., Robinson, D. P., & Dixon, T. H. (2009b). The 2007 Pisco, Peru, earthquake (M8.0): seismology and geodesy. *Geophysical Journal International*, 176, 657–669.
- Biggs, J., Lu, Z., Fournier, T., & Freymueller, J. T. (2010). Magma flux at Okmok Volcano, Alaska, from a joint inversion of continuous GPS, campaign GPS and interferometric synthetic aperture radar. *Journal of Geophysical Research*, 115, B12401.
- Biggs, J., Ebmeier, S. K., Aspinall, W. P., Lu, Z., Pritchard, M. E., Sparks, R. S. J., et al. (2014). Global link between deformation and volcanic eruption quantified by satellite imagery. *Nature Communications*, 5, 3471.
- Blakely, R. J., Christiansen, R. L., Guffanti, M., Wells, R. E., Donnelly-Nolan, J. M., Muffler, L. J. P., et al. (1997). Gravity anomalies, Quaternary vents, and Quaternary faults in the southern Cascade Range, Oregon and California; implications for arc and backarc evolution. *Journal of Geophysical Research*, 102, 22513–22527.
- Caricchi, L., Biggs, J., Annen, C., & Ebmeier, S. (2014). The influence of cooling, crystallisation and re-melting on the interpretation of geodetic signals in volcanic systems. *Earth and Planetary Science Letters*, 388, 166–174.
- Cayol, V., & Cornet, F. H. (1998). Effects of topography on the interpretation of the deformation field of prominent volcanoes: Application to Etna. *Geophysical Research Letters*, 25(11), 1979–1982.
- Chaussard, E., Amelung, F., & Aoki, Y. (2013). Characterization of open and closed volcanic systems in Indonesia and Mexico using InSAR time series. *Journal of Geophysical Research*, 118(8), 3957–3969.
- de Zeeuw-van Dalfsen, E., Pedersen, R., Hooper, A., & Sigmundsson, F. (2012). Subsidence of Askja caldera 2000–2009: Modelling of deformation processes at an extensional plate boundary constrained by time series InSAR analysis. *Journal of Volcanology and Geothermal Research*, 213, 72–82.
- Doin, M.-P., Lasserre, C., Peltzer, G., Cavalie, O., & Doubre, C. (2009). Correction of stratified atmospheric delays in SAR interferometry: Validation with global atmospheric models. *Journal of Applied Geophysics*, 69, 35–50.
- Donnelly-Nolan, J. M. (1988). A magmatic model of Medicine Lake volcano, California. *Journal of Volcanology and Geothermal Research*, 93, 4412–4420.
- Donnelly-Nolan, J. M. (2010). Geologic map of Medicine Lake volcano, northern California. U.S. Geological Survey Scientific Investigations Map 2927, scale 1:50,000.
- Donnelly-Nolan, J. M., & Lanphere, M. A. (2005). Argon dating at and near Medicine Lake volcano, California: Results and data. U.S. Geological Survey Open-File Report (2005–1416).
- Donnelly-Nolan, J. M., Champion, D. E., Miller, C. D., Grove, T. L., & Trimble, D. A. (1990). Post-11,000-year volcanism at Medicine Lake Volcano, Cascade Range, Northern California. *Journal of Geophysical Research*, 95(B12), 19693–19704.
- Donnelly-Nolan, J. M., Grove, T. L., Lanphere, M. A., & Champion, D. E. (2008). Eruptive history and tectonic setting of Medicine Lake Volcano, a large rear-arc volcano in the southern Cascades. *Journal of Volcanology and Geothermal Research*, 177, 313–328.
- Dzurisin, D. (2007). *Volcano deformation: Geodetic monitoring techniques*. Chichester, UK: Springer-Praxis.
- Dzurisin, D., Donnelly-Nolan, J. M., Evans, J. R., & Walter, S. R. (1991). Crustal subsidence, seismicity, and structure near Medicine Lake volcano. *California. Journal of Geophysical Research*, 96(B10), 16319–16333.
- Dzurisin, D., Wicks, J. C., & Thatcher, W. (1999). Renewed uplift at the Yellowstone Caldera measured by levelling surveys and satellite radar interferometry. *Bulletin of Volcanology*, 61(6), 349–355.

- Dzurisin, D., Poland, M. P., & Bürgmann, R. (2002). Steady subsidence of Medicine Lake Volcano, Northern California, revealed by repeated levelling surveys. *Journal of Geophysical Research*, 107(B12), 2372.
- Ebmeier, S. K., Biggs, J., Mather, T. A., & Amelung, F. (2013b). On the lack of InSAR observations of magmatic deformation at Central American volcanoes. *Journal of Geophysical Research*, 118(5), 2571–2585.
- Elliott, J. R., Biggs, J., Parsons, P., & Wright, T. J. (2008). InSAR slip rate determination on the Altyn Tagh Fault, northern Tibet, in the presence of topographically correlated atmospheric delays. *Geophysical Research Letters*, 35(12), L12309.
- Evans, J. R., & Zucca, J. J. (1998). Active high-resolution seismic tomography of compressional wave velocity and attenuation structure at Medicine Lake Volcano, Northern California Cascade Range. *Journal of Geophysical Research*, 93(B12), 15016–15036.
- Farr, T. G., & Kobrick, M. (2000). Shuttle radar topography mission produces a wealth of data. *Eos, Transactions American Geophysical Union*, 81(48), 583–585.
- Ferretti, A., Prati, C., & Rocca, F. (2001). Permanent scatterers in SAR interferometry. *IEEE Transactions on Geoscience and Remote Sensing*, 39(1), 8–20.
- Fialko, Y., Khazan, Y., & Simons, M. (2001a). Deformation due to a pressurised horizontal circular crack in an elastic half-space, with applications to volcano geodesy. *Geophysical Journal International*, 146(1), 181–190.
- Finn, C., & Williams, D. L. (1982). Gravity evidence for a shallow intrusion under Medicine Lake Volcano. *California Geology*, 10(10), 503–507.
- Foster, J., Brooks, B., Cherubini, T., Shacat, C., Businger, S., & Werner, C. L. (2006). Mitigating atmospheric noise for InSAR using a high resolution weather model. *Geophysical Research Letters*, 33(16), L16304.
- Fuis, G. S., Zucca, J. J., Mooney, W. D., & Milkereit, B. (1987). A geological interpretation of seismic refraction results in north-eastern California. *Bulletin of the Geological Society of America*, 98(1), 53–65.
- Garthwaite, M. C., Wang, H., & Wright, T. J. (2013). Broadscale interseismic deformation and fault slip rates in the central Tibetan Plateau observed using InSAR. *Journal of Geophysical Research*, 118(9), 5071–5083.
- Goldstein, R., & Werner, C. (1998). Radar interferogram filtering for geophysical applications. *Geophysical Research Letters*, 25(21), 4035–4038.
- Goldstein, R., Zebker, H., & Werner, C. (1988). Satellite radar interferometry: Two dimensional phase unwrapping. *Radio Science*, 23(4), 713–720.
- Gourmelen, N., Amelung, F., & Lanari, R. (2010). Interferometric synthetic aperture radar-GPS integration: Interseismic strain accumulation across the Hunter Mountain fault in the eastern California shear zone. *Journal of Geophysical Research*, 115(B9), B09408.
- Hamling, I. J., Wright, T. J., Calais, E., Lewi, E., & Fukahata, Y. (2014). InSAR observations of post-rifting deformation around the Dabbahu rift segment, Afar. *Ethiopia. Geophysical Journal International*, 197(1), 33–49.
- Hanssen, R. F. (2001). *Radar interferometry: Data interpretation and analysis*. Norwell, MA, US: Kluwer Academic.
- Heiken, G. (1978). Plinian-type eruptions in the Medicine Lake Highland, California, and the nature of the underlying magma. *Journal of Volcanology and Geothermal Research*, 4(3), 375–402.
- Hildreth, W. (2007). Quaternary magmatism in the Cascades - geological perspectives. U.S. Geological Survey Professional Paper (1744).
- Hooper, A., Segall, P., & Zebker, H. (2007). Persistent scatterer interferometric synthetic aperture radar for crustal deformation analysis, with application to Volcán Alcedo. *Galápagos. Journal of Geophysical Research*, 112(B7), B07407.
- Hooper, A., Pedersen, R., & Sigmundsson, F. (2009). *Constraints on magma intrusion at Eyjafjallajökull and Katla volcanoes in Iceland, from time series SAR interferometry. The VOLUME project-volcanoes: understanding subsurface mass movement* (pp. 13–24) Dublin: University College.

- Hooper, A., Zebker, H., Segall, P., & Kampes, B. (2004). A new method for measuring deformation on volcanoes and other natural terrains using InSAR persistent scatterers. *Geophysical Research Letters*, 31(23), 1–5.
- Johanson, I. A., & Bürgmann, R. (2005). Creep and quakes on the northern transition zone of the San Andreas fault from GPS and InSAR data. *Geophysical Research Letters*, 32(14), L14306.
- Jónsson, S., Zebker, H., Segall, P., & Amelung, F. (2002). Fault slip distribution of the 1999 Mw 7.1 Hector Mine, California, earthquake, estimated from satellite radar and GPS measurements. *Bulletin of the Seismological Society of America*, 92(4), 1377–1389.
- Li, Z. W., Ding, X. L., Huang, C., Wadge, G., & Zheng, D. W. (2006b). Modeling of atmospheric effects on InSAR measurements by incorporating terrain elevation information. *Journal of Atmospheric and Solar-Terrestrial Physics*, 68(11), 1189–1194.
- Lohman, R., & Simons, M. (2005). Some thoughts on the use of InSAR data to constrain models of surface deformation: Noise structure and data downsampling. *Geochemistry, Geophysics, Geosystems*, 6(1), Q01007.
- Lowenstern, J. B., Donnelly-Nolan, J., Wooden, J. L., & Charlier, B. L. A. (2003). Volcanism, plutonism and hydrothermal alteration at Medicine Lake volcano, California. *Proceedings, Twenty-Eighth Workshop on Geothermal Reservoir Engineering, Stanford University, Stanford, California* (p. 8).
- Lu, Z., & Dzurisin, D. (2014). *InSAR Imaging of Aleutian Volcanoes: Monitoring a Volcanic Arc from Space*. Chichester, UK: Springer-Praxis.
- Lyons, S., & Sandwell, D. (2003). Fault creep along the southern San Andreas from InSAR, permanent scatterers and stacking. *Journal of Geophysical Research*, 108(B1), 2047–2070.
- Massonnet, D., Feigl, K. L., Vadon, H., & Rossi, M. (1996). Coseismic deformation field of the M = 6.7 Northridge, California earthquake of January 17, 1994 recorded by two radar satellites using interferometry. *Geophysical Research Letters*, 23(9), 969–972.
- Mogi, K. (1958). Relations between eruptions of various volcanoes and the deformations of the ground surfaces around them. *Bulletin of the Earthquake Research Institute of the University of Tokyo*, 36, 99–134.
- Ofeigsson, B. G., Hooper, A., Sigmundsson, F., Sturkell, E., & Grapenthin, R. (2011). Deep magma storage at Hekla volcano, Iceland, revealed by InSAR time series analysis. *Journal of Geophysical Research*, 116(B5), B05401.
- Okada, Y. (1985). Surface deformation due to shear and tensile faults in a half-space. *Bulletin of the Seismological Society of America*, 75(4), 1135–1154.
- Parks, M. M., Biggs, J., Mather, T. A., Pyle, D. M., Amelung, F., Monsalve, M. L., et al. (2011). Co-eruptive subsidence at Galeras identified during an InSAR survey of Colombian volcanoes (2006–2009). *Journal of Volcanology and Geothermal Research*, 202(3), 228–240.
- Pinel, V., Hooper, A., De la Cruz-Reyna, S., Reyes-Davila, G., Doin, M.-P., & Bascou, P. (2011). The challenging retrieval of the displacement field from InSAR data for andesitic stratovolcanoes: Case study of Popocatepetl and Colima Volcano, Mexico. *Journal of Volcanology and Geothermal Research*, 200(1), 49–61.
- Poland, M. P., & Lu, Z. (2008). Radar interferometry observations of surface displacements during pre- and co-eruptive periods at Mount St. Helens, Washington, 1992–2005. *U.S. geological survey professional paper* (Vol. 1750, pp. 361–382).
- Poland, M. P., Bürgmann, R., Dzurisin, D., Lisowski, M., Masterlark, T., Owen, S., et al. (2006). Constraints on the mechanism of long-term, steady subsidence at Medicine Lake volcano, northern California, from GPS, levelling and InSAR. *Journal of Volcanology and Geothermal Research*, 150(1), 55–78.
- Pyle, D. M., Mather, T. A., & Biggs, J. (2013). Remote sensing of volcanoes and volcanic processes: Integrating observation and modelling-introduction. *Geological Society, London, Special Publications*, 380(1), 1–13.
- Riddick, S. N., & Schmidt, D. A. (2011). Time-dependent changes in volcanic inflation rate near three sisters, Oregon, revealed by InSAR. *Geochemistry, Geophysics, Geosystems*, 12(12), Q12005.

- Riddick, S. N., Schmidt, D. A., & Deligne, N. I. (2012). An analysis of terrain properties and the location of surface scatterers from persistent scatterer interferometry. *ISPRS Journal of Photogrammetry and Remote Sensing*, 73, 50–57.
- Ritter, J. R. R., & Evans, J. R. (1997). Deep structure of Medicine Lake volcano. *California Tectonophysics*, 275(1), 221–241.
- Rosen, P., Hensley, S., Peltzer, G., & Simons, M. (2004). Updated repeat orbit interferometry package released. *EOS, Transactions of the AGU*, 85(5), 47.
- Rosen, P. A., Hensley, S., Zebker, H. A., & Webb, F. H. (1996). Surface deformation and coherence measurements of Kilauea Volcano, Hawaii, from SIR-C radar interferometry. *Journal of Geophysical Research*, 101(E10), 23109–23125.
- Rosen, P. A., Hensley, S., Joughin, I. R., Li, F. K., Madsen, S. N., Rodriguez, E., et al. (2000). Synthetic aperture radar interferometry. *Proceedings of the IEEE*, 88(3), 333–382.
- Segall, P. (2010). *Earthquake and volcano deformation*. Princeton, New Jersey, US: Princeton University Press.
- Seymour, M., & Cumming, I. (1994). *Maximum likelihood estimation for SAR interferometry*. Institute of Electrical and Electronics Engineers, Piscataway, NJ (pp. 2272–2275).
- Sparks, R. S. J., Biggs, J., & Neuberg, J. W. (2012). Monitoring volcanoes. *Science*, 335(6074), 1310–1311.
- Turcotte, D. L., & Schubert, G. (1982). *Geodynamics*. Cambridge, UK: Cambridge University Press.
- Wadge, G., Zhu, M., Holley, R. J., James, I. N., Clark, P. A., Wang, C., et al. (2010). Correction of atmospheric delay effects in radar interferometry using a nested mesoscale atmospheric model. *Journal of Applied Geophysics*, 72(2), 141–149.
- Wang, H., & Wright, T. J. (2012). Satellite geodetic imaging reveals internal deformation of western Tibet. *Geophysical Research Letters*, 39(7), L07303.
- Wang, H., Wright, T. J., & Biggs, J. (2009). Interseismic slip rate of the northwestern Xianshuihe fault from InSAR data. *Geophysical Research Letters*, 36(3), L03302.
- Wang, H., Wright, T. J., Yu, Y., Lin, H., Jiang, L., Li, C., et al. (2012). InSAR reveals coastal subsidence in the Pearl River Delta. *China Geophysical Journal International*, 191(3), 1119–1128.
- Wright, T., Lu, Z., Wicks, C. (2004a) Constraining the slip distribution and fault geometry of the Mw 7.9, 3 November 2002, Denali Fault earthquake with interferometric synthetic aperture radar and Global Positioning System Data. *Bulletin of the Seismological Society of America*, 94(6B), S175–S189.
- Wright, T. J., Parsons, B. E., & Lu, Z. (2004b). Toward mapping surface deformation in three dimensions using InSAR. *Geophysical Research Letters*, 31(1), L01607.
- Zebker, H. A., & Villasenor, J. (1992). Decorrelation in interferometric radar echoes. *IEEE Transactions on Geoscience and Remote Sensing*, 30(5), 950–959.
- Zebker, H., Rosen, P., & Goldstein, R. M. (1994). On the derivation of co-seismic displacement fields using differential radar interferometry: The Landers earthquake. *Journal of Geophysical Research*, 99(B10), 19617–19634.
- Zucca, J. J., Fuis, G. S., Milkereit, B., Mooney, W. D., & Catchings, R. D. (1986). Crustal structure of northeastern California. *Journal of Geophysical Research*, 91(B7), 7359–7382.

# Chapter 3

## Systematic Assessment of Atmospheric Uncertainties for InSAR Data at Volcanic Arcs Using Large-Scale Atmospheric Models: Application to the Cascade Volcanoes

**Abstract** Satellite Radar Interferometry (InSAR) is suited to monitoring ground deformation on the scale of volcanic arcs, providing insight into the eruptive cycle over both long and short time periods. However, these measurements are often contaminated with atmospheric artefacts caused by changes in the refractivity of the atmosphere. Here, we test the use of two large-scale atmospheric models, ERA-Interim (ERA-I) and North American Regional Reanalysis (NARR), to correct atmospheric uncertainties in InSAR data from the Cascades Volcanic Arc, United States. At Lassen Volcanic Center, we find that NARR reduces interferogram standard deviation in 79% of cases by an average of 22%. Using NARR, we develop a strategy to produce a priori estimates of atmospheric uncertainties on an arc-wide basis. We show that in the Cascades, the RMS variation in range change is dependent upon volcano topography and increases by 0.7 cm per kilometre of relief. We use this to estimate detection thresholds for long-term monitoring of small magnitude (1 cm/year) deformation signals, and short-term monitoring of ground deformation associated with pre-eruptive unrest. This new approach of assessing atmospheric uncertainties a priori is widely applicable to other volcanic arcs, and provides realistic estimates of atmospheric uncertainties suitable for use in near-real-time analysis of InSAR data during periods of volcanic unrest.

### 3.1 Introduction

In the past two decades, Interferometric Synthetic Aperture Radar (InSAR) has changed the way in which volcanic ground deformation is studied. Unlike ground-based techniques such as leveling or GPS, InSAR uses pairs of satellite radar images to produce 2D maps of ground displacements known as interferograms (for a full description see Massonnet and Feigl 1998; Bürgmann et al. 2000; Simons and Rosen 2007 and Pinel et al. 2014). The spatial extent of these measurements (100s km) enables surveys of ground deformation across whole volcanic arcs (e.g. Pritchard and Simons 2004; Chaussard et al. 2013; Ebmeier et al. 2013a; Lu and Dzurisin 2014), and the synthesis of measurements on a global scale (Fournier et al. 2010; Biggs et al. 2014), rather than geodetic studies of individual edifices. In addition



to being significant from a hazard monitoring perspective, this also allows us to better understand the role of regional tectonics in volcanism (e.g. Biggs et al. 2009; Ebmeier et al. 2013b; Chaussard and Amelung 2014).

The potential for large-scale InSAR studies has increased with the launch of new satellites, e.g. Sentinel-1A (European Space Agency) and ALOS-2 (Japanese Aerospace Exploration Agency), providing imagery for InSAR globally every 12 and 14 days respectively (Hanssen and Rocca 2009; Suzuki et al. 2009). However, despite advances in data acquisition, sources of noise continue to limit InSAR measurements of small magnitude ground deformation. The most significant of these is spatiotemporal variability in atmospheric refractivity between satellite acquisitions, resulting in atmospheric artefacts in interferograms that may mask or lead to false interpretations of ground deformation (e.g. Beauducel et al. 2000; Poland and Lu 2008). Improving the accuracy of satellite-based measurements of volcano deformation is essential for regional and global volcano monitoring strategies, as ground deformation is shown to have strong evidential links to eruption (Biggs et al. 2014). When monitoring volcanic arcs using InSAR, there is therefore a need for a priori estimates of atmospheric uncertainties at a large number of volcanic edifices. Given their spatial coverage, large-scale atmospheric models are well suited to this task, and can be used to estimate detection thresholds on arc-wide scales. In this study we test this approach using two large-scale atmospheric models and InSAR data from the Cascades, which has atmospheric conditions broadly representative of a large number of other volcanic arcs (Foster et al. 2013).

### ***3.1.1 The Cascades Volcanic Arc***

The Cascades Volcanic Arc is located in the western US., spanning over 1000 km through Washington, Oregon and California. The arc consists of a chain of N-S trending stratovolcanoes, lava domes, cinder cones, and shield volcanoes, with 13 principle edifices ranging in elevation between 2400 m (Medicine Lake Volcano, CA) and over 4000 m (Mount Rainier, WA) (Fig. 3.1). Amongst the volcanoes lie numerous population centres, including the cities of Seattle and Portland, and major infrastructure such as Interstate 5. In addition to seismicity, geodetic measurements are an essential component of monitoring the arc (e.g. Ewert et al. 2005), and InSAR data are ideal for cases where access is difficult (e.g. Mount Baker, WA), or where little ground-based equipment is deployed (e.g. Mount Adams, WA). A significant archive of InSAR data exists for the Cascades, including ERS-1/2 and ENVISAT data accessible via the WInSAR consortium, and ALOS data available from the Alaska Satellite Facility. Measurements have been made at Three Sisters, OR (Wicks et al. 2002; Dzurisin et al. 2006, 2009; Riddick and Schmidt 2011), Medicine Lake Volcano, CA (Poland et al. 2006; Parker et al. 2014), and Lassen Volcanic Center, CA (Poland et al. 2004). However, overall, the application of InSAR data in the Cascades has been limited. Whilst this is partly due to poor coherence and a lack of significant deformation, measurements are also limited by extensive atmospheric noise, and

published InSAR studies are of variable success. For example, interferograms from different satellite tracks covering the 2004–2008 eruption of Mount St Helens show conflicting evidence of edifice inflation and deflation (Poland and Lu 2008).

## 3.2 Atmospheric Noise in InSAR Studies at Volcanoes

### 3.2.1 *Causes and Effects*

Atmospheric phase delays can be split into a hydrostatic component, which is a function of pressure, and a “wet” component, dependent upon the water vapour content of the atmosphere (e.g. Hanssen 2001; Bevis et al. 1992). Although the magnitude of the hydrostatic delay is several times larger than that of the wet delay, the atmospheric water vapour content is far more variable between satellite acquisitions and is therefore the dominant source of noise for differential SAR measurements (Zebker et al. 1997). However, it is necessary to account for both wet and hydrostatic components to fully describe atmospheric phase delays in regions of significant topography (e.g. Elliott et al. 2008; Doin et al. 2009; Jolivet et al. 2014). Atmospheric phase delays are commonly a few cm in magnitude (Hanssen 2001), with a 20% change in relative humidity between acquisitions resulting in a 10 cm path delay (Zebker et al. 1997). The deformation signal measured by InSAR can therefore be modified or even reversed by atmospheric noise (e.g. Heleno et al. 2010).

Atmospheric artefacts observed in interferograms are divided into two types: stratified and turbulent (Hanssen 2001). Vertical stratification of the atmosphere results in variable phase delays over low topography (large amounts of atmospheric water vapour) and small magnitude delays over higher topography (small amounts of atmospheric water vapour) (e.g. Ebmeier et al. 2013a). The effects are therefore most prevalent in regions of significant topographic relief including volcanic arcs (e.g. Webley et al. 2004). The resulting artefacts are correlated with elevation and appear as concentric fringes centred on the volcanic edifice as was first observed at Mount Etna, Italy (Massonnet et al. 1995; Delacourt et al. 1998; Beauducel et al. 2000). This is particularly misleading as volcano deformation also typically correlates with topography, and alternating periods of uplift and subsidence interpreted to reflect changes in magma storage have, in some cases, been shown to arise due to topographically correlated atmospheric artefacts. (e.g. Llaima volcano, Chile: Bathke et al. 2011; Remy et al. 2015). Unlike stratification, turbulent mixing of the atmosphere is not directly correlated with topography. Instead, artefacts typically exhibit spatial correlation over length scales of  $\sim 10$  km (e.g. Jónsson et al. 2002; Lohman and Simons 2005), although steep stratovolcanoes are commonly associated with turbulence on 1 km scales (Webley et al. 2004).

Volcanic arcs act as significant topographic barriers and we may therefore expect variations in atmospheric phase delays due to orographic effects (e.g. Wadge et al. 2002; Puysségur et al. 2007; Doin et al. 2009; Wadge et al. 2010). As the prevailing

wind blows air towards the arc it may be forced to rise. As the air cools, clouds and precipitation form on the windward slope, causing lower levels of water vapour and precipitation on the leeward slope (Price et al. 2013). At the Cascades Volcanic Arc, the arc axis is orientated perpendicular to the direction of the prevailing wind and within ~150km of the Pacific ocean (Fig. 3.1). As such, atmospheric conditions are strongly influenced by the interaction between the moist marine boundary, the drier air of the interior, and the complex orography (Foster et al. 2013). The result is a significant contrast between the environment of the windward and leeward sides of the arc. This is observable in maps of precipitation and the Köppen climate classification (Peel et al. 2007), one of the most widely used climate classification systems (Fig. 3.1). West of the Cascades, the climate is marine-dominated, with moderate temperatures and persistent winter precipitation (Mass 2008). To the east, the climate is continental, with hot summers, cold winters, and low levels of precipitation (Price et al. 2013). Contrasts are also apparent between the north and south of the arc, as volcanoes at lower latitudes receive higher levels of solar radiation than those in the north.

### Impact upon Interferogram Coherence

At volcanoes, snow cover and vegetation cause scatterers on the ground to vary rapidly over time, significantly decreasing the coherence of InSAR data (e.g. Lu and

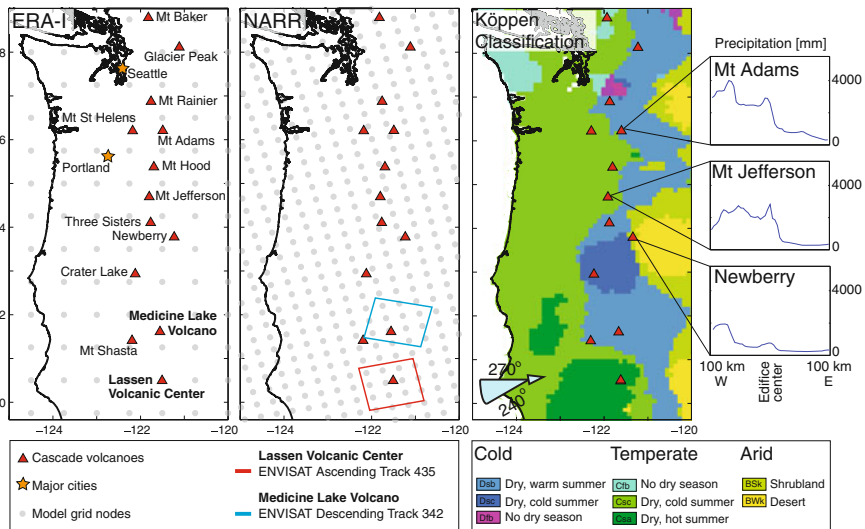


**Fig. 3.1** Map of the western U.S. showing model grid nodes for ERA-I (left) and NARR (centre). Labeled are the Cascade volcanoes, major population centres and tracks of ENVISAT data used in this study. Right Köppen Classification map with different temperature regimes highlighted. See Peel et al. (2007) for a full description of categories. The prevailing wind direction is shown by the blue arrow. Profiles show examples of cross edifice variations in average precipitation between 1981 and 2010 from PRISM Climate Group, Oregon State University, (Daly et al. 1997)

Freymueller 1998; Lu et al. 2002). The extents of both snow and vegetation cover relate to atmospheric conditions. Volcanoes that experience lower temperatures, due to latitude or elevation, will have greater snow cover resulting in poorer coherence. For example in the Cascades, snow cover has inhibited the use of InSAR at Mount Baker, WA, in the north of the arc (Zhong Lu, personal comm.). Volcanoes that are subject to orographic effects will have more vegetation on the windward flanks where precipitation is greater. For example, west to east across the Cascades arc, vegetation changes from dense forests to shrubs and grasses, significantly reducing the coherence on the western flank of Three Sisters, OR (Wicks et al. 2002; Dzurisin et al. 2006, 2009; Riddick and Schmidt 2011; Riddick et al. 2012).

Volcano size also influences atmospheric conditions and the development of vegetation (the Massenerhebung effect), as the larger the mountain “mass”, the greater the heat retention and the slower the rate at which temperature decreases with elevation (e.g. Grubb 1971; Bell 2012). At Three Sisters Volcano, OR, where three peaks join to form a relatively large land mass above 1800 m, alpine vegetation is well developed (Price et al. 2013) and we may therefore expect poor coherence. This contrasts to the less massive Mount Hood, OR, where the timberline is 150–300 m lower, alpine vegetation is considerably more impoverished (Price et al. 2013), and vegetation is therefore likely to have a lesser impact upon coherence. In combination, atmospheric artefacts and incoherence make interferogram phase-unwrapping extremely challenging on the steep slopes of stratovolcanoes (Pinel et al. 2011).

### 3.2.2 *Atmospheric Corrections for Volcano InSAR Studies*

Multiple interferograms can be used to reduce the effects of atmospheric noise and improve the signal-to-noise ratio of InSAR imagery. If the atmospheric component is random in time, stacking  $N$  independent interferograms will reduce the standard deviation of atmospheric errors by a factor of  $\sqrt{N}$  (e.g. Ewardson et al. 2003; Biggs et al. 2007). However, this is less useful for removing stratified delays, which do not vary randomly in space or time (Doin et al. 2009), or in the case of discrete deformation events that may be covered by a single or small number of interferograms. In cases of transient deformation, a time-series approach (e.g. SBAS; Berardino et al. 2002) may be more useful, but there is a risk of aliasing seasonal atmospheric effects into time-series analysis (e.g. Doin et al. 2009). As time-series measurements are made relative to a far field region of the interferogram, local differences in atmospheric delay may also dominate the time-series (Ebmeier et al. 2013a). Beyond simple time-averaging approaches, significant progress has been made towards correcting atmospheric noise in InSAR data, including a number of studies that tackle the problem in volcanic settings. These methods are broadly categorised in two groups: empirical and predictive (e.g. Jolivet et al. 2014).

## Empirical Atmospheric Corrections

The most common empirical approach to correcting atmospheric errors is quantifying the correlation between elevation and delay to identify phase delays due to atmospheric stratification (Delacourt et al. 1998). This is done by plotting the phase of interferogram pixels against elevations from a digital elevation model (e.g. Taylor and Peltzer 2006; Elliott et al. 2008). From this, a correlation coefficient and elevation-delay relationship are calculated. The latter may be approximated as linear (e.g. Wicks et al. 2002; Cavalié et al. 2007), although for steep-sided volcanoes a non-linear model may be more appropriate (e.g. Remy et al. 2003). In the presence of lateral heterogeneities in stratification, for example due to orographic effects, a single empirical relationship may not be applicable across a whole scene (e.g. Puységur et al. 2007; Bekaert et al. 2015). More advanced empirical methods therefore involve prediction of the elevation-delay relationship over different spatial scales using either Gaussian filters of varying width (Lin et al. 2010), or wavelet transforms to identify correlations over varying spatial frequencies (Shirzaei and Bürgmann 2012). However, as volcano deformation typically correlates with edifice topography, empirical corrections are particularly likely to introduce artefacts or remove elements of the deformation signal (Ebmeier et al. 2013a).

## Predictive Atmospheric Corrections

Predictive methods utilise inputs from external sources to estimate atmospheric parameters and produce maps of the expected atmospheric delay. This includes the use of large-scale atmospheric models (e.g. Popocatepetl and Colima Volcano: Pinel et al. 2011), datasets such as GPS (e.g. Mt Etna: Li et al. 2006b), local weather data (e.g. Mt Etna: Delacourt et al. 1998), plus estimates of water vapour from multi-spectral imagery (e.g. Fogo Volcano and Mount Cameroon: Heleno et al. 2010). In addition to large-scale atmospheric models, mesoscale models have also been used in volcanic settings and are often implemented in a nested fashion within the coarser grid of a large-scale model (Foster et al. 2006; Eff-Darwich et al. 2012).

Atmospheric corrections using predictive methods have been of varied success. At Mount Etna, Li et al. (2006b) and Webley et al. (2004) report a  $\sim 30\%$  reduction in interferogram phase standard deviation following corrections using GPS data and forward models of the atmosphere respectively. However predictive methods are not always successful: in their study at Mount St. Helens, Foster et al. (2013) assimilated ground based and remote sensing data with the predictive, mesoscale MM5 atmospheric circulation model, but found this provided no mean benefit for interferogram analysis.

The applicability of predictive methods is dependent upon the availability of external data. Multi-spectral imagery, such as that provided by MERIS and MODIS, relies upon cloud free, day-time conditions, and ground based measurements/GPS are typically sparse, except for intensely monitored volcanoes. Many external datasets also suffer from timing issues, as data are not acquired at the same time as InSAR passes, and atmospheric conditions vary rapidly over timescales of  $< 1$  h (Hanssen 2001). In this respect, atmospheric models are advantageous: large-scale atmospheric models

provide multiple simulations each day (e.g. Pinel et al. 2011), and nested models can be run to any time step (e.g. Foster et al. 2006). However, these results are not necessarily accurate as atmospheric models are notoriously sensitive to initialisation conditions (e.g. Wadge et al. 2002) and the time at which atmospheric phenomena are modelled to have occurred may be offset from the actual time (Zhu et al. 2007). The large grid spacing of regional and global-scale models may also be insufficient to simulate smaller scale atmospheric heterogeneities such as those associated with turbulent mixing (Webley et al. 2004; Jolivet et al. 2014). So far these predictive methods have been applied to individual volcanoes on a case by case basis (see references mentioned throughout this section). This study therefore presents the first application of large-scale atmospheric models to assess atmospheric uncertainties over an entire volcanic arc.

### 3.3 Methods

#### 3.3.1 InSAR

We test the application of large-scale weather models in the Cascades using examples of InSAR data that show artefacts due to both atmospheric stratification and turbulent mixing. By assessing past deformation studies in the Cascades (discussed in Sect. 3.1.1) and processing test scenes for volcanoes throughout the arc, we select two case study volcanoes, Lassen Volcanic Center and Medicine Lake Volcano, which demonstrate atmospheric noise of varying characteristics. We choose these case study volcanoes as they are located in regions with the driest, warmest Köppen classification (Fig. 3.1), and are therefore most likely to have good coherence due to minimal snow cover and vegetation. They also represent two different types of volcano topography as defined by the Smithsonian Global Volcanism Program: Medicine Lake Volcano is classed as a broad shield volcano with summit caldera, whereas Lassen Volcanic Center is a stratovolcano. For each volcano we use a dataset summarised in Table 3.1, with a full list of interferograms supplied in the Appendix (Tables 3.4 and 3.5). Deformation rates at these volcanoes during the observation period have been measured to be  $\sim 1$  cm/year (Dzurisin et al. 2002; Poland et al.

**Table 3.1** InSAR datasets used in this study and shown in Fig. 3.1

Volcano	Satellite	Track	Acquisitions	Interferograms	Dates spanned
Lassen volcanic center	ENVISAT	435 (Ascending)	44	38	May 2004–Aug 2010
Medicine lake volcano	ENVISAT	342 (Descending)	32	54	Nov 2005–Oct 2010

2006). Rather than masking the volcanic edifice (e.g. Doin et al. 2009), we use interferograms with duration  $< 1$  year (maximum deformation signal 1 cm), which allows us to minimise any bias caused by topographically-correlated deformation signals whilst preserving the region of interest in the interferograms.

Interferograms from Lassen Volcanic Center exhibit topographically correlated phase signals and therefore present examples of noise related to atmospheric stratification. The dataset covering this volcano consists of 44 C-band SAR images from ENVISAT ascending track 435 (Fig. 3.1), which are used to produce 38 interferograms spanning May 2004–August 2010. The second dataset, covering Medicine Lake Volcano, has been used in past InSAR studies and contains short wavelength phase heterogeneities that are not correlated with topographic features (Parker et al. 2014). These interferograms present examples of turbulent atmospheric phase delays that are known to be problematic for InSAR studies. The dataset covering Medicine Lake Volcano consists of 32 acquisitions from ENVISAT descending track 342, which are used to produce 54 interferograms spanning November 2005–October 2010.

All interferograms used were produced using the JPL/Caltech ROI\_PAC software (Rosen et al. 2004), and a 90 m SRTM digital elevation model (Farr et al. 2007). Interferograms were filtered using a power spectrum filter (Goldstein and Werner 1998), unwrapped using a branch cut algorithm (Goldstein and Werner 1988), downsampled to a final resolution of  $\sim 500$  m (e.g. Goldstein and Werner 1988; Jónsson et al. 2002), and then converted from phase to millimetre range change with positive displacements corresponding to movement towards the satellite.

### 3.3.2 Atmospheric Models

We use two atmospheric models, ERA-Interim (ERA-I) and the North American Regional Reanalysis (NARR). Both of these atmospheric models are based upon data reanalysis such that past observations of the atmosphere are reassessed using a numerical weather prediction forecast and analysis system (Berrisford et al. 2011). Both ERA-I and NARR are freely available online along with documentation describing the format of the data.

ERA-I is a global atmospheric model from the European Center for Medium-Range Weather Forecasts (ECMWF) (Simmons et al. 2007; Uppala et al. 2008; Dee et al. 2011). The model is produced using a sequential data assimilation scheme, the core component of which is a 4-dimensional variational analysis which advances in 12-hourly analysis cycles. Within each cycle, observations are combined with prior information from a forecast model to estimate the evolving state of the global atmosphere (Dee et al. 2011). The number of observations assimilated each day is of the order of  $10^7$ , with the majority of data originating from satellites. The analyses are then used to initialise a short-range model forecast, which provides the prior state estimates needed for the next analysis cycle (Dee et al. 2011). The outputs of ERA-I used in this study are estimates of temperature, relative humidity, and geopotential

height, defined at 37 pressure levels (1000–1 hPa), and a spatial resolution of  $\sim 75$  km (Fig. 3.1).

NARR is from the National Center for Environmental Prediction/National Center for Atmospheric Research (NCEP/NCAR) and provides coverage for North and Central America (Mesinger et al. 2006). The NARR assimilation system operates over 3 h cycles, with the preceding cycle serving as the first estimate for the next cycle (Rogers et al. 2001). Data sources include rawinsondes, dropsondes, aircraft, satellite and surface based measurements such as observed precipitation (Mesinger et al. 2006). Like ERA-I, NARR defines a set of meteorological parameters, including temperature, geopotential height, and specific humidity, at 29 pressure levels (1000–100 hPa), and a spatial resolution of 32 km (Fig. 3.1).

For both models, pressure levels are more densely spaced at lower elevations (higher pressure) and widely spaced at higher elevations (lower pressure). We select the cycle that is closest to the time of SAR acquisition, which for both models is within 30 min of ENVISAT ascending pass ( $\sim 0600$  UTC) and ENVISAT descending pass ( $\sim 1800$  UTC). To produce maps of atmospheric delay, we convert relative and specific humidities to partial pressure of water vapour, and geopotential to altitude. We then interpolate the atmospheric parameters onto altitude profiles at each model node using a spline interpolation (Jolivet et al. 2011; Walters et al. 2013; Jolivet et al. 2014). The formulation of Baby et al. (1988) is then used to calculate the zenith total delay, which can be converted to the slant total delay (STD) that is sampled by the radar wave:

$$STD = \frac{10^6}{\cos(\theta)} \left[ \frac{k_1 R_d}{g_0} P(z_0) + \int_{z_0}^{z_{ref}} \left( k'_2 \frac{P_w}{T} Z_w^{-1} + k_3 \frac{P_w}{T^2} Z_w^{-1} \right) dz \right] \quad (3.1)$$

where  $\theta$  is the incidence angle of the satellite at each pixel (Doin et al. 2009). The first term relates to the hydrostatic delay and is calculated using the specific gas constant for dry air ( $R_d$ ), gravitational acceleration at ground level ( $g_0$ ) and pressure ( $P$ ) at the elevation of ground level ( $z_0$ ). The second term is integrated between ground level ( $z_0$ ) and a reference height ( $z_{ref}$ ) of 15 km. This term relates to the wet delay and is calculated using the partial pressure of water vapour ( $P_w$ ), absolute temperature ( $T$ ) and the inverse compressibility factor for wet air ( $Z_w^{-1}$ ). We assume  $Z_w^{-1} = 1$  i.e. negate compressibility (e.g. Baby et al. 1988; Doin et al. 2009). The remaining parameters  $k_1$ ,  $k'_2$  and  $k_3$  are atmospheric refractivity constants from Smith and Weintraub (1953). The resulting vertical profiles of STD are horizontally interpolated to the resolution of a digital elevation model (90 m SRTM: Farr et al. 2007) using a bilinear interpolation. For each pixel the correct altitude is selected to produce a 2D map of atmospheric delay measured in millimetres, hereby referred to as an atmospheric phase screen (APS).

In this study we take the simplest and most easily transferable approach and estimate all components of the atmospheric phase screen using atmospheric reanalysis data only. These are the only datasets to provide all of the required fields (temperature, pressure, specific humidity) in a physically consistent way. Other archived



data such as MERIS and MODIS also provide global measurements of atmospheric water vapour, albeit only in cloud free, day time conditions, and therefore need to be combined in a self-consistent manner with measurements of pressure and temperature from other sources to calculate STD using Eq. 3.1 (Pinel et al. 2011; Walters et al. 2013). In response to increases in the use of large-scale atmospheric models to correct InSAR data, systematic global validations between the wet delay retrieved from ERA-I and MERIS are being undertaken (Walters et al. 2015). These results will aid in estimating the uncertainties on the wet delay calculated using ERA-I, and will therefore help to identify regions where it may be beneficial to use data from other sources.

### 3.4 Case Study Volcanoes

In this section, we evaluate the use of ERA-I and NARR for correcting atmospheric errors in interferograms. First we compare the performance of ERA-I and NARR using the InSAR dataset covering Lassen Volcanic Center. To correct each interferogram, we produce a differential APS for the interferometric pair using the method in Sect. 3.3.2 and then subtract this from the interferogram (Fig. 3.2a). Long wavelength orbital errors are accounted for by solving for linear ramps either before correction for the uncorrected interferograms, or after correction for the corrected interferogram (Biggs et al. 2007; Gourmelen et al. 2010). We compute the reduction in interferogram standard deviation after removal of each APS to determine which model is most applicable in this setting (e.g. Li et al. 2006b; Jolivet et al. 2014).

We use the chosen model, and interferograms from Lassen Volcanic Center and Medicine Lake Volcano, to assess how the effect of the model prediction relates to different types of atmospheric artefacts (stratified or turbulent) after Jolivet et al. (2014). To systematically differentiate between the two types of noise, we plot the pixel delay of each uncorrected interferogram against corresponding elevations from a digital elevation model and calculate the correlation coefficient,  $r^2$  (Sect. 3.2.2). Large  $r^2$  values indicate that interferograms are dominated by topographically-correlated atmospheric artefacts, and therefore low levels of atmospheric turbulence. We then compare the  $r^2$  values to the reduction in standard deviation (Jolivet et al. 2014), and describe any artefacts in the interferograms that are not corrected by atmospheric models.

#### 3.4.1 Comparison Between ERA-I and NARR

Using the dataset covering Lassen Volcanic Center, we compare interferogram standard deviation ( $\sigma$ ) prior to and post correction with NARR and ERA-I and identify cases where: (a)  $\sigma$  is reduced by both models; (b)  $\sigma$  is increased by both models; and (c) where  $\sigma$  is reduced by one model and increased by the other (Fig. 3.2a).

We find that  $\sigma$  is reduced in 79 % of interferograms corrected by NARR compared to 58 % of interferograms corrected using ERA-I (Fig. 3.2b). The mean  $\sigma$  reduction for NARR is 22 % and for ERA-I is 18 %. For cases where  $\sigma$  has been increased (21 % of interferograms for NARR and 32 % for ERA-I), the increase in  $\sigma$  is 8 % for NARR compared to 14 % for ERA-I. Overall we therefore find that NARR reduces interferogram  $\sigma$  more than ERA-I in this setting (Fig. 3.2b), most likely due to the higher temporal resolution of data assimilations (3 h compared to 12 h for ERA-I) and higher spatial resolution of model grid nodes (Fig. 3.1). We therefore select NARR to use for further analysis. These findings are comparable to those of Jolivet et al. (2014) who, using an interferogram at Kilauea volcano, found NARR reduced the standard deviation by 83 % compared to 27 % for ERA-I.

### 3.4.2 *Correcting Stratified and Turbulent Atmospheric Delays Using NARR*

At Lassen Volcanic Center, we find a correlation between atmospheric stratification and the reduction in  $\sigma$  (Fig. 3.3a). This agrees with our observation that stratified atmospheric artefacts dominate interferograms at this volcano. These atmospheric conditions are well replicated by the model (see example in Fig. 3.3b), as they are stable over wavelengths comparable to the model node spacing (32 km), and the resulting artefacts closely resemble the topography from the digital elevation model. When we observe an increase in  $\sigma$ , this may be due to NARR mismodelling atmospheric processes, particularly the distribution of atmospheric water vapour (Doin et al. 2009).

At Medicine Lake Volcano we find that, although there is an overall reduction in  $\sigma$  for 60 % of interferograms, NARR has a relatively minimal effect upon the data, reducing  $\sigma$  by 8 % on average and by a maximum of 22 % (Fig. 3.3a). We do not observe a correlation between the extent of atmospheric stratification and  $\sigma$  reduction. The topography of Medicine Lake Volcano is less significant than that of Lassen Volcanic Center, and therefore the extent of topographically-correlated atmospheric artefacts is limited. This agrees with visual inspection of interferograms, and past InSAR studies, that suggest turbulent atmospheric artefacts dominate in this dataset (Parker et al. 2014). Turbulence in the lower troposphere is not predicted by NARR using Eq. 3.1 (Doin et al. 2009; Jolivet et al. 2011, 2014) and we therefore do not expect atmospheric artefacts in data from Medicine Lake Volcano to be removed using this method.

The atmospheric artefacts in interferograms from Medicine Lake Volcano have quasi-systematic characteristics (Fig. 3.3b), which have been referred to as ripples (Li et al. 2006a) or atmospheric rolls (Parker et al. 2014) and have a typical wavelength of 4–12 km. Similar features in interferograms across the Los Angeles basin are attributed to gravity waves (Li et al. 2006a). Medicine Lake Volcano is located east of the main Cascades axis, and Mount Shasta (elevation  $\sim$ 3.5 km), lies between

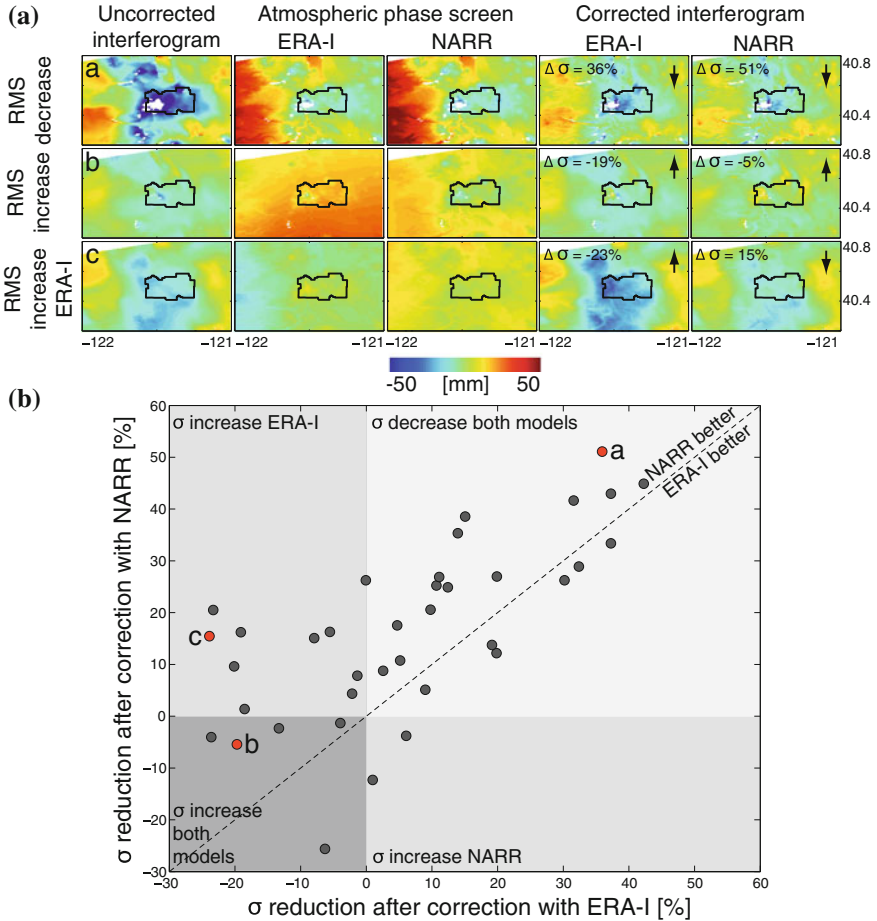


**Fig. 3.2** **a** Examples of APS corrections from ERA-I and NARR using data from Lassen Volcanic Center. Interferograms used are: *a* 050707-060622, *b* 071129-080417, *c* 080626-080731, where dates are in yymmdd-yymmdd format. Corrected interferograms are labelled with the standard deviation ( $\sigma$ ) reduction and an arrow indicating a decrease or increase. Example (a) Interferogram  $\sigma$  is reduced by both models. Example (b) Interferogram  $\sigma$  is increased by both models. Example (c) Interferogram  $\sigma$  is decreased by NARR only. Black lines show the outline of Lassen Volcanic National Park. **b** Comparison between  $\sigma$  reduction for the full set of interferograms that have been corrected using ERA-I and NARR. Dashed line is a 1:1 line - above the line NARR correction is better, below the line ERA-I correction is better. Circles represent interferograms, with red circles indicating the examples used in A. Shaded regions are labelled to highlight that more interferograms have a  $\sigma$  increase after correction with ERA-I than NARR

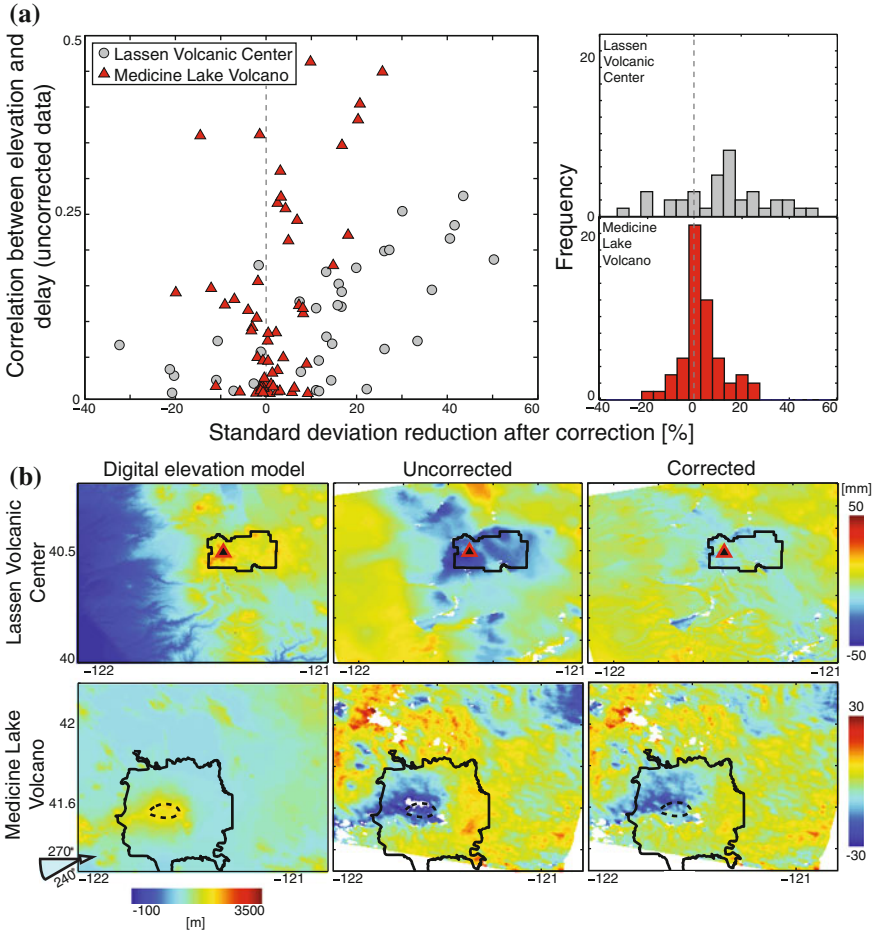


**Fig. 3.3** **a** Assessment of the correlation between topographically-correlated atmosphere errors in uncorrected interferograms and reduction in interferogram standard deviation ( $\sigma$ ) after correction. NARR significantly improves  $\sigma$  for Lassen Volcanic Center but has little impact upon data from Medicine Lake Volcano where atmospheric turbulence dominates. **b** Digital elevation models and example interferograms for each volcano. Example for Lassen Volcanic Center (070712-071025) demonstrates topographically-correlated delays, with Lassen Volcanic National Park shown by the *black line* and Lassen Peak marked by a *triangle*. Example for Medicine Lake Volcano (080515-080619) demonstrates both topographically-correlated and turbulent delays, with the extent of lava flows and caldera shown by *solid* and *dashed black lines* respectively. The direction of the prevailing wind is shown by the *blue arrow* as in Fig. 3.1

Medicine Lake Volcano and the Pacific Ocean in the path of the prevailing wind (Fig. 3.1). When wind passes such a topographic obstacle, a train of downwind lee-waves may be created with an average wavelength of 2–40 km (Price et al. 2013). This phenomenon is not predicted at the resolution of NARR (~32 km), but by incorporating other parameters such as wind speed, there may be scope to systematically identify conditions that would introduce such atmospheric artefacts.

These results suggest that uniformly correcting all interferograms using NARR may result in spurious results at some volcanoes, and that the effects will depend upon the prevailing atmospheric conditions. For volcanoes where topographically-correlated atmospheric artefacts dominate (e.g. Lassen Volcanic Center), correcting all interferograms may reduce the period of time required to measure deformation at a given rate, whereas if turbulent atmospheric conditions prevail, (e.g. Medicine Lake Volcano) this would not necessarily be the case.

### 3.5 Arc-Wide Assessment of Atmospheric Uncertainties

InSAR studies commonly investigate uncertainties due to atmospheric stratification using the gradient between the elevation and delay of interferogram pixels (e.g. Delacourt et al. 1998; Taylor and Peltzer 2006), and estimate temporal variations in atmospheric delays using time-series methods (e.g. Ebmeier et al. 2013a). By using APS data rather than interferograms, we show how these approaches can be used a priori to independently estimate the magnitude of atmospheric uncertainties on an arc-wide scale. Implementing this for all volcanoes in the Cascades, we assess the influence of topographic and geographic variables upon atmospheric uncertainties by comparing these values to the elevation of each edifice, elevation of surrounding region, relief of each edifice, surface area of each edifice above a threshold elevation, and latitude.

#### 3.5.1 Method

Elevation-delay gradients and time-series of atmospheric delay are calculated by using NARR to produce 100 km x 100 km APSs centered on each edifice, simulating atmospheric conditions for an ascending SAR acquisition on the first day of each month throughout 2009 and 2010 (Sect. 3.3.2).

Elevation-delay gradients are calculated by plotting the simulated atmospheric delay from the APS against elevation from corresponding pixels of a digital elevation model (Sect. 3.2.2), and using linear regression to solve for the best-fitting straight line. Although the relationship between altitude and atmospheric water vapour is approximately exponential (Foster and Bevis 2003), linear fits have been shown to provide a good approximation over small scales (e.g. Wicks et al. 2002; Cavalié et al.

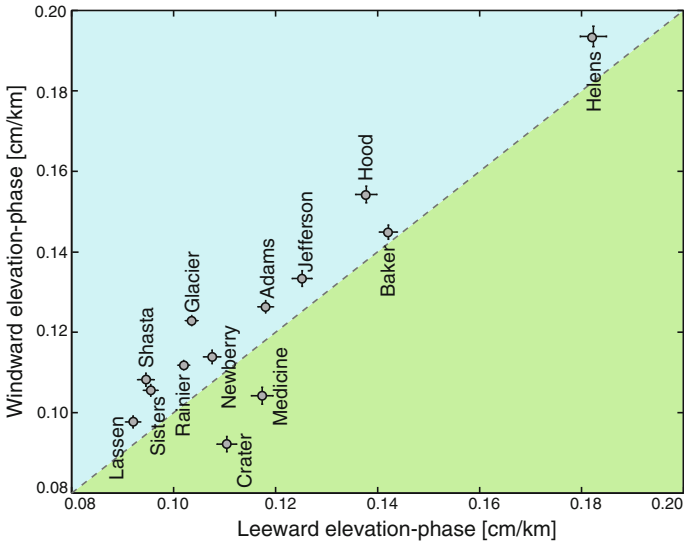


**Fig. 3.4** Comparison between elevation-delay gradients calculated for the windward and leeward flank of the APSs at each volcano. *Dashed* is a 1:1 line. In all cases elevation-delay gradients are the mean values calculated for the 2009 and 2010 test period and *error bars* are  $1\sigma$  of these values

2007; Elliott et al. 2008). The elevation-delay gradient at each volcano is the mean gradient calculated over the two year test period (Fig. 3.4).

The temporal variability of atmospheric delay at each volcano is calculated using time-series of the delay within 3 km of the volcano summit relative to a reference annulus at 15–20 km distance (Fig. 3.5a). The RMS of the time-series is used as a measure of the temporal variability of atmospheric delays, and we compare the values from the Cascades to those of Ebmeier et al. (2013a), who applied a similar method to interferograms from the Central American Volcanic Arc (Fig. 3.5b).

Finally, we use the elevation-phase gradients and time-series RMS to investigate the influence of geographic and topographic variables on atmospheric uncertainties. Topographic variables are calculated using a digital elevation model: the absolute elevation of the edifice is found by averaging the elevation of pixels within 3 km of the volcano summit; the elevation of the surrounding region is calculated by averaging the elevation of pixels within an annulus 15–20 km from the summit; the relief of the volcano is calculated by differencing the summit and reference elevations; and the volcano “mass” (surface area of the edifice above a threshold elevation) is found using the percentage of pixels located within 15 Km of the volcano that have an elevation  $>80\%$  of the summit elevation (Fig. 3.6). This threshold elevation is selected to ensure no pixels are within the reference annulus at 15–20 km distance. We also test the use of different radii to calculate the absolute and reference elevations to ensure that the values chosen do not significantly affect the analysis. (Note that there is a degree of correlation between the topographic parameters as shown in Fig. 3.7 in the

Appendix.) We plot each topographic and geographic factor against the elevation-delay gradients and temporal variabilities calculated for each Cascade volcano and calculate the correlation coefficient,  $R^2$ , from a linear regression (Fig. 3.6). A large  $R^2$  value indicates that the variable has a significant influence on atmospheric uncertainties, whereas a small  $R^2$  value indicates that the variable has minimal influence. We discuss any correlations observed, identifying which characteristics are associated with large atmospheric artefacts in the Cascades.

### 3.5.2 Elevation-Delay Gradients

The majority of atmospheric water vapour lies below elevations of 2 km (Price et al. 2013), and we observe a significant correlation ( $R^2 = 0.78$ ) between the elevation-delay gradient and the elevation of the reference annuli (Fig. 3.6). The correlation with the absolute and relative summit elevations is weaker ( $R^2 = 0.12$  and  $0.03$  respectively), suggesting that the gradient of atmospheric stratification is greater at volcanoes at lower elevations, with little dependence upon the absolute height of the edifice. The correlation between volcano mass and elevation-delay gradient ( $R^2 = 0.24$ ) suggests that more massive volcanoes may have smaller gradients of atmospheric stratification, although a larger sample size is required to thoroughly investigate the significance of this correlation. This agrees with the observation that volcanoes with greater landmass at a given elevation will elevate the average temperature (Price et al. 2013), reducing the difference between atmospheric conditions at the base and summit of the edifice.

Elevation-delay gradients vary significantly between the windward and leeward sides of each edifice. At 85 % of volcanoes we observe elevation-delay gradients that are up to 15 % larger in the windward half of the APSs, where levels of water vapour and precipitation are greater (Fig. 3.4). The correlation between the elevation-delay gradient and latitude ( $R^2 = 0.27$ ) shows that volcanoes at higher latitudes (lower temperatures) tend to exhibit steeper gradients of atmospheric stratification (Fig. 3.6). Thus the effects discussed in Sect. 3.2.1 not only affect the coherence of interferograms but also the magnitude of the atmospheric artefacts.

### 3.5.3 Temporal Atmospheric Variability

Temporal atmospheric variability is most significantly correlated with the relative elevation (relief) of each edifice ( $R^2 = 0.71$ ), with weaker correlations for the absolute elevation of the summit ( $R^2 = 0.64$ ), elevation of the reference annulus ( $R^2 = 0.10$ ), and volcano mass ( $R^2 = 0.35$ ) (Figs. 3.5 and 3.6). Linear regression shows that the gradient of temporal atmospheric variability and volcano relief is 0.7 cm/km. This is lower than a gradient of 1.86 cm/km obtained for volcanoes in Central America

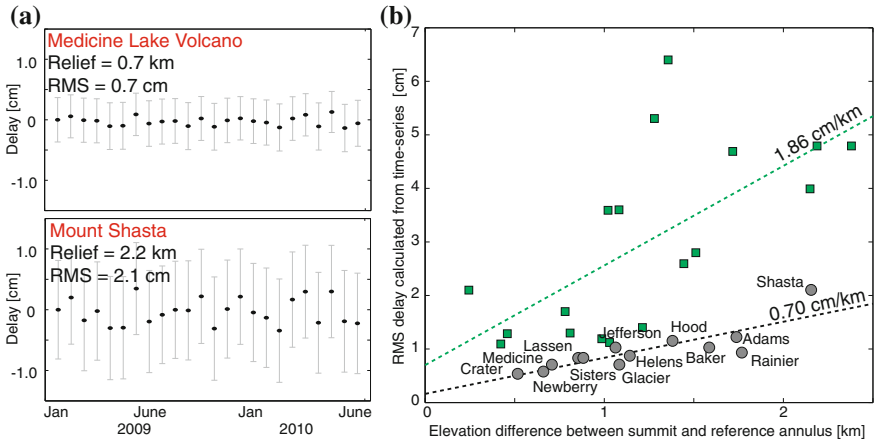


**Fig. 3.5** **a** Time-series of atmospheric delay at Medicine Lake Volcano and Mount Shasta calculated using NARR. *Error bars* are  $1\sigma$  of the values within 3 km of the volcano summit. *Mount Shasta* shows more variability due to greater topographic relief. **b** The relationship between volcano relief and RMS delay calculated using the RMS of the time-series in part **a**. Cascade volcanoes are shown by *circles*. *Green squares* represent Central American volcanoes and are from Ebmeier et al. (2013a). *Dashed lines* are best fit lines labelled with the best-fitting gradient

(Fig. 3.5), as equatorial, tropical regions have higher and more variable amounts of atmospheric water vapour (Ebmeier et al. 2013a).

We find that the average temporal variability of atmospheric delays is not linearly related to volcano latitude, which suggests that, whilst volcanoes in the northern Cascades may have larger gradients of stratification, the temporal variability of temperature and water vapour is not dependent upon latitude.

### 3.6 Discussion

Large-scale atmospheric models provide estimates of stratified atmospheric delays in the Cascades, which can be used to reduce topographically-correlated atmospheric artefacts in InSAR data. This is in agreement with studies at the Kunlun Fault, Tibet (Jolivet et al. 2011), Makran, Pakistan and Parkfield, California (Jolivet et al. 2014). Using APS data for the whole Cascades Volcanic Arc, we have demonstrated that large-scale atmospheric models can also be used to investigate atmospheric uncertainties on regional scales, and we estimate that the magnitude of atmospheric uncertainties in the Cascades ranges between 2.1 cm at Mount Shasta, and 0.16 cm at Crater Lake (Fig. 3.5, Table 3.2). Here we show how these independent, a priori estimates of atmospheric uncertainties can be used to define detection thresholds and errors for long- and short-term monitoring strategies on an arc-wide basis.



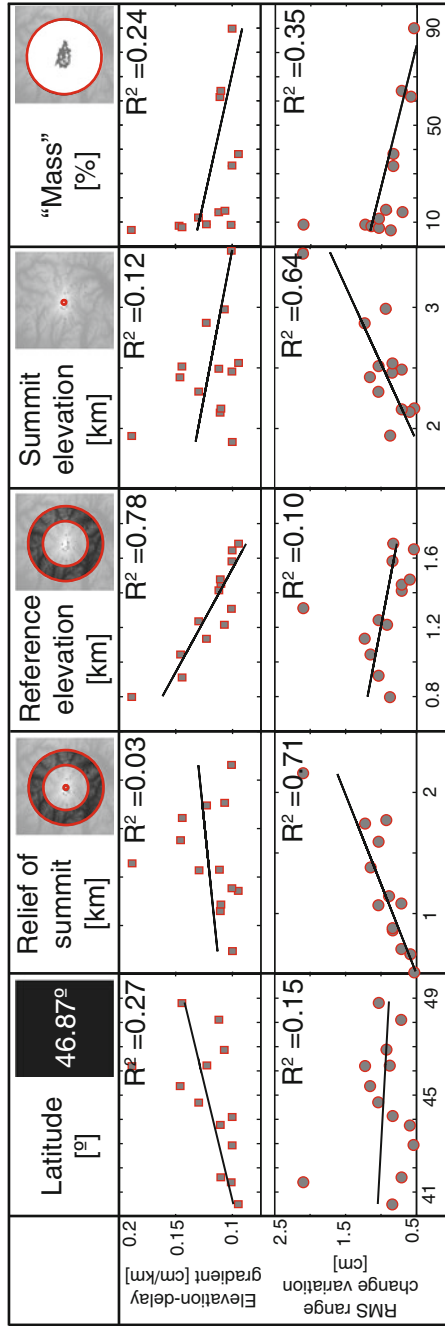


**Fig. 3.6** Summary of the correlation between topographic and geographic variables and average delays due to atmospheric stratification (given by elevation-delay gradients) and temporal atmospheric variability (given by RMS variations in delay over time) calculated in Sect. 3.5.1. Variables are illustrated with examples from Mount Rainier. Best fitting *straight lines* found by linear regression are shown in *black* with  $R^2$  values from the text

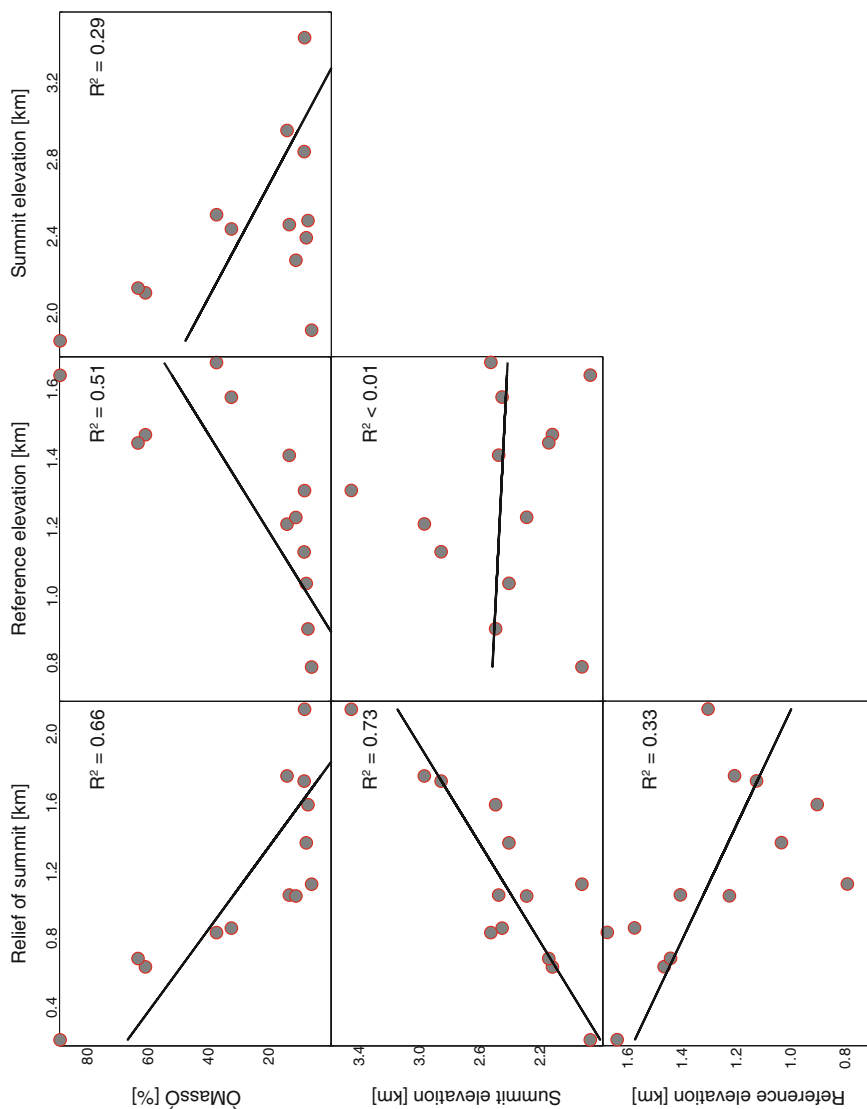


**Fig. 3.7** Plots showing the correlation between topographic parameters used to investigate stratified atmospheric artefacts. The relief of the volcano summit is most correlated with the absolute summit elevation

### 3.6.1 Detection Thresholds for InSAR Studies at the Cascade Volcanoes

InSAR studies commonly use techniques that combine information from many interferograms to reduce atmospheric noise and identify small magnitude deformation signals (see references in Sect. 3.2.2). Using the magnitude of atmospheric uncertainties predicted using NARR, we estimate the number of interferograms required to detect long-term, small magnitude deformation signals, or the minimum magnitude of deformation detectable during periods of volcanic unrest. Long-term deformation, such as subsidence at Medicine Lake Volcano (Poland et al. 2006), may be linear with time, but inter-eruptive and pre-eruptive displacements are often non-linear (e.g. Three Sisters: Dzurisin et al. 2009) and may be aliased between SAR acquisitions. However, for simplicity here we assume linear rates of deformation.

Past studies in the Cascades found that poor coherence due to temporal decorrelation limited the use of InSAR (Wicks et al. 2002; Poland et al. 2004, 2006; Poland and Lu 2008; Parker et al. 2014). We therefore focus on multi temporal methods that use the shortest duration interferograms to minimise the loss of coherence over time. For acquisitions at epochs 1 to  $N$ , we would expect to produce  $N - 1$  short duration interferograms, where the temporal separation between each epoch (and timespan of each interferogram) is equal to the repeat time of the satellite,  $t_r$ . Past satellites had repeat intervals of 35–46 days e.g. ERS-1/2, ENVISAT and ALOS, but here we look forward to Sentinel 1A, which will have a repeat interval of 12 days for each satellite, therefore reducing temporal decorrelation (Chap. 1). The resulting interferograms may be chain-stacked such that the slave image of the first interferogram is the master of the second (Biggs et al. 2007; Walters et al. 2013). Assuming that the deformation measurements are linearly proportional to the time span of the interferogram, we can then use a weighted least squares problem to solve for a linear deformation rate,  $\frac{d\phi}{dt}$ :

$$\mathbf{T} \frac{d\phi}{dt} = \mathbf{P}, \quad (3.2)$$

where  $\mathbf{T} = [t_r, 2t_r, \dots, Nt_r]^T$  are the total duration of the observations between epochs 1 to  $N$ , and  $\mathbf{P} = [d_{1,2}, d_{1,3}, \dots, d_{1,N}]^T$  are the InSAR measurements of cumulative displacement acquired over these times, with the subscripts indicating the epochs. The inversion is weighted by  $\Sigma_p$ , the variance covariance matrix for the InSAR displacement observations  $\mathbf{P}$ . The variance of each interferogram,  $\sigma_i^2$ , appears on the diagonal of  $\Sigma_p$ . Rather than calculating  $\sigma_i^2$  from a set of interferograms (e.g. Hanssen 2001), we use the a priori estimates of atmospheric uncertainties calculated using the RMS of the time-series of atmospheric delay described in Sect. 3.5.3. We assume that each epoch can be treated independently therefore the variance on each interferogram,  $\sigma_i^2$ , is the sum of the variances on each epoch,  $\sigma_e^2$ , such that  $\sigma_i^2 = 2\sigma_e^2$ . As all interferograms share a common master image (the first epoch), every observation in  $\mathbf{P}$  has a covariance of  $\sigma_e^2$  with every other observation, and so

**Table 3.2** Operational outputs of APS analysis for deformation studies in the Cascades: long-term monitoring of volcano deformation using Sentinel 1A

RMS atmospheric variability (cm)	Examples <sup>a</sup>	Data to measure signal of 1 cm/year	
		Days <sup>b</sup>	Interferograms
0.1–0.5	Crater	48–84	3–6
0.6–1.0	Newberry, St Helens, Rainier, Medicine, Sisters, Lassen, Glacier	84–108	6–8
1.1–1.5	Baker, Adams, Hood, Jefferson	108–120	8–9
1.6–2.0	–	120–132	9–10
2.1–2.5	Shasta	132–144	10–11

<sup>a</sup>Categorised based upon estimates of temporal atmospheric variability from Sect. 3.5.3

<sup>b</sup>Assuming a period of 12 days before the first satellite pass

the off-diagonal terms of  $\Sigma_p$  are equal to  $\sigma_e^2$ . The standard error associated with the linear deformation rate is then,

$$\sigma_r = \sqrt{(\mathbf{T}^T \Sigma_p^{-1} \mathbf{T})^{-1}}, \tag{3.3}$$

which we can use to estimate operational parameters for long- and short-term volcano monitoring.

**Long-Term Volcano Deformation**

Long-term, linear deformation rates in the Cascades are measured to be  $\sim 1$  cm/year at Medicine Lake Volcano (Dzurisin et al. 2002) and Lassen Volcanic Center (Poland et al. 2004). Using Eq. 3.3, we estimate how many consecutive interferograms would be required to measure deformation at this rate at each Cascade volcano such that  $\sigma_r <$  deformation rate. At the repeat interval of Sentinel 1A, between 4 and 11 interferograms are required to measure this small magnitude signal in the Cascades (Table 3.2) equating to monitoring periods of between 60 (Crater Lake) and >130 days (Mount Shasta). This is the minimum period of monitoring required to measure such deformation, and a longer observation period would be necessary if interferograms in the chain were not useable due to incoherence. Past studies in the Cascades have found that in some cases only interferograms formed during summer months (July–October) are coherent (e.g. Three Sisters: Dzurisin et al. 2009, which would increase the required monitoring period by up to 1 year (Mount Shasta). The extent to which incoherence compromises estimates of minimum monitoring periods will vary between geographical regions.

**Short-Term Pre-eruptive Unrest**

Using InSAR to monitor ground deformation during periods of volcanic unrest avoids exposure of ground-based personnel to the dangers posed by an active volcano (e.g.

**Table 3.3** Operational outputs of APS analysis for deformation studies in the Cascades: short-term monitoring of pre-eruptive volcanic unrest using Sentinel 1A

Volcano type	Examples <sup>a</sup>	Duration of unrest <sup>b</sup> (days)	Number of consecutive sentinel interferograms	Detection threshold <sup>c</sup> (cm)
Complex volcano	Sisters	<1 week	0	–
Stratovolcano	Baker, Glacier, Rainier, St Helens, Adams, Hood, Jefferson, Shasta, Lassen	1 month	<5	5–10
Caldera	Crater	2 months	5	1–2
Shield volcano	Newberry, Medicine	4 months	10	<1

<sup>a</sup>As defined in the Smithsonian database of Holocene volcanoes

<sup>b</sup>Median values from Phillipson et al. (2013)

<sup>c</sup>Calculated using Eq. 3.3 and temporal atmospheric variability from Sect. 3.5.3

Dzurisin 2007). As such, satellite measurements have been used to monitor pre-eruptive behaviour (e.g. Piton de la Fournaise: Peltier et al. 2010) and make decisions during periods of unrest (e.g. Merapi: Pallister et al. 2013).

Time-scales of unrest preceding volcanic eruptions span several orders of magnitude (Passarelli and Brodsky 2012), and estimating the duration of pre-eruptive unrest at volcanoes requires numerous judgements and assumptions about what characterises unrest. However, studies have identified statistical links between run-up time and composition (Passarelli and Brodsky 2012) or volcano type (Phillipson et al. 2013). To define a duration of pre-eruptive unrest for each Cascade volcano, we use the volcano type as defined by the Smithsonian Global Volcanism Program, and a global synthesis of volcanic activity, which shows that unrest preceding eruptions spans a median average of 2 days for complex volcanoes, 1 month for stratovolcanoes, 2 months for calderas and 4 months for shield volcanoes (Phillipson et al. 2013). We compare these values to the repeat time of Sentinel 1A (12 days) to calculate the minimum number of interferograms spanning typical pre-eruptive unrest periods at each volcano type. Using Eq. 3.3, we then estimate the standard error for chain stacks of these InSAR measurements, and therefore the minimum observable deformation preceding eruption (Table 3.3). (Note that the unrest periods from Phillipson et al. (2013) are associated with large uncertainties and we include a table in the Appendix (Table 3.6) that reflects the full range of durations.)

At stratovolcanoes (which includes 9 of the 13 Cascade volcanoes) we expect pre-eruptive unrest to last on the order of 1 month, which would be covered by up to 5 interferograms. Of the Cascade stratovolcanoes, the lowest detection threshold is at Lassen Volcanic Center (<4 cm) and the highest is at Mount Shasta (~7 cm). For calderas, the expected period of unrest is on the order of 2 months, equivalent to ~5 consecutive interferograms, and equating to a detection threshold of 1–2 cm for

calderas in the Cascades. The longest pre-eruptive unrest periods are associated with shield volcanoes ( $\sim 4$  months), which we expect to be covered by  $\sim 10$  Sentinel 1A interferograms. Shield volcanoes therefore yield the smallest detection thresholds of  $< 1$  cm. Our analysis suggests that no pre-eruptive unrest would be detectable at complex volcanoes such as Three Sisters Volcano, where unrest periods are on the order of days and therefore less than the repeat interval of Sentinel 1A (Phillipson et al. 2013).

The only Cascade volcano to have undergone unrest and eruption in the last century is Mount St Helens. In the 3–4 weeks prior to the catastrophic May 18th 1980 eruption, ground-based measurements revealed that the “bulge” forming on the northern flank of the volcano deformed at up to 2.5 m/day (Lipman and Mullineaux 1981). Deformation of this magnitude would result in incoherence, but signal on the periphery of the bulge would likely be measurable above atmospheric noise in a single interferogram. However, when Mount St Helens reawakened in 2004, deformation rates equated to  $< 1$  cm of ground deformation measurable in a single interferogram, and hence InSAR measurements were dominated by atmospheric artefacts (Poland and Lu 2008).

### 3.6.2 *Applicability to Regional Volcano InSAR Studies*

As the temporal coverage of global SAR data increases, large-scale atmospheric models are an accessible method of quantifying and correcting atmospheric errors in InSAR datasets. Almost all global regions are covered by models such as ERA-I, and in many regions higher resolution models (e.g. NARR) are also available. Not only are these model datasets available online, but documented open source software such as PyAPS (Python-based Atmospheric Phase Screen) implements the methods used in this study to calculate APSs (Agram et al. 2013).

Unsurprisingly, our tests with data from the Cascade volcanoes show that local, turbulent atmospheric artefacts are not well replicated by atmospheric models as localised, km-scale features such as leewaves are not reproduced by the coarse model-node spacing. Instead, turbulent phenomena may be simulated using non-hydrostatic models such as NH3D (Miranda and James 1992), which has been used to compute the forcing of air over and around the orography of Mount Etna (Wadge et al. 2002; Webley et al. 2004). However, this approach not been widely used to correct InSAR data and is best suited to specific targets where atmospheric conditions are well constrained (Wadge et al. 2010) rather than large-scale surveys. Although there remains a need for widely applicable methods of modelling atmospheric turbulence, spatial and temporal averaging utilised by multi temporal analysis goes some way towards mitigating these phase delays (e.g. Zebker et al. 1997; Ferretti et al. 2001; Cavalié et al. 2007; Doin et al. 2009), and it is possible to identify and avoid acquisitions associated with tropospheric turbulence using pair-wise logic (e.g. Massonnet and Feigl 1995). We suggest that there is also scope to use parameters from large-scale atmospheric

models, or elevation-delay correlations as in Sect. 3.4.2, to systematically identify cases where turbulent conditions dominate and therefore the corrections used in this study may not be effective. Identifying data in this way would be advantageous as focus shifts towards rapid automated processing and correction of interferograms.

At volcanoes across the globe, whether covered by many or few SAR acquisitions, steep topography, extensive vegetation, snow cover, unstable deposits, and the surrounding ocean all contribute to incoherence (e.g. Rosen et al. 1996; Massonnet et al. 1996; Lu and Freymueller 1998). Where InSAR data are coherent, coverage is often restricted to near field deposits, which may be undergoing deformation associated with deposition (Ebmeier et al. 2014). Poor coherence inhibits the use of empirical estimations of the correlation between elevation and delay, even with the use of advanced spatial filtering techniques. Corrections using external datasets are also limited, as few volcanoes are covered by GPS networks or other local weather data. In these cases, atmospheric models provide a globally applicable alternative to correcting and estimating the magnitude of topographically-correlated atmospheric uncertainties on the scale of volcanic arcs.

InSAR data is being used increasingly in timely evaluations of volcanic hazards (e.g. Pallister et al. 2013), and future developments will involve expanding the use of InSAR from a research tool used after the fact, to an active monitoring tool that can inform hazard management during unfolding volcanic crises (Pinel et al. 2014). Data from Sentinel 1 A is expected to be available within minutes of acquisition, but at present, atmospheric reanalysis such as ERA-I and NARR are available only after a 3–6 month delay. Therefore, although large-scale atmospheric models are shown to remove atmospheric artefacts in InSAR data from a variety of settings (Doin et al. 2009; Pinel et al. 2011; Jolivet et al. 2011; Walters et al. 2013; Jolivet et al. 2014), using these models to calculate and remove APSs from interferograms in near-real-time during volcanic unrest may be an unrealistic goal. In this study, we present an alternative use of large-scale atmospheric models, and demonstrate how they can be used independently from InSAR data to estimate atmospheric uncertainties and calculate detection thresholds a priori. These estimates of uncertainties can be used to establish errors for time-series analysis, and provide decision-makers with an appropriate representation of the accuracy of InSAR data at a given volcano. Using this approach on an arc-wide scale is also informative for the placement of other geodetic equipment, such as continuous GPS stations, as volcanoes that have higher detection thresholds may benefit more from additional ground-based geodetic equipment than those where uncertainties are predicted to be much lower.

### 3.7 Conclusions

Atmospheric artefacts continue to be the most dominant noise source in InSAR datasets. Here we use large-scale atmospheric models to correct topographically-correlated atmospheric artefacts in interferograms from Lassen Volcanic Center. We find that ERA-I and NARR reduce interferogram  $\sigma$  in 58 and 79 % of cases respec-

tively, and that NARR is more suited to reducing stratified atmospheric artefacts due to higher temporal and spatial resolution of the model. Using NARR to assess topographically-correlated atmospheric artefacts throughout the Cascades Volcanic Arc we find that:

- Elevation-delay gradients range between 0.09 and 0.19 cm/km and are largest for volcanoes located at lower elevations (e.g. Mount Baker). At 85% of Cascade volcanoes elevation-delay gradients are also up to 15% larger on the windward side of the edifice.
- The temporal variability of stratified atmospheric delays increases by 0.7 cm per kilometre of edifice relief, which is much less than estimates for volcanoes in the Central American Volcanic Arc.

Following this analysis we develop a strategy using large-scale atmospheric models to produce a priori estimates of atmospheric uncertainties on the scale of volcanic arcs. For the application of data from Sentinel 1 A to the Cascade volcanoes we suggest that:

- A minimum of between 60 and 130 days are required to detect long-term linear deformation at a rate of 1 cm/year.
- During periods of pre-eruptive unrest, ground deformation is most likely to be observed at shield volcanoes (detection threshold <1 cm) and least likely to be observed at complex volcanoes, where pre-eruptive unrest has historically lasted <1 week.

Using this approach we can better integrate InSAR data into long- and short-term monitoring efforts by defining the number of images required for multi-temporal analysis, and establishing the sensitivity of data to topographically-correlated atmospheric noise. Estimating atmospheric uncertainties a priori is particularly valuable for near-real-time monitoring of volcanic unrest, when atmospheric reanalysis data is not immediately available and InSAR data may not be coherent enough to use empirical methods alone. With the launch of new dedicated SAR satellites and the development of automated processing regimes, quantifying and correcting for atmospheric uncertainties in this way is a useful step towards using InSAR data in near-real-time.

## Appendix

See Tables 3.4, 3.5 and 3.6.



**Table 3.4** ENVISAT interferograms used to assess atmospheric artefacts at Lassen Volcanic Center. Dates are in the format master (yyyy mm dd) slave (yyyy mm dd)

2004 06 17 2004 11 04	2004 06 17 2005 03 24
2004 09 30 2005 07 07	2004 11 04 2005 03 24
2004 12 09 2005 11 24	2005 07 07 2006 06 22
2006 11 09 2007 01 18	2006 11 09 2007 08 16
2006 11 09 2007 09 20	2007 01 18 2007 09 20
2007 01 18 2007 11 29	2007 07 12 2007 10 25
2007 07 12 2008 05 22	2007 07 12 2008 06 26
2007 08 16 2007 09 20	2007 08 16 2008 04 17
2007 09 20 2007 11 29	2007 09 20 2008 04 17
2007 09 20 2008 09 04	2007 10 25 2008 01 03
2007 10 25 2008 05 22	2007 10 25 2008 06 26
2007 10 25 2008 07 31	2007 11 29 2008 04 17
2007 11 29 2008 09 04	2008 01 03 2008 05 22
2008 04 17 2008 09 04	2008 05 22 2008 06 26
2008 05 22 2008 07 31	2008 06 26 2008 07 31
2009 07 16 2009 08 20	2009 07 16 2010 05 27
2009 08 20 2010 05 27	2009 10 29 2010 01 07
2009 10 29 2010 05 27	2009 10 29 2010 08 05
2010 01 07 2010 08 05	2010 05 27 2010 08 05

**Table 3.5** ENVISAT interferograms used to assess atmospheric artefacts at Medicine Lake Volcano. Dates are in the format master (yyyy mm dd) slave (yyyy mm dd)

2005 11 17 2005 12 22	2005 12 22 2006 03 02
2006 03 02 2007 02 15	2007 01 11 2007 02 15
2007 02 15 2007 10 18	2007 02 15 2007 12 27
2007 10 18 2007 11 22	2007 10 18 2008 05 15
2007 10 18 2008 08 28	2007 11 22 2007 12 27
2007 11 22 2008 06 19	2007 12 27 2008 03 06
2008 03 06 2008 05 15	2008 05 15 2008 06 19
2008 05 15 2008 08 28	2008 05 15 2009 02 19
2008 05 15 2009 04 30	2008 06 19 2008 07 24
2008 06 19 2009 01 15	2008 06 19 2009 06 04
2008 07 24 2008 08 28	2008 08 28 2009 01 15
2008 08 28 2009 02 19	2008 08 28 2009 06 04
2009 01 15 2009 02 19	2009 01 15 2009 06 04
2009 02 19 2009 03 26	2009 02 19 2009 04 30
2009 02 19 2009 08 13	2009 03 26 2009 04 30
2009 03 26 2010 02 04	2009 04 30 2009 06 04

(continued)

**Table 3.5** (continued)

2005 11 17 2005 12 22	2005 12 22 2006 03 02
2009 04 30 2009 12 31	2009 04 30 2010 03 11
2009 06 04 2009 08 13	2009 06 04 2010 04 15
2009 06 04 2010 05 20	2009 08 13 2009 12 31
2009 08 13 2010 03 11	2009 12 31 2010 02 04
2009 12 31 2010 03 11	2009 12 31 2010 09 02
2010 02 04 2010 03 11	2010 02 04 2010 04 15
2010 02 04 2010 10 07	2010 03 11 2010 04 15
2010 03 11 2010 06 24	2010 04 15 2010 05 20
2010 04 15 2010 10 07	2010 05 20 2010 06 24
2010 05 20 2010 09 02	2010 06 24 2010 07 29
2010 06 24 2010 09 02	2010 07 29 2010 09 02
2010 09 02 2010 10 07	

**Table 3.6** Operational outputs of APS analysis for monitoring pre-eruptive volcanic unrest in the Cascades. This table is a replicate of Table 3.3 but accounts for uncertainties from Phillipson et al. (2013)

Volcano type	Examples <sup>a</sup>	Duration of unrest <sup>b</sup> (days)	Number of consecutive sentinel interferograms	Detection threshold <sup>c</sup> (cm)
Complex volcano	Sisters	<1 week	0	–
Stratovolcano	Baker, Glacier, Rainier, St Helens, Adams, Hood, Jefferson, Shasta, Lassen	1 week–3 months	<5–~100	5–<0.01
Caldera	Crater	2 weeks–5 months	5–30	2–<0.01
Shield volcano	Newberry, Medicine	3 weeks–5 years	10–>150	<1

<sup>a</sup>As defined in the Smithsonian database of holocene volcanoes

<sup>b</sup>Using upper and lower quartile values from Phillipson et al. (2013)

<sup>c</sup>Calculated using Eq. 3.3 and temporal atmospheric variability from Sect. 3.5.3

## References

- Agram, P. S., Jolivet, R., Riel, B., Lin, Y. N., Simons, M., Hetland, E., Doin, M. P., & Lasserre, C. (2013). New Radar Interferometric Time Series Analysis Toolbox released. *Eos, Trans. AGU* 94(7), 69–76.
- Baby, H., Gole, P., & Lavernat, J. (1988). A model for the tropospheric excess path length of radio waves from surface meteorological measurements. *Radio Science*, 23(6), 1023–1038.
- Bathke, H., Shirzaei, M., & Walter, T. R. (2011). Inflation and deflation at the steep-sided Llaima stratovolcano (Chile) detected by using InSAR. *Geophysical Research Letters*, 38(10).
- Beauducel, F., Briole, P., & Froger, J.-L. (2000). Volcano-wide fringes in ERS synthetic aperture radar interferograms of Etna (1992–1998): Deformation or tropospheric effect? *Journal of Geophysical Research*, 105(B7), 16391–16402.
- Bekaert, D. P. S., Hooper, A., & Wright, T. J. (2015). A spatially-variable power-law tropospheric correction technique for InSAR data. *Journal of Geophysical Research*, 120(2), 1345–1356.
- Bell, S. (2012). *Landscape: pattern, perception and process*. New York, US: Routledge.
- Berardino, P., Fornaro, G., Lanari, R., & Sansosti, E. (2002). A new algorithm for surface deformation monitoring based on small baseline differential SAR interferograms. *IEEE Transactions on Geoscience and Remote Sensing*, 40, 2375–2383.
- Berrisford, P., Kållberg, P., Kobayashi, S., Dee, D., Uppala, S., Simmons, A. J., et al. (2011). Atmospheric conservation properties in ERA-Interim. *Quarterly Journal of the Royal Meteorological Society*, 137(659), 1381–1399.
- Bevis, M., Businger, S., Herring, T. A., Rocken, C., Anthes, R. A., & Ware, R. H. (1992). GPS meteorology: Remote sensing of atmospheric water vapor using the Global Positioning System. *Journal of Geophysical Research*, 97(D14), 15787–15801.
- Biggs, J., Wright, T., Lu, Z., & Parsons, P. (2007). Multi-interferogram method for measuring inter seismic deformation: Denali Fault, Alaska. *Geophysical Journal International*, 170, 1165–1179.
- Biggs, J., Anthony, E. Y., & Ebinger, C. J. (2009). Multiple inflation and deflation events at Kenyan volcanoes. *East African Rift. Geology*, 37(11), 979–982.
- Bürgmann, R., Rosen, P. A., & Fielding, E. J. (2000). Synthetic aperture radar interferometry to measure Earth's surface topography and its deformation. *Annual Review of Earth and Planetary Sciences*, 28(1), 169–209.
- Biggs, J., Ebmeier, S. K., Aspinall, W. P., Lu, Z., Pritchard, M. E., Sparks, R. S. J., Mather, T. A. (2014). Global link between deformation and volcanic eruption quantified by satellite imagery. *Nature Communications* 5.
- Cavalié, O., Doin, M.-P., Lasserre, C., & Briole, P. (2007). Ground motion measurement in the Lake Mead area, Nevada, by differential synthetic aperture radar interferometry time series analysis: Probing the lithosphere rheological structure. *Journal of Geophysical Research*, 112(B3).
- Chaussard, E., Amelung, F., & Aoki, Y. (2013). Characterization of open and closed volcanic systems in Indonesia and Mexico using InSAR time series. *Journal of Geophysical Research*, 118(8), 3957–3969.
- Chaussard, E., & Amelung, F. (2014). Regional controls on magma ascent and storage in volcanic arcs. *Geochemistry, Geophysics, Geosystems*, 15(4), 1407–1418.
- Daly, C., Taylor, G. H., Gibson, W. P. (1997). The PRISM approach to mapping precipitation and temperature. In *Proceedings of the 10th AMS Conference on Applied Climatology*. pp. 20–23.
- Dee, D. P., Uppala, S. M., Simmons, A. J., Berrisford, P., Poli, P., Kobayashi, S., et al. (2011). The ERA-Interim reanalysis: Configuration and performance of the data assimilation system. *Quarterly Journal of the Royal Meteorological Society*, 137(656), 553–597.
- Delacourt, C., Briole, P., & Achache, J. A. (1998). Tropospheric corrections of SAR interferograms with strong topography. *Application to Etna. Geophysical Research Letters*, 25(15), 2849–2852.
- Doin, M.-P., Lasserre, C., Peltzer, G., Cavalie, O., & Doubre, C. (2009). Correction of stratified atmospheric delays in SAR interferometry: Validation with global atmospheric models. *Journal of Applied Geophysics*, 69, 35–50.

- Dzurisin, D., Poland, M. P., & Bürgmann, R. (2002). Steady subsidence of Medicine Lake Volcano, Northern California, revealed by repeated levelling surveys. *Journal of Geophysical Research*, *107*(B12).
- Dzurisin, D., Lisowski, M., Wicks, C. W., Poland, M. P., & Endo, E. T. (2006). Geodetic observations and modeling of magmatic inflation at the Three Sisters volcanic center, central Oregon Cascade Range, USA. *Journal of Volcanology and Geothermal Research*, *150*(1), 35–54.
- Dzurisin, D. (2007). *Volcano deformation: geodetic monitoring techniques*. Chichester, UK: Springer-Praxis.
- Dzurisin, D., Lisowski, M., & Wicks, C. W. (2009). Continuing inflation at Three Sisters volcanic center, central Oregon Cascade Range, USA, from GPS, leveling, and InSAR observations. *Bulletin of Volcanology*, *71*(10), 1091–1110.
- Ebmeier, S. K., Biggs, J., Mather, T. A., & Amelung, F. (2013a). Applicability of InSAR to tropical volcanoes: insights from Central America. *Geological Society, London, Special Publications*, *380*(1), 15–37.
- Ebmeier, S. K., Biggs, J., Mather, T. A., & Amelung, F. (2013b). On the lack of InSAR observations of magmatic deformation at Central American volcanoes. *Journal of Geophysical Research*, *118*(5), 2571–2585.
- Ebmeier, S. K., Biggs, J., Muller, C., & Avaró, G. (2014). Thin-skinned mass-wasting responsible for widespread deformation at Arenal volcano. *Frontiers in Earth Science*, *2*, 35.
- Eff-Darwich, A., Pérez, J. C., Fernández, J., García-Lorenzo, B., González, A., & González, P. J. (2012). Using a mesoscale meteorological model to reduce the effect of tropospheric water vapour from DInSAR data: A case study for the island of Tenerife. *Canary Islands. Pure and applied geophysics*, *169*(8), 1425–1441.
- Elliott, J. R., Biggs, J., Parsons, P., & Wright, T. J. (2008). InSAR slip rate determination on the Altyn Tagh Fault, northern Tibet, in the presence of topographically correlated atmospheric delays. *Geophysical Research Letters*, *35*(12).
- Emardson, T. R., Simons, M., & Webb, F. H. (2003). Neutral atmospheric delay in interferometric synthetic aperture radar applications: Statistical description and mitigation. *Journal of Geophysical Research*, *108*(B5).
- Ewert, J. W., Guffanti, M., Murray, T. L. (2005). An assessment of volcanic threat and monitoring capabilities in the United States: framework for a National Volcano Early Warning System NVEWS. U.S. Geological Survey Open File Report (2005-1164).
- Farr, T. G., Rosen, P. A., Caro, E., Crippen, R., Duren, R., Hensley, S., et al. (2007). The shuttle radar topography mission. *Reviews of Geophysics*, *45*(2).
- Ferretti, A., Prati, C., & Rocca, F. (2001). Permanent scatterers in SAR interferometry. *IEEE Transactions on Geoscience and Remote Sensing*, *39*(1), 8–20.
- Foster, J., & Bevis, M. (2003). Lognormal distribution of precipitable water in Hawaii. *Geochemistry, Geophysics, Geosystems*, *4*(7).
- Foster, J., Brooks, B., Cherubini, T., Shacat, C., Businger, S., & Werner, C. L. (2006). Mitigating atmospheric noise for InSAR using a high resolution weather model. *Geophysical Research Letters*, *33*(16).
- Foster, J., Kealy, J., Cherubini, T., Businger, S., Lu, Z., & Murphy, M. (2013). The utility of atmospheric analyses for the mitigation of artifacts in InSAR. *Journal of Geophysical Research*, *118*(2), 748–758.
- Fournier, T. J., Pritchard, M. E., & Riddick, S. N. (2010). Duration, magnitude, and frequency of subaerial volcano deformation events: New results from Latin America using InSAR and a global synthesis. *Geochemistry, Geophysics, Geosystems*, *11*(1).
- Goldstein, R., Zebker, H., & Werner, C. (1988). Satellite radar interferometry: Two dimensional phase unwrapping. *Radio Science*, *23*(4), 713–720.
- Goldstein, R., & Werner, C. (1998). Radar interferogram filtering for geophysical applications. *Geophysical Research Letters*, *25*(21), 4035–4038.

- Gourmelen, N., Amelung, F., & Lanari, R. (2010). Interferometric synthetic aperture radar-GPS integration: Interseismic strain accumulation across the Hunter Mountain fault in the eastern California shear zone. *Journal of Geophysical Research*, 115(B9).
- Grubb, P. J. (1971). Interpretation of the Massenerhebung effect on tropical mountains. *Nature*, 229, 44–45.
- Hanssen, R., Rocca, F. (2009). Sentinel 1: Interferometric applications. In *Proceedings of the Geoscience and Remote Sensing Symposium*, Vol. 1 (pp. 1–56). IEEE International, IGARSS 2009.
- Hanssen, R. F. (2001). *Radar Interferometry: Data Interpretation and Analysis*. Norwell, MA, US: Kluwer Acad.
- Heleno, S. I. N., Frischknecht, C., & dOreye, N., Lima, J. N. P., Faria, B., Wall, R., Kervyn, F. (2010). Seasonal tropospheric influence on SAR interferograms near the ITCZ-The case of Fogo Volcano and Mount Cameroon. *Journal of African Earth Sciences*, 58(5), 833–856.
- Jolivet, R., Grandin, R., Lasserre, C., & M.-P., D., Peltzer, G., (2011). Systematic InSAR tropospheric phase delay corrections from global meteorological reanalysis data. *Geophysical Research Letters*, 38(L17311).
- Jolivet, R., Agram, P. S., Lin, N. Y., Simons, M., Doin, M.-P., Peltzer, G., et al. (2014). Improving InSAR geodesy using global atmospheric models. *Journal of Geophysical Research*, 119(3), 2324–2341.
- Jónsson, S., Zebker, H., Segall, P., & Amelung, F. (2002). Fault slip distribution of the 1999 Mw 7.1 Hector Mine, California, earthquake, estimated from satellite radar and GPS measurements. *Bulletin of the Seismological Society of America*, 92(4), 1377–1389.
- Li, Z., Fielding, E. J., Cross, P., & Muller, J.-P. (2006a). Interferometric synthetic aperture radar atmospheric correction: GPS topography-dependent turbulence model. *Journal of Geophysical Research*, 111(B2).
- Li, Z. W., Ding, X. L., Huang, C., Wadge, G., & Zheng, D. W. (2006b). Modeling of atmospheric effects on InSAR measurements by incorporating terrain elevation information. *Journal of Atmospheric and Solar-Terrestrial Physics*, 68(11), 1189–1194.
- Lin, Y. N., Simons, M., Hetland, E. A., Muse, P., & DiCaprio, C. (2010). A multiscale approach to estimating topographically correlated propagation delays in radar interferograms. *Geochemistry, Geophysics, Geosystems*, 11(9).
- Lipman, P. W., & Mullineaux, D. R. E. (1981). The 1980 Eruptions of Mount St. Helens, Washington. *U.S. Geological Survey Professional Paper*, 1250, 844p.
- Lohman, R., & Simons, M. (2005). Some thoughts on the use of InSAR data to constrain models of surface deformation: Noise structure and data downsampling. *Geochemistry, Geophysics, Geosystems*, 6(1).
- Lu, Z., Power, J. A., McConnell, V. S., Wicks, C., & Dzurisin, D. (2002). Preeruptive inflation and surface interferometric coherence characteristics revealed by satellite radar interferometry at Makushin Volcano, Alaska: 1993–2000. *Journal of Geophysical Research*, 107(B11).
- Lu, Z., & Dzurisin, D. (2014). *InSAR Imaging of Aleutian Volcanoes: Monitoring a Volcanic Arc from Space*. Chichester, UK: Springer-Praxis.
- Lu, Z., & Freymueller, J. T. (1998). Synthetic aperture radar interferometry coherence analysis over Katmai volcano group, Alaska. *Journal of Geophysical Research*, 103(B12), 29887–29894.
- Mass, C. F. (2008). *The Weather of the Pacific Northwest*. WA, US: University of Washington Press.
- Massonnet, D., Feigl, K. L., Vadon, H., Rossi, M., 1996. Coseismic deformation field of the M = 6.7 Northridge, California earthquake of January 17. (1994). recorded by two radar satellites using interferometry. *Geophysical Research Letters*, 23(9), 969–972.
- Massonnet, D., Briole, P., & Arnaud, A. (1995). Deflation of Mount Etna monitored by spaceborne radar interferometry. *Nature*, 375(6532), 567–570.
- Massonnet, D., & Feigl, K. L. (1995). Discrimination of geophysical phenomena in satellite radar interferograms. *Geophysical Research Letters*, 22(12), 1537–1540.
- Massonnet, D., & Feigl, K. L. (1998). Radar interferometry and its application to changes in the Earth's surface. *Reviews of Geophysics*, 36(4), 44–500.

- Mesinger, F., DiMego, G., Kalnay, E., Mitchell, K., Shafran, P. C., Ebisuzaki, W., et al. (2006). North American Regional Reanalysis. *Bull. Am. Meteor. Soc.*, 87(3), 343–360.
- Miranda, P. M. A., & James, I. N. (1992). Non-Linear Three-Dimensional Effects On Gravity-Wave Drag: Splitting Flow and Breaking Waves. *Quarterly Journal of the Royal Meteorological Society*, 118(508), 1057–1081.
- Pallister, J. S., Schneider, D. J., Griswold, J. P., Keeler, R. H., Burton, W. C., Noyles, C., et al. (2013). Merapi 2010 eruption-Chronology and extrusion rates monitored with satellite radar and used in eruption forecasting. *Journal of Volcanology and Geothermal Research*, 261, 144–152.
- Parker, A. L., Biggs, J., & Lu, Z. (2014). Investigating long-term subsidence at Medicine Lake Volcano, CA, using multi temporal InSAR. *Geophys. J. Int.*, 199(2), 844–859.
- Passarelli, L., & Brodsky, E. E. (2012). The correlation between run-up and repose times of volcanic eruptions. *Geophys. J. Int.*, 188(3), 1025–1045.
- Peel, M. C., Finlayson, B. L., & McMahon, T. A. (2007). Updated world map of the Köppen-Geiger climate classification. *Hydrology and Earth System Sciences*, 11(5), 1633–1644.
- Peltier, A., Bianchi, M., Kaminski, E., Komorowski, J.-C., Rucci, A., & Staudacher, T. (2010). PSInSAR as a new tool to monitor pre-eruptive volcano ground deformation: Validation using GPS measurements on Piton de la Fournaise. *Geophysical Research Letters*, 37(12).
- Phillipson, G., Sobradelo, R., & Gottsmann, J. (2013). Global volcanic unrest in the 21st century: an analysis of the first decade. *Journal of Volcanology and Geothermal Res.*, 264, 183–196.
- Pinel, V., Hooper, A., De la Cruz-Reyna, S., Reyes-Davila, G., Doin, M.-P., & Bascou, P. (2011). The challenging retrieval of the displacement field from InSAR data for andesitic stratovolcanoes: Case study of Popocatepetl and Colima Volcano, Mexico. *Journal of Volcanology and Geothermal Research*, 200(1), 49–61.
- Pinel, V., Poland, M. P., & Hooper, A. (2014). Volcanology: Lessons learned from Synthetic Aperture Radar imagery. *Journal of Volcanology and Geothermal Research*, 289, 81–113.
- Poland, M., Bawden, G., Lisowski, M., Dzurisin, D. (2004). Newly discovered subsidence at Lassen Peak, southern Cascade Range, California, from InSAR and GPS. [abs.]: Eos (American Geophysical Union Transactions) vol. 85, Fall Meeting Supplement, abs. G51A-0068.
- Poland, M. P., Bürgmann, R., Dzurisin, D., Lisowski, M., Masterlark, T., Owen, S., et al. (2006). Constraints on the mechanism of long-term, steady subsidence at Medicine Lake volcano, northern California, from GPS, levelling and InSAR. *Journal of Volcanology and Geothermal Research*, 150(1), 55–78.
- Poland, M. P., & Lu, Z. (2008). Radar Interferometry Observations of Surface Displacements During Pre- and Coeruptive Periods at Mount St. Helens, Washington, 1992–2005. *U. S. Geological Survey Professional Paper*, 1750, 361–382.
- Price, M. F., Byers, A. C., Friend, D. A., Kohler, T., & Price, L. W. (2013). *Mountain Geography: Physical and Human Dimensions*. US: University of California Press, CA.
- Pritchard, M. E., & Simons, M. (2004). An InSAR-based survey of volcanic deformation in the central Andes. *Geochemistry, Geophysics, Geosystems*, 5(2).
- Puysségur, B., Michel, R., & Avouac, J.-P. (2007). Tropospheric phase delay in interferometric synthetic aperture radar estimated from meteorological model and multispectral imagery. *Journal of Geophysical Research*, 112(B5).
- Remy, D., Chen, Y., Froger, J. L., Bonvalot, S., Cordoba, M., & Fustos, J. (2015). Revised interpretation of recent InSAR signals observed at Llaima volcano (Chile). *Geophysical Research Letters*, 42(10).
- Remy, D., Bonvalot, S., Briole, P., & Murakami, M. (2003). Accurate measurements of tropospheric effects in volcanic areas from SAR interferometry data: Application to Sakurajima volcano (Japan). *Earth and Planetary Science Letters*, 213(3), 299–310.
- Riddick, S. N., & Schmidt, D. A. (2011). Time-dependent changes in volcanic inflation rate near Three Sisters, Oregon, revealed by InSAR. *Geochemistry, Geophysics, Geosystems*, 12(12), 20111217.

- Riddick, S. N., Schmidt, D. A., & Deligne, N. I. (2012). An analysis of terrain properties and the location of surface scatterers from persistent scatterer interferometry. *ISPRS Journal of Photogrammetry and Remote Sensing*, 73, 50–57.
- Rogers, E., Ek, M., Lin, Y., Mitchell, K., Parrish, D., & DiMego, G. (2001). *Changes to the NCEP Meso Eta analysis and forecast system: Assimilation of observed precipitation, upgrades to land-surface physics, modified 3DVAR analysis*. NCEP: EMC.
- Rosen, P., Hensley, S., Peltzer, G., & Simons, M. (2004). Updated Repeat Orbit Interferometry package released. EOS, Trans. AGU 85 (5).
- Rosen, P. A., Hensley, S., Zebker, H. A., & Webb, F. H. (1996). Surface deformation and coherence measurements of Kilauea Volcano, Hawaii, from SIR-C radar interferometry. *Journal of Geophysical Research*, 101(E10), 23109–23125.
- Shirzaei, M., & Bürgmann, R. (2012). Topography correlated atmospheric delay correction in radar interferometry using wavelet transforms. *Geophysical Research Letters*, 39(1).
- Simmons, A., Uppala, S., & D., D., Kobayashi, S. (2007). ERA-Interim: New ECMWF reanalysis products from 1989 onwards. *ECMWF Newsletter*, 110, 25–35.
- Simons, M., & Rosen, P. A. (2007). *Interferometric synthetic aperture radar geodesy*, 3, 391–446.
- Smith, E. K., & Weintraub, S. (1953). The constants in the equation for atmospheric refractive index at radio frequencies. *Proceedings of the IRE*, 41(8), 1035–1037.
- Suzuki, S., Osawa, Y., Hatooka, Y., Watanabe, T. (2009). The Post-ALOS program. In *Proceedings of the 27th ISTS International Symposium on Space Technology and Science*. Vol. 2009-n-02.
- Taylor, M., & Peltzer, G. (2006). Current slip rates on conjugate strike-slip faults in central Tibet using synthetic aperture radar interferometry. *Journal of Geophysical Research*, 111(B12).
- Uppala, S., & D., D., Kobayashi, S., Berrisford, P., Simmons, A.,... (2008). Towards a climate data assimilation system: status update of ERA-Interim. *ECMWF Newsletter*, 115, 12–18.
- Wadge, G., Webley, P. W., James, I. N., Bingley, R., Dodson, A., Waugh, S., et al. (2002). Atmospheric models, GPS and InSAR measurements of the tropospheric water vapour field over Mount Etna. *Geophysical Research Letters*, 29(19), 11–1.
- Wadge, G., Zhu, M., Holley, R. J., James, I. N., Clark, P. A., Wang, C., et al. (2010). Correction of atmospheric delay effects in radar interferometry using a nested mesoscale atmospheric model. *Journal of Applied Geophysics*, 72(2), 141–149.
- Walters, R. J., Bekaert, D., Wright, T. J., Parker, D. J., Hooper, A. J., Crippa, P., Li, Z. (2015). A Global Validation of ERA-Interim Atmospheric Correction for InSAR. In: Proc., Fringe 2015 Workshop. No. 108.
- Walters, R. J., Elliott, J. R., Li, Z., & Parsons, B. (2013). Rapid strain accumulation on the Ashkabad fault (Turkmenistan) from atmosphere-corrected InSAR. *Journal of Geophysical Research*, 118(7), 3674–3690.
- Webley, P. W., Wadge, G., & James, I. N. (2004). Determining radio wave delay by non-hydrostatic atmospheric modelling of water vapour over mountains. *Physics and Chemistry of the Earth*, 29(2), 139–148.
- Wicks, C. W., Dzurisin, D., Ingebritsen, S., Thatcher, W., Lu, Z., & Iverson, J. (2002). Magmatic activity beneath the quiescent Three Sisters volcanic center, central Oregon Cascade Range. *USA. Geophysical Research Letters*, 29(7), 26–1.
- Zebker, H. A., Rosen, P. A., & Hensley, S. (1997). Atmospheric effects in interferometric synthetic aperture radar surface deformation and topographic maps. *Journal of Geophysical Research*, 102(B4), 7547–7563.
- Zhu, M., Wadge, G., Holley, R. J., James, I. N., Clark, P. A., Wang, C., et al. (2007). High-resolution forecast models of water vapor over mountains: comparison with MERIS and meteosat data. *Geoscience and Remote Sensing Letters, IEEE*, 4(3), 401–405.

## Chapter 4

# Time Constraints on Magma Intrusion from Thermal Models of Long-Term Subsidence: Medicine Lake Volcano, CA

**Abstract** Magma intrusion plays a fundamental role in the eruptive cycle. The geodetic response to intrusion is thought to persist over years - decades as magma cools and crystallises, reducing in volume. However, past thermal modelling approaches do not explain ground deformation over these time-scales. Here we combine an existing thermal model with simple geodetic and petrological constraints to show that subsidence resulting from cooling and crystallising magma intrusions (volume  $< 3 \text{ km}^3$ ) may persist over decadal time-scales. We find that the rate and time-scale of subsidence is dependent upon the magma composition, the intrusion geometry, and the thermal state of the surrounding country rock. The early stages of volume change are most dependent upon cooling and crystallisation at the intrusion contact, which is a function of surface area and country rock temperature. Changes in the rate of volume change over time are slower for sills of lower aspect ratio (thicker) and correspond to changes in the crystallising assemblage. We apply this modelling approach to long-term, steady subsidence of Medicine Lake Volcano, CA, using realistic petrological and geometrical inputs. Comparing the results to the geodetic record, we identify a suite of best-fitting models with initial volumes of  $1\text{--}2.5 \text{ km}^3$  that reproduce  $>65$  years of subsidence measured at the volcano. These results suggest that magma intrusion has occurred on the order of hundreds of years before present, more recently than the time of the last eruption  $\sim 1 \text{ ka}$ , and that subsidence may continue for decades. Long-term subsidence is observed at numerous volcanic centres and, through this modelling approach, can be used to provide insight into crustal magma fluxes and the timing of magma intrusion.

## 4.1 Introduction

Global estimates of intrusion-to-extrusion ratios at volcanic arcs range between 1 and 16 (Shaw et al. 1980; Wadge 1980; Blackwell et al. 1982; Crisp 1984; Ingebritsen et al. 1989, 1994; Pritchard 2003; Sadofsky et al. 2008; Taran 2009), with a ratio of 5 viewed to be common to most magmatic systems (Ingebritsen et al. 1994; White et al. 2006). The intrusion of magma therefore plays a significant part in the eruptive cycle, having a fundamental role in endogenous volcanic growth (e.g. Staudigel and



Schmincke 1984; Annen et al. 2001) and the building of continental crust (e.g. Thorpe et al. 1981; Reymer and Schubert 1984; Francis and Hawkesworth 1994).

Episodes of volcanic uplift measured over periods of days to months may be interpreted as the intrusion of magmatic material (e.g. Atka, Okmok and Peulik, Aleutians: Lu and Dzurisin 2014; Eyjafjallajökull, Iceland: Pedersen and Sigmundsson 2006). However, the geodetic response to intrusion is thought to persist over longer time-scales (years - decades) as magma cools and crystallises, reducing in volume (e.g. Pyle et al. 2013). Of over 100 volcanoes known to be deforming, almost a fifth are thought to be undergoing long-term subsidence, albeit with periodic uplift too in some instances (Caricchi et al. 2014). In a number of cases this has been linked to cooling magmatic intrusions (see Table 4.1), however existing thermal modelling approaches do not explain ground deformation over the required time-scales (e.g. Dzurisin et al. 2002; Mann and Freymueller 2003; Pritchard and Simons 2004b).

The subsurface volume loss due to cooling and crystallisation may be estimated most simply by using a 1D analytical expression to quantify thermoelastic contraction that occurs via conductive cooling of magma:

$$\Delta V_{conduction} = \alpha \cdot V \cdot \Delta T, \quad (4.1)$$

where  $V$  is the initial volume,  $\Delta T$  is temperature change and  $\alpha$  is the coefficient of thermal expansion (e.g. Dzurisin et al. 2002; Mann and Freymueller 2003). Assuming that the country rock begins and remains cold, the diffusion timescale of cooling may then be given by:

$$t \approx l^2 / \kappa, \quad (4.2)$$

where  $l$  is the length-scale of cooling and  $\kappa$  is diffusivity. A volume decrease also occurs due to crystallisation, as the solid phase is generally denser than the melt from which it crystallises (Lange 1994). This volume change is much larger than that occurring through conduction alone (Pritchard 2003), and is commonly approximated using the density difference between the liquid ( $\rho_{liquid}$ ) and solid ( $\rho_{solid}$ ) phases:

$$\Delta V_{crystallisation} = \frac{\rho_{liquid}}{\rho_{solid}}, \quad (4.3)$$

(e.g. Sturkell and Sigmundsson 2000) which has been shown to be  $\sim 10\%$  (Sigmundsson et al. 1997).

These simple approaches to estimate the volumetric effects of cooling and crystallisation fail to account for two key phenomena. Firstly, the parameters that govern heat transfer by conduction (thermal diffusivity and conductivity) are strongly temperature dependent (Carslaw and Jaeger 1959; Delaney 1988). As temperature increases, conductivity decreases, therefore as the surrounding country rock heats up it becomes a more effective thermal insulator. Secondly, analytical models cannot account for the release of latent heat that occurs during crystallisation (Carslaw and Jaeger 1959; Delaney 1988). The positive feedback between these two effects reduces the cooling rate, promoting an increased melt fraction (Whittington et al. 2009). By

**Table 4.1** Volcanoes undergoing long-term subsidence attributed to cooling and crystallisation

Volcano	Reference	Subsidence observed	Period	Modelling approach
Alcedo, Galapagos	Hooper et al. (2007)	40 mm/yr	1997–2001	Eqs. 4.2, 4.3: 0.6–12 % volume decrease
Amukta, Aleutians	Lu and Dzurisin (2014)	5 mm/yr	1993–2009	–
Aniakchak, Aleutians	Kwoun et al. (2006)	13 mm/yr	1992–2002	–
Askja, Iceland	Sturkell and Sigmundsson (2000)	10–7 mm/yr (Exponential decay)	1993–1998	Eq. 4.3: 10 % volume decrease
Basiluzzo, Aeolian Islands	Tallarico et al. (2003)	3.75 ± 0.10 m (1.87 mm/yr)	2000 ± 50 years BP	Contraction of spherical chamber due to time-dependent conduction
Cerro Blanco, Andes	Pritchard and Simons (2004b)	25 decreasing to 18 mm/yr	1992–2000	1D spherical conductive cooling accounting for phase changes
Emmons Lake, Aleutians	Lu and Dzurisin (2014)	8 mm/yr	2003–2009	–
Fisher Caldera, Aleutians	Mann and Freymueller (2003)	1.5 mm/yr	1998–2001	Eq. 4.1, Gas release
Krafla, Iceland	Sigmundsson et al. (1997)	24 mm/yr	1992–1995	Eq. 4.2: 2 % volume decrease Eq. 4.3: 9 % volume decrease
Makushin, Aleutians	Lu and Dzurisin (2014)	10 mm/yr	1995–2009	–
Mount Baker, Cascades	Hodge and Crider (2010)	<5 mm/yr	1981–2007	Eq. 4.1
Seguam, Aleutians	Lu and Dzurisin (2014)	15 mm/yr	1993–2009	–

not accounting for these temperature-dependent factors, past studies require unrealistically large initial volumes of magmatic material to sustain cooling (and therefore volume decrease) over decadal time-scales (e.g. Dzurisin et al. 2002; Mann and Freymueller 2003; Pritchard and Simons 2004b; Hodge and Crider 2010).

The limitations of analytical thermal models can be overcome by using numerical methods which, when constrained by inputs from petrology, track the release of latent heat due to crystallisation, and allow for variations in thermal properties with

temperature (Carslaw and Jaeger 1959). A recent study using this approach to interpret transient, inter-eruptive deformation at Okmok, Aleutians, suggests that magma cooling could be sufficient to produce multi-year volcanic subsidence (Caricchi et al. 2014). Here we test this hypothesis, and assess whether cooling and crystallisation of magma intrusions can cause subsidence over decadal time-scales. As the thermal evolution of an intrusion is strongly dependent upon its geometry (Annen et al. 2008), we build upon past approaches by also incorporating geometrical constraints from analytical source models found by inversion of geodetic datasets (Dzurisin 2007; Segall 2010; Chap. 2).

We explore the effects of intrusion geometry and magma composition before applying the model to the case study of Medicine Lake Volcano, CA, where cooling and crystallisation of subsurface material is linked to volcano-wide subsidence that has persisted for > 65 years at a constant rate of  $\sim 1$  cm/yr (Dzurisin et al. 2002; Poland et al. 2006; Parker et al. 2014). At Medicine Lake Volcano, geodetic measurements began during a period of steady subsidence, and the onset of deformation is unknown. We therefore demonstrate how this modelling approach may be used to constrain the timing and scale of magma intrusion. Combining this with evidence from geological surveys, we also estimate the ratio of intruded to extruded magmatic material at Medicine Lake Volcano.

## 4.2 Model Setup

Here we describe the modelling approach used to investigate the long-term volumetric effects of cooling and crystallisation (Fig. 4.1a). We assume the case of heat loss by conduction only, but the effects of convection are tested in Sect. 4.5. The model is constrained by geometrical inputs from geodetic inversions, compositional inputs from petrology, and uses a quasi 3D finite-difference numerical scheme as described by Annen et al. (2008). This setup has been compared and benchmarked against Carslaw and Jaeger (1959) 1D analytical model of conductive heat loss. The non-variable model inputs used in this study are given in Table 4.2.

The model quantifies the temperature, crystal fraction and resulting volume change of an intrusion that cools by conduction (Annen et al. 2008). The intrusion and surrounding country rock are discretised in 2D and represented by a grid of square cells, each of which is characterised by a temperature and melt fraction (Fig. 4.1b). The initial temperature of the country rock is defined by a geothermal gradient, and intrusion occurs at time  $t = 0$  with melt at the liquidus temperature. Calculations for the evolving temperature and melt fraction are then performed in cylindrical coordinates, with the 2D domain representing a slice of the axisymmetric 3D system. Boundary conditions are set such that the thermal anomaly is smaller than the model domain using Eq. 4.2 (Annen et al. 2008), and each simulation is run for 1000 years.

As the intrusion cools it decreases in volume. The rate of volume change is dependent on the density of the material, the ratio between the solid and liquid

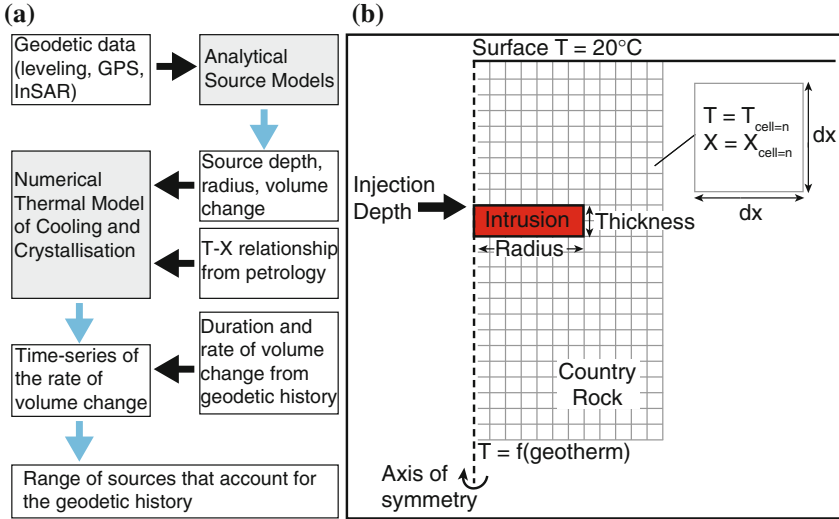


**Fig. 4.1** a Flowchart summarising the combined geodetic and thermal modelling approach. Inputs are shown by black arrow and outputs are shown by blue arrows. T–X relationships are temperature–melt fraction relationships. b Schematic of thermal model setup after Annen et al. (2008)

**Table 4.2** Non variable inputs for thermal modelling

Parameter	Symbol	Value	Reference
Thermal conductivity	$K$	2 W/mK	Robertson (1988)
Specific heat	$c_p$	1000 J/kg K	Robertson (1988)
Latent heat	$L$	$4 \times 10^5$ J/kg	Bohrson and Spera (2001)
Width of domain		10 km	
Top depth of domain		1 km	
Bottom depth of domain		20 km	
Grid size		10 m	

phases, the volume and composition of magma, the thermal state of the crust, and the amount of heat released during crystallisation (Philpotts 1990; Caricchi et al. 2014). These are calculated by first solving the time-dependent heat equation for conduction in a solid medium:

$$\rho c_p \frac{\partial T}{\partial t} + \rho L \frac{\partial X}{\partial t} = K \nabla^2 T, \quad (4.4)$$

where  $\rho$  is magma density,  $c_p$  is magma heat capacity,  $T$  is temperature,  $X$  is melt fraction,  $t$  is time, and  $K$  is temperature dependent thermal conductivity. Conductivities are taken from Robertson (1988), and the relationship between  $T$  and  $K$  is inferred from diffusivity such that  $K$  decreases as  $T$  increases (Whittington et al. 2009).

The second term in the equation describes latent heat,  $L$ , released during crystallisation and requires knowledge of the relationship between the temperature ( $T$ ) and melt fraction ( $X$ ) of the intruded magma (Annen 2009).  $T$ - $X$  measurements are made during phase equilibria experiments, which show that different minerals crystallise from the magma over different temperature ranges, causing the crystal assemblage to vary over time. Direct measurements of  $X$  are restricted to mid-high values (e.g.  $0.96 > X > 0.44$ : Grove et al. 1997), and solidus and liquidus temperatures are therefore inferred from Piwinski and Wyllie (1968); Holloway and Burnham (1972); Green (1973); Whitney (1988) and Baumgartner et al. (2007).  $T$ - $X$  relationships may be non-linear, produced by interpolating between values of  $X$  measured at discrete temperature intervals, or parameterised as linear functions by, for example, collating experimental datasets (e.g. Petford and Gallagher 2001). Here we assume that the country rock has the same composition as the magma, and therefore absorbs latent heat resulting in melting according to the same  $T$ - $X$  relationship (Annen et al. 2008). This accounts for possible buffering effects of wall rock partial melting (e.g. Huppert and Sparks 1988). For simplicity, calculations are performed for a two-phase system (crystals and melt). We therefore assume that the magma is volatile undersaturated or continuously degassing, but the implications of this assumption are discussed in Sect. 4.5.

The intrusion geometry is parameterised in terms of a depth, radius and thickness (Fig. 4.1b), and may be constrained by best-fitting analytical models to geodetic datasets (Fig. 4.1a). These analytical source models can be used to distinguish between dyke-like (i.e. vertically elongate) or sill-like (i.e. horizontally elongate) deformation sources. Sill-like intrusions may be modelled as rectangular (Okada 1985) or circular (Fialko et al. 2001a), and yield the depth, plus the length and width or radius of the source.

Whilst analytical models provide estimates of subsurface volume change, they do not constrain the initial volume, and therefore the thickness, of the intrusion. Experimental and field datasets imply that the aspect ratio (length/thickness) of sills is  $< 1000$  (e.g. Valentine and Krogh 2006; Galland et al. 2007; Menand and Phillips 2007), and that the relationship between intrusion thickness ( $h$ ) and length ( $L$ ) can be described using the power law  $h = 0.12L^{0.88}$  (Cruden and McCaffrey 2002). Where  $h$  is large, it is likely that the thickness of the body is built up by the amalgamation of small magma sheets (Habert and De Saint-Blanquat 2004; Annen et al. 2015), although this must occur over short enough time-scales for the intrusion to remain molten (Annen et al. 2008). This implies that the whole intrusion behaves and deforms as a single entity (Michaut 2011). Therefore throughout this study, the thickness we refer to is considered to be an “effective” intrusion thickness, and may in fact represent a body that has accumulated by more than one magma pulse, or a body that is built up by a distributed network of sills. We further test the effects of incrementally accreted magma intrusions in Sect. 4.5.

### 4.3 Results

We first investigate the model outputs - time-series of temperature, melt fraction and rate of volume change - using an example intrusion with thickness,  $h$ , 200 m, and radius,  $r$ , 2 km. Injection occurs at a depth of 9.5 km into country rock that is characterised by a linear geothermal gradient of  $40^{\circ}\text{C}/\text{km}$ . The melt is andesitic in composition and crystallises according to a non-linear T-X relationship from Grove et al. (1997) (Fig. 4.2). Comparing the time-series to a corresponding phase appearance sequence, plus outputs produced using a linear T-X relationship, we investigate the influence of the changing crystal assemblage upon the rate of volume change (and therefore surface deformation).

Using the same model inputs, we then explore the model parameter space by performing one-at-a-time sensitivity tests. We vary the intrusion geometry and starting composition, and evaluate the effects upon the magnitude and time-scales of surface deformation resulting from cooling and crystallisation.

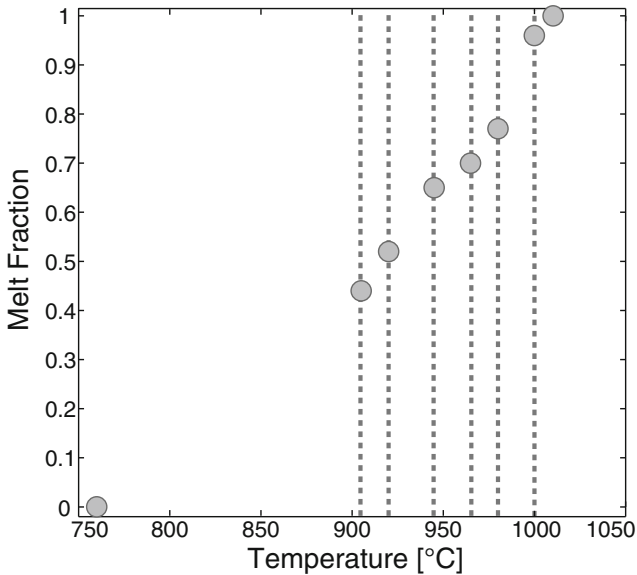


**Fig. 4.2** T-X relationship for andesite used in parameter experiments and to investigate the evolving crystal assemblage during cooling. *Dashed lines* mark experimentally determined melt fractions from (Grove et al. 1997). Solidus and liquidus temperatures are inferred from Piwinski and Wyllie (1968); Whitney (1988)

### 4.3.1 Evolving Crystal Assemblage

The andesite we use has a solidus temperature of 760 °C and liquidus temperature of 1010 °C (Piwinskii and Wyllie 1968; Whitney 1988). Whilst the linear T–X relationship is produced by linearly interpolating between these values, the non-linear T–X relationship is derived from measurements of X made at 6 temperatures between 1000 and 905 °C (Grove et al. 1997) (Fig. 4.2), at which times the mineral assemblage was also recorded. At the highest temperature experiments (T = 1000 °C, X = 0.96) olivine and high-Ca pyroxene were present in the crystallising assemblage. By 980 °C (X = 0.77) the assemblage contained four phases: olivine + amphibole + hi-Ca pyroxene + plagioclase. At ~965 °C (X = 0.70) hi-Ca pyroxene disappeared from the crystallising assemblage as it reacted with liquid to produce amphibole. Olivine was then removed from the assemblage as it also reacted to produce amphibole, and the lowest temperature experiments (905 °C, X = 0.44) contained amphibole, plagioclase and spinel (Fig. 4.3).

Using a linear T–X relationship results in smoother variations in melt fraction with changing temperature (Fig. 4.3). The largest discrepancies between the two models occur at the intrusion centre, where the linear T–X relationship yields melt fractions that are up to 15% greater than those for the non-linear case. Overall the rate of volume change output at each time-step is comparable between the two models (Fig. 4.3). However, whereas for a linear T–X relationship, variations in the rate of volume change are smooth, the time-series produced using the non-linear T–X relationship can be split into 4 time periods (Fig. 4.3), which correspond to the changes in mineral assemblage described above.

- Stage 1: During this stage the dominant effect is of cooling at the intrusion margin. At time  $t = 0$ , injection occurs at the liquidus temperature (1010 °C) resulting in a significant temperature contrast (> 600 °C) between the intrusion contact and the country rock. Initially the melt fraction at the margin decreases rapidly from 1 to 0.3, resulting in a large peak in the rate of volume change. As the surrounding country rock heats up, the temperature contrast reduces by >200 °C, and the country rock becomes a more effective insulator (Whittington et al. 2009), reducing the rate of crystallisation at the intrusion margin. This results in a decrease in the rate of volume change. Throughout this stage, the mean melt fraction reduces by <20%, and the temperature at the centre of the intrusion remains at the liquidus. For the example in Fig. 4.3, Stage 1 lasts <50 years (Fig. 4.3).
- Stage 2: At the onset of the second stage, the temperature at the intrusion centre falls below the liquidus, and the intrusion centre begins to crystallise. However, the mean temperature of the intrusion decreases below the range over which high-Ca pyroxene crystallises (~945 °C), causing a decrease in the mean rate of crystallisation. Crystallisation at the intrusion margin also slows down, and overall the result is a decrease in the rate of volume change. For the example shown, Stage 2 is complete ~100 years after intrusion.
- Stage 3: At the onset of the third stage, olivine and high-Ca pyroxene continue to crystallise from the melt at the intrusion center, but the mean temperature of the

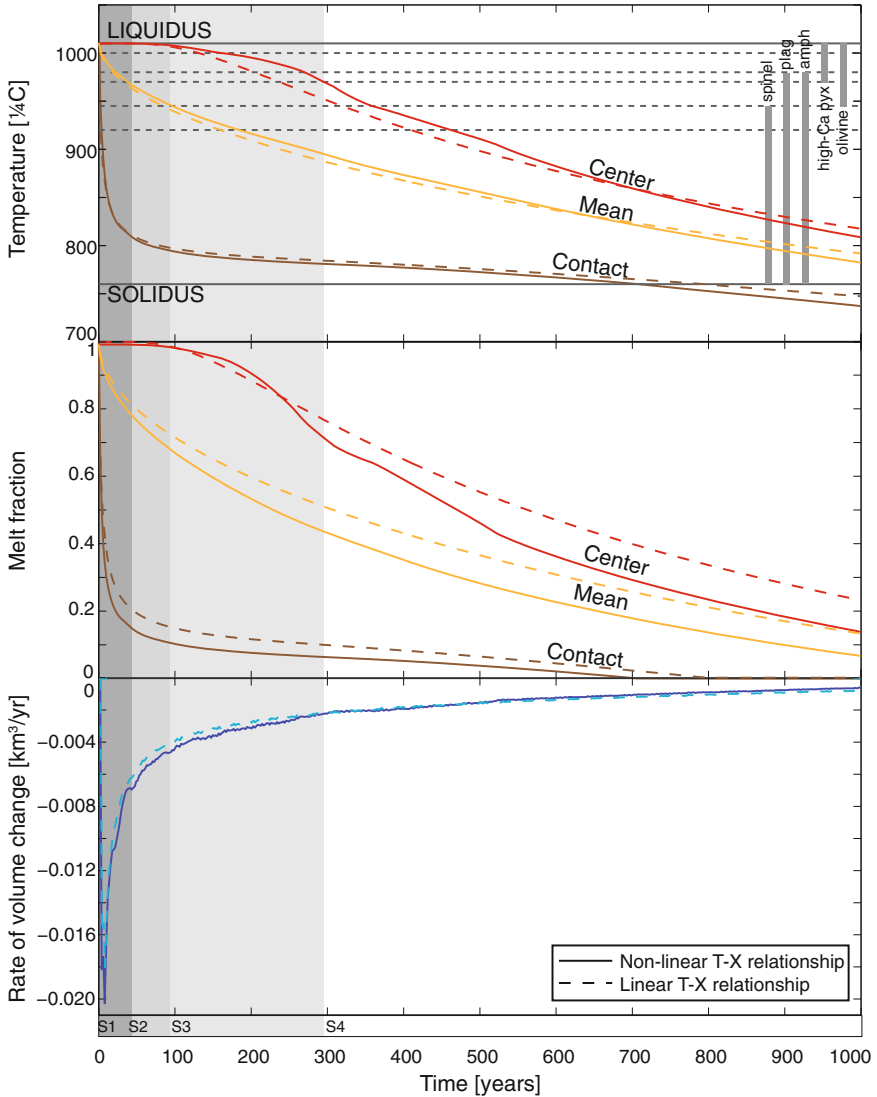


**Fig. 4.3** Time-series of temperature ( $T$ ) and melt fraction ( $X$ ) measured at the intrusion contact, intrusion centre, and the mean for the whole intrusion. *Solid* and *dashed* time-series are produced using non-linear and linear  $T$ - $X$  relationships respectively. *Dashed horizontal lines* correspond to temperatures used to derive the  $T$ - $X$  relationship and *vertical grey bars* mark the assemblage of the glass at those temperatures (Grove et al. 1997). Solidus and liquidus temperatures (inferred from Piwinski and Wyllie (1968); Whitney (1988)) are marked by *solid lines*. The time-series of the rate of volume change can be split into 4 stages (shown by the time-line) corresponding to changes in the composition of the melt. Each stage is described in the text



melt decreases below the range over which olivine crystallises ( $\sim 920^\circ\text{C}$ ), causing a further decrease in the rate of crystallisation. During this stage, the mean melt fraction decreases from 0.7 to 0.4, but the melt fraction at the intrusion margin remains almost constant as the temperature approaches the solidus. The result is a further decrease in the rate of volume change, but at a more gradual rate than that observed during Stage 2. For the example shown, Stage 3 is complete by 300 years after intrusion.

- Stage 4: At the onset of the fourth stage, the temperature at the centre of the intrusion reaches  $\sim 945^\circ\text{C}$ , and high-Ca pyx therefore ceases to crystallise from any of the remaining melt. By the end of the simulation, olivine also no longer crystallises from the melt and thus the remaining assemblage consists of plagioclase, amphibole and spinel. During this period, the rate of temperature change throughout the intrusion slows down, the mean melt fraction decreases steadily by  $>50\%$  from  $\sim 0.45$  to  $\sim 0.1$ , and the temperature at the contact falls below the solidus as the intrusion margin becomes completely solidified. The result of this is a further decrease in the rate of volume change, at a more gradual rate than that observed during Stages 2 and 3.

### 4.3.2 Parameter Space Exploration

The intrusion geometry is changed by (a) varying the intrusion aspect ratio (radius/thickness); and (b) varying the temperature contrast between the intrusion and the country rock at time  $t = 0$ . In each case we find the best fitting exponential to describe the time-series of the rate of volume change:

$$\frac{dV}{dt} = A_0 e^{\lambda_1 t} + B_0 e^{\lambda_2 t}, \quad (4.5)$$

and compare the coefficients  $A_0$ ,  $B_0$ ,  $\lambda_1$  and  $\lambda_2$ , which are found by non-linear inversion. Two terms are required to describe both the large initial variations in the rate of volume change (Stages 1–3: Fig. 4.3), and the gradual decrease in the rate of volume change (Stage 4: Fig. 4.3). The larger the coefficients  $A_0$ ,  $B_0$ , the larger the initial rate of volume change, and the smaller the decay constants  $\lambda_1$  and  $\lambda_2$ , the longer the time-scale of cooling and crystallisation.

We then compare the use of three different T–X relationships for magmas of different composition (basalt, andesite, dacite) to investigate the effects of the starting melt composition. These experiments are summarised in Tables 4.3, and 4.4.

#### Geometrical Variables

The intrusion aspect ratio ( $r/h$ ) is varied between 5 and 25 by either increasing intrusion radius,  $r$ , (Fig. 4.4a) or decreasing intrusion thickness,  $h$  (Fig. 4.4b). This range of aspect ratios is in agreement with experimental and field data, which suggest values between  $<10 - 1000$  (Riddick and Schmidt 2011). In both cases an aspect

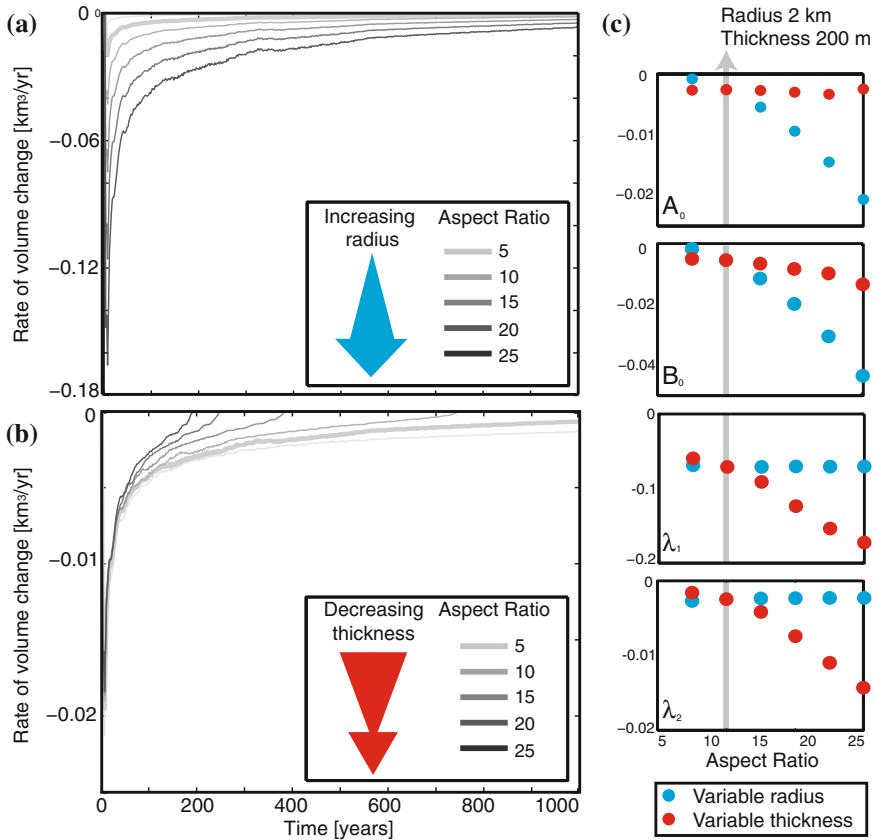


**Fig. 4.4** Parameter experiments: intrusion aspect ratio. **a** Time-series of the rate of volume change for intrusions with fixed thickness (200 m) and variable radius. **b** Time-series of the rate of volume change for intrusions with fixed radius (2 km) and variable radius. The time-series for an intrusion with aspect ratio = 10 is shown in bold in both **a** and **b**. **c** Comparison between the coefficients of exponential decay (Eq. 4.4) for intrusions of different aspect ratio. The grey lines mark an aspect ratio of 10

ratio of 10 is equal to an intrusion with  $r = 2$  km and  $h = 200$  m. Cooling immediately after injection is dependent upon the surface area of the intrusion: the larger the surface area, the more rapid heat transfer to the country rock will be and therefore the faster the rate of cooling and crystallisation. The terms  $A_0$  and  $B_0$ , which describe the initial rate of volume change, therefore relate to the surface area,  $A$ , of the intrusion that is in contact with the country rock at time  $t = 0$ . As  $A \propto r^2 + rh$ ,  $A_0$  and  $B_0$  are most sensitive to changes in aspect ratio caused by varying the intrusion radius ( $r$ ) rather than intrusion thickness ( $h$ ) (Fig. 4.4c).

As cooling progresses, most heat is transferred in the direction normal to the largest dimension of the intrusion (Annen et al. 2008). Therefore the thicker the intrusion, the longer it will take to solidify. Accordingly the constants  $\lambda_1$  and  $\lambda_2$ ,

**Table 4.3** Parameter experiments: summary of geometrical variables used

Aspect ratio	Fixed radius (m)	Thickness <sup>a</sup> (m)	Fixed thickness (m)	Radius (m)
5	2000	400	200	1000
10	2000	200	200	2000
15	2000	130	200	3000
20	2000	100	200	4000
25	2000	80	200	5000
30	2000	70	200	6000
$\Delta T$ at $t = 0^\circ\text{C}$	Fixed depth (km)	Geotherm ( $^\circ\text{C}/\text{km}$ )	Fixed geotherm ( $^\circ\text{C}/\text{km}$ )	Depth <sup>a</sup> (km)
772.5	9.5	25	40	5.95
725	9.5	30	40	7.13
677.5	9.5	35	40	8.30
630	9.5	40	40	9.50
582.5	9.5	45	40	10.69
535	9.5	50	40	11.88

<sup>a</sup>Thickness/depths are rounded to the nearest multiple of 10 in accordance with the model grid size

**Table 4.4** Parameter experiments: summary of petrological variables used

Composition	T-X Experiments	Solidus	Density <sup>a</sup> ( $\text{kg}/\text{m}^3$ )
Basalt (Medicine Lake Volcano) SiO <sub>2</sub> 50.0 to 56.1 wt.%	1.0 > X > 0.53 Wagner et al. (1995)	Holloway and Burnham (1972), Green (1973)	2900
Andesite (Medicine Lake Volcano) SiO <sub>2</sub> 50.0 to 62.8 wt.%	0.96 > X > 0.44 Grove et al. (1997)	Piwinskii and Wyllie (1968), Whitney (1988)	2700
Dacite (Volcán San Pedro) SiO <sub>2</sub> 66 wt.%	0.97 > X > 0.67 Costa et al. (2004)	Baumgartner et al. (2007)	2600

<sup>a</sup>From Lange (1994)

which describe the decay of the rate of volume change over time, are sensitive to changes in intrusion thickness rather than changes in intrusion radius (Fig. 4.4c). The time-scales of surface deformation resulting from cooling and crystallising intrusions are therefore significantly dependent upon intrusion thickness, whereas initial rates are a function of intrusion radius.

The initial temperature contrast between the intrusion and country rock is varied between 725 and 535°C by changing the intrusion depth or the geothermal gradient, which for this experiment is assumed to be linear. For the first set of experiments the intrusion depth is fixed to 9.5 km and the geothermal gradient is varied between 25°C/km (representative for continental crust interiors) to 50°C/km (Fig. 4.5a), which is comparable to the geothermal gradient in the Cascades (Blackwell et al. 1982; Rothstein and Manning 2003). We then fix the geothermal

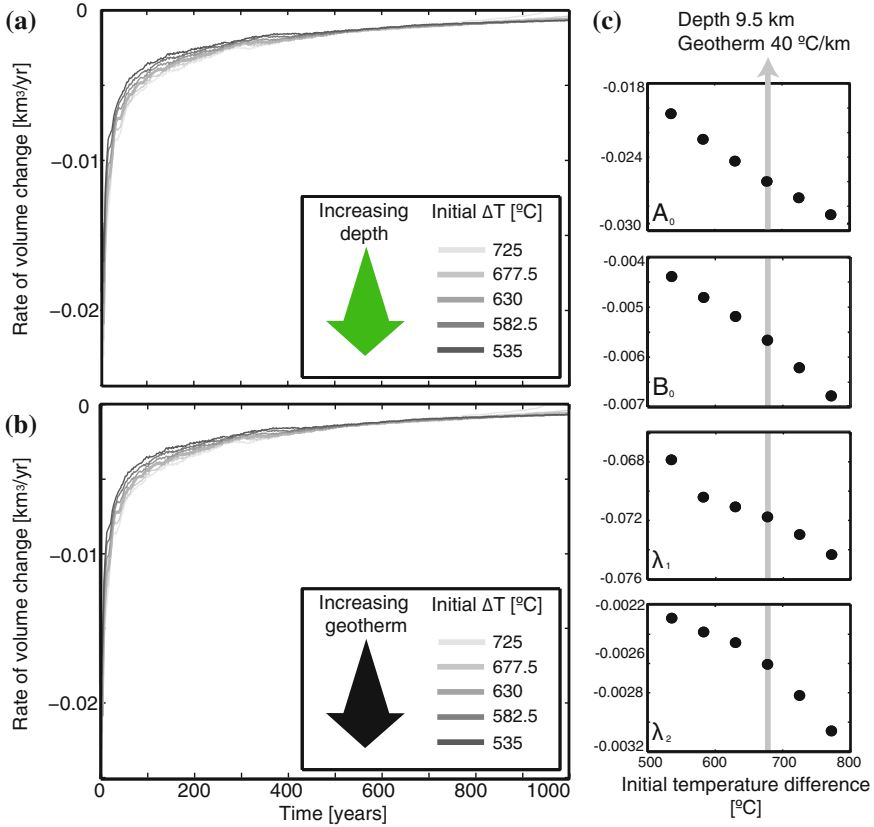


**Fig. 4.5** Parameter experiments: initial temperature contrast between intrusion and country rock. **a** Time-series of the rate of volume change for intrusions with variable depth. **b** Time-series of the rate of volume change for intrusions emplaced in country rock with variable geothermal gradient. Both **a** and **b** are for an intrusion with fixed radius (2 km) and thickness (20 m). **c** Comparison between the coefficients of exponential decay (Eq. 4.4) for intrusions with different initial temperature contrast. The grey lines mark an initial temperature contrast of 630 °C

gradient to a median value of 40 °C/km, and vary the intrusion depth between 5.95 and 11.88 km (Fig. 4.5b). In both cases an initial temperature contrast of 630 °C occurs when the injection takes place at 9.5 km depth into country rock with geothermal gradient 40 °C/km.

Changing the initial temperature contrast by either varying the geothermal gradient or the intrusion depth has the same effect upon cooling of the intrusion (Fig. 4.5a, b). Larger initial temperature contrasts (shallower emplacement depths and smaller geothermal gradients) result in rapid cooling, with larger initial rates of volume change and hence larger values of  $A_0$  and  $B_0$  (Fig. 4.5c). As the intrusion cools down quickly, the time to reach complete solidification is shorter and therefore the decay constants  $\lambda_1$  and  $\lambda_2$  are larger (Fig. 4.5c). Conversely, small initial temperature con-

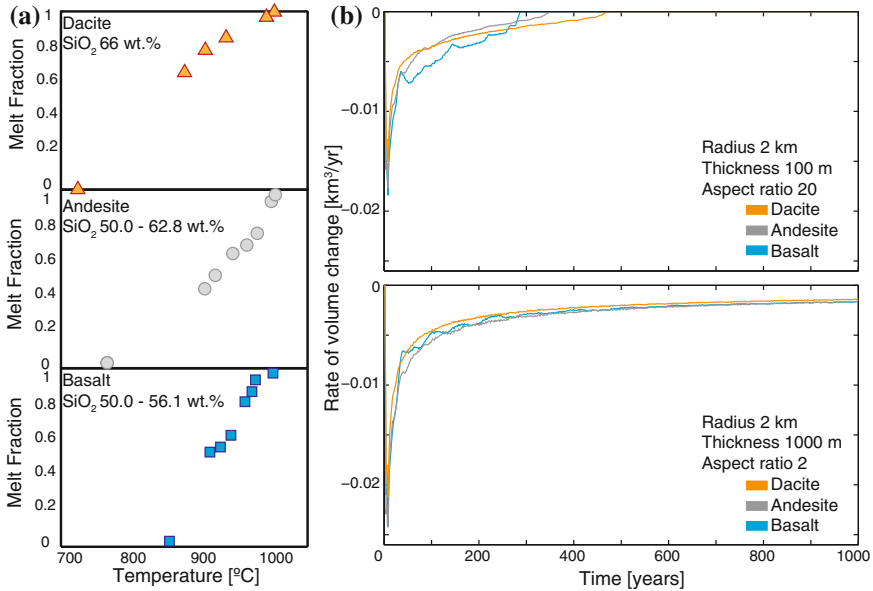


**Fig. 4.6** **a** T–X relationships for the three magma compositions listed in Table 4.4. Dacite is from Volcán San Pedro, Chile (Costa et al. 2004), and basalt and andesite are from Medicine Lake Volcano, CA (Wagner et al. 1995; Grove et al. 1997). **b** Comparison between time-series of the rate of volume change for intrusions of different initial composition and two different thicknesses. Results are labelled with the intrusion radius, thickness and aspect ratio

trasts result in smaller initial volume changes (lower values of  $A_0$  and  $B_0$ ) and longer cooling times (smaller values of  $\lambda_1$  and  $\lambda_2$ ). These results suggest that intrusions located at greater depths or in regions with higher geothermal gradients (such as extensional rifts: Turcotte and Schubert 1982) are likely to exhibit subsidence of a smaller magnitude over a longer time-scale, whereas intrusions located at shallow depths are likely to undergo larger rates of subsidence for shorter amounts of time.

### Petrological Variables

We compare the effect of the starting magma composition using three sets of pre-existing T–X data for melts with varying initial silica ( $\text{SiO}_2$ ) content. These are basalt (50.0–56.1 wt.%  $\text{SiO}_2$ ; Wagner et al. 1995) and andesite (50.0–62.8 wt.%  $\text{SiO}_2$ ; Grove et al. 1997) from lavas erupted at Medicine Lake Volcano, California, and dacite (66 wt.%  $\text{SiO}_2$ ; Costa et al. 2004) from lavas erupted at Volcán San Pedro, Chilean Andes (Table 4.4). All T–X relationships are non-linear (Fig. 4.6a).

Mafic magmas (basaltic) are higher temperature than intermediate or felsic magmas (andesitic or dacitic), and therefore have higher solidus and liquidus temperatures (Fig. 4.6a). As each intrusion is injected at the liquidus temperature, this means there is a greater initial temperature contrast between a mafic intrusion and the surrounding country rock. As was observed in Sect. 4.3.2, this results in more rapid cooling

and crystallisation (Fig. 4.6b). This is consistent with previous comparisons between basaltic and granitic melts, which found that the basaltic melt cooled rapidly whereas, after an initial high value, the mean temperature of the granitic melt remained fairly constant (Petford and Gallagher 2001).

The effect of differing solidus and liquidus temperatures is amplified when decreases in melt fraction occur at the highest rate, either during the earliest stages of cooling (Stage 1: Fig. 4.3), or for sills with a large aspect ratio (Sect. 4.3.2). We therefore look at the effects of composition for two sill geometries with aspect ratios that differ by a factor of 10 (Fig. 4.6b). For the high aspect ratio intrusion, the most mafic composition (basalt) results in larger initial rates of volume change, with the intrusion reaching complete solidification more quickly than for an andesitic or dacitic composition. For the low aspect ratio intrusion, the long-term rates of volume change (Stage 4: Fig. 4.3) are comparable (within 2%) between magmas of different composition (Fig. 4.6b). This suggests that over short time-scales, or for sills with high aspect ratio, surface deformation due to cooling and crystallisation is variable between magmas of different compositions, but over longer time-scales, the effects of composition are less.

## 4.4 Application to Medicine Lake Volcano

As described in Chap. 2, Medicine Lake Volcano is a broad shield volcano located at the southern end of the Cascades Volcanic Arc. Subsidence of the edifice is centred on the  $7 \times 12$  km caldera (Fig. 4.7) and extends over 10 km from the volcano summit (Dzurisin et al. 1991). To account for the spatial wavelength of the signal, geodetic datasets suggest that the deformation source lies at  $>6$  km depth (Dzurisin et al. 2002; Poland et al. 2006; Parker et al. 2014). Gravity, electrical and magnetic studies show that at these depths the edifice is underlain by an intrusive complex of sills and dykes rather than a central magma chamber (Finn and Williams 1982; Zucca et al. 1986; Fuis et al. 1987; Lowenstern et al. 2003). Seismic tomography studies indicate that a subsolidus pluton could be present within this intrusive column (Ritter and Evans 1997), and also detect a small, shallow reservoir at 1–7 km depth associated with the most recent eruption  $\sim 1$  ka at Glass Mountain (Evans and Zucca 1998).

Medicine Lake Volcano has been prospected as a source of geothermal energy since the 1980s (Iovenetti and Hill 1997). The summit caldera is associated with a  $10 \times 7$  km thermal anomaly (Fig. 4.7), and alteration mineralogy indicates the presence of a high temperature (300 °C) geothermal system (Hulen and Lutz 1999; Bargar 2001). The heat source driving geothermal activity is thought to be the small, shallow reservoir beneath Glass Mountain or basalt intruded in late Holocene times. (Donnelly-Nolan et al. 1990).

Given the intrusive subsurface environment and active geothermal system, past geodetic studies at Medicine Lake Volcano identify cooling and crystallisation of magmatic material as a possible cause of volume loss at depth (Dzurisin et al. 2002; Poland et al. 2006; Parker et al. 2014). In an assessment of leveling surveys between

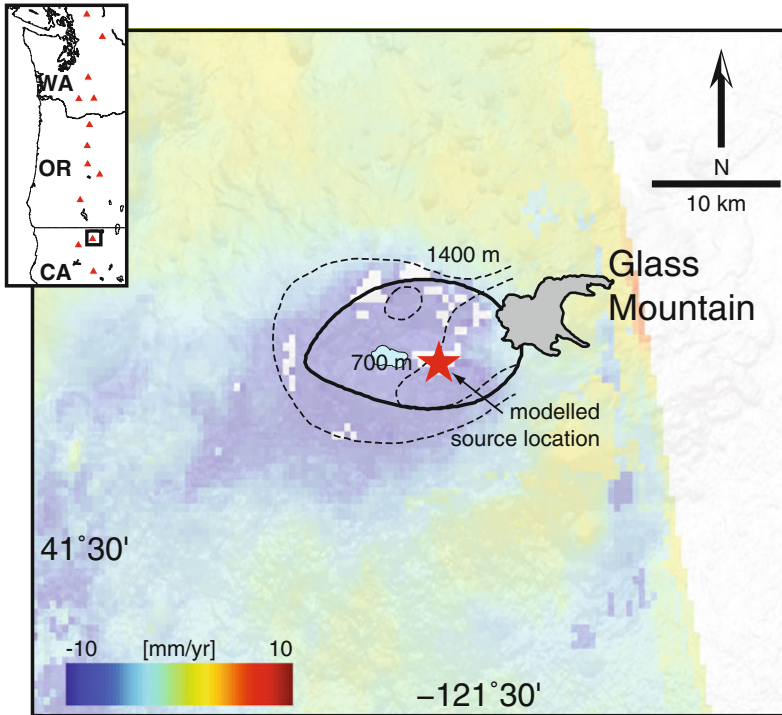


**Fig. 4.7** Rate-map from ALOS covering 2007–2011 (Parker et al. 2014, Chap. 2) showing subsidence of Medicine Lake Volcano. The caldera outline is shown by the *black line*, with *dashed lines* showing the top of the hydrothermal system from Iovenetti and Hill (1997). Lava flows of the most recent eruption (Glass Mountain) are shown in *grey* (Donnelly-Nolan et al. 2007). The *star* shows the location of the best fitting analytical source model used to constrain the thermal model. *Inset* map of the western US, with *red triangles* showing the Cascade volcanoes. Medicine Lake Volcano is shown by the *black rectangle*

1954 and 1999, Dzurisin et al. (2002) use Eq. 4.1 and CONFLOW (Mastin and Ghiorsio 2000) to calculate the volume change due to cooling and crystallisation of a small intrusive body at  $>10$  km depth. However they find that this requires either an unrealistically large initial volume ( $\gg 10 \text{ km}^3$ ), or an unrealistically rapid rate of crystallisation ( $>1\%$  per year). Poland et al. (2006) combine leveling measurements, campaign GPS data collected between 1996 and 2004, and a finite-element model, to quantify subsidence due to cooling of the larger, vertically elongate intrusive complex over a 10,000 year time period. However, this source geometry does not predict the high ratio of vertical to horizontal displacements observed at the volcano (Poland et al. 2006).

The eruptive style of Medicine Lake Volcano is strongly influenced by Basin and Range extension (Donnelly-Nolan et al. 2008). Eruptions are typically via fissures, with ground cracks and eruptive vents aligned perpendicular to the direction of least

compressive stress (E-W) (Donnelly-Nolan et al. 2008). Under this stress regime magma transport is likely to occur via vertical dykes. However analytical models to different geodetic datasets all infer that the deformation source at Medicine Lake Volcano is horizontally elongate (Dzurisin et al. 2002; Poland et al. 2006; Parker et al. 2014). It is therefore likely that magmatic material initially propagated vertically as a dyke before reaching a rigidity contrast (Kavanagh et al. 2006; Menand 2008), lithological contact (Kavanagh and Pavier 2014) or stress boundary (Gudmundsson 2011) and propagating laterally to form a sill. This mechanism of magma transport is inferred in other extensional environments such as East Africa, where continental rifting is accommodated by the emplacement of vertical dykes (Wright et al. 2006), but deformation measured at volcanic centres is mostly vertical (Biggs et al. 2011) implying horizontally orientated sources.

Here we use a similar approach to Dzurisin et al. (2002), applying our modelling approach to cooling and crystallisation of a sill at depth. We do not aim to model the small Glass Mountain reservoir eruption, as this is linked to depths shallower than 6 km (Grove et al. 1997), rather we aim to investigate comparable intrusive activity that may be associated with this thermal input into the system.

#### 4.4.1 Model Constraints

The intrusion geometry is inferred from inversions of InSAR data (Parker et al. 2014; Chap. 2), which suggest that the source is located at 9–10 km depth. The source is orientated horizontally to reproduce the large ratio of vertical to horizontal displacements as observed by comparing leveling and GPS measurements (Poland et al. 2006), or interferograms from multiple satellite tracks (Parker et al. 2014). Circular and rectangular sources with radius/length up to 2 km fit the data to within 1% and consequently we run simulations with radius = 1000, 1250, 1500, 1750, 2000 m.

The initial volume (and therefore thickness) of the source is not parameterised in analytical models, as geodetic observations provide measurements of relative volume change rather than absolute subsurface volumes. However, the initial volume can be constrained using evidence from the most recent eruptive products at Glass Mountain, which are thought to be produced by fractional crystallisation of andesite and crustal melting (Grove et al. 1997). The amount of heat required to generate the crustal component of these lavas implies magma volumes of 2–2.5 km<sup>3</sup> (Grove et al. 1997), which we use as a realistic upper bound upon the initial volume of melt. We then use T–X relationships measured from andesitic melt inclusions within these erupted products (Andesite: Fig. 4.6a), linking the model to the most recent known magmatic inputs to the Medicine Lake Volcano system (Grove et al. 1997).

The initial temperature of the country rock is defined by a non linear, steady state geothermal gradient (Turcotte and Schubert 1982):

$$T(z) = T_o + \frac{q_o}{k}z - \frac{A}{zk}z^2, \quad (4.6)$$



which is a function of the surface temperature,  $T_o$ , (approximated to be 20°C), conductivity,  $k$ , (Table 4.2), depth,  $z$ , and radiogenic heat production for continental crust,  $A$ , ( $2.9 \times 10^{-6} \text{ W/m}^3$ ; Wollenberg and Smith 1987).  $q_o$  is the surface heat flow and is the product of conductivity and the surface geotherm, (estimated to be 45°C/km in the Cascades: Blackwell et al. 1982; Rothstein and Manning 2003). Other model inputs are as defined in Table 4.2. Each simulation is run for 1000 years, which is representative of the time since the last eruption.

#### 4.4.2 Comparison to the Geodetic Record

In order to reproduce the ground deformation observed at Medicine Lake Volcano, an intrusion must undergo volume change at the rate, and for the duration, recorded in the geodetic history. The rate of volume change required by the geodetic observations can be derived from analytical models of circular sills, as these models are formulated such that the the volume change at depth is equivalent to the surface volume change (Fialko et al. 2001a). The magnitude and spatial extent of subsidence at Medicine Lake Volcano have remained constant since the 1950s (Dzurisin et al. 2002; Poland et al. 2006; Parker et al. 2014), suggesting that this rate of volume change is applicable for the length of the geodetic record (Fig. 4.8a, b). To reproduce the deformation history, an intrusion must therefore undergo cooling such that the rate of volume change fits two criteria:

- (1) the rate of volume change is  $-0.0011$  to  $-0.0013 \text{ km}^3/\text{yr}$  (equal to the best fitting source model)
- (2) the rate of volume change remains constant for  $>65$  years (the length of the geodetic record).

Comparing the output of the thermal model to the rate of volume change predicted by Parker et al. (2014), we identify a range of sills with initial volumes  $<2.5 \text{ km}^3$  that can account for 65 years of volcano-wide subsidence at Medicine Lake Volcano at  $\sim 1 \text{ cm/yr}$  (Fig. 4.8c). These sills vary in radius between 1000 and 2000 m, and range in thickness from 150 to 800 m, with aspect ratios ( $r/h$ ) of 1–20. The smallest sill has an initial volume of  $\sim 1 \text{ km}^3$  and the largest sill has an initial volume of  $\sim 2.5 \text{ km}^3$ .

#### 4.4.3 Constraints upon Magma Intrusion at Medicine Lake Volcano

As geodetic measurements at Medicine Lake Volcano began during an extended period of ground deformation, the onset of subsidence and therefore the timing of possible magma intrusion is unknown. Here we show how the geodetic constraints

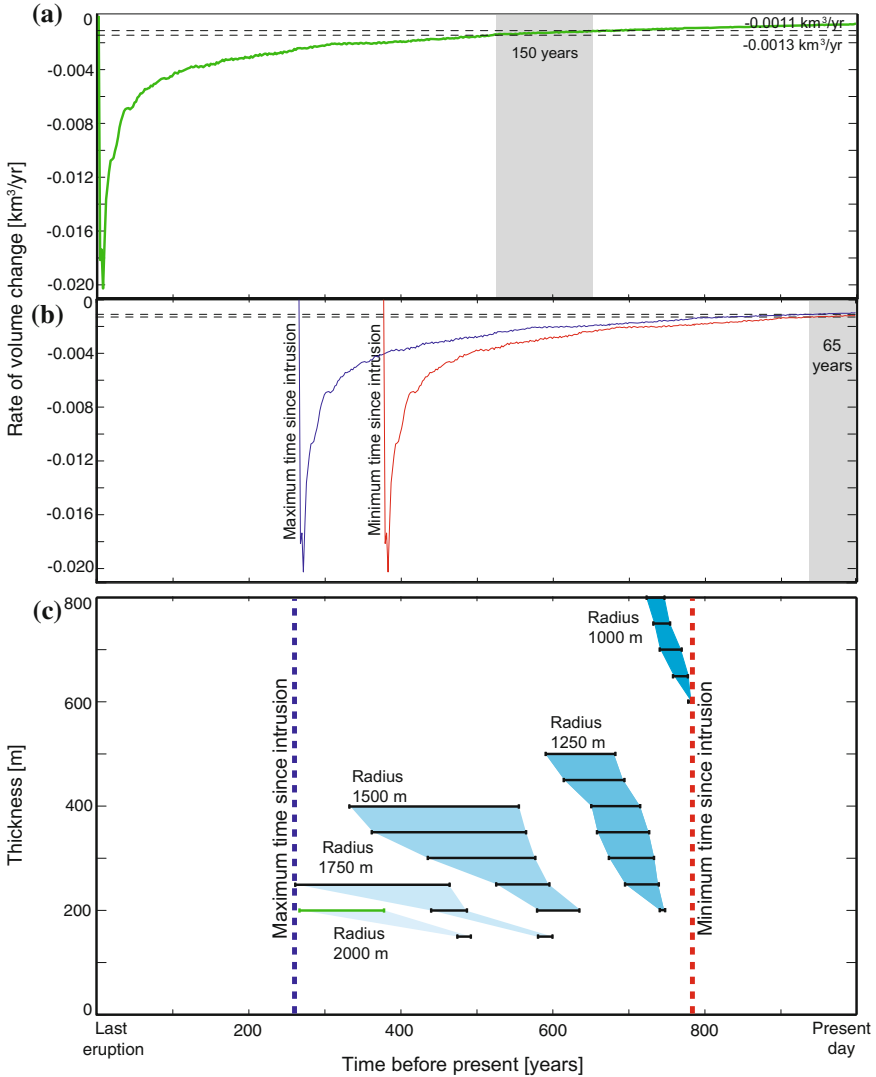
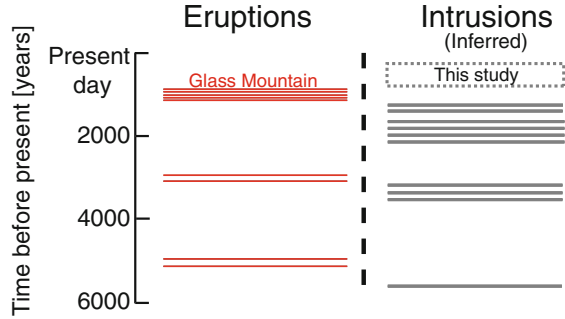


**Fig. 4.8** **a** Example of a time-series of the rate of volume change for an intrusion with radius 2000m, thickness 200 m. *Dashed lines* show the rate of volume change inferred from the analytical source models. For this example the rate of volume change is between these bounds for ~150 years. **b** The *red* time-series is the same as that in part **a** but has been shifted to show the minimum time since intrusion. The *blue* time-series has been shifted to show the maximum time since intrusion. **c** Summary of best-fitting models that fit the history of volume change at Medicine Lake Volcano. *Dashed lines* mark the minimum and maximum times since intrusion for these solutions. The *green bar* shows the intrusion with radius = 2000 m, thickness = 200 m as in parts **a** and **b**

**Fig. 4.9** Timeline of intrusions and eruptions at Medicine Lake Volcano throughout the late Holocene after Donnelly-Nolan et al. (2007). The dashed box represents the minimum and maximum time since intrusion for the best-fitting models inferred in this study



listed in Sect. 4.4.2 can be combined with the results of thermal modelling to constrain the timing of intrusion.

For each best fitting model described in Sect. 4.4.2, the rate of volume change remains between  $-0.0011$  and  $-0.0013 \text{ km}^3/\text{yr}$  for longer than the length of the geodetic record (65 years) (Fig. 4.8a). In one end-member scenario, it is possible that subsidence was ongoing prior to the first geodetic measurements, but would not be evident in any future measurements (Fig. 4.8b). This constrains the maximum time since intrusion, which we find to be up to  $\sim 750$  years before present (Fig. 4.8c). In the other end-member scenario, the rate of volume change reached its current value at the time of the first geodetic measurements in 1954, but will be ongoing at the current rate in future measurements (Fig. 4.8b). This constrains the minimum time since intrusion, which we find to be  $\sim 200$  years before present (Fig. 4.8c). In this case, the model suggests that subsidence may continue at current rates for up to  $\sim 100$  years.

These best-fitting models suggest that intrusion at Medicine Lake Volcano has occurred on the order of hundreds of years before present (Fig. 4.9). This is significant for hazard assessments at the volcano, as it implies magmatic input at Medicine Lake Volcano has occurred more recently than the time of the last eruption  $\sim 1$  ka.

At Medicine Lake Volcano, the occurrence of intrusive events unaccompanied by eruption is thought to be common, and is supported by petrological evidence from postglacial erupted products, which document multiple intrusions of mafic magma (Grove et al. 1997; Donnelly-Nolan et al. 2008). Throughout the late Holocene, Donnelly-Nolan et al. (2007) suggest at least 20 intrusive and extrusive events have occurred at Medicine Lake Volcano with an average repeat interval of 250 years (Fig. 4.9). This suggests that over 1000 years, between 1 and up to 4 intrusive events may occur. Assuming that the intruded volumes of the best-fitting models in this study ( $1\text{--}2.5 \text{ km}^3$ ) are representative, this provides an intrusion rate of  $1\text{--}10 \text{ km}^3$  per thousand years. Comparing this to estimates of the effusion rate ( $\sim 0.6\text{--}1.2 \text{ km}^3$  per thousand years; Donnelly-Nolan et al. 2008) yields intrusion-to-extrusion ratios between 0.8 and 17. These values are in agreement with intrusion-to-extrusion ratios estimated elsewhere in the Cascades (e.g. Blackwell et al. 1982; Ingebritsen et al. 1989, 1994).

## 4.5 Additional Factors

The intrusion geometry used in this study may in fact represent an intrusion that has accumulated by more than one magma pulse (Sect. 4.2). After emplacement, magma cooling will occur not only by conduction but also via convective heat transfer (e.g. Annen 2009). The resulting volume loss during cooling and crystallisation will also be influenced by degassing due to volatiles within the melt (e.g. Caricchi et al. 2014; Girona et al. 2014). Here we address each of these factors, considering how they would effect the resulting ground deformation, and whether they would change the conclusion that magma intrusion is likely to have occurred at Medicine Lake Volcano more recently than the time of the last eruption. In each case we use the model setup described in Sect. 4.4 and an intrusion with thickness = 200 m, radius = 2 km.

### 4.5.1 Incremental Magma Intrusion

Both numerical simulations and field studies suggest that magma bodies may be built up by successive intrusions of magma (de Saint-Blanquat et al. 2006; Pasquarè and Tibaldi 2007; Menand 2008; Michel et al. 2008; Annen 2009), and intrusive episodes imaged geodetically have been observed to last from weeks (e.g. Dabbahu, Afar: Wright et al. 2006) to decades (e.g. Krafla, Iceland: Sigmundsson 2006). In the case of pulsatory magmatic inputs, the cooling history of magma may be different, as initially intrusions with high aspect ratio will cool more rapidly (Sect. 4.3.2), but eventually successive intrusions act to heat up the crust, incubating the remaining melt (Michaut and Jaupart 2006; Annen et al. 2008; Annen 2009, 2011).

We test the effects of sequential magma intrusions by intruding 20 m thick magma pulses in increments of 1, 5, 10, and 20 years (Fig. 4.10a–e). In total we intrude 10 magma pulses equating to a total thickness of 200 m. Under these conditions, we find that the long-term rate of volume change (Stage 4: Fig. 4.3) for a magma body built incrementally is comparable to the case of a single intrusion (Fig. 4.10). As the interval between increments increases, the maximum time since intrusion decreases. However, the effect is relatively small (Fig. 4.10a–e), and for intrusion intervals of 20 years, the decrease is <10%. This suggests that our assumption of an “effective” intrusion thickness (Sect. 4.2) is applicable when investigating long-term subsidence, but that the interval between, and size of, magma pulses are significant parameters when considering cooling during Stages 1–3 (Fig. 4.3). The use of this modelling approach to investigate the geodetic response to incrementally accreted magma bodies is further discussed in Sect. 4.6.

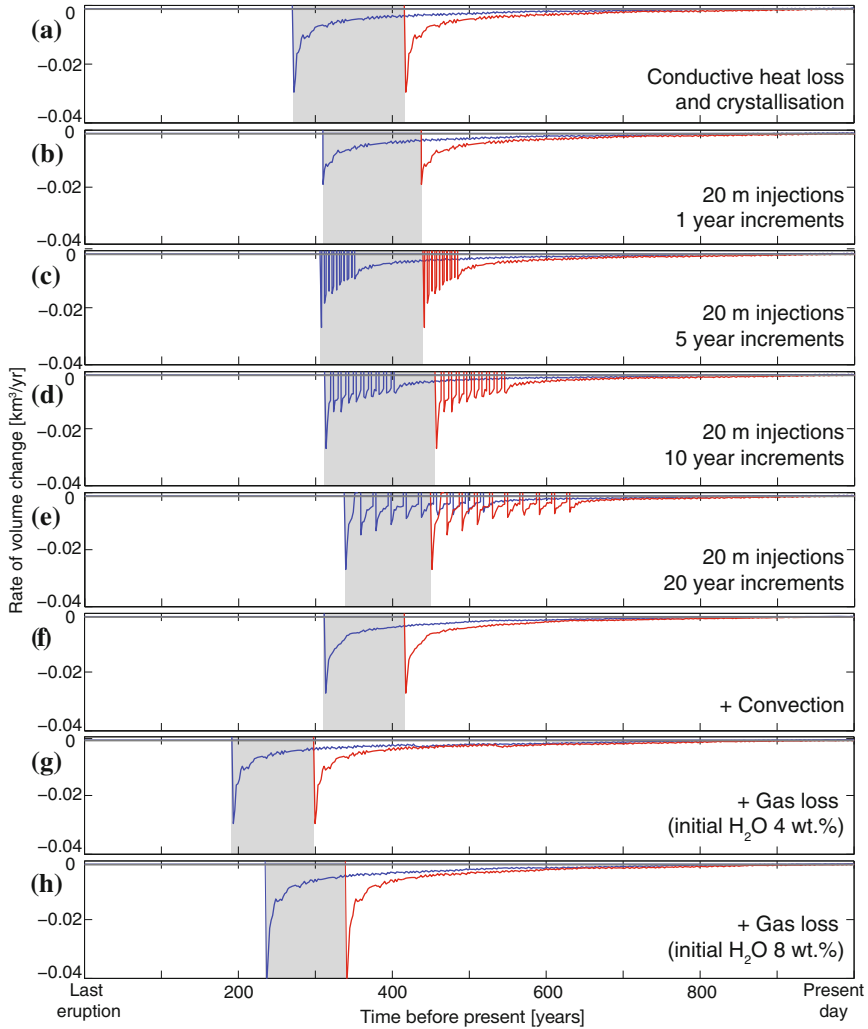


**Fig. 4.10** Time-series of the rate of volume change for an intrusion with radius = 2000 m, thickness 200 m as in Fig. 4.8. *Blue* indicates the maximum time since intrusion and *red* shows the minimum time since intrusion for the case of: **a** Conductive heat loss and crystallisation only; **b** 20 m thick magma pulses intruded at 1 year intervals; **c** 20 m thick magma pulses intruded at 5 year intervals; **d** 20 m thick magma pulses intruded at 10 year intervals; **e** 20 m thick magma pulses intruded at 20 year intervals; **f** Conductive heat loss and crystallisation plus convection; **g** Conductive heat loss and crystallisation plus gas loss for a melt with initial H<sub>2</sub>O 4 wt.%; and **h** Conductive heat loss and crystallisation plus gas loss for a melt with initial H<sub>2</sub>O 8 wt.%

### 4.5.2 Convection

Convection is an effective mechanism of heat transfer, and for melt fractions above 40–60 %, reduces the solidification time by approximately half (Worster et al. 1990). To simply test the effect of convection we double heat transfer for cells where the melt fraction exceeds 50 % and compare the rate of crystallisation and volume change to the case where heat loss occurs via conduction only (Fig. 4.10a, f). The effects of convection are most significant during the early stages of cooling when rates of crystallisation are largest. However, the efficiency of convection is limited by the ability of the surrounding country rock to conduct heat away from the intrusion (Annen 2009), which decreases as the country rock heats up over time (Whittington et al. 2009). This was observed in Stage 1 of cooling in Fig. 4.3, where rapid crystallisation at the intrusion margin slowed as the temperature contrast between the intrusion and country rock decreased. After Stage 3 (Sect. 4.3.1), when melt fractions are lower, the effects of convection are less, and for the example in Fig. 4.10, rates of volume change are within 5 % of those for the case of conduction only (Fig. 4.10a, f). The effects of convection will therefore be greatest for intrusions with larger aspect ratios, mafic compositions, or for intrusions located in colder country rock, as in each of these cases Stages 1–3 (Sect. 4.3.1) dominate the cooling history (Figs. 4.4, 4.5 and 4.6).

Heat loss by convection decreases the time it takes for an intrusion to solidify. For the application to Medicine Lake Volcano, this reduces the length of time that the rate of volume change matches that recorded in the geodetic history. This narrows the interval between the minimum and maximum time since intrusion, and suggests that intrusion may have occurred more recently than in the case for conductive heat loss only (Fig. 4.10a, f).

### 4.5.3 Gas Loss

In this study we have focused on a two phase system (crystals - melt), but during crystallisation, volatiles partition into the remaining melt, and once saturation is reached, bubbles may form allowing gas to escape (e.g. Dzurisin et al. 2002). Passive degassing of magma can reduce the pressure in shallow magma chambers by several MPa on interruptive time-scales (months - years), thereby contributing to subsidence (Girona et al. 2014). This is supported by findings at Okmok volcano, Alutians, where inter-eruptive subsidence (duration 1 year) can be explained by degassing of water vapour from a cooling injection of magma at 3–4 km depth (Caricchi et al. 2014). Gas loss is also thought to contribute to subsidence at Mount Baker, USA (Hodge and Crider 2010), Satsuma-Iwojima, Japan, and Masaya, Nicaragua (Girona et al. 2014).

We estimate the rate of volume change due to degassing at Medicine Lake Volcano using time-series of the intrusion temperature and melt fraction (see example time-

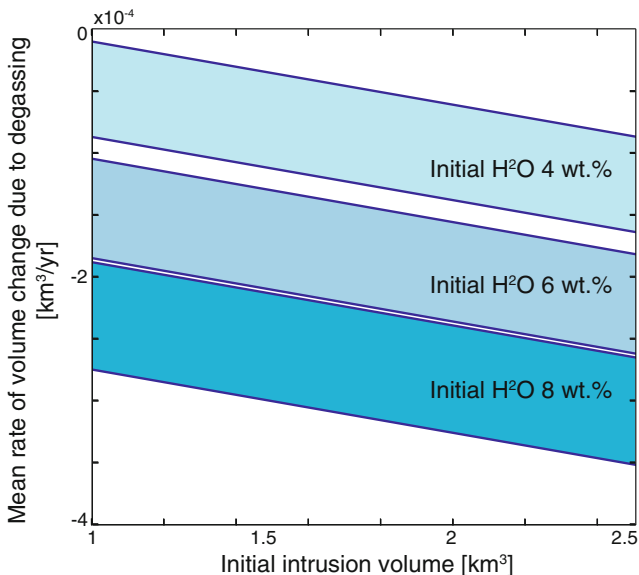


**Fig. 4.11** Mean rate of volume loss due to degassing for the best-fitting models at Medicine Lake Volcano described in Sect. 4.4.2. The rate of volume change is proportional to the initial volume of the intrusion

series in Fig. 4.3). We assume that the main gas released is H<sub>2</sub>O. The solubility of H<sub>2</sub>O in magma is dependent upon composition and pressure. Mafic magmas dissolve less gas, therefore we would expect the volume contribution from gas loss to be less for a basaltic magma (e.g. Philpotts 1990). Conversely, solubility increases with pressure (Henry's Law), as higher pressures favour more hydrous melts (e.g. Burnham 1979). We estimate the solubility of H<sub>2</sub>O using a pressure of 250 MPa (equivalent to ~9.5 km depth) and a composition consistent with that used in Sect. 4.4, which yields a solubility of 7–8% (Papale et al. 2006).

In the absence of further compositional constraints, we vary the initial H<sub>2</sub>O content of the magma from 4 wt.% (undersaturated) to 8 wt.% (saturated). We use the incremental difference in melt fraction between each time-step to calculate the amount of H<sub>2</sub>O in the melt i.e. for a change in melt fraction from 1 to 0.5, the H<sub>2</sub>O wt.% increases by a factor of 2 from 4 to 8 wt.%. If the H<sub>2</sub>O wt.% is greater than the solubility of H<sub>2</sub>O in the melt, the excess gas will be exsolved, and assuming the gas is able to escape, a volume loss will occur.

Using the mass of the remaining melt at each time-step, the H<sub>2</sub>O saturation, and the molar mass of H<sub>2</sub>O, we calculate the number of moles of gas exsolved. Combining this with the molar volume of H<sub>2</sub>O (calculated using the ideal gas law), we estimate the volume change due to degassing. This is then compared to the volume loss due to conductive cooling and crystallisation at each time-step.

As degassing contributes to subsurface volume loss, the magnitude of surface deformation is increased from the case of conductive cooling only (Fig. 4.10g, h). For the application to Medicine Lake Volcano, this implies that a smaller volume loss from cooling and crystallisation would be required to produce subsidence of 1 cm/yr. This rate of volume change would be achieved later, implying that time of intrusion had in fact occurred earlier than in the case of conductive heat loss only (Fig. 4.10g, h). For the range of best fitting models in Fig. 4.8c, the rates of volume change due to degassing are around an order of magnitude less than those obtained for cooling and crystallisation. The onset of degassing is dependent upon the initial H<sub>2</sub>O wt.% of the melt. For the lowest H<sub>2</sub>O contents (4 wt.%), degassing begins up to 700 years after intrusion. The mean rate of volume change due to degassing is proportional to the initial intrusion volume, with larger initial volumes exsolving more gas (Fig. 4.11). In reality, the presence of water would lower the liquidus temperature of the melt (e.g. Philpotts 1990), which is shown in Sect. 4.3.2 to prolong the time-scale of cooling. The ability of an intrusion to degas will also depend upon the permeability of the overburden and the presence of pathways to allow the gas to escape.

## 4.6 Discussion

Observations of ground deformation provide unique insight into episodes of magma intrusion, particularly in remote regions or in the absence of other surface manifestations of unrest. Space-based InSAR measurements have been particularly valuable in identifying intrusive events that may have otherwise gone unnoticed, providing estimates of current magma fluxes in the crust (e.g. Pritchard and Simons 2004a; Sparks et al. 2008). For example, large-scale InSAR surveys of the Aleutian arc between 1992 and 2010 provide evidence of magma intrusion at 60 % of Aleutian volcanoes (Lu and Dzurisin 2014). With the launch of new satellites, and an increase in the temporal and spatial coverage of data, it is probable that more intrusive events will be captured using InSAR. Given the high ratios of intruded to extruded material at volcanic arcs (Sect. 4.1), developing simple modelling approaches to understand how these events manifest geodetically, and quantify the length-scales and time-scales of resulting ground deformation, is a useful exercise.

By coupling an existing thermal model with petrological and geodetic constraints from Medicine Lake Volcano, we have shown that cooling and crystallisation of magmatic intrusions with volumes  $<3 \text{ km}^3$  may result in volcanic subsidence at steady rates over decadal time-scales. Exploring the thermal model parameter space, we find that (a) the early stages of volume change are most dependent upon cooling and crystallisation at the intrusion contact, which is a function of surface area and country rock temperature, and (b) changes in the rate of volume change are slower for sills of lower aspect ratio (thicker) and correspond to changes in the crystallising assemblage. In the following discussion, we identify several additional ways in which this modelling approach could be further applied to better understand the geodetic response to magma intrusions.



### 4.6.1 Further Applications

Using the case study of Medicine Lake Volcano, we have investigated a linear subsidence signal where the onset of deformation is unconstrained. In doing so we have been able to constrain the timing of intrusion and also forecast time-scales of continued surface deformation. This model could be applied to other cases of long-term volcanic subsidence (e.g. Aniackchack, Makushin, Seguam: Kwoun et al. 2006; Lu and Dzurisin 2014); for cases where past modelling approaches do not support cooling and crystallisation as a cause of deformation (e.g. Fisher Caldera: Mann and Freymueller 2003), and where better temporal constraints, such as changes in the rate of subsidence, are available (e.g. Cerro Blanco: Pritchard 2003; Pritchard and Simons 2004a). For volcanoes where no direct T–X measurements are available, we have shown that linearly interpolating between realistic solidus and liquidus values provides results that are comparable to the first order (Fig. 4.3).

In this study we have also begun to investigate the geodetic response to incrementally intruded magma bodies. This is thought to be the mechanism by which large magma bodies are built (de Saint-Blanquat et al. 2006; Pasquarè and Tibaldi 2007; Menand 2008; Michel et al. 2008; Annen 2009). By combining estimates of subsurface volume change from thermal models with analytical source models, there is scope to forward model the geodetic response to the incremental development of plutons and large magma chambers. This will help to further establish whether magmatic pulse rates suggested by modelling and field studies (Crisp 1984; Coleman et al. 2004; Matzel et al. 2006; Leuthold et al. 2012) are in agreement with geodetic inflation/deflation rates (e.g. Sparks et al. 2008).

There is an inherent link between magma intrusions and crustal rheology, as the thermal effects of magma intrusion induce changes in crustal viscosity. The geodetic model used in this study assumes an elastic rheology. Whilst this is valid for crustal material with temperatures lower than the brittle-ductile transition (300–500°C: Del Negro et al. 2009), in high-temperature environments, a viscoelastic rheology is more appropriate (e.g. Bonafede et al. 1986; Newman et al. 2001). Accounting for a viscoelastic rheology decreases crustal viscosity and Young's Modulus, reducing the pressure/volume changes required to produce measurable ground deformation (Bonafede et al. 1986; Newman et al. 2001; Del Negro et al. 2009), and increasing the magnitude of displacements by up to 3 times (Gregg et al. 2012). Viscoelastic effects also increase time-scales of surface deformation as, after the instantaneous elastic displacement, the response continues at an exponentially decreasing rate (e.g. Masterlark 2007; Segall 2010).

Consequently, both analytical models (Dragoni and Magnanensi 1989; Segall 2010; Parks et al. 2015) and finite-element models (Masterlark et al. 2010; Hickey et al. 2013) have been used to assess how viscoelastic rheologies modulate deformation signals. Field studies show that magma intrusions may be surrounded by a thermal, ductile, aureole (Hodge 1974). This acts to relax stresses between the intrusion and the country rock, and has been modelled analytically as a viscoelastic shell surrounding a spherical magma body (e.g. Dragoni and Magnanensi 1989; Segall

2010; Parks et al. 2015). In this case, the relaxation time,  $t_R$ , is given by:

$$t_R = \frac{3\eta(1 - \nu)R_2^3}{\mu(1 - \nu)R_1^3} \quad (4.7)$$

where  $\eta$  is the viscosity,  $\nu$  is Poisson's ratio,  $\mu$  is the shear modulus, and  $R_1$  and  $R_2$  are the radii of the magma body and viscous shell (Segall 2010). Post intrusion, we would expect surface displacements to continue for a period of time that scales with  $t_R$ , where  $t_R$  increases with increasing crustal viscosity and shell radius.

Rather than using a single value of crustal viscosity (Dragoni and Magnanensi 1989; Segall 2010), the viscosity of the crust may be modelled as temperature-dependent (e.g. Del Negro et al. 2009; Gregg et al. 2012), such that high temperature magma intrusions increase the ductility of the surrounding country rock (e.g. Annen and Sparks 2002), and magma cooling acts to increase the viscosity. The temperature distribution calculated from the thermal model in this study could therefore be used to derive the viscoelastic properties of the crust, allowing the rheology of the country rock to evolve in space and time as a function of local temperature. This would allow a thorough and systematic assessment of the role of viscoelasticity in modulating the deformation signals associated with cooling magma intrusions of different geometry and composition. Providing better constraints upon crustal viscoelasticity is also significant for studies of the accumulation of large magma volumes, as the ductility induced by magma intrusions inhibits further development of sills and dikes and reduces the likelihood of eruption (Jellinek and DePaolo 2003).

## 4.7 Conclusions

Magma intrusion is fundamental to the growth of volcanic edifices, magma reservoirs, and crustal plutons. Here we combine an existing thermal model with simple geodetic constraints to show that subsidence resulting from cooling and crystallising magma intrusions (volume  $< 3 \text{ km}^3$ ) may persist over decadal time-scales. The rate and time-scale of subsidence is dependent upon the magma composition, the intrusion geometry, and the thermal state of the surrounding country rock. Such ground deformation is observed at numerous volcanic centres and, through this modelling approach, can be used to provide insight into crustal magma fluxes and the timing of magma intrusion.

We apply this modelling approach to long-term, steady subsidence of Medicine Lake Volcano using realistic petrological and geometrical inputs. Comparing the results to the geodetic record, we identify a suite of best-fitting models with initial volumes of  $1\text{--}2.5 \text{ km}^3$  that reproduce  $>65$  years of subsidence measured at the volcano. These results suggest that magma intrusion has occurred on the order of hundreds of years before present, more recently than the time of the last eruption  $\sim 1 \text{ ka}$ , and that subsidence may continue for decades.

## References

- Annen, C. (2009). From plutons to magma chambers: Thermal constraints on the accumulation of eruptible silicic magma in the upper crust. *Earth and Planetary Science Letters*, *284*, 409–416.
- Annen, C. (2011). Implications of incremental emplacement of magma bodies for magma differentiation, thermal aureole dimensions and plutonism-volcanism relationships. *Tectonophysics*, *500*(1), 3–10.
- Annen, C., & Sparks, R. S. J. (2002). Effects of repetitive emplacement of basaltic intrusions on thermal evolution and melt generation in the crust. *Earth and Planetary Science Letters*, *203*(3), 937–955.
- Annen, C., Lénat, J.-F., & Provost, A. (2001). The long-term growth of volcanic edifices: numerical modelling of the role of dyke intrusion and lava-flow emplacement. *Journal of Volcanology and Geothermal Research*, *105*(4), 263–289.
- Annen, C., Pichavant, M., Bachmann, O., & Burgisser, A. (2008). Conditions for the growth of a long-lived shallow crustal magma chamber below Mount Pelee volcano (Martinique, Lesser Antilles Arc). *Journal of Geophysical Research*, *113*(B07209).
- Annen, C., Blundy, J. D., Leuthold, J., & Sparks, R. S. J. (2015). Construction and evolution of igneous bodies: Towards an integrated perspective of crustal magmatism. *Lithos*, *230*, 206–221.
- Bargar, K. E. (2001). Fluid-Inclusion Studies of Hydrothermal Minerals from Geothermal Drill Holes at Medicine Lake Volcano, Northern California. *California Geology*, *13*.
- Baumgartner, L. A., Michel, J., Putlitz, B., Leuthold, J., Muüntener, O., Robyr, M., et al. (2007). The Torres del Paine Igneous Complex and its Contact Aureole. *International Geological Conference on the Southern Hemisphere*.
- Biggs, J., Bastow, I. D., Keir, D., & Lewi, E. (2011). Pulses of deformation reveal frequently recurring shallow magmatic activity beneath the Main Ethiopian Rift. *Geochemistry, Geophysics, Geosystems*, *12*(9).
- Blackwell, D. D., Bowen, R. G., Hull, D. A., Riccio, J., & Steele, J. L. (1982). Heat flow, arc volcanism, and subduction in northern Oregon. *Journal of Geophysical Research*, *87*(B10), 8735–8754.
- Bohrson, W. A., & Spera, F. J. (2001). Energy-constrained open-system magmatic processes II: application of energy-constrained assimilation-fractional crystallization (EC-AFC) model to magmatic systems. *Journal of Petrology*, *42*(5), 1019–1041.
- Bonafede, M., Dragoni, M., & Quarenì, F. (1986). Displacement and stress fields produced by a centre of dilation and by a pressure source in a viscoelastic half-space: Application to the study of ground deformation and seismic activity at Campi Flegrei, Italy. *Geophysical Journal International*, *87*(2), 455–485.
- Burnham, C. W. (1979). *The importance of volatile constituents* (pp. 439–482). Princeton, NJ: Princeton University Press.
- Caricchi, L., Biggs, J., Annen, C., & Ebmeier, S. (2014). The influence of cooling, crystallisation and re-melting on the interpretation of geodetic signals in volcanic systems. *Earth and Planetary Science Letters*, *388*, 166–174.
- Carlsaw, H. S., & Jaeger, J. C. (1959). *Conduction of heat in solids*. London, UK: Oxford University Press.
- Coleman, D. S., Gray, W., & Glazner, A. F. (2004). Rethinking the emplacement and evolution of zoned plutons: Geochronologic evidence for incremental assembly of the Tuolumne Intrusive Suite, California. *Geology*, *32*(5), 433–436.
- Costa, F., Scaillet, B., & Pichavant, M. (2004). Petrological and experimental constraints on the pre-eruption conditions of Holocene dacite from Volcán San Pedro (36 S, Chilean Andes) and the importance of sulphur in silicic subduction-related magmas. *Journal of Petrology*, *45*(4), 855–881.
- Crisp, J. A. (1984). Rates of magma emplacement and volcanic output. *Journal of Volcanology and Geothermal Research*, *20*(3), 177–211.

- Cruden, A. R., & McCaffrey, K. J. W. (2002). *Different scaling laws for sills, laccoliths and plutons: Mechanical thresholds on roof lifting and floor depression* (pp. 15–17). Wissenschaftliche Mitteilungsanstalt für Geologie Technische Universität Bergakademie Freiberg, Freiberg, Germany.
- de Saint-Blanquat, M., Habert, G., Horsman, E., Morgan, S. S., Tikoff, B., Launeau, P., et al. (2006). Mechanisms and duration of non-tectonically assisted magma emplacement in the upper crust: The Black Mesa pluton, Henry Mountains, Utah. *Tectonophysics*, 428(1), 1–31.
- Del Negro, C., Currenti, G., & Scandura, D. (2009). Temperature-dependent viscoelastic modeling of ground deformation: Application to Etna volcano during the 1993–1997 inflation period. *Physics of the Earth and Planetary Interiors*, 172(3), 299–309.
- Delaney, P. T. (1988). Fortran 77 programs for conductive cooling of dikes with temperature-dependent thermal properties and heat of crystallization. *Computers & Geosciences*, 14(2), 181–212.
- Donnelly-Nolan, J. M., Champion, D. E., Miller, C. D., Grove, T. L., & Trimble, D. A. (1990). Post-11,000-year volcanism at Medicine Lake Volcano, Cascade Range, Northern California. *Journal of Geophysical Research*, 95(B12), 19693–19704.
- Donnelly-Nolan, J. M., Nathenson, M., Champion, D. E., Ramsey, D. W., Lowenstern, J. B., Ewert, J. W. (2007). Volcano hazards assessment for medicine Lake Volcano, Northern California. U.S. Geological Survey Scientific Investigations Report (2007-5174-A).
- Donnelly-Nolan, J. M., Grove, T. L., Lanphere, M. A., Champion, & D. E. (2008). Eruptive history and tectonic setting of Medicine Lake Volcano, a large rear-arc volcano in the southern Cascades. *Journal of Volcanology and Geothermal Research*, 117.
- Dragoni, M., & Magnanensi, C. (1989). Displacement and stress produced by a pressurized, spherical magma chamber, surrounded by a viscoelastic shell. *Physics of the Earth and Planetary Interiors*, 56(3), 316–328.
- Dzurisin, D. (2007). *Volcano deformation: Geodetic monitoring techniques*. Chichester, UK: Springer-Praxis.
- Dzurisin, D., Donnelly-Nolan, J. M., Evans, J. R., & Walter, S. R. (1991). Crustal subsidence, seismicity, and structure near Medicine Lake volcano, California. *Journal of Geophysical Research*, 96(B10), 16319–16333.
- Dzurisin, D., Poland, M. P., & Bürgmann, R. (2002). Steady subsidence of Medicine Lake Volcano, Northern California, revealed by repeated levelling surveys. *Journal of Geophysical Research*, 107(B12), 2372.
- Evans, J. R., & Zucca, J. J. (1998). Active high-resolution seismic tomography of compressional wave velocity and attenuation structure at Medicine Lake Volcano, Northern California Cascade Range. *Journal of Geophysical Research*, 93(B12), 15016–15036.
- Fialko, Y., Khazan, Y., & Simons, M. (2001a). Deformation due to a pressurized horizontal circular crack in an elastic half-space, with applications to volcano geodesy. *Geophysical Journal International*, 146(1), 181–190.
- Finn, C., & Williams, D. L. (1982). Gravity evidence for a shallow intrusion under Medicine Lake Volcano, California. *Geology*, 10(10), 503–507.
- Francis, P. W., & Hawkesworth, C. J. (1994). Late Cenozoic rates of magmatic activity in the Central Andes and their relationships to continental crust formation and thickening. *Journal of the Geological Society*, 151(5), 845–854.
- Fuis, G. S., Zucca, J. J., Mooney, W. D., & Milkereit, B. (1987). A geological interpretation of seismic refraction results in north-eastern California. *Bulletin of the Geological Society of America*, 98(1), 53–65.
- Galland, O., Cobbold, P. R., de Bremond d'Arès, J., & Hallot, E. (2007). Rise and emplacement of magma during horizontal shortening of the brittle crust: Insights from experimental modeling. *Journal of Geophysical Research*, 112(B6), 0.
- Girona, T., Costa, F., Newhall, C., & Taisne, B. (2014). On depressurization of volcanic magma reservoirs by passive degassing. *Journal of Geophysical Research*, 119(12), 8667–8687.

- Green, D. H. (1973). Experimental melting studies on a model upper mantle composition at high pressure under water-saturated and water-undersaturated conditions. *Earth and Planetary Science Letters*, 19(1), 37–53.
- Gregg, P. M., De Silva, S. L., Grosfils, E. B., & Parmigiani, J. P. (2012). Catastrophic caldera-forming eruptions: Thermomechanics and implications for eruption triggering and maximum caldera dimensions on Earth. *Journal of Volcanology and Geothermal Research*, 241, 1–12.
- Grove, L. T., Donnelly-Nolan, J. M., & Housh, T. (1997). Magmatic processes that generated the rhyolite of Glass Mountain, Medicine Lake Volcano, N. California. *Contributions to Mineralogy Petrology*, 127, 205–223.
- Gudmundsson, A. (2011). Deflection of dykes into sills at discontinuities and magma-chamber formation. *Tectonophysics*, 500(1), 50–64.
- Habert, G., & De Saint-Blanquat, M. (2004). Rate of construction of the Black Mesa bysalmith, Henry Mountains, Utah. *Geological society* (Vol. 234(1), pp. 163–173). London: Special Publications.
- Hickey, J., Gottsmann, J., & Potro, R. (2013). The large-scale surface uplift in the Altiplano-Puna region of Bolivia: A parametric study of source characteristics and crustal rheology using finite element analysis. *Geochemistry, Geophysics, Geosystems*, 14(3), 540–555.
- Hodge, D. S. (1974). Thermal model for origin of granitic batholiths. *Nature*, 251, 297–299.
- Hodge, B. E., & Crider, J. G. (2010). Investigating mechanisms of edifice deflation 1981–2007, at Mount Baker volcano, Washington, United States. *Journal of Geophysical Research*, 105, 25671–25684.
- Holloway, J. R., & Burnham, C. W. (1972). Melting relations of basalt with equilibrium water pressure less than total pressure. *Journal of Petrology*, 13(1), 1–29.
- Hooper, A., Segall, P., & Zebker, H. (2007). Persistent scatterer interferometric synthetic aperture radar for crustal deformation analysis, with application to Volcán Alcedo, Galápagos. *Journal of Geophysical Research*, 112(B7).
- Hulen, J. B., & Lutz, S. J. (1999). Altered volcanic rocks as hydrologic seals on the geothermal system of Medicine Lake volcano, California. *Geothermal Resource Council Bulletin*, 28, 217–222.
- Huppert, H. E., & Sparks, R. S. J. (1988). The generation of granitic magmas by intrusion of basalt into continental crust. *Journal of Petrology*, 29(3), 599–624.
- Ingebritsen, S. E., Mariner, R. H., & Sherrod, D. R. (1994). Hydrothermal systems of the Cascade Range, north-central Oregon. 1044-L.
- Ingebritsen, S., Sherrod, D., & Mariner, R. (1989). Heat flow and hydrothermal circulation in the Cascade Range, north-central Oregon. *Science*, 243(4897), 1458–1462.
- Iovenetti, J., & Hill, D. (1997). Baseline hydrogeology evaluation report for Telephone Flat geothermal project, Medicine Lake, California: Emeryville, California. Weiss Associates, Report prepared for CalEnergy Corporation.
- Jellinek, A. M., & DePaolo, D. J. (2003). A model for the origin of large silicic magma chambers: precursors of caldera-forming eruptions. *Bulletin of Volcanology*, 65(5), 363–381.
- Kavanagh, J. L., & Pavier, M. J. (2014). Rock interface strength influences fluid-filled fracture propagation pathways in the crust. *Journal of Structural Geology*, 63, 68–75.
- Kavanagh, J. L., Menand, T., & Sparks, R. S. J. (2006). An experimental investigation of sill formation and propagation in layered elastic media. *Earth and Planetary Science Letters*, 245(3), 799–813.
- Kwoun, O., Lu, Z., Neal, C., & Wicks, C. (2006). Quiescent deformation of the Aniakchak Caldera, Alaska, mapped by InSAR. *Geology*, 34(1), 5–8.
- Lange, R. A. (1994). The effect of H<sub>2</sub>O, CO<sub>2</sub> and F on the density and viscosity of silicate melts. *Volatiles in Magmas. Reviews in Mineralogy*, 30, 331–369.
- Leuthold, J., Müntener, O., Baumgartner, L. P., Putlitz, B., Ovtcharova, M., & Schaltegger, U. (2012). Time resolved construction of a bimodal laccolith (Torres del Paine, Patagonia). *Earth and Planetary Science Letters*, 325, 85–92.

- Lowenstern, J. B., Donnelly-Nolan, J., Wooden, J. L., & Charlier, B. L. A. (2003). Volcanism, Plutonism and Hydrothermal Alteration at Medicine Lake Volcano, California. In *Proceedings, Twenty-Eighth Workshop on Geothermal Reservoir Engineering* (p. 8). Stanford, California: Stanford University.
- Lu, Z., & Dzurisin, D. (2014). *InSAR imaging of Aleutian volcanoes: Monitoring a volcanic arc from space*. Chichester, UK: Springer-Praxis.
- Mann, D., & Freymueller, J. (2003). Volcanic and tectonic deformation on Unimak Island in the Aleutian Arc, Alaska. *Journal of Geophysical Research*, 108(B2), 2108.
- Masterlark, T. (2007). Magma intrusion and deformation predictions: Sensitivities to the Mogi assumptions. *Journal of Geophysical Research*, 112(B6).
- Masterlark, T., Haney, M., Dickinson, H., Fournier, T., & Searcy, C. (2010). Rheologic and structural controls on the deformation of Okmok volcano, Alaska: FEMs, InSAR and ambient seismic noise tomography. *Journal of Geophysical Research*, 115(B02409).
- Mastin, L. G., & Ghiorso, M. S. (2000). A numerical program for steady-state flow of magma-gas mixtures through vertical eruptive conduits. U.S. Geological Survey Open File Report 00-209, 61.
- Matzel, J. E. P., Bowring, S. A., & Miller, R. B. (2006). Time scales of pluton construction at differing crustal levels: Examples from the Mount Stuart and Tenpeak intrusions, North Cascades, Washington. *Geological Society of America Bulletin*, 118(11–12), 1412–1430.
- Menand, T. (2008). The mechanics and dynamics of sills in layered elastic rocks and their implications for the growth of laccoliths and other igneous complexes. *Earth and Planetary Science Letters*, 267, 93–99.
- Menand, T., & Phillips, J. C. (2007). Gas segregation in dykes and sills. *Journal of Volcanology and Geothermal Research*, 159(4), 393–408.
- Michaut, C. (2011). Dynamics of magmatic intrusions in the upper crust: Theory and applications to laccoliths on Earth and the Moon. *Journal of Geophysical Research*, 116(B5).
- Michaut, C., & Jaupart, C. (2006). Ultra-rapid formation of large volumes of evolved magma. *Earth and Planetary Science Letters*, 250(1), 38–52.
- Michel, J., Baumgartner, L., Putlitz, B., Schaltegger, U., & Ovtcharova, M. (2008). Incremental growth of the Patagonian Torres del Paine laccolith over 90 ky. *Geology*, 36(6), 459–462.
- Newman, A. V., Dixon, T. H., Ofoegbu, G. I., & Dixon, J. E. (2001). Geodetic and seismic constraints on recent activity at Long Valley Caldera, California: Evidence for viscoelastic rheology. *Journal of Volcanology and Geothermal Research*, 105(3), 183–206.
- Okada, Y. (1985). Surface deformation due to shear and tensile faults in a half-space. *Bulletin of the Seismological Society of America*, 75(4), 1135–1154.
- Papale, P., Moretti, R., & Barbato, D. (2006). The compositional dependence of the saturation surface of H<sub>2</sub>O + CO<sub>2</sub> fluids in silicate melts. *Chemical Geology*, 229, 78–95.
- Parker, A. L., Biggs, J., & Lu, Z. (2014). Investigating long-term subsidence at Medicine Lake Volcano, CA, using multi temporal InSAR. *Geophys. J. Int.*, 199(2), 844–859.
- Parks, M. M., Moore, J., Papanikolaou, X., Biggs, J., Mather, T. A., Pyle, D. M., et al. (2015). From quiescence to unrest-20 years of satellite geodetic measurements at Santorini volcano. *Greece. Journal of Geophysical Research*, 120(2), 1309–1328.
- Pasquarè, F., & Tibaldi, A. (2007). Structure of a sheet-laccolith system revealing the interplay between tectonic and magma stresses at Stardalur Volcano, Iceland. *Journal of Volcanology and Geothermal Research*, 161(1), 131–150.
- Pedersen, R., & Sigmundsson, F. (2006). Temporal development of the 1999 intrusive episode in the Eyjafjallajökull volcano, Iceland, derived from InSAR images. *Bulletin of Volcanology*, 68(4), 377–393.
- Petford, N., & Gallagher, K. (2001). Partial melting of mafic (amphibolitic) lower crust by periodic influx of basaltic magma. *Earth and Planetary Science Letters*, 193(3), 483–499.
- Philpotts, A. (1990). *Principles of igneous and metamorphic petrology*. Old Tappan, NJ, US: Prentice-Hall.

- Piwinskii, A. J., & Wyllie, P. J. (1968). Experimental studies of igneous rock series: a zoned pluton in the Wallowa batholith, Oregon. *The Journal of Geology*, 76(2), 205–234.
- Poland, M. P., Bürgmann, R., Dzurisin, D., Lisowski, M., Masterlark, T., Owen, S., et al. (2006). Constraints on the mechanism of long-term, steady subsidence at Medicine Lake volcano, northern California, from GPS, levelling and InSAR. *Journal of Volcanology and Geothermal Research*, 150(1), 55–78.
- Pritchard, M. E. (2003). *Recent crustal deformation in west-central south America*. Ph.D. thesis, Calif. Inst. Technol., Pasadena, from, <http://etd.caltech.edu/etd/available/etd-06022003-105512/>.
- Pritchard, M. E., & Simons, M. (2004a). An InSAR-based survey of volcanic deformation in the central Andes. *Geochemistry, Geophysics, Geosystems*, 5(2).
- Pritchard, M. E., & Simons, M. (2004b). Surveying volcanic arcs with satellite radar interferometry: The Central Andes, Kamchatka, and beyond. *GSA Today*, 14(8), 4–10.
- Pyle, D. M., Mather, T. A., & Biggs, J. (2013). Remote sensing of volcanoes and volcanic processes: Integrating observation and modelling-introduction. *Geological Society, London, Special Publications*, 380(1), 1–13.
- Reymer, A., & Schubert, G. (1984). Phanerozoic addition rates to the continental crust and crustal growth. *Tectonics*, 3(1), 63–77.
- Riddick, S. N., & Schmidt, D. A. (2011). Time-dependent changes in volcanic inflation rate near Three Sisters, Oregon, revealed by InSAR. *Geochemistry, Geophysics, Geosystems*, 12(12).
- Ritter, J. R. R., & Evans, J. R. (1997). Deep structure of Medicine Lake volcano, California. *Tectonophysics*, 275(1), 221–241.
- Robertson, E. C. (1988). Thermal properties of rocks. U.S. Geological Survey Open File Report 88-441.
- Rothstein, D. A., Manning, C. E. (2003). Geothermal gradients in continental magmatic arcs: Constraints from the eastern Peninsular Ranges batholith, Baja California, México (pp. 337–354). Special Papers - Geological Society of America.
- Sadofsky, S. J., Portnyagin, M., Hoernle, K., & van den Bogaard, P. (2008). Subduction cycling of volatiles and trace elements through the Central American volcanic arc: evidence from melt inclusions. *Contributions to Mineralogy and Petrology*, 155(4), 433–456.
- Segall, P. (2010). *Earthquake and volcano deformation*. Princeton, New Jersey, US: Princeton University Press.
- Shaw, H. R., Jackson, E. D., & Bargar, K. E. (1980). Volcanic periodicity along the Hawaiian-Emperor chain. *American Journal of Science*, 280, 667–708.
- Sigmundsson, F. (2006). *Iceland geodynamics: Crustal deformation and divergent plate tectonics*. Chichester, UK: Springer-Praxis.
- Sigmundsson, F., Vadon, H., & Massonnet, D. (1997). Readjustment of the Krafla spreading segment to crustal rifting measured by Satellite Radar Interferometry. *Geophysical Research Letters*, 24(15), 1843–1846.
- Sparks, R. S. J., Folkes, C. B., Humphreys, M. C. S., Barfod, D. N., Clavero, J., Sunagua, M. C., et al. (2008). Uturuncu volcano, Bolivia: Volcanic unrest due to mid-crustal magma intrusion. *American Journal of Science*, 308(6), 727–769.
- Staudigel, H., & Schmincke, H. (1984). The Pliocene seamount series of La Palma/Canary Islands. *Journal of Geophysical Research*, 89(B13), 11195–11215.
- Sturkell, E., & Sigmundsson, F. (2000). Continuous deflation of the Askja caldera, Iceland, during the 1983–1998 non eruptive period. *Journal of Geophysical Research*, 115(B04401), 671–684.
- Tallarico, A., Dragoni, M., Anzidei, M., & Esposito, A. (2003). Modeling long-term ground deformation due to the cooling of a magma chamber: Case of Basiluzzo island, Aeolian Islands, Italy. *Journal of Geophysical Research*, 108(B12), 2568.
- Taran, Y. A. (2009). Geochemistry of volcanic and hydrothermal fluids and volatile budget of the kamchatka-kuril subduction zone. *Geochimica et Cosmochimica Acta*, 73(4), 1067–1094.

- Thorpe, R. S., Francis, P. W., & Harmon, R. S. (1981). Andean andesites and crustal growth. *Philosophical Transactions of the Royal Society of London. Series A, Mathematical and Physical Sciences*, 301(1461), 305–320.
- Turcotte, D. L., & Schubert, G. (1982). *Geodynamics*. Cambridge, UK: Cambridge University Press.
- Valentine, G. A., & Krogh, K. E. C. (2006). Emplacement of shallow dikes and sills beneath a small basaltic volcanic center—the role of pre-existing structure (Paiute Ridge, southern Nevada, USA). *Earth and Planetary Science Letters*, 246(3), 217–230.
- Wadge, G. (1980). Output rate of magma from active central volcanoes. *Nature*, 288, 253–255.
- Wagner, T. P., Donnelly-Nolan, J. M., & Grove, T. L. (1995). Evidence of hydrous differentiation and crystal accumulation in the low Mg-O, high-Al<sub>2</sub>O<sub>3</sub> Lake Basalt from Medicine Lake Volcano, California. *Contributions to Mineralogy Petrology*, 121, 201–216.
- White, S. M., Crisp, J. A., & Spera, F. J. (2006). Long-term volumetric eruption rates and magma budgets. *Geochemistry, Geophysics, Geosystems*, 7(3), 1–20.
- Whitney, J. A. (1988). The Origin of Granite - the role and source of water in the evolution of Granitic Magmas. *Geological Society of America Bulletin*, 100, 1886–1897.
- Whittington, A. G., Hofmeister, A. M., & Nabelek, P. (2009). Temperature-dependent thermal diffusivity of Earth's crust and implications for magmatism. *Nature*, 458, 319–321.
- Wollenberg, H. A., & Smith, A. R. (1987). Radiogenic heat production of crustal rocks: An assessment based on geochemical data. *Geophysical Research Letters*, 14(3), 295–298.
- Worster, M. G., Huppert, H. E., & Sparks, R. S. J. (1990). Convection and crystallization in magma cooled from above. *Earth and Planetary Science Letters*, 101(1), 78–89.
- Wright, T. J., Ebinger, C., Biggs, J., Ayele, A., Yirgu, G., Keir, D., et al. (2006). Magma-maintained rift segmentation at continental rupture in the 2005 Afar dyking episode. *Nature*, 442(7100), 291–294.
- Zucca, J. J., Fuis, G. S., Milkereit, B., Mooney, W. D., & Catchings, R. D. (1986). Crustal structure of northeastern California. *Journal of Geophysical Research*, 91(B7), 7359–7382.



## Chapter 5

# Constraining Mechanisms of Volcanic Subsidence at Lassen Volcanic Center, CA, Using InSAR

**Abstract** Lassen Volcanic Center, southern Cascades, has subsided in recent decades, but the onset, temporal evolution, and cause of subsidence remain unconstrained. Here we use multiple sets of InSAR data, each corrected using the North American Regional Reanalysis atmospheric model, to determine the temporal and spatial characteristics of deformation between 2004 and 2010. ENVISAT data shows that the rate of subsidence at LaVC has decreased over time from  $13 \pm 2.7$  mm/yr between 2004 and 2007 to  $8 \pm 1.6$  mm/yr between 2007 and 2010. Time-series analysis shows that this may be due to either a decrease in the rate of subsurface volume change or an increase in source depth. Comparing these observations to past geodetic studies suggests that the onset of deformation was in the early 1990s. Combining multiple tracks of InSAR data, we find that the ratio of horizontal to vertical displacements is high, and geophysical inversions suggest that subsidence is driven by a point source located at  $\sim 9$  km depth. This source geometry, and the temporal evolution of deformation, contrasts to steady subsidence observed at nearby Medicine Lake Volcano since the 1950s. We evaluate possible causes of subsidence in light of hydrothermal and seismic activity at LaVC, and suggest that deformation is driven by changes in the distribution of magmatic/hydrothermal fluids and/or magma cooling, in addition to tectonic extension. Lassen Volcanic Center was one of  $>10$  volcanic/geothermal centers to experience triggered seismicity after the 1992  $M_w 7.3$  Landers earthquake, but further constraints are required to assess whether the earthquake had a role in the onset of recent subsidence.

## 5.1 Introduction

Lassen Volcanic Center (LaVC) is the southernmost volcano of the Cascades Volcanic Arc (Fig. 5.1a) and the only Cascade volcano other than Mount St. Helens to have erupted during the 20th century (Clynne et al. 2012). LaVC is also one of two volcanic centres in northern California known to be subsiding (Dzurisin et al. 1991; Poland et al. 2004), although whether subsidence is associated with the eruption (e.g. viscoelastic relaxation or withdrawal of magmatic fluids), the vigorous hydrothermal system, or regional tectonics, is undetermined (Poland et al. 2004).

Observing and understanding ground deformation at volcanoes provides insight into the dynamics of the magmatic and/or hydrothermal system (see Pinel et al. (2014) and references therein). InSAR observations alone document deformation at >500 volcanoes worldwide (Biggs et al. 2014). These studies identify ground deformation ranging from: exponentially decaying inflation, linked to constant magmatic recharge from a deeper source (e.g. Grímsvötn Volcano: Reverso et al. 2014); to cyclical bradyseisms, associated with the interaction between magmatic fluids and hydrothermal systems (e.g. Campi Flegrei: Chiodini et al. 2015); and long wavelength, steady uplift, related to heat transfer and crustal ductility induced by deep magma bodies (e.g. Sorocco: Pearse and Fialko 2010). Constraining the onset, rate, and spatial characteristics of subsidence at LaVC is therefore crucial in determining the current state of the volcano. This has implications for hazard assessments, as LaVC is located within a National Park, and lies in the path of major air traffic corridors, gas pipelines and power lines (Clynne et al. 2012).

Geodetic surveys of LaVC prior to 1996 consisted of leveling (1932, 1934, 1991: Dzurisin 1999, repeated electronic distance measurements (EDM) and dry tilt surveys (1981, 1982, 1984: Poland et al. 2004), all of which showed no evidence of ground deformation (Fig. 5.1b). However, an InSAR survey of the volcano in 1996–2000 indicated up to  $\sim 10$  mm/yr of subsidence over a  $\sim 40$  km diameter area centred 5 km southeast of Lassen Peak (Poland et al. 2004). This motivated a survey of 5 EDM lines using GPS in 2004, which revealed that line lengths had shortened by up to 145 mm since 1981 (Poland et al. 2004). Here we consolidate past geodetic measurements at LaVC with a detailed InSAR survey between 2004 and 2010 to constrain the spatial and temporal evolution of ground deformation. Using these results, we evaluate possible mechanisms of subsidence and also compare deformation to that recorded at Medicine Lake Volcano located 100 km to the north.

### ***5.1.1 Tectonic and Geological Setting***

Northern California marks the southern end of the Cascade volcanic arc and the interaction between subduction along the Cascadia subduction zone and extension of the Basin and Range province (e.g. Wells et al. 1998; Hildreth 2007; Chap. 1). The interaction of these tectonic regimes is reflected in eruptive products across northern CA: hydrous calcalkaline basalts, observed throughout the Cascades and related to subduction, are found erupted close in temporal and spatial proximity to dry, primitive, high-alumina olivine tholeiite, a common eruptive product of the Basin and Range province (Guffanti et al. 1990; Donnelly-Nolan et al. 2008).

LaVC is located on a discrete segment of the Cascade arc, separated from Medicine Lake Volcano and Mount Shasta to the north by a region containing no recognized Quaternary volcanic vents (Guffanti and Weaver 1988; Chap. 1). LaVC is the youngest of 5 large, long-lived volcanic centres that define the axis of the southernmost Cascades (Klemetti and Clynne 2014).

The LaVC region is also coincident with a transitional zone of the Walker Lane fault system, where horizontal stress is transferred from NW dextral shear in the southeast, to E-W extension in the north (Janik and McLaren (2010); Fig. 5.1a). Few surface ruptures of the Walker Lane are identified within LaVC, but NNW trending breaks between Lassen Peak and Reading Peak have been described as a zone of tensional surface deformation, possibly related to a near-surface dike emplaced just prior to the 1914 eruption (Clynne and Muffler 2010).

Volcanism at LaVC began with the Rockland caldera complex  $\sim 825$  ka, followed by the formation of Brokeoff Volcano  $\sim 590$  ka (Clynne and Muffler 2010). Brokeoff Volcano has since been eviscerated, and the most recent feature of LaVC is the Lassen Domefield, containing over 20 domes that have erupted since  $\sim 315$  ka (Turrin et al. 1998; Clynne and Muffler 2010). During the last 1100 years, three eruptions have occurred in LaVC, including the 1914–1918 eruption at Lassen Peak (Clynne and Muffler 2010). This eruption was associated with a relatively small erupted volume ( $0.003 \text{ km}^3$ ), but was comprised of a dacite dome and lava flow, dacite pyroclastic flow, plus phreatic, avalanche, debris-flow, flood and fall deposits (Clynne and Muffler 2010), resulting in what is now known as the Devastated Area within Lassen Volcanic National Park.

The LaVC magmatic system is interpreted to contain one or more small dispersed bodies of magma in a larger, but mostly solidified zone of silicic magma beneath the volcanic center (Clynne 1985). Inclusions within silicic lavas document the presence of mafic magma that otherwise did not reach the surface (Clynne 1999). Similarly, zircon age analysis provides evidence of mush rejuvenation (and remobilisation) by basaltic intrusions on timescales of 10–1000s years, which facilitate eruptions of magma from within an otherwise cooling magmatic body (Klemetti and Clynne 2014). This is in agreement with seismic surveys, which reveal low-velocity zones suggesting the presence of magma in the crust, but do not identify a discrete magma reservoir larger than the detection limit (5 km diameter) (Clynne 1985). This is comparable to the magmatic model proposed for Medicine Lake Volcano, located 100 km to the north (Dzurisin et al. 2002; Donnelly-Nolan et al. 2008).

### ***5.1.2 Hydrothermal and Seismic Activity***

Hydrothermal activity at LaVC is the most vigorous in the Cascades, with steam vents, hot springs, and extensive alteration of surface rocks that has resulted in numerous landslides (Clynne et al. 2012). Heat discharge occurs via fumaroles (120 MW) (Sorey and Colvard 1994), thermal springs (26 MW) (Sorey et al. 1994), and slightly thermal springs (Sorey et al. 1994; Paulson and Ingebritsen 1991) ( $< 1$  MW). Many of the hydrothermal features of LaVC are located within the depression of Brokeoff Volcano (Fig. 5.1a), or are situated on mapped faults of the Walker Lane Fault Zone (Janik and McLaren 2010). Geochemical and seismic analysis suggests that there are two separate hydrothermal cells at  $\sim 5$  km depth that circulate within the greater Lassen hydrothermal system (Janik and McLaren 2010). One cell is located

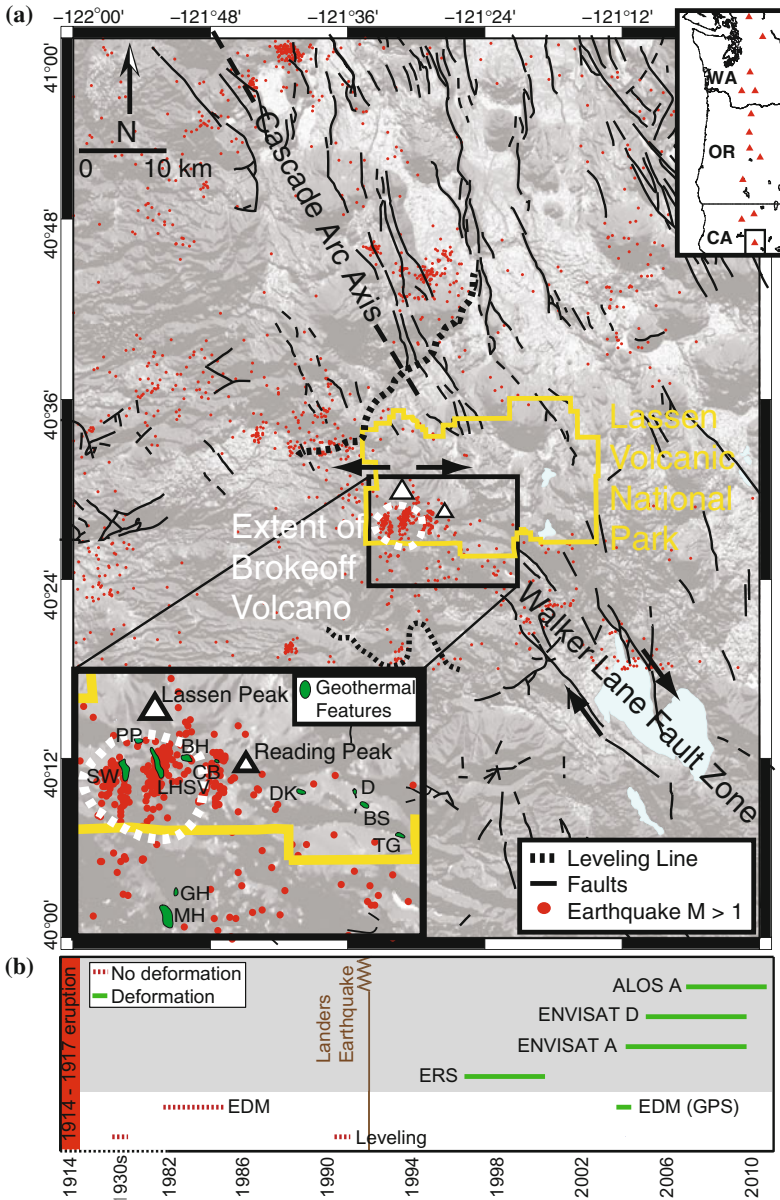


**Fig. 5.1** **a** Map of LaVC including main structural features after Clyne and Muffler (2010) and earthquake locations for the Northern California Earthquake Data Center. The leveling line is from Dzurisin (1999). *Top inset* map shows the location of LaVC in the Cascades Volcanic Arc. *Bottom inset* lineations of seismicity and hydrothermal features. **b** Timeline summarising published past geodetic studies at LaVC (Leveling: Dzurisin 1999; EDM/tilt/InSAR: Poland et al. 2004). *Dashed lines* correspond to surveys that did not show deformation and *solid lines* mark surveys that show subsidence. InSAR datasets are shown by the *grey box*. The time of the Landers earthquake (1992) is shown for reference

within the Brokeoff volcano depression, feeding steam to Little Hot Springs Valley, Bumpass Hell, Sulphur Works and Pilot Pinnacle solfataras (LHSV, BH, SW and PP in Fig. 5.1a), and the second cell beneath the Devil’s Kitchen (DK in Fig. 5.1a) area, recharged by precipitation that percolates via permeable faults of the Walker Lane (Janik and McLaren 2010).

LaVC is also one of the most seismically active Cascade volcanoes. Approximately 25 % of events are attributed to the hydrothermal system (Klein 1979; Walter et al. 1984) due to the interaction between meteoric waters and hot, brittle rock (Janik and McLaren 2010). The majority of events are within the vicinity of hydrothermal features, occurring at depths <7 km in three N-S elongate zones (the west, middle and east clusters) (Humphrey and McLaren 1995) (Fig. 5.1a). Seismicity in the east cluster is also the result of motion along the Walker Lane (McLaren and Janik 1996). Deeper events (7–10 km depth) occur beneath Devil’s Kitchen, and correlate with local fault orientations (Janik and McLaren 2010).

Events of larger magnitude at LaVC are both tectonic and volcanic in origin. Three vigorous earthquake sequences, with events up to  $M_w$ 5.5, occurred in 1936, 1945–1947, and 1950, and were attributed to approximately east-west extension localised on Basin and Range normal faults (Norris et al. 1997). Long period (LP) earthquakes (associated with the movement of magma at depth and magmatic/hydrothermal interactions) are also common. These events typically occur in clusters in a region 5–8 km west of Lassen Peak at depths of 13–23 km (Pitt et al. 2002). Between 2003 and 2011 an average of 11 LP earthquakes were detected per year (A.M. Pitt, unpublished data in Clynne et al. 2012).

## 5.2 Methods

### 5.2.1 InSAR Data and Processing

We use three sets of InSAR data spanning 2003–2010 to investigate subsidence at LaVC (Table 5.1). This includes imagery from the European Space Agency C-band satellite ENVISAT ascending track 435 (82 interferograms) and descending track 342

**Table 5.1** Interferograms (igrams) used in this study and for stacking

Satellite	Track	Mode	Dataset		Stack	
			Igrams	Span	Igrams	Span
ENVISAT	435	Ascending	82	May 2004–Aug 2010	25	Aug 2004–Aug 2010
ENVISAT	342	Descending	104	Nov 2005–Oct 2010	34	Jul 2005–Sep 2010
ALOS	163	Ascending	16	Mar 2007–Nov 2010	6	Sep 2007–Nov 2010

(104 interferograms), plus imagery from the JAXA satellite ALOS ascending track 163 (16 interferograms). Interferograms were processed using JPL/Caltech software ROI\_PAC (Rosen et al. 2004), filtered using a power spectrum filter (Goldstein and Werner 1998), unwrapped using a branch-cut algorithm at 16 looks (Goldstein et al. 1988) and down-sampled to a final resolution of  $\sim 300$  m (e.g. Jónsson et al. 2002). Orbital errors were removed using linear ramps (Biggs et al. 2007; Gourmelen et al. 2010), and topographically-correlated atmospheric artefacts were reduced using the North American Regional Reanalysis atmospheric model as described in Jolivet et al. (2011); Walters et al. (2013); Parker et al. (2015); and Chap. 3. Multi temporal analysis was then used to combine information from many interferograms, increasing the signal to noise ratio of the datasets and allowing us to investigate the evolution of deformation over time.

## 5.2.2 Stacking

Visual inspection of interferograms reveals that the deformation signal is spatially consistent over the observation period (2004–2010). We therefore use stacking to first investigate the location and spatial extent of subsidence. We use stacking rather than more advanced multi temporal techniques such as  $\pi$ -RATE (Biggs et al. 2007; Wang et al. 2009) or StaMPS (Hooper et al. 2007) as interferogram coherence in this region is high (Parker et al. 2015; Chap. 3) and topographically correlated atmospheric delays have been reduced using atmospheric models.

Interferograms were selected for stacking based upon the criteria described by Parker et al. (2014); (Chap. 2), whereby analysis of the coherence and noise properties of the dataset is used to set selection thresholds (Fig. 5.2). The interferograms we use

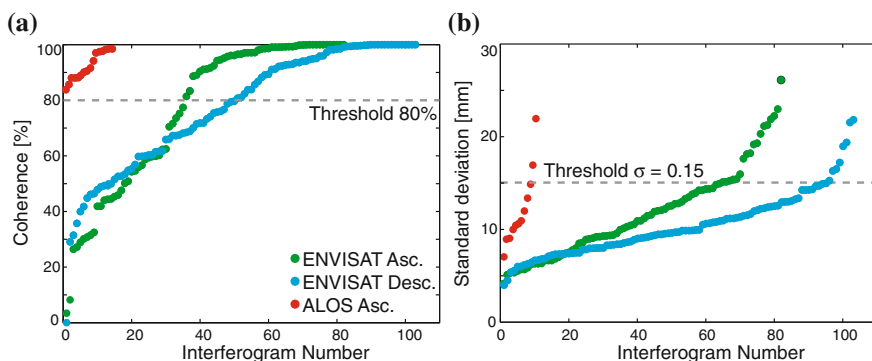


**Fig. 5.2** **a** Coherence of all interferograms listed in Table 5.1. Only interferograms with coherence  $> 80\%$  are used for stacking. **b** Standard deviation ( $\sigma$ ) of all interferograms listed in Table 5.1 calculated using covariance analysis (Hanssen 2001), (Eq. 2.3). Only interferograms with  $\sigma < 0.15$  are used for further analysis

have coherence  $>80\%$  and  $\sigma < 0.15$ , where  $\sigma$  is interferogram standard deviation calculated using covariance analysis (Eq. 2.3), (Hanssen 2001). The resulting data subsets (Table 5.1) contain 25 ENVISAT ascending track interferograms (August 2004–August 2010); 34 ENVISAT descending track interferograms (July 2007–September 2010) and 6 ascending track ALOS interferograms (September 2007–November 2010). Ratemaps were produced on a pixel-wise basis for all pixels that are coherent in at least 2 interferograms. We sum together the displacements from all interferograms coherent at each pixel, and divide by the total duration of the constituent interferograms. Measurements are then referenced to a far-field, non-deforming region.

Using the results of stacking, we solve for the horizontal (E - W) and vertical components of the deformation field,  $\mathbf{u} = (u_E, u_Z)^T$ , by combining data from different satellite look directions (e.g. Fialko et al. 2001b; Wright et al. 2004b; Biggs et al. 2009b; Samsonov and d'Oreye 2012; Chap. 2). We do not solve for N - S motion as the satellite line of sight (LOS) is least sensitive to this component (Wright et al. 2004b).

We use ratemaps calculated for ENVISAT ascending and descending tracks, each of which records displacements in a different LOS. In each case, the LOS is described by the satellite unit look vector,  $l$ , and the LOS displacements,  $d_{LOS}$ , are equal to the product of the satellite unit look vector and the vector components of displacement:

$$d_{LOS} = \begin{pmatrix} -\cos\phi\sin\theta \\ \cos\theta \end{pmatrix} \cdot \begin{pmatrix} u_E \\ u_Z \end{pmatrix}, \quad (5.1)$$

where  $\theta$  is the look angle of the satellite at each pixel and  $\phi$  is the heading direction of the satellite (Wright et al. 2004b). The horizontal and vertical components of motion may be calculated using  $\mathbf{D} = \mathbf{L}\mathbf{u}$ , where  $\mathbf{D}$  are the line of sight interferogram displacements for each dataset, and  $\mathbf{L}$  is a matrix containing the look vector for each dataset. The inversion is weighted using a covariance matrix, which contains the mean value of  $\sigma$  for each dataset (Wright et al. 2004b). This allows us to calculate the error of each displacement component.

### 5.2.3 Source Modelling

Using the results of stacking, we carry out analytical source modelling to provide first order constraints upon the geometry and depth of the deformation source. Although these models are an oversimplification of the real earth and do not account for heterogeneities in crustal structure or rheology, they are a valuable first step in understanding the cause of volcanic subsidence (e.g. Dzurisin 2007; Segall 2010). Such models can be used to distinguish between shallow- and deep-seated deformation mechanisms e.g. hydrothermal system depressurisation versus magma cooling (Mann and Freymueller 2003); and to differentiate between vertical or horizontally elongate geometries, which may be used to shed light on mechanisms of magma transport and

emplacement (e.g. Bagnardi et al. 2013). This simple modelling approach also provides a useful mode of comparison between ground deformation at other volcanoes.

We use the ratio of horizontal to vertical displacements to guide source modelling. Sills (horizontally elongate sources) modelled as horizontal dislocations (Okada 1985) or circular cracks (Fialko et al. 2001a), produce larger vertical than horizontal displacements. Equi-dimensional (e.g. Mogi 1958) or vertically elongate sources, such as prolate ellipsoids (Yang et al. 1988) generate larger horizontal displacements than horizontal sources.

We begin with the simplest point source (parameterised as an  $[x, y]$  location, depth and volume change (Mogi 1958)), before testing more complex geometries, including an ellipsoid. In addition to an  $[x, y]$  location, depth, and strength term, this parameterisation requires a major axis and ratio between major and minor axes describing the eccentricity of the source, and plunge and strike describing its inclination and orientation (Yang et al. 1988).

We follow the same modelling procedure as in Parker et al. (2014); Chap. 2, downsampling data to an initial resolution of  $\sim 450$  m (e.g. Hamling et al. 2014). The best-fitting source parameters are obtained using a Monte Carlo type simulated annealing algorithm (Amelung and Bell 2003), which provides an efficient way of testing a wide range of source parameters. We exploit the fact that we have constraints upon different components of the deformation field and simultaneously solve for all datasets. The initial range of source parameters is made broad enough to ensure that solutions do not saturate at the parameter bounds. As the source models are non-unique, we investigate the uncertainties and trade-offs between source parameters using a Monte Carlo approach (Wright et al. 2004a; Biggs et al. 2009a). As described in Parker et al. (2014); Chap. 2, we use covariance analysis to create 100 sets of synthetic noise, which are added to the ratemaps shown in Fig. 5.3 before rerunning the same inversion scheme.

### 5.2.4 Time-Series

Next we use time-series analysis (e.g. Lundgren et al. 2001; Bernardino et al. 2002) to assess the temporal characteristics of deformation. As measurements are made from multiple satellite tracks, we use a joint inversion technique that combines multiple sets of InSAR data (Biggs et al. 2010). In this approach, the observations of ground displacement are converted to incremental subsurface volume changes that arise due to point source pressure variations at depth (Mogi 1958). The surface displacement at any point can be predicted by the three component LOS unit vector,  $l$  (Eq. 5.1), and the three component displacement vector predicted by a Mogi model,  $M$  (Biggs et al. 2010). For an observation point with location  $[x, y, z]$ ,  $M$  is equal to:

$$\begin{pmatrix} m_x \\ m_y \\ m_z \end{pmatrix} = \frac{\Delta V}{\pi} (1 - \nu) \begin{pmatrix} \frac{x}{R^3} \\ \frac{y}{R^3} \\ \frac{z}{R^3} \end{pmatrix}, \quad (5.2)$$



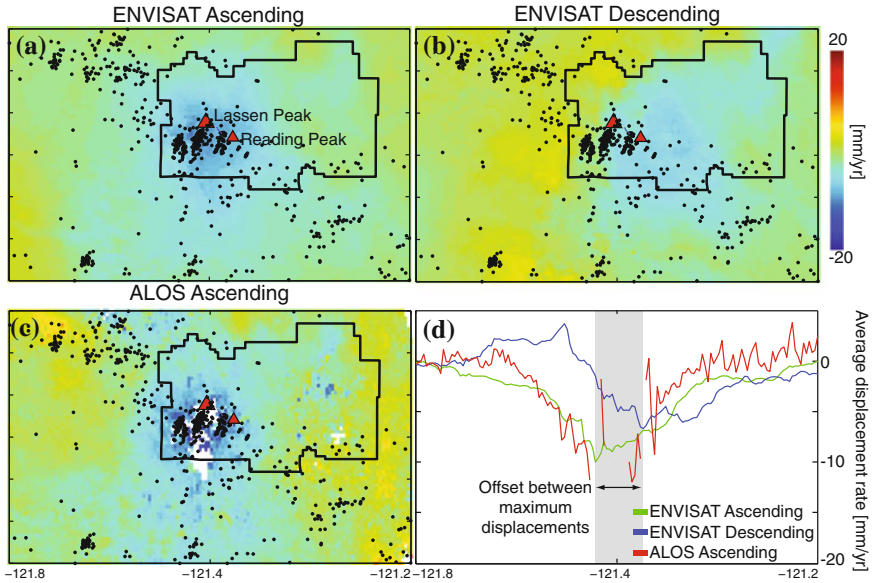


**Fig. 5.3** a–c Ratemaps for ENVISAT ascending, ENVISAT descending and ALOS ascending datasets produced using the interferograms listed in Table 5.1. Black line shows the outline of Lassen Volcanic National Park and earthquakes locations are as in Fig. 5.1. d Profiles draw at the latitude of Reading Peak show the offset between maximum subsidence between ascending and descending datasets

where  $\Delta V$  is a volume change,  $\nu$  is Poisson’s ration (0.25), and  $R$  is the distance from the point source to the observation. Using measurements of incremental surface displacement,  $b$ , and  $M$  for the case of a volume change of  $1 \text{ km}^3$ , we can solve for the incremental volume change of the Mogi source,  $V$ :

$$\begin{pmatrix} (\mathbf{l}_a \cdot \mathbf{M}_a) \mathbf{A}_a \\ (\mathbf{l}_b \cdot \mathbf{M}_b) \mathbf{A}_b \\ \vdots \end{pmatrix} \begin{pmatrix} V_{12} \\ V_{23} \\ \vdots \end{pmatrix} = \begin{pmatrix} \mathbf{b}_a \\ \mathbf{b}_b \\ \vdots \end{pmatrix} \quad (5.3)$$

where  $A$  is a temporal design matrix documenting the epochs used to produce each displacement observation (Biggs et al. 2010). The subscripts correspond to different InSAR datasets, each of which has a different LOS unit vector  $l$ . The solution is integrated to account for the different duration of each time-step (Biggs et al. 2010), and the error on each observation is calculated using the phase standard deviation of pixels  $> 10 \text{ km}$  from the source location (Parks et al. 2015).

## 5.3 Results

### 5.3.1 Stacking

Stacks show maximum LOS displacement rates of  $-8.5$  mm/yr (ENVISAT ascending),  $-7$  mm/yr (ENVISAT descending) and  $-11$  mm/yr (ALOS ascending), with subsidence extending over a broad ( $\sim 40$  km) region (Fig. 5.3a–c). For ascending track imagery (Fig. 5.3a, c), subsidence is centred on the middle cluster of seismicity, S of Lassen Peak and W of Reading Peak, whereas descending track imagery

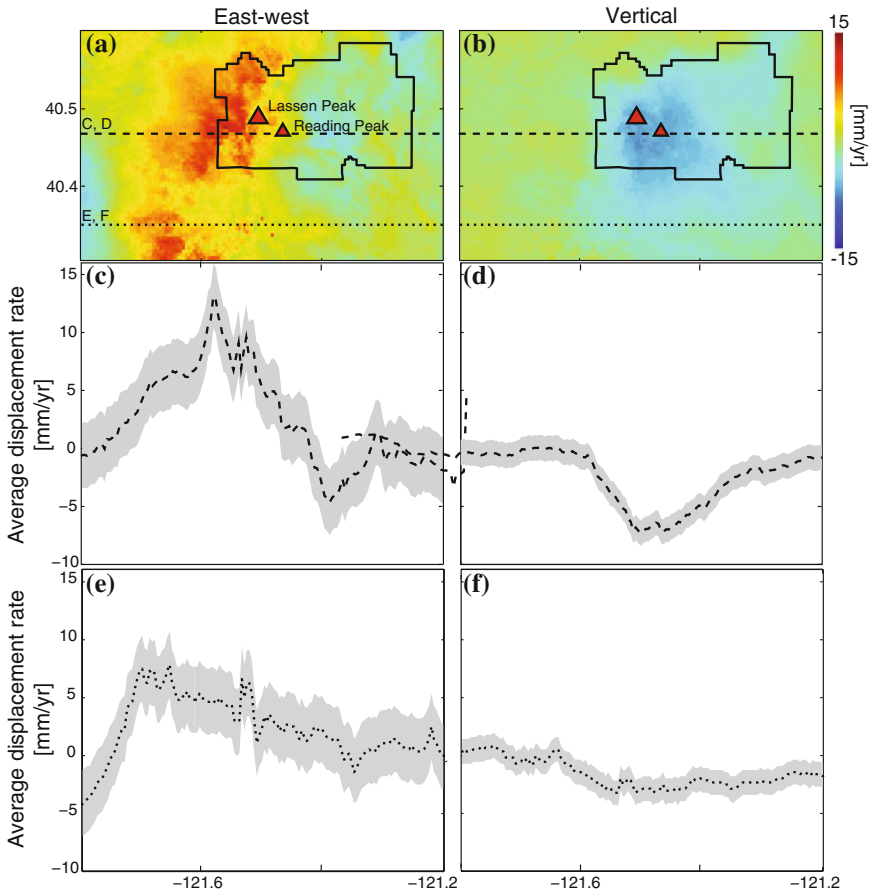


**Fig. 5.4** a, b. Horizontal (E-W) and vertical components of motion found by combining ENVISAT ascending and descending track ratemaps (Fig. 5.4). Black line shows the outline of Lassen Volcanic National Park. Dashed lines mark the location of the profiles drawn in c, d, e and f. c, d Profiles of horizontal and vertical components of motion with errors calculated using the method described in the text. e, f As for c and d but for the profile line drawn further south in a

shows maximum subsidence S of Reading Peak and E of Reading Peak, centred on the eastern cluster (Fig. 5.4b). Drawing displacement profiles E-W at the latitude of Reading Peak and N-S at the longitude of Lassen Peak, we find that the latitude of the maximum displacement is the same between ascending and descending datasets, but the longitude of the maximum displacement is offset by 8–10 km (Fig. 5.3d). As InSAR data is acquired from a side-looking satellite platform, the EW component of horizontal deformation is positive (towards satellite) for a descending orbit and negative (away from satellite) for an ascending orbit (e.g. Rosen et al. 2000), and this discrepancy is therefore likely to be due to a component of horizontal motion (e.g. Hooper et al. 2007).

Combining ascending and descending ENVISAT stacks using Eq. 5.1, we find that the maximum horizontal displacements at LaVC are  $\sim 10\text{--}15$  mm/yr, and maximum vertical displacements are  $\sim 5\text{--}10$  mm/yr (Fig. 5.4a, b). Drawing displacement profiles shows that the maximum vertical displacements, and the change from positive to negative horizontal displacements, occur SE of Lassen Peak at the latitude of Reading Peak (Fig. 5.4c, d). Whilst the vertical component of displacement is focussed on the edifice, the horizontal component extends over a broader region. We investigate whether this is indicative of tectonic motion across the volcano by drawing an additional displacement profile further south (Fig. 5.4e, f). This profile shows up to  $\sim 7$  mm/yr of motion, but displacements are in the opposite sense to tectonic extension inferred by normal faults in the region. A thorough analysis of GPS data is required to provide additional constraints upon the tectonic contribution to horizontal motion at LaVC, as was carried out at Medicine Lake Volcano (Poland et al. 2006).

### 5.3.2 Source Modelling

Given the ratio of horizontal to vertical displacements, we model subsidence of LaVC using a point or vertically elongate source. For all model geometries, the  $[x, y]$  location of the source is well constrained to be SW of Reading Peak and SE of Lassen Peak (Fig. 5.5), which is in agreement with preliminary models presented by Poland et al. (2004) (Table 5.2).

For the point source model, we identify a trade-off between source depth and source strength (Fig. 5.5c). The best fitting depth is  $\sim 9$  km, slightly shallower than that predicted by Poland et al. (2004), but consistent with a source located in the deeper part of the magmatic system. This model depth corresponds to a mean rate of volume change of  $-0.00325$  km<sup>3</sup>/yr between 2004 and 2010. The RMS error for this source geometry is 1.46, 1.81 and 2.39 mm for ENVISAT ascending, descending and ALOS ascending datasets respectively (Fig. 5.5a).

To model a vertically elongate geometry, we use a prolate ellipsoid (Yang et al. 1988) rather than a vertical dislocation (Okada 1985). Vertical dislocations have been used to model the opening or closing of a dyke (e.g. Jónsson et al. 1999), and although dyke intrusions are thought to have occurred at LaVC in the last century

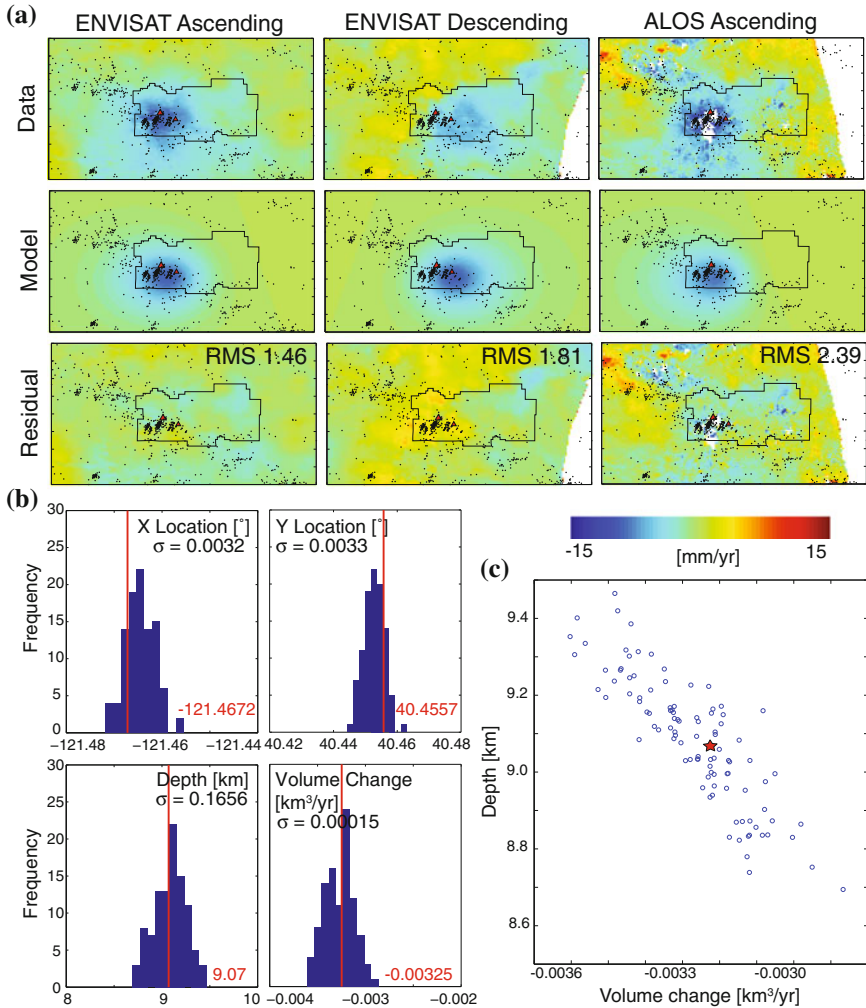


**Fig. 5.5** Results of Mogi modelling. **a** Data, model, and residuals for ENVISAT ascending, descending and ALOS ascending datasets. *Black dots* show seismicity as in Fig. 5.1. The *blues line* shows the outline of Lassen Volcanic National Park and the *red triangles* show Lassen and Reading Peak. Residual plots are labelled with RMS misfits. **b** Histograms show the distribution of model parameters found via Monte Carlo analysis. *Red lines* and *text* describe the best fitting model, with  $1\sigma$  values also labelled. **c** Scatter plot shows the trade off between the rate of volume change and the source depth, with the best fitting solution marked with the red star

**Table 5.2** Best-fitting analytical source models with bounds from Monte Carlo Error Analysis

Source	Reference	Longitude (°)	Latitude (°)	Depth (km)	Volume change (km <sup>3</sup> /yr)
Mogi	Poland et al. (2004)	-121.47	40.46	11.60	-0.0070
Mogi	This study	-121.47	40.45	8.91	-0.0031
		-121.46	40.49	9.24	-0.0034

(Clynne and Muffler 2010), this models predicts a characteristic tri-lobe deformation pattern that is inconsistent with the results of stacking. The ratio between the major and minor axes of the prolate ellipsoid is able to vary between 1 (for a sphere) and  $\rightarrow 0$  (for a closed pipe). Through Monte Carlo analysis, we find that models of prolate ellipsoids saturate at the minimum possible axis ratio and therefore, as the Mogi model provides a good fit to the data, we do not favour this as a realistic source geometry.

### 5.3.3 Time-Series of Source Volume Change

We have shown that subsidence of LaVC is well approximated using a point source (Fig. 5.5). Using the  $[x, y]$  location and depth of the source described in Table 5.2, we produce time-series of incremental source volume change for the displacements recorded by ENVISAT ascending and descending datasets. We choose to use all interferograms with  $\sigma < 0.15$ , but time-series produced using all interferograms, or the subsets of interferograms listed in Table 5.1, are contained within the Appendix (Fig. 5.8) and show comparable results.

Time-series analysis reveals that the rate of source volume change at LaVC has decreased over time, with a faster rate of volume loss between 2004 and 2007 than between 2007 and 2010 (Fig. 5.6a). Consequently the best fitting models to interferograms prior to 2005 require larger volume changes than for interferograms after 2007 (see examples in Fig. 5.6b). In total the cumulative volume decrease is  $\sim 0.015 \text{ km}^3$ , which is 5 times greater than the small estimated erupted volume from the 1914–1918 eruption (Clynne and Muffler 2010).

As there is an inherent trade off between Mogi source depth and strength (e.g. Fig. 5.5c), we perform an additional check to assess whether the change in rate could in fact be a function of varying source depth. We produce two ratemaps covering 2004–2007 and 2007–2010 (Fig. 5.7a) using all ENVISAT ascending track interferograms. This is the only dataset containing enough interferograms during both time periods such that both ratemaps are coherent within 5–10 km of the best fitting source location. The maximum displacement rates recorded by these stacks are  $-13 \pm 2.7 \text{ mm/yr}$  and  $-8 \pm 1.6 \text{ mm/yr}$  respectively. The error on the measurements is estimated using the mean value of  $\sigma$  found in Sect. 5.2.3 (Fig. 5.2). As we use

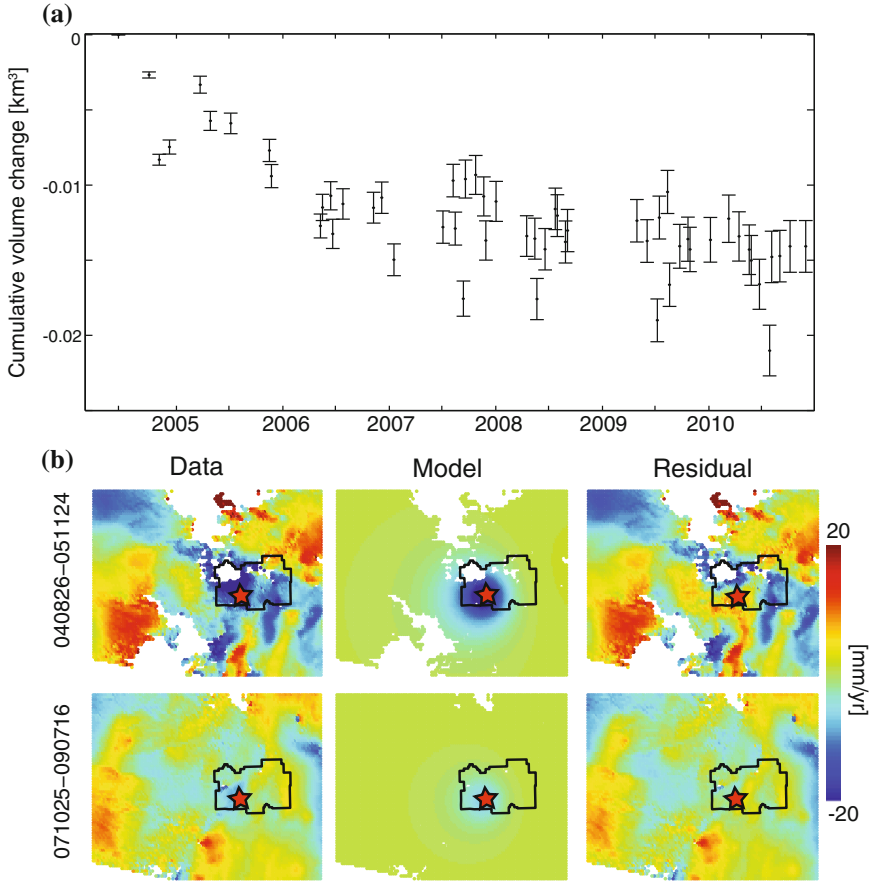


**Fig. 5.6** **a** Time-series of the rate of volume change found using ENVISAT ascending and descending track interferograms. Errorbars are calculated using phase  $\sigma$  beyond 10 km from the volcano summit. **b** Examples of data, model, residuals for interferograms within the period of rapid volume loss (*top*) and slower volume loss (*bottom*). The source location used in the inversion is shown by the star and described in Table 5.2

multiple interferograms, the error is reduced to  $\sigma/\sqrt{N}$ , where  $N$  is the number of observations and  $\sigma$  is assumed to be uncorrelated between observations (e.g. Parks et al. 2011). We then use the method described in Sect. 5.2.3 to produce trade off curves between source depth and strength for each stack (Fig. 5.7b). We find that the range of source depths span 5–15 km for both time periods, but that solutions for the later time period tend to be at greater depths. This suggests that the decrease in the rate of volume change could also be linked to a deepening of the source.

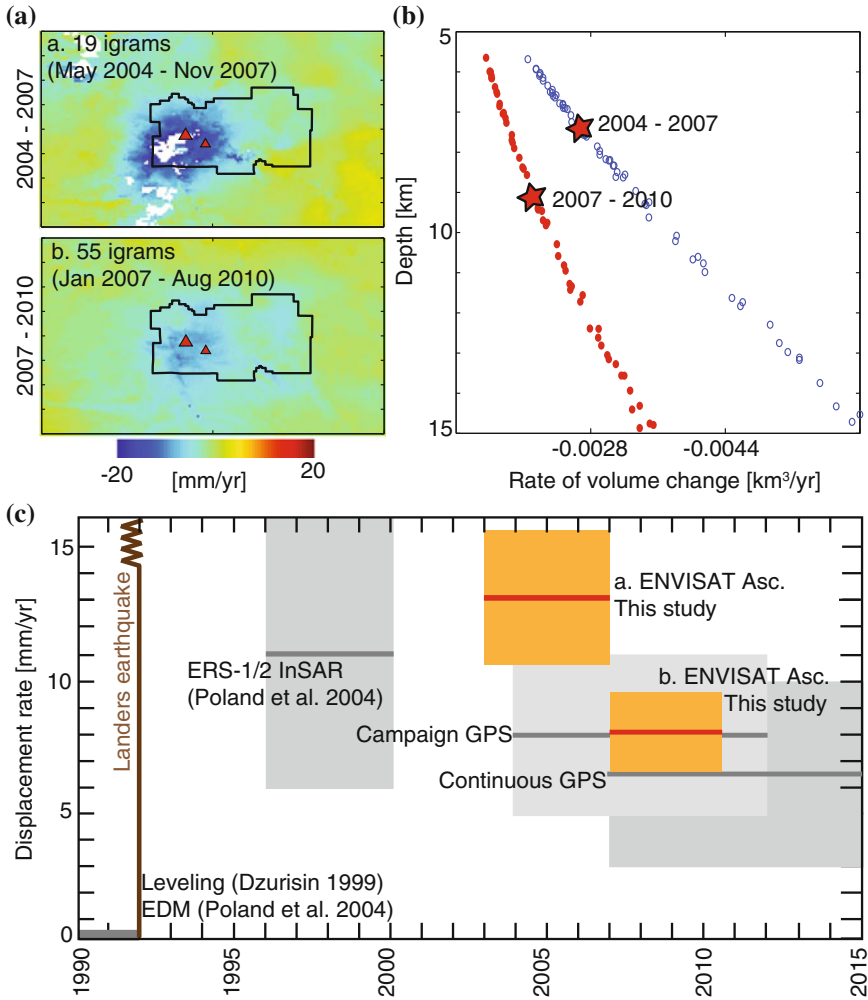


**Fig. 5.7** **a** ENVISAT ascending stacks for interferograms that cover **a.** 2004–2007 and **b.** 2007–2010, labelled with the number of interferograms (igrams) used. *Triangles* mark Lassen and Reading Peaks. **b** Scatter plot showing the trade off between the rate of volume change and the source depth for best fitting models to both time periods from Monte Carlo error analysis as in Fig. 5.5c. The [x,y] location is fixed to that described in Table 5.2. The best fitting solution for each stack is marked with the red star. **c** Schematic comparing subsidence rates from this study (*red*) and those obtained from other geodetic measurements (*grey*). Errorbars on ENVISAT InSAR measurements are described in the text

### 5.3.4 *Comparison with Past Geodetic Measurements*

The decrease in the rate of volume change (and therefore subsidence) over time appears to be consistent with other geodetic measurements made at the volcano (Fig. 5.7c). ERS interferograms between August 1996 and September 2000 show  $\sim 4.5$  cm of subsidence suggesting an average deformation rate of  $\sim 11$  mm/yr (Poland et al. 2004). This is larger than the maximum subsidence of  $\sim 8$  mm/yr documented by U.S. Geological Survey GPS campaigns between 2004 and 2012 (M. Lisowski, personal comm.). The lowest rates of subsidence were recorded by U.S. Geological Survey continuous GPS stations, which show maximum subsidence of 6–7 mm/yr between 2007 and 2015 (M. Lisowski, personal comm.). Whilst this is not a quantitative comparison between datasets, it suggests that the decrease in the rate of subsidence is a longer-lived feature.

Between 1981 and 2004, the EDM network at LaVC was resurveyed with GPS, which showed line-length changes of up to 145 mm (Poland et al. 2004). Assuming that the deformation rate has indeed decreased over time, a maximum bound can be placed upon the onset of subsidence by assuming line-length changes occurred at a minimum rate of 11 mm/yr (Poland et al. 2004). This implies that the onset of deformation was in the early 1990s. This agrees with leveling surveys, which showed that up to 1991 there had been no deformation greater than uncertainty in the measurements (10–20 mm) (Dzurisin 1999).

## 5.4 Discussion

Any mechanism inferred to account for subsidence at LaVC must fit the following constraints from the geodetic record and source models: (i.) the onset of deformation was in the early 1990s as inferred by EDM/GPS surveys and the rate of deformation derived from time-series analysis; (ii.) the rate of subsidence has decreased over time; and (iii.) the ratio of horizontal to vertical displacements is high, suggesting a point or vertically elongate rather than horizontally elongate source. In light of these constraints we draw comparisons with deformation observed at Medicine Lake Volcano located 100 km to the north. We then evaluate possible causes of subsidence, identifying which hypotheses warrant further investigation, and which mechanisms are unlikely to have contributed to ground deformation recorded in recent decades.

### 5.4.1 *Comparison with Medicine Lake Volcano*

Subsidence of Medicine Lake Volcano is also well characterised by geodetic measurements including leveling surveys which began in the 1950s (Dzurisin et al. 1991,



2002). Unlike subsidence at LaVC, these measurements show that deformation has been occurring at a constant rate of  $\sim 10$  mm/yr for over 65 years (Chap. 2). GPS and InSAR measurements show that the vertical component of deformation is  $\sim 3$  times larger than the horizontal component (Poland et al. 2006; Parker et al. 2014). Source models at Medicine Lake Volcano therefore infer a horizontally orientated source, which contrasts with best fitting models of LaVC (Table 5.2).

Given the comparable rate of deformation and proximity within the Cascades Volcanic Arc, Poland et al. (2004) suggest that the cause of subsidence at LaVC may be similar to that at Medicine Lake Volcano. Subsidence at Medicine Lake Volcano is thought to result from a combination of mechanisms including surface loading, combined with tectonic extension (Dzurisin et al. 2002), and cooling hot rock beneath the volcano (Poland et al. 2006; Chap. 4). However, we have shown that the source geometry and time-scales of deformation at the two volcanoes are quite different, and suggest that there are additional mechanisms that could be acting at LaVC. This includes the most recent eruption (1914–1918) and the prevalent hydrothermal system, which are discussed here in addition to the tectonic and thermal mechanisms implicated at Medicine Lake Volcano.

### 5.4.2 *Causes of Subsidence at LaVC*

#### **Crustal Extension and Surface Loading**

Like Medicine Lake Volcano, LaVC is located in a region of tectonic extension, and focal mechanisms within the East, Middle and West seismic clusters are consistent with extension of the Basin and Range (Janik and McLaren 2010). Subsidence of other volcanoes in extensional settings, including Medicine Lake Volcano, has been partly attributed to loading above hot, weak, extended crust (Dzurisin et al. 2002; Poland et al. 2006; Dzurisin 2007; de Zeeuz-van Daltsen et al. 2012). At Medicine Lake Volcano the current rate of subsidence is thought to be anomalously high. This is at odds with GPS measurements of current extension rates, which do not show resolvable extensional strain across the edifice. Consequently extension is thought to enhance subsidence rather than be the driving mechanism (Poland et al. 2006).

At LaVC, it is difficult to envisage why tectonic extension would cause the sudden onset of subsidence in recent decades. The deformation signal is also confined to the summit region, and there is no evidence from InSAR of peripheral uplift that may indicate loading of the edifice (e.g. Dzurisin et al. 2002). The localised nature of deformation, plus evidence of intrusive material, and the vigorous hydrothermal system, suggest that tectonic extension is likely to contribute to subsidence at LaVC rather than be the principal cause of deformation.

## Cooling and Crystallisation

Seismic and petrological observations at LaVC provide strong evidence for a magmatic heat source (Sect. 5.1.2). This is in agreement with models of the LaVC hydrothermal system, which suggest that hydrothermal features are located above hot, brittle rock, overlying residual magma (Janik and McLaren 2010). In Chap. 4, we show that cooling and crystallisation of subsurface magma (volume  $< 3\text{ km}^3$ ) may sustain subsidence over decadal time-scales. We use the example of Medicine Lake Volcano to investigate a linear subsidence signal, but by exploring the parameter space, show that the rate of volume change decreases in the decades immediately after intrusion. This is comparable to the time-series of volume change at LaVC found using ENVISAT ascending and descending datasets (Fig. 5.6a).

At LaVC we have a record of apparent quiescence preceding the onset of deformation. The apparent lack of uplift prior to subsidence suggests that any magma body that is now cooling was preexisting, but in thermal equilibrium with the surrounding country rock, or that compressibility of the country rock facilitated intrusion without causing deformation (e.g. Mastin et al. 2009; de Zeeuw-van Dalssen et al. 2013). Further testing is required to assess the role of cooling and crystallisation of subsurface magma in recent subsidence at LaVC, but given the evidence for subsurface magma bodies from seismic imaging (Clynne 1985), we suggest that this mechanism is likely to be contributing to deformation.

## Eruption

The 1914–1918 eruption of Lassen Peak resulted in the extrusion of  $0.003\text{ km}^3$  of material (Clynne and Muffler 2010), which would have resulted in a volume loss at depth. Co-eruptive volume loss has been linked to subsidence at numerous volcanoes, although such deformation typically lasts on the order of days - months rather than years - decades (Pyle et al. 2013). Deformation may continue for longer periods of time at an exponentially decreasing rate due to the viscoelastic response of high-temperature material surrounding the eruption source (Dragoni and Maganensi 1989; Chap. 4). However, this is unlikely to be directly linked to present day subsidence, as geodetic surveys up until at least the 1990s do not show evidence of surface displacements. We therefore do not consider eruptive volume loss or viscoelastic relaxation following the 1914–1918 eruption to be a likely cause of subsidence.

## Changes in the Distribution of Magmatic/Hydrothermal Fluids

Volcanic subsidence has also been linked to the migration of fluids from a magmatic or hydrothermal reservoir. At Campi Flegrei, periods of subsidence are interpreted to represent the drainage of fluids from the hydrothermal system (e.g. Lundgren et al. 2001; Battaglia et al. 2006). Subsidence at Askja, Iceland, is also thought to result, in part, from drainage of magma from shallow depths to a deeper storage zone (de Zeeuw-van Dalssen et al. 2013). Downward drainage of magmatic or hydrothermal fluids would result in an increase in source depth over time, which is supported

by comparing the results of Mogi modelling at LaVC for 2004–2007 and 2007–2010 (Fig. 5.7b). The occurrence of LP earthquakes at LaVC also suggests the movement of magma/fluids at depth, but these events are located further west of the modelled source location and the western cluster of seismicity (Pitt et al. 2002), (Fig. 5.1a).

The apparent onset of subsidence at LaVC is coincident with the 1992  $M_w$  7.3 Landers earthquake, which occurred 840 km SSE, and is known to have triggered 38 seismic events at the volcano including a  $M_w$  3.5 event within 13 min of the mainshock (Hill et al. 1993; McLaren and Janik 1996). Recent observations of large magnitude subduction zone earthquakes in Chile and Japan suggest that earthquake-triggered subsidence may be a widespread phenomenon in active volcanic chains (Takada and Fukushima 2013; Pritchard et al. 2013). In both cases, subsidence was observed at hydrothermally active volcanoes and is linked to tensional static stresses imparted during the earthquake. In the weeks following the 2010  $M_w$  8.8 Maule earthquake in Chile, 5 volcanoes subsided by up to 15 cm (Pritchard et al. 2013). Deformation is attributed to the co-seismic release of hydrothermal fluids due to shaking, and an increase in tensional static stress. In Japan, 5 volcanoes rapidly subsided in response to the 2011  $M_w$  9.0 Tohoku earthquake (Takada and Fukushima 2013). Again deformation is attributed to tensional static stress changes, which are inferred to have displaced the sides of hot, low viscosity magmatic complexes underlying the volcanoes, displacing the tops downwards (Takada and Fukushima 2013).

The volcanoes in Chile and Japan were all located <200 km from the earthquake epicentral region. Static stress changes decrease with distance as  $1/r^3$ , and for the Landers earthquake were insignificant (less than daily tidal stress fluctuations) beyond ~200 km (Hill et al. 1995). However, dynamic stresses due to the propagation of surface waves reach further, decreasing as  $1/r^{3/2}$ . One case of surface deformation triggered by earthquakes has been identified at distances >400 km. This was Long Valley Caldera, California following the 1992  $M_w$  7.3 Landers earthquake. Here a compressional strain transient was recorded, which is attributed to dynamic stress changes facilitating a magmatic intrusion in a region already under tectonic extension (Hill et al. 1995); bubble formation during shaking (Linde et al. 1994); and/or an upward surge of high pressure fluids (Johnston et al. 1995). In all of these discussed settings, ground deformation was observed within days or weeks of the mainshock. These mechanisms are therefore unlikely to apply directly to LaVC, where subsidence has continued for at least the last 2 decades.

Dynamic stresses imparted by the Landers earthquake reached 1 -2 bar in the LaVC region, and triggered seismicity is attributed to variations in pore pressure (Hill et al. 1993). Hydrothermal poro-elastic variations have been linked to deformation over longer time-scales (e.g. Kiska, Aleutians: Lu et al. 2002). At LaVC the extent of subsidence is in good agreement with the location of the main hydrothermal features, and the best fitting source location is at the intersection between the two proposed cells of the hydrothermal system described in Sect. 5.1 (Janik and McLaren 2010). However, hydrothermal systems typically circulate at shallow depths, where

temperatures and the pressure of the overburden facilitate permeability (Brace 1972), whereas the modelled source depth at LaVC is thought to be  $>5$  km (Table 5.2). Another plausible mechanism is that dynamic stresses during the Landers earthquake perturbed the hydrothermal system, increasing permeability and allowing meteoric fluids to penetrate to greater depths. This may result in a thermal disequilibrium, as heat is removed from the system by fluid convection in the overburden at a faster rate than it is supplied via conduction from the underlying magma body (e.g. Norton and Knight 1977). In this case the permeable region would extend downwards due to contraction and tensile cracking (Fournier 2007), which agrees with a possible increase in source depth over time (Fig. 5.6b). Further modelling of the LaVC system is required to realistically validate the role of the Landers earthquake in subsidence at LaVC, but changes in the distribution of magmatic/hydrothermal fluids, along with thermal and tectonic contributions, are likely to play a role in the observed time-dependent subsidence.

## 5.5 Conclusions

Lassen Volcanic Center is one of only two Cascade volcanoes to have erupted in the past century. The volcano has also subsided in recent years. Here we present a summary of InSAR observations at the volcano between 2004 and 2010 to constrain the onset, temporal evolution, and spatial characteristics of deformation. Time-series analysis shows that the rate of subsidence and subsurface volume loss has decreased over time from  $>10$  mm/yr in 2004–2007 to  $\sim 8$  mm/yr in 2007–2010. Combining multiple tracks of InSAR data we find that the ratio of horizontal to vertical displacements is high, and through inverse modelling we find that the source of deformation is well represented by a point source at  $\sim 9$  km depth. Subsidence is unlikely to be linked to the 1914–1918 eruption, but may be associated with cooling within the magmatic system, and/or changes in the distribution of fluids within the magmatic/hydrothermal system. Additional constraints are required to investigate whether the 1992  $M_w 7.3$  Landers earthquake played a role in the onset of subsidence.

## Appendix

See Fig. 5.8.

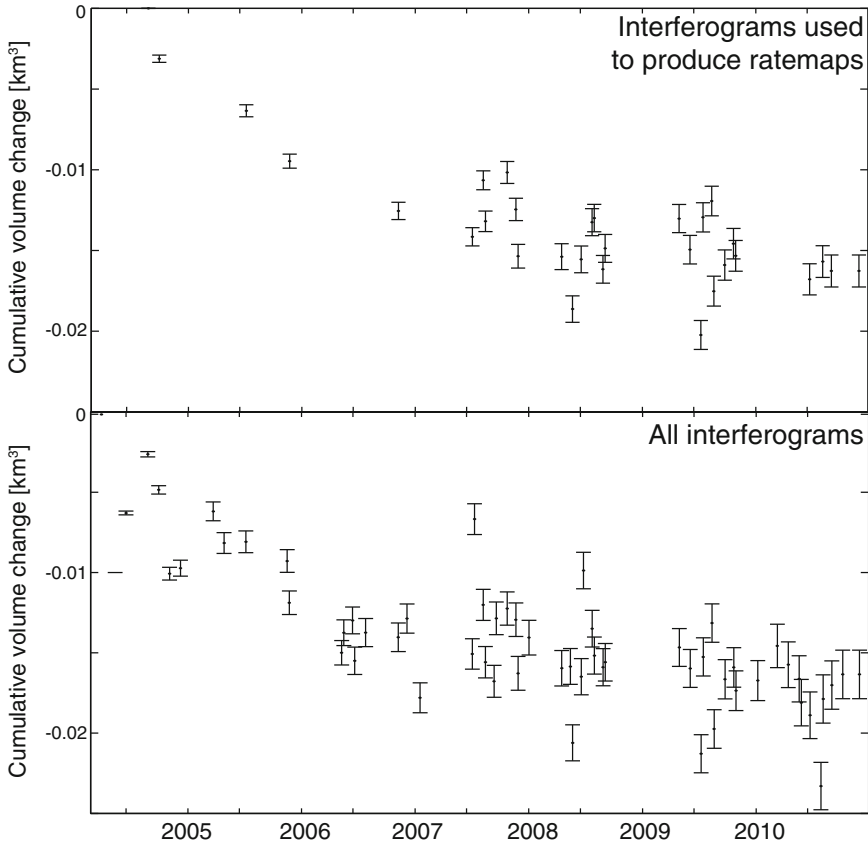


**Fig. 5.8** Time-series of the rate of volume change found using different subsets of ENVISAT ascending and descending track interferograms. *Top* interferograms used for stacking as detailed in Table 5.1. *Bottom* all interferograms as detailed in Table 5.1. Errorbars are calculated using phase  $\sigma$  beyond 10km from the volcano summit

## References

- Amelung, F., & Bell, J. (2003). Interferometric synthetic aperture radar observations of the 1994 Double Spring Flat, Nevada, earthquake (M5.9): Main shock accompanied by triggered slip on a conjugate fault. *Journal of Geophysical Research*, 108(B9).
- Bagnardi, M., Amelung, F., & Poland, M. P. (2013). A new model for the growth of basaltic shields based on deformation of Fernandina volcano, Galápagos Islands. *Earth and Planetary Science Letters*, 377, 358–366.
- Battaglia, M., Troise, C., Obrizzo, F., Pingue, F., & De Natale, G. (2006). Evidence for fluid migration as the source of deformation at Campi Flegrei caldera, Italy. *Geophysical Research Letters*, 33(L01307).
- Berardino, P., Fornaro, G., Lanari, R., & Sansosti, E. (2002). A new algorithm for surface deformation monitoring based on small baseline differential SAR interferograms. *IEEE Transactions on Geoscience and Remote Sensing*, 40, 2375–2383.

- Biggs, J., Wright, T., Lu, Z., & Parsons, P. (2007). Multi-interferogram method for measuring inter seismic deformation: Denali Fault, Alaska. *Geophysical Journal International*, 170, 1165–1179.
- Biggs, J., Anthony, E. Y., & Ebinger, C. J. (2009a). Multiple inflation and deflation events at Kenyan volcanoes, East African Rift. *Geology*, 37(11), 979–982.
- Biggs, J., Robinson, D. P., & Dixon, T. H. (2009b). The 2007 Pisco, Peru, earthquake (M8.0): Seismology and geodesy. *Geophysical Journal International*, 176, 657–669.
- Biggs, J., Lu, Z., Fournier, T., & Freymueller, J. T. (2010). Magma flux at Okmok Volcano, Alaska, from a joint inversion of continuous GPS, campaign GPS and interferometric synthetic aperture radar. *Journal of Geophysical Research*, 115(B12401).
- Biggs, J., Ebmeier, S. K., Aspinall, W. P., Lu, Z., Pritchard, M. E., Sparks, R. S. J., & Mather, T. A. (2014). Global link between deformation and volcanic eruption quantified by satellite imagery. *Nature Communications*, 5, 3471.
- Brace, W. F. (1972). Pore pressure in geophysics. In H. C. Heard, I. Y. Borg, N. L. Carter, C. B. Raleigh (Eds.), *Flow and fracture of rocks*, Geophysical monograph (Vol. 16, pp. 265–273).
- Chiodini, G., Vandemeulebroeck, J., Caliro, S., D’Auria, L., De Martino, P., Mangiacapra, A., et al. (2015). Evidence of thermal-driven processes triggering the 2005–2014 unrest at Campi Flegrei caldera. *Earth and Planetary Science Letters*, 414, 58–67.
- Clynne, M. A. (1985). Quaternary volcanism in the southernmost cascade range, California. In M. Guffanti & L. J. P. Muffler (Eds.), *Proceedings of the Workshop on Geothermal Resources of the Cascade Range: U.S. Geological Survey Open-File Report 85521*, p. 2430.
- Clynne, M. A., & Muffler, L. J. P. (2010). Geologic map of Lassen volcanic national park and vicinity, California. U.S. Geological Survey Scientific Investigations Map I2899, scale 1:50,000, 110 p.
- Clynne, M. A., Robinson, J. E., Nathenson, M., Muffler, L. J. P. (2012). Volcano hazards assessment for the Lassen region, Northern California. U.S. Geological Survey Scientific Investigations Report 2012-5176-A, 56 p.
- Clynne, M. A. (1999). A complex magma mixing origin for rocks erupted in 1915, Lassen Peak, California. *Journal of Petrology*, 40(1), 105–132.
- de Zeeuw-van Dalen, E., Rymer, H., Sturkell, E., Pedersen, R., Hooper, A., Sigmundsson, F., et al. (2013). Geodetic data shed light on ongoing caldera subsidence at Askja, Iceland. *Bulletin of Volcanology*, 75(5), 1–13.
- de Zeeuw-van Dalen, E., Pedersen, R., Hooper, A., & Sigmundsson, F. (2012). Subsidence of Askja caldera 2000–2009: Modelling of deformation processes at an extensional plate boundary constrained by time series InSAR analysis. *Journal of Volcanology and Geothermal Research*, 213, 72–82.
- Donnelly-Nolan, J. M., Grove, T. L., Lanphere, M. A., & Champion, D. E. (2008). Eruptive history and tectonic setting of Medicine Lake Volcano, a large rear-arc volcano in the southern Cascades. *Journal of Volcanology and Geothermal Research*, 117, 313.
- Dragoni, M., & Magnanensi, C. (1989). Displacement and stress produced by a pressurized, spherical magma chamber, surrounded by a viscoelastic shell. *Physics of the Earth and Planetary Interiors*, 56(3), 316–328.
- Dzurisin, D. (1999). Results of repeated leveling surveys at Newberry Volcano, Oregon, and near Lassen Peak Volcano, California. *Bulletin of Volcanology*, 61(1–2), 83–91.
- Dzurisin, D. (2007). *Volcano deformation: Geodetic monitoring techniques*. Chichester: Springer-Praxis.
- Dzurisin, D., Donnelly-Nolan, J. M., Evans, J. R., & Walter, S. R. (1991). Crustal subsidence, seismicity, and structure near Medicine Lake volcano, California. *Journal of Geophysical Research*, 96(B10), 16319–16333.
- Dzurisin, D., Poland, M. P., & Bürgmann, R. (2002). Steady subsidence of Medicine Lake Volcano, Northern California, revealed by repeated levelling surveys. *Journal of Geophysical Research*, 107(B12), ECV 8-1.
- Fialko, Y., Khazan, Y., & Simons, M. (2001a). Deformation due to a pressurised horizontal circular crack in an elastic half-space, with applications to volcano geodesy. *Geophysical Journal International*, 146(1), 181–190.

- Fialko, Y., Simons, M., & Agnew, D. (2001b). The complete (3-D) surface displacement field in the epicentral area of the 1999 Mw7. 1 Hector Mine earthquake, California, from space geodetic observations. *Geophysical Research Letters*, 28(16), 3063–3066.
- Fournier, R. O. (2007). *Hydrothermal systems and volcano geochemistry* (pp. 323–341). Chichester: Springer-Praxis.
- Goldstein, R., Zebker, H., & Werner, C. (1988). Satellite radar interferometry: Two dimensional phase unwrapping. *Radio Science*, 23(4), 713–720.
- Goldstein, R., & Werner, C. (1998). Radar interferogram filtering for geophysical applications. *Geophysical Research Letters*, 25(21), 4035–4038.
- Gourmelen, N., Amelung, F., & Lanari, R. (2010). Interferometric synthetic aperture radar-GPS integration: Interseismic strain accumulation across the Hunter Mountain fault in the eastern California shear zone. *Journal of Geophysical Research*, 115(B9).
- Guffanti, M., & Weaver, C. S. (1988). Distribution of late Cenozoic volcanic vents in the Cascade Range: Volcanic arc segmentation and regional tectonic considerations. *Journal of Geophysical Research*, 93(B6), 6513–6529.
- Guffanti, M., Clyne, M. A., Smith, J. G., Muffler, L. J. P., & Bullen, T. D. (1990). Late Cenozoic volcanism, subduction, and extension in the Lassen region of California, southern Cascade Range. *Journal of Geophysical Research*, 95(B12), 19453–19464.
- Hamling, I. J., Wright, T. J., Calais, E., Lewi, E., & Fukahata, Y. (2014). InSAR observations of post-rifting deformation around the Dabbahu rift segment, Afar, Ethiopia. *Geophysical Journal International*, 197(1), 33–49.
- Hanssen, R. F. (2001). *Radar interferometry: Data interpretation and analysis*. Norwell: Kluwer Academic.
- Hildreth, W. (2007). *Quaternary magmatism in the Cascades - geological perspectives*. U.S. Geological Survey Professional Paper (1744).
- Hill, D. P., Reasenber, P. A., Michael, A., Arabaz, W. J., Beroza, G., Brumbaugh, D., et al. (1993). Seismicity remotely triggered by the magnitude 7.3 Landers, California, earthquake. *Science*, 260(5114), 1617–1623.
- Hill, D. P., Johnston, M. J. S., Langbein, J. O., & Bilham, R. (1995). Response of Long Valley caldera to the Mw = 7.3 Landers, California, earthquake. *Journal of Geophysical Research*, 100(B7), 12985–13005.
- Hooper, A., Segall, P., & Zebker, H. (2007). Persistent scatterer interferometric synthetic aperture radar for crustal deformation analysis, with application to Volcán Alcedo, Galápagos. *Journal of Geophysical Research*, 112(B7).
- Humphrey, J., & McLaren, M. (1995). Seismicity along the boundary between the modoc plateau, southern cascade mountains, and northern sierra nevada. In W. D. Page (Ed.), *Quaternary Geology Along the Boundary Between the Modoc Plateau, Southern Cascade Mountains and Northern Sierra Nevada*, Appendix A (27 pp.). 1995 Pacific Cell Field Trip: Friends of the Pleistocene.
- Janik, C. J., & McLaren, M. K. (2010). Seismicity and fluid geochemistry at Lassen Volcanic National Park, California: Evidence for two circulation cells in the hydrothermal system. *Journal of Volcanology and Geothermal Research*, 189(3), 257–277.
- Johnston, M. J. S., Hill, D. P., Linde, A. T., Langbein, J., & Bilham, R. (1995). Transient deformation during triggered seismicity from the 28 June 1992 Mw = 7.3 Landers earthquake at Long Valley volcanic caldera, California. *Bulletin of the Seismological Society of America*, 85(3), 787–795.
- Jolivet, R., Grandin, R., Lasserre, C., & M.-P., D., Peltzer, G. (2011). Systematic InSAR tropospheric phase delay corrections from global meteorological reanalysis data. *Geophysical Research Letters*, 38(L17311).
- Jónsson, S., Zebker, H., Cervelli, P., Segall, P., Garbeil, H., Mouginiis-Mark, P., et al. (1999). A shallow-dipping dike fed the 1995 flank eruption at Fernandina volcano, Galapagos, observed by satellite radar interferometry. *Geophysical Research Letters*, 26(8), 1077–1080.
- Jónsson, S., Zebker, H., Segall, P., & Amelung, F. (2002). Fault slip distribution of the 1999 Mw 7.1 Hector Mine, California, earthquake, estimated from satellite radar and GPS measurements. *Bulletin of the Seismological Society of America*, 92(4), 1377–1389.

- Klein, F. W. (1979). Earthquakes in Lassen Volcanic National Park, California. *Bulletin of the Seismological Society of America*, 69(3), 867–875.
- Klemetti, E. W., & Clynnne, M. A. (2014). Localized rejuvenation of a crystal mush recorded in Zircon temporal and compositional variation at the Lassen Volcanic Center, Northern California. *PLoS one*, 9(12), e113157.
- Linde, A. T., Sacks, I. S., Johnston, M. J. S., Hillt, D. P., & Bilham, R. G. (1994). Increased pressure from rising bubbles as a mechanism for remotely triggered seismicity. *Nature*, 371(6496), 408–410.
- Lu, Z., Power, J. A., McConnell, V. S., Wicks, C., & Dzurisin, D. (2002). Preeruptive inflation and surface interferometric coherence characteristics revealed by satellite radar interferometry at Makushin Volcano, Alaska: 1993–2000. *Journal of Geophysical Research*, 107(B11), ECV 1-1–ECV 1-13.
- Lundgren, P., Usai, S., Sansosti, E., Lanari, R., Tesauro, M., Fornaro, G., et al. (2001). Modeling surface deformation observed with synthetic aperture radar interferometry at Campi Flegrei caldera. *Journal of Geophysical Research*, 106(B9), 19355–19366.
- Mann, D., & Freymueller, J. (2003). Volcanic and tectonic deformation on Unimak Island in the Aleutian Arc, Alaska. *Journal of Geophysical Research*, 108(B2), 2108.
- Mastin, L., Lisowski, M., Roeloffs, E., & Beeler, N. (2009). Improved constraints on the estimated size and volatile content of the Mount St. Helens magma system from the 2004–2008 history of dome growth and deformation. *Geophysical Research Letters*, 36(L20304).
- McLaren, M. K., & Janik, C. J. (1996). Microearthquake clusters and the Lassen hydrothermal system, northern California. *Eos, Transactions American Geophysical Union*, 77(F513).
- Mogi, K. (1958). Relations between eruptions of various volcanoes and the deformations of the ground surfaces around them. *Bulletin of the Earthquake Research Institute of the University of Tokyo*, 36, 99–134.
- Norris, R. D., Meagher, K. L., & Weaver, C. S. (1997). The 1936, 1945–1947, and 1950 earthquake sequences near Lassen Peak, California. *Journal of Geophysical Research*, 102(B1), 449–457.
- Norton, D., & Knight, J. (1977). Transport phenomena in hydrothermal systems: cooling plutons. *American Journal of Science*, 277, 937–981.
- Okada, Y. (1985). Surface deformation due to shear and tensile faults in a half-space. *Bulletin of the Seismological Society of America*, 75(4), 1135–1154.
- Parker, A. L., Biggs, J., & Lu, Z. (2014). Investigating long-term subsidence at Medicine Lake Volcano, CA, using multi temporal InSAR. *Geophysical Journal International*, 199(2), 844–859.
- Parker, A. L., Biggs, J., Walters, R. J., Ebmeier, S. K., Wright, T. J., Teanby, N. A., et al. (2015). Systematic assessment of atmospheric uncertainties for InSAR data at volcanic arcs using large-scale atmospheric models: Application to the Cascade volcanoes, United States. *Remote Sensing of Environment*, 170, 102–114.
- Parks, M. M., Biggs, J., Mather, T. A., Pyle, D. M., Amelung, F., Monsalve, M. L., et al. (2011). Co-eruptive subsidence at Galeras identified during an InSAR survey of Colombian volcanoes (2006–2009). *Journal of Volcanology and Geothermal Research*, 202(3), 228–240.
- Parks, M. M., Moore, J., Papanikolaou, X., Biggs, J., Mather, T. A., Pyle, D. M., et al. (2015). From quiescence to unrest-20 years of satellite geodetic measurements at Santorini volcano, Greece. *Journal of Geophysical Research*, 120(2), 1309–1328.
- Paulson, K. M., & Ingebritsen, S. E. (1991). Sodium and chloride data from selected streams in the Lassen area, north-central California, and their relation to thermal-fluid discharge from the Lassen hydrothermal system. U.S. Geological Survey Water- Resources Investigations Report 90-4201, 29 pp.
- Pearse, J., & Fialko, Y. (2010). Mechanics of active magmatic intraplate tectonics in the Rio Grande Rift near Socorro, New Mexico. *Journal of Geophysical Research*, 115(B7).
- Pinel, V., Poland, M. P., & Hooper, A. (2014). Volcanology: Lessons learned from synthetic aperture radar imagery. *Journal of Volcanology and Geothermal Research*, 289, 81–113.



- Pitt, A. M., Hill, D. P., Walter, S. W., & Johnson, M. J. S. (2002). Midcrustal, long-period earthquakes beneath northern California volcanic areas. *Seismological Research Letters*, 73(2), 144–152.
- Poland, M., Bawden, G., Lisowski, M., & Dzurisin, D. (2004). Newly discovered subsidence at Lassen Peak, southern Cascade Range, California, from InSAR and GPS. [abs.]: Eos (American Geophysical Union Transactions) v. 85, Fall Meeting Supplement, abs. G51A-0068.
- Poland, M. P., Bürgmann, R., Dzurisin, D., Lisowski, M., Masterlark, T., Owen, S., et al. (2006). Constraints on the mechanism of long-term, steady subsidence at Medicine Lake volcano, northern California, from GPS, levelling and InSAR. *Journal of Volcanology and Geothermal Research*, 150(1), 55–78.
- Pritchard, M. E., Jay, J. A., Aron, F., Henderson, S. T., & Lara, L. E. (2013). Subsidence at southern Andes volcanoes induced by the 2010 Maule, Chile earthquake. *Nature Geoscience*, 6(8), 632–636.
- Pyle, D. M., Mather, T. A., & Biggs, J. (2013). Remote sensing of volcanoes and volcanic processes: integrating observation and modelling-introduction. *Geological Society, London, Special Publications*, 380(1), 1–13.
- Reverso, T., Vandemeulebrouck, J., Jouanne, F., Pinel, V., Villemin, T., Sturkell, E., et al. (2014). A two-magma chamber model as a source of deformation at Grímsvötn Volcano, Iceland. *Journal of Geophysical Research*, 119(6), 4666–4683.
- Rosen, P. A., Hensley, S., Joughin, I. R., Li, F. K., Madsen, S. N., Rodriguez, E., et al. (2000). Synthetic Aperture Radar Interferometry. *Proceedings of the IEEE*, 88(3), 333–382.
- Rosen, P., Hensley, S., Peltzer, G., & Simons, M. (2004). Updated repeat orbit interferometry package released. *EOS, Transactions AGU*, 85(5), 47.
- Samsonov, S., & d'Oreye, N. (2012). Multidimensional time-series analysis of ground deformation from multiple InSAR data sets applied to Virunga Volcanic Province. *Geophysical Journal International*, 191(3), 1095–1108.
- Segall, P. (2010). *Earthquake and volcano deformation*. Princeton: Princeton University Press.
- Sorey, M. L., & Colvard, E. M. (1994). Measurements of heat and mass flow from thermal areas in Lassen Volcanic National Park, California, 1984 - 1993. U.S. Geological Survey Water-Resources Investigations Report 94-4180-A, 35 pp.
- Sorey, M. L., Colvard, E. M., & Ingebritsen, S. E. (1994). Measurements of thermal-water discharge outside Lassen Volcanic National Park, California, 1983-94. U.S. Geological Survey Water-Resources Investigations Report 94-4180-B, 45 pp.
- Takada, Y., & Fukushima, Y. (2013). Volcanic subsidence triggered by the 2011 Tohoku earthquake in Japan. *Nature Geoscience*, 6(8), 637–641.
- Turrin, B. D., Christiansen, R. L., Clynne, M. A., Champion, D. E., Gerstel, W. J., Muffler, L. J. P., et al. (1998). Age of Lassen Peak, California, and implications for the ages of late Pleistocene glaciations in the southern Cascade Range. *Geological Society of America Bulletin*, 110(7), 931–945.
- Walter, S., Rojas, V., & Kollman, A. (1984). Seismicity of the Lassen Peak area, California. *Geothermal Resources Council Transactions*, 8, 523–527.
- Walters, R. J., Elliott, J. R., Li, Z., & Parsons, B. (2013). Rapid strain accumulation on the Ashkabad fault (Turkmenistan) from atmosphere-corrected InSAR. *Journal of Geophysical Research*, 118(7), 3674–3690.
- Wang, H., Wright, T. J., & Biggs, J. (2009). Interseismic slip rate of the northwestern Xianshuihe fault from InSAR data. *Geophysical Research Letters*, 36(3).
- Wells, R. E., Weaver, C. S., & Blakely, R. J. (1998). Fore-arc migration in Cascadia and its neotectonic significance. *Geology*, 26(8), 759–762.
- Wright, T., Lu, Z., & Wicks, C. (2004a). Constraining the slip distribution and fault geometry of the Mw 7.9, 3 November 2002, Denali fault earthquake with interferometric synthetic aperture radar and global positioning system data. *Bulletin of the Seismological Society of America*, 94(6B), S175–S189.

- Wright, T. J., Parsons, B. E., & Lu, Z. (2004b). Toward mapping surface deformation in three dimensions using InSAR. *Geophysical Research Letters*, 31(1).
- Yang, X.-M., Davis, P. M., & Dieterich, J. H. (1988). Deformation from inflation of a dipping finite prolate spheroid in an elastic half-space as a model for volcanic stressing. *Journal of Geophysical Research*, 93(B5), 4249–4257.

# Chapter 6

## Summary and Outlook

Within this thesis I use sub-optimal InSAR data to investigate long-term subsidence of volcanoes in the southern Cascades. I approach this problem from two perspectives: firstly in improving the application of InSAR data in the Cascades Volcanic Arc using multi temporal analysis and large-scale atmospheric models; and secondly, in developing a modelling approach to interpret long-term volcanic subsidence related to cooling magmatic intrusions. In this summary, I review the outcomes of each thesis chapter, identifying the main findings and highlighting where further advances could be made. I then finish by discussing the future role of InSAR as a tool in volcanology.

### 6.1 Application of InSAR Data in the Cascades Volcanic Arc

Past InSAR surveys throughout the Cascades have been of variable success due to dense vegetation, snow cover and atmospheric artefacts (Poland et al. 2006; Poland and Lu 2008; Parker et al. 2014). In Chap. 2 (Parker et al. 2014), I demonstrate how InSAR may be successfully used in a mountainous, vegetated volcanic arc, by applying a suite of multi temporal analysis methods designed to improve interferogram coherence, and reduce atmospheric and orbital sources of error. Using the case study of Medicine Lake Volcano, I apply three methods to investigate steady subsidence: a stacking strategy based upon the noise characteristics of each dataset; pixel-wise rate-map formation ( $\pi$ -RATE); and persistent scatterer InSAR (StaMPS). I find that  $\pi$ -RATE significantly improves coherence close to the volcano summit (>30% increase for ENVISAT data), and suggest that this approach is well suited to investigating linear deformation signals in volcanic settings. Like  $\pi$ -RATE, StaMPS significantly improves coherence at the volcano summit, particularly in regions covered by lava flows. Whilst I do not use StaMPS to produce time-series of ground displacements, this method is also well suited to investigating volcano deformation that is not linear in time. The results of Chap. 2 (Parker et al. 2014) could be further

improved by unwrapping the small baseline interferograms in 3-D (space and time) (Hooper and Zebker 2007), and by implementing combined persistent scatterer - small baseline methods (Hooper 2008) as described in Chap. 1.

In Chap. 3 (Parker et al. 2015), I address topographically correlated atmospheric artefacts using two large-scale atmospheric models, ERA-Interim (ERA-I) and North American Regional Reanalysis (NARR). Previous studies have used these models to correct interferograms in retrospect (Doin et al. 2009; Pinel et al. 2011; Jolivet et al. 2011; Walters et al. 2013; Jolivet et al. 2014), and I expand upon this by correcting the archive of InSAR data at Lassen Volcanic Center. I find that NARR reduces interferogram standard deviation in 79 % of cases by an average of 22 %. Comparing the two models shows that ERA-I reduces interferogram standard deviation in fewer cases, but the geographical coverage of this model means that it is widely applicable to volcanoes across the globe. This approach of correcting atmospheric uncertainties does not account for turbulent atmospheric effects, which will remain problematic, but may be reduced by the use of multiple interferograms as is shown in Chap. 2 (Parker et al. 2014).

InSAR data is being used increasingly as an active monitoring tool in evaluations of volcanic hazards, and as the temporal coverage of global InSAR data increases, approaches are required to account for atmospheric uncertainties in a timely way. The use of atmospheric models and other datasets to correct individual interferograms is dependent upon the availability of external data, which varies in both space (from a single continuous GPS receiver to a continuous GPS network) and in time (from days for continuous GPS data to 3–6 months for atmospheric reanalysis). Empirical methods that do not rely on the immediate availability of other datasets are also useful (e.g. Bekaert et al. 2015), but only when data are coherent enough to approximate the relationship between elevation and phase over different length-scales. This may be problematic for volcano applications, where coherence is often limited to near-field deposits. In Chap. 3 (Parker et al. 2015) I therefore develop a novel strategy, using past atmospheric reanalysis data to quantify atmospheric uncertainties in InSAR datasets a priori on arc-wide scales. I demonstrate that the RMS variation in range change is dependent upon volcano topography, and for the Cascade volcanoes increases by 7 mm per kilometre of relief. I use this relationship to estimate detection thresholds for long-term monitoring of small magnitude (10 mm/yr) deformation signals, and short-term monitoring of ground deformation associated with pre-eruptive unrest. I find that a minimum of between 60–130 days are required to detect long-term linear deformation at the Cascade volcanoes, and that during periods of pre-eruptive unrest, ground deformation is most likely to be observed at shield volcanoes (detection threshold < 10 mm) and least likely to be observed at complex volcanoes, where pre-eruptive unrest has historically lasted < 1 week. This approach is widely applicable to volcano deformation monitoring at other volcanic arcs.

These advances in making InSAR measurements at volcanoes in northern California have immediate implications for other Cascade volcanoes that are known to have deformed in recent decades. Mount Baker and Mount St. Helens, both located in the Washington Cascades, have subsided following/during periods of magmatic unrest (Chap. 1), but past InSAR measurements have either been unsuccessful (e.g.

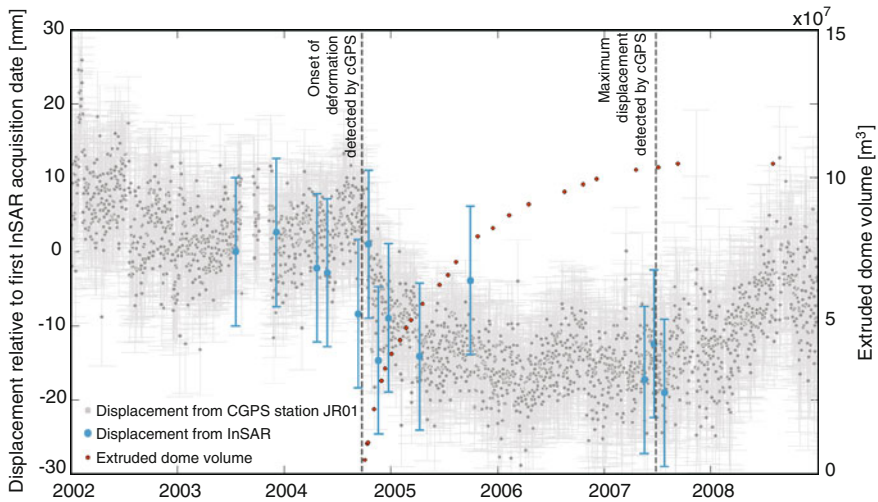


**Fig. 6.1** Preliminary time-series of co-eruptive subsidence at Mount St. Helens. Continuous GPS (CGPS) data are from Lisowski et al. (2008) with the onset of eruption and maximum displacements marked by the *dashed lines*. Erupted volume data was provided by L. Mastin. InSAR measurements were produced using the small baseline time-series approach of Berardino et al. (2002) with error bars calculated using atmospheric analysis described in Chap. 3

Mount Baker: Z. Lu, personal comm.) or have shown conflicting results (e.g. Mount St. Helens: Poland and Lu 2008). Both volcanoes are covered by >80 SAR acquisitions from ERS-1/2, ENVISAT and ALOS in multiple satellite look directions between 1992–2011. Preliminary small baseline time-series results from Mount St. Helens show up to 30 mm of subsidence during the 2004–2008 eruption, which is in agreement with continuous GPS measurements (Fig. 6.1). This suggests that, through the use of multi temporal analysis and/or atmospheric models, there is scope to gain useful information from InSAR data elsewhere in the Cascades. Unrest at both Mount Baker and Mount St. Helens during the last 40 years (Table 1.2) implies that magma is present at shallow depths (Crider et al. 2008; Sherrod et al. 2008; Werner et al. 2009; Crider et al. 2011). Future geodetic monitoring of both volcanoes is therefore essential, particularly at Mount Baker, where there is no ground-based geodetic network. Analysis of atmospheric phase contributions in Chap. 3 (Parker et al. 2015) suggests that a minimum of 8–9 and 6–8 consecutive Sentinel 1A interferograms would be required to measure deformation of 10 mm/yr at Mount Baker and Mount St. Helens respectively.

## 6.2 Volcano Deformation in the Southern Cascades

Both Medicine Lake Volcano and Lassen Volcanic Center are considered to be high - very high threat having exhibited seismic and/or eruptive unrest during the last century (Ewert et al. 2005). Measurements of ground deformation are therefore required to provide constraints upon the current state of each volcano. At Medicine Lake Volcano, past ground based geodetic surveys document subsidence at rates of  $\sim -10$  mm/yr since the 1950s, whereas at Lassen Volcanic Center, relatively little is known about the onset, temporal evolution, and source of deformation. Using the methods described above, I better constrain the spatial and temporal characteristics of deformation at each volcano, and use geophysical inversion methods and Monte Carlo error analysis to obtain the best fitting source geometry to InSAR data.

At Medicine Lake Volcano, I extend the geodetic record to 2011, and show that subsidence continued at historical rates of  $\sim 10$  mm/yr between 2004–2011 (Chap. 2; Parker et al. 2014). Combining multiple InSAR datasets I confirm that the ratio of vertical to horizontal displacements is high, which infers that the source is horizontally elongate. Analytical source models to past geodetic datasets show a discrepancy in source depth, which has implications upon interpretations of the process driving deformation. I provide additional constraints upon source models using the high spatial density of InSAR measurements, and find that the best fitting model is a horizontal sill located at 9–10 km depth. This source is similar to those constrained by past datasets and fits the hypothesis that deformation at Medicine Lake Volcano is caused by a combination of tectonic mechanisms, plus a component of volume loss at depth. A likely cause of volume loss is cooling and crystallisation of magmatic material (Chap. 4), and the depth of the model suggests that this may originate from within the intrusive complex imaged beneath the volcano.

At Lassen Volcanic Center, I carry out the first comprehensive investigation into ground deformation (Chap. 5). I use stacking techniques to constrain the spatial extent of the deformation field, and use time-series analysis to calculate the change in source volume over time. I find that, whilst Medicine Lake Volcano and Lassen Volcanic Center are currently subsiding at similar rates, the source geometry and time-scales of deformation are in fact quite different. Whereas subsidence of Medicine Lake Volcano has been ongoing since measurements began, I infer that the onset of subsidence at Lassen Volcanic Center was in the early 1990s. Time-series analysis and a qualitative comparison with past geodetic datasets suggests that subsidence of the volcano has decreased in rate over time from  $>10$  mm/yr in 2004–2007 to  $\sim 8$  mm/yr in 2007–2010. This decrease in rate may be due to either a decrease in the rate of volume change, or an increase in source depth. Combining ENVISAT datasets I demonstrate that the ratio of vertical to horizontal displacements at the volcano favours a point source. Evaluating a range of hypotheses, I suggest that subsidence is linked to cooling of subsurface magma and/or changes in the distribution of magmatic/hydrothermal fluids. Whether the 1992  $M_w 7.3$  Landers earthquake had a role in triggering subsidence requires further investigation, which will include adding

observations from other datasets such as ERS-1/2 interferograms and continuous GPS.

An additional dataset that has been used in volcano monitoring in the Cascades (e.g. Mount Baker: Crider et al. 2008) and elsewhere (e.g. Askja, Iceland: de Zeeuw-van D. et al. 2005) are repeat gravity measurements that constrain changes in the subsurface mass/density distribution over time (Rymer and Williams-Jones 2000). This technique would compliment deformation surveys at Medicine Lake Volcano and Lassen Volcanic Center, by helping to identify, for example, the drainage of fluids to greater depths (Chap. 5). Consequently gravity field campaigns at volcanoes in northern California are considered to be a priority by the U.S. Geological Survey Cascades Volcano Observatory (M. Poland, personal comm.).

### 6.3 Long-Term Volcanic Subsidence

Ground deformation recorded at the volcanoes of the southern Cascades presents an ideal opportunity to study volcanic subsidence that continues over decadal time-scales. Long-term volcanic subsidence provides insight into inter-eruptive processes, which comprise the longest portion of the eruptive cycle, and is a common but poorly understood phenomenon at volcanoes globally (Chap. 4). Based upon the inferred source of deformation at Medicine Lake Volcano (Chap. 2; Parker et al. 2014), I focus on intrusive processes that occur during non-eruptive periods. The identification of intrusive episodes is considered to be one of the greatest achievements of volcano InSAR (e.g. Lu and Dzurisin 2014), and using the example of Medicine Lake Volcano, I investigate how these events manifest geodetically over decadal time-scales.

I develop a new modelling approach to assess the rate of subsurface volume change arising from cooling and crystallising magma bodies (Chap. 4). This combines the outputs of geodetic models with petrological information and an existing thermal model. Exploring the parameter space demonstrates that the time-scale of magma cooling is dependent upon the intrusion geometry, the initial temperature contrast between intrusion and country rock, and magma composition. I find that (a) the early stages of volume change are most dependent upon cooling and crystallisation at the intrusion contact, which is a function of surface area and country rock temperature, and (b) changes in the rate of volume change are slower for sills of lower aspect ratio and correspond to changes in the crystallising assemblage. Cooling and crystallisation of intrusions with volume  $<3 \text{ km}^3$  may result in steady rates of volume loss, and therefore linear rates of subsidence, over decadal time-scales.

I use the results of Chap. 2 (Parker et al. 2014) to apply the modelling approach to subsidence at Medicine Lake Volcano. Comparing the results to the geodetic history, I identify a suite of models with initial volumes of  $1\text{--}2.5 \text{ km}^3$  that reproduce  $>65$  years of subsidence. These results suggest that magma intrusion has occurred on the order of hundreds of years before present. This is significant for hazard assessments and long-term monitoring at the volcano, as it suggests that magma intrusion has occurred more recently than the time of the last eruption  $\sim 1 \text{ ka}$ , and that subsidence

may continue for decades. Assuming these intrusive volumes are representative, this suggests that the intrusion to extrusion ratio at Medicine Lake Volcano is 0.8–17, which is in agreement with other estimates for the Cascades (e.g. Ingebritsen et al. 1989, 1994).

Such ground deformation is observed at numerous volcanic centres, and this modelling approach presents a physically reasonable and simple way of coupling geodetic and petrological measurements to provide insight into crustal magma fluxes and the timing of magma intrusion. In Chap. 4 I identify several additional applications of this model, including an investigation into the role of temperature-dependent viscoelasticity in modulating deformation signals associated with magmatic intrusions.

## 6.4 Future Role of InSAR in Volcanology

Previously the global distribution of InSAR measurements has been uneven in space and time, often with no obvious correlation between satellite acquisitions and the location of historically active volcanoes, or the time of volcanic activity. However, new satellites are either tasked to collect data over regions of interest (e.g. TerraSAR-X), or have more systematic acquisition strategies at higher repeat intervals (e.g. Sentinel 1A). Imagery from these satellites is available in a matter of days to hours, which is now lending SAR to becoming an operation monitoring tool during eruptive crises (e.g. Eyjafjallajökull: Sigmundsson et al. 2010). The increasing temporal resolution of satellite acquisitions will also aid in reducing the effects of temporal decorrelation (described in Chap. 1). This is particularly valuable in tropical regions, which have been under-represented in InSAR studies due to temporal decorrelation caused by dense vegetation (Ebmeier et al. 2013a). The higher repeat intervals will also be key to making observations of processes that occur over short time-scales. This will benefit our understanding of phenomena such as dike emplacement and dome growth, which occur over hours–days (Pinel et al. 2014), and cyclical deformation signals, such as bradyseisms, which may have previously been aliased. Maximising the impact of the large volumes of SAR data now being acquired will require new advances in automated processing, methods of automatically flagging possible deformation signals (e.g. Spaans and Hooper 2014), plus procedures for cataloguing such large datasets (Pinel et al. 2014).

An overarching aim of volcanology is the ability to forecast volcanic eruptions. Eruptions are often preceded by periods of unrest, but the probability that unrest anticipates eruption, and whether the progression of unrest is linked to the nature/magnitude of eruption, is unclear (Sparks et al. 2012; Phillipson et al. 2013). Key to answering these questions will be the collation of a global dataset of observations which, from a ground deformation perspective, will require building upon the fragmented InSAR observations of past satellite missions.

Of 1390 named subaerial Holocene volcanoes, 540 have been studied (including the reporting of null results) using InSAR for at least 3 years (Biggs et al. 2014). This includes systematic studies from, but not limited to, the Aleutian arc (Lu and



Dzurisin 2014); Central America (Ebmeier et al. 2013b); the Andes (Pritchard 2003); and east Africa (Biggs et al. 2009, 2011). In many other regions where InSAR data are abundant, such as the Cascades, the record of published InSAR measurements is dominated by studies of individual volcanoes known to have deformed. In other cases, InSAR measurements have not been made at all due to difficulties in applying data. This latter category includes many regions, particularly in the tropics, that are rich in volcanological activity but remain unstudied geodetically. For example, Papua New Guinea is host to more than 28 potentially active volcanoes, with over 1 million people living within 30 km of a volcano (United Nations Global Assessment Report on Disaster Risk Reduction 2015). The remoteness of these volcanoes, and the limited geophysical resources available to monitor them, makes regional-scale InSAR an ideal monitoring tool, and one of few realistic ways of identifying eruption hazards.

The ESA Sentinel 1A mission is the first opportunity for on-going, systematic, regional-scale C-band InSAR surveys at volcanic arcs globally, and with a satellite repeat interval that may be high enough to overcome the effects of temporal decorrelation in the tropics. This instrument will therefore aid in ensuring uniformity of measurements of ground deformation, and by adopting a systematic approach globally, it is possible to overcome any bias towards the reporting of unrest that results in eruption (e.g. Moran et al. 2011). The next step will then be determining when, and how, these large datasets can be used to derive probabilities for individual systems (Cashman and Biggs 2014). This includes taking a probabilistic approach in determining the significance of volcano deformation as a precursor for volcanic eruptions (Biggs et al. 2014).

## References

- Bekaert, D. P. S., Hooper, A., & Wright, T. J. (2015). A spatially-variable power-law tropospheric correction technique for InSAR data. *Journal of Geophysical Research*, 120(2), 1345–1356.
- Berardino, P., Fornaro, G., Lanari, R., & Sansosti, E. (2002). A new algorithm for surface deformation monitoring based on small baseline differential SAR interferograms. *IEEE Transactions on Geoscience and Remote Sensing*, 40, 2375–2383.
- Biggs, J., Anthony, E. Y., & Ebinger, C. J. (2009). Multiple inflation and deflation events at Kenyan volcanoes. *East African Rift. Geology*, 37(11), 979–982.
- Biggs, J., Bastow, I. D., Keir, D., & Lewi, E. (2011). Pulses of deformation reveal frequently recurring shallow magmatic activity beneath the Main Ethiopian Rift. *Geochemistry, Geophysics, Geosystems*, 12(9)
- Biggs, J., Ebmeier, S. K., Aspinall, W. P., Lu, Z., Pritchard, M. E., Sparks, R. S. J., et al. (2014). Global link between deformation and volcanic eruption quantified by satellite imagery. *Nature Communications* 5.
- Cashman, K., & Biggs, J. (2014). Common processes at unique volcanoes - a volcanological conundrum. *Frontiers in Earth Science*, 2, 28.
- Crider, J. G., Hill, J. K., & Williams-Jones, G. (2008). Thirty-year gravity change at Mount Baker Volcano, Washington, USA: Extracting the signal from under the ice. *Geophysical Research Letters*, 35(20)

- Crider, J. G., Frank, D., Malone, S. D., Poland, M. P., Werner, C., & Caplan-Auerbach, J. (2011). Magma at depth: a retrospective analysis of the 1975 unrest at Mount Baker, Washington. *USA. Bulletin of Volcanology*, 73(2), 175–189.
- de Zeeuw-van, D. E., Rymer, H., Sigmundsson, F., & Sturkell, E. (2005). Net gravity decrease at Askja volcano, Iceland: constraints on processes responsible for continuous caldera deflation, 1988–2003. *Journal of Volcanology and Geothermal Research*, 139(3), 227–239.
- Doin, M.-P., Lasserre, C., Peltzer, G., Cavalie, O., & Doubre, C. (2009). Correction of stratified atmospheric delays in SAR interferometry: Validation with global atmospheric models. *Journal of Applied Geophysics*, 69, 35–50.
- Ebmeier, S. K., Biggs, J., Mather, T. A., & Amelung, F. (2013a). Applicability of InSAR to tropical volcanoes: insights from Central America. *Geological Society, London, Special Publications*, 380(1), 15–37.
- Ebmeier, S. K., Biggs, J., Mather, T. A., & Amelung, F. (2013b). On the lack of InSAR observations of magmatic deformation at Central American volcanoes. *Journal of Geophysical Research*, 118(5), 2571–2585.
- Ewert, J. W., Guffanti, M., & Murray, T. L. (2005). An assessment of volcanic threat and monitoring capabilities in the United States: framework for a National Volcano Early Warning System NVEWS. U.S. Geological Survey Open File Report (2005-1164).
- Hooper, A. (2008). A multi-temporal InSAR method incorporating both persistent scatterer and small baseline approaches. *Geophysical Research Letters*, 35(16), L16302–L16312
- Hooper, A., & Zebker, H. A. (2007). Phase unwrapping in three dimensions with application to InSAR time series. *Journal of the Optical Society of America*, 24(9), 2737–2747.
- Ingebritsen, S. E., Mariner, R. H., & Sherrod, D. R. (1994). Hydrothermal systems of the Cascade Range, north-central Oregon. No. 1044-L.
- Ingebritsen, S., Sherrod, D., & Mariner, R. (1989). Heat flow and hydrothermal circulation in the Cascade Range, north-central Oregon. *Science*, 243(4897), 1458–1462.
- Jolivet, R., Grandin, R., Lasserre, C., & M.-P., D., Peltzer, G... (2011). Systematic InSAR tropospheric phase delay corrections from global meteorological reanalysis data. *Geophysical Research Letters*, 38(L17311),
- Jolivet, R., Agram, P. S., Lin, N. Y., Simons, M., Doin, M.-P., Peltzer, G., et al. (2014). Improving InSAR geodesy using global atmospheric models. *Journal of Geophysical Research*, 119(3), 2324–2341.
- Lisowski, M., Dzurisin, D., Delinger, R. P., & Iwatsubo, E. Y. (2008). Analysis of GPS-Measured Deformation Associated with the 2004–2006 Dome-Building Eruption of Mount St. Helens, Washington. U.S. *Geological Survey Professional Paper*, 1750, 301–333.
- Lu, Z., & Dzurisin, D. (2014). *InSAR Imaging of Aleutian Volcanoes: Monitoring a Volcanic Arc from Space*. Chichester: Springer-Praxis.
- Moran, S. C., Newhall, C., & Roman, D. C. (2011). Failed magmatic eruptions: late-stage cessation of magma ascent. *Bulletin of Volcanology*, 73(2), 115–122.
- Parker, A. L., Biggs, J., & Lu, Z. (2014). Investigating long-term subsidence at Medicine Lake Volcano, CA, using multi temporal InSAR. *Geophys. J. Int.*, 199(2), 844–859.
- Parker, A. L., Biggs, J., Walters, R. J., Ebmeier, S. K., Wright, T. J., Teanby, N. A., et al. (2015). Systematic assessment of atmospheric uncertainties for InSAR data at volcanic arcs using large-scale atmospheric models: Application to the Cascade volcanoes, United States. *Remote Sensing of Environment*, 170, 102–114.
- Phillipson, G., Sobradelo, R., & Gottsmann, J. (2013). Global volcanic unrest in the 21st century: an analysis of the first decade. *Journal of Volcanology and Geothermal Research*, 264, 183–196.
- Pinel, V., Hooper, A., De la Cruz-Reyna, S., Reyes-Davila, G., Doin, M.-P., & Bascou, P. (2011). The challenging retrieval of the displacement field from InSAR data for andesitic stratovolcanoes: Case study of Popocatepetl and Colima Volcano, Mexico. *Journal of Volcanology and Geothermal Research*, 200(1), 49–61.
- Pinel, V., Poland, M. P., & Hooper, A. (2014). Volcanology: Lessons learned from Synthetic Aperture Radar imagery. *Journal of Volcanology and Geothermal Research*, 289, 81–113.

- Poland, M. P., Bürgmann, R., Dzurisin, D., Lisowski, M., Masterlark, T., Owen, S., et al. (2006). Constraints on the mechanism of long-term, steady subsidence at Medicine Lake volcano, northern California, from GPS, levelling and InSAR. *Journal of Volcanology and Geothermal Research*, 150(1), 55–78.
- Poland, M. P., & Lu, Z. (2008). Radar Interferometry Observations of Surface Displacements During Pre- and Coeruptive Periods at Mount St. Helens, Washington, 1992–2005. *U. S. Geological Survey Professional Paper*, 1750, 361–382.
- Pritchard, M. E. (2003). Recent crustal deformation in west- central south america,. Ph.D. thesis, Calif. Inst. Technol., Pasadena. (Available at <http://etd.caltech.edu/etd/available/etd-06022003-105512/>).
- Rymer, H., & Williams-Jones, G. (2000). Volcanic eruption prediction: Magma chamber physics from gravity and deformation measurements. *Geophysical Research Letters*, 27(16), 2389–2392.
- Sherrod, D. R., Scott, W. E., & Stauffer, P. H. E., (2008). A Volcano Rekindled: The Renewed Eruption of Mount St. Helens, 2004-2006. U.S. Geological Survey Professional Paper (p. 856) (1750)
- Sigmundsson, F., Hreinsdóttir, S., Hooper, A., Árnadóttir, T., Pedersen, R., Roberts, M. J., et al. (2010). Intrusion triggering of the 2010 Eyjafjallajökull explosive eruption. *Nature*, 468(7322), 426–430.
- Spaans, K., & Hooper, A. J. (2014). Improving volcano monitoring through rapid, automatic InSAR processing. abs.]: Eos (American Geophysical Union Transactions), Fall Meeting Supplement, abs. G31A-0403.
- Sparks, R. S. J., Biggs, J., & Neuberg, J. W. (2012). Monitoring Volcanoes. *Science*, 335(6074), 1310–1311.
- Walters, R. J., Elliott, J. R., Li, Z., & Parsons, B. (2013). Rapid strain accumulation on the Ashk-abad fault (Turkmenistan) from atmosphere-corrected InSAR. *Journal of Geophysical Research*, 118(7), 3674–3690.
- Werner, C., Evans, W. C., Poland, M., Tucker, D. S., & Doukas, M. P. (2009). Long-term changes in quiescent degassing at Mount Baker Volcano, Washington, USA; Evidence for a stalled intrusion in 1975 and connection to a deep magma source. *Journal of Volcanology and Geothermal Research*, 186(3), 379–386.

# Curriculum Vitae

## Amy L. Parker

**Current Address** Department of Spatial Sciences, Western Australia School of Mines, Curtin University, Perth, Western Australia.  
**Mobile telephone** +61 426 052 221  
**Email** amylauraparker@gmail.com  
**Date of Birth** 03/03/1990

My expertise lies in the application of InSAR data to monitor, measure, and understand ground displacements occurring due to natural and man-made phenomena. I am broadly interested in how InSAR can be implemented as a low-cost reservoir monitoring tool, and am currently involved in a project to measure subsidence of the Perth Basin due to groundwater abstraction. Other research interests include carbon capture and storage, hydrofracturing and induced seismicity.

### Employment

<b>Nov 2015–present</b> Curtin University, Australia	<b>Research Associate</b> My research involves the application of InSAR data to monitor, measure, and understand ground displacements occurring due to natural and man-made phenomena. I am broadly interested in how InSAR can be implemented as a low-cost reservoir monitoring tool, and am currently involved in a project to measure subsidence of the Perth Basin due to groundwater abstraction.
<b>July–Oct 2015</b> University of Bristol, UK	<b>Postdoctoral Researcher</b> Working with new satellite datasets to investigate volcanic crises  Publication of research undertaken during my Ph.D.

### **Academic Background**

**2011–2015**

University of Bristol,  
UK

#### **Ph.D. - Monitoring Cascade Volcanoes Using InSAR**

My Ph.D. thesis received the Springer Thesis Award in recognition of scientific excellence and impact on research Development of strategies to improve the application of InSAR in challenging conditions (testing/developing advanced InSAR analysis techniques, application of weather models)

Modelling the long term geodetic response to magmatic intrusions (geodetic, thermal and viscoelastic modelling) Arc-wide assessment of the application of InSAR in the Cascades

**2008–2011**

University of  
Liverpool, UK

#### **First Class BSc. (Hons) Geophysics (Geology)**

Mathematics and Physics trainings

Geology training: e.g. Geological Mapping, Structural Geology

Geophysical training: e.g. Signal Processing, Exploration Geophysics

Honours project: Geodetic and remote sensing investigation of the 2010 Haiti earthquake. Forward and inverse modelling of co/post-seismic deformation from InSAR. Assessment of the implications of the earthquake upon future seismic hazard

### **Training and Experience**

**Nov 2015**

**EAGE Workshop: Reservoir Monitoring using InSAR, Perth, Aus.**

**Jun–Aug 2012, 2013**

**USGS - Cascades Volcano Observatory, WA, USA.**

Gained experience of working in a government run volcano observatory, building collaborations, establishing common research interests and identifying how my research may benefit volcano monitoring in the USA

**Jun 2013**

**UNAVCO GPS Processing Course, CO, USA.**

Used GAMIT/GLOBK software to process campaign and continuous GPS data

**May 2013**

**Seismic/GPS Geophysical Fieldwork, Ethiopia.**

Organised and carried out fieldwork as part of a two man team servicing seismic and continuous GPS networks at Ethiopian volcanoes

**Aug 2012**

**UNAVCO InSAR Processing Course, CO, USA.**

Consolidated knowledge of InSAR processing and error analysis

- Jul 2012** **Independent Fieldwork, Medicine Lake Volcano, CA, USA.**  
Secured funding for, organised and led fieldwork based upon my work with InSAR
- 2011–2015** **Assisting with supervision of postgraduate research students**  
University of Bristol MSc students and visiting Ph.D. students from Nigeria and Ethiopia. Teaching InSAR processing and basic interpretation using MATLAB.
- 2011–2015** **Teaching assistant for undergraduate classes.**  
ArcGIS, Geological Mapping, MATLAB programming, Geophysical field-skills
- Jan 2011** **Geophysical exploration fieldwork, Tenerife, Spain.**  
Data collection using gravity, magnetics, GPR, resistivity, seismics etc.
- Jun–Aug 2010** **USGS: National Earthquake Information Centre, CO, USA.**  
Independently organised a funded internship with the USGS to produce regional seismic hazard summaries
- Jun 2009** **Geological mapping training, Cantabria, Spain.**  
Comprehensive geological mapping course and independent mapping
- Scholarships and Awards**
- Dec 2015** Springer Thesis Prize
- Dec 2014** University of Bristol Alumni Foundation Grant
- Jun 2014** Volcanic and Magmatic Studies Group Conference Grant (VMMSG, UK)
- Dec 2013** AGU Fall Meeting Student Travel Grant (American Geophysical Union, USA)
- Jun 2013** Volcanic and Magmatic Studies Group Workshop Grant (VMMSG, UK)
- Jun 2013** UNAVCO Student Support Grant (UNAVCO, CO, USA)
- Jul 2012** UNAVCO Student Support Grant (UNAVCO, CO, USA)
- Jun 2012** Jack Kleinman Grant for Volcano Research (Community Foundation for Southwest Washington, WA, USA)
- 2011–2015** Natural Environment Research Council Ph.D. Studentship
- Jul 2011** NW Geological Society Prize for Geophysics (NW Geological Society, UK)
- 2008, -09, -10** Bibby Attainment Scholarship (University of Liverpool, UK)

- Public Outreach and Communication**
- May 2014** **Pint of Science International Science Festival**  
Organised, publicised and hosted the Bristol leg of this international science festival designed to bring popular science to a public forum
- May 2014** **Geological Remote Sensing Group Newsletter**  
Authored an article on advanced InSAR analysis methods
- April 2014** **University of Bristol Cabot Institute Blog**  
Authored a blog post in response to the launch of the ESA Sentinel-1 and the compilation of global volcano deformation data
- May 2013** **Short film on Ethiopian Volcanoes**  
Whilst on fieldwork in Ethiopia I was accompanied by a film crew and interviewed about geophysics, volcano monitoring and volcanic hazards
- 2012–2015** **University of Bristol, Cabot Institute Press Gang**  
Coordinate press releases for upcoming publications from the School of Earth Sciences, several of which have been featured online/in the press
- Jun 2015** **Formal Science Communication (Selected Examples)**  
**British Geological Survey Meeting, Bristol, UK**  
Using InSAR to monitor ground subsidence and induced seismicity
- Sep 2014** **Wegener: Measuring and Modelling our Dynamic Planet, Leeds, UK**  
Investigating the long-term geodetic response to magmatic intrusion at volcanoes in northern California
- Dec 2013, 2015** **American Geophysical Union Fall Meeting, CA, USA**  
Investigating Subsidence at Volcanoes in Northern California Using InSAR
- Sept 2013** **European Space Agency Living Planet Symposium, Edinburgh, UK**  
Monitoring Cascade Volcanoes Using Multi-Temporal InSAR
- Aug 2013** **USGS Cascades Volcano Observatory, WA, USA**  
Monitoring Cascade Volcanoes Using InSAR: Medicine Lake Volcano
- Additional Skills**
- Membership** European Association of Geoscientists and Engineers; The Centre of Observing and Modelling Earthquakes, volcanoes and Tectonics (COMET); British Geophysical Association; American Geophysical Union; Geological Remote Sensing Group; Royal Astronomical Society

<b>Datasets</b>	SAR, LandSAT, digital elevation models, global weather models, maps, plus seismic and other geophysical datasets
<b>Software</b>	Experience with MATLAB, bash, FORTRAN and other scripting languages, GMT, Adobe Illustrator, ArcGIS and other graphics applications

## Publications

**Parker, A. L.**, InSAR Observations of Ground Deformation: Application to the Cascades Volcanic Arc, *Springer Thesis Series*, ISBN:978-3-319-39033-8, 2016

**Parker, A. L.**, J. Biggs, Z. Lu, Constraining mechanisms of volcanic subsidence at Lassen Volcanic Center, CA, using InSAR, *Journal of Volcanology and Geothermal Research*, (doi:[10.2016/j.jvolgeores.2016.04.013](https://doi.org/10.2016/j.jvolgeores.2016.04.013)), 2016

**Parker, A. L.**, J. Biggs, R. J. Walters et al., Systematic arc-scale assessment of atmospheric uncertainties in InSAR data using large-scale atmospheric models: application to the Cascades, *Remote Sensing of Environment*, (doi:[10.1016/j.rse.2015.09.003](https://doi.org/10.1016/j.rse.2015.09.003)), 2015

**Parker, A. L.**, J. Biggs, and Z. Lu, Investigating long-term subsidence at Medicine Lake Volcano, CA, using multitemporal InSAR. *Geophysical Journal International*, (doi:[10.1093/gji/ggu304](https://doi.org/10.1093/gji/ggu304)), 2014

**Parker, A. L.**, J. Biggs, C. Annen, Time constraints on magma intrusion from thermal models of long-term subsidence: Medicine Lake Volcano, CA, in prep  
Turner, B., J. Jenkins, R. Turner, **A.L. Parker**, et al., Seismicity of the Earth 1900–2010 Himalaya and vicinity, *U.S. Geological Survey Open-File Report 2010-1083-J*, 2013

J. Jenkins, B. Turner, R. Turner, G. P. Hayes, A. Sinclair, S. Davies, **A. L. Parker**, et al., Seismicity of the Earth 1900–2010 Middle East and vicinity, *U.S. Geological Survey Open-File Report 2010-1083-K*, 2013

## Referees

Dr Juliet Biggs, (Academic Supervisor)	Prof. Zhong Lu, (USGS Collaborator)
University of Bristol, UK	Southern Methodist University, USA
Juliet.Biggs@bristol.ac.uk	zhonglu@smu.edu
+44117 331 5001	214 768 0101